Training and validation of a human ventricular cardiac action potential model to predict action potential duration response to acute inhibition of two major ionic currents

Yann-Stanislas Hubert Marc Barral
Wolfson College
University of Oxford

A thesis submitted for the degree of
Doctor of Philosophy

Hilary 2023

Abstract

Drugs can perturb the electrical activity of cardiac muscle cells, which may lead to cardiac adverse events. The inhibition of a potassium current (I_{Kr}) has been shown to prolong the cellular and ventricular repolarisation time, respectively characterised by the action potential (AP) duration (APD) and the QT interval on the ECG, promoting arrhythmia. The *in vitro* characterisation of I_{Kr} inhibition is a key part of pre-clinical cardiac safety assessment for drug candidates. The proarrhythmic risk is further evaluated clinically, with particular focus on QT.

The inhibition of a calcium current (I_{CaL}) can mitigate the prolongation of APD and QT induced by I_{Kr} inhibition. Because pre-clinical and clinical guidelines are based on different endpoints, compounds inhibiting both I_{Kr} and I_{CaL} may be incorrectly deemed proarrhythmic pre-clinically, in which case compounds with a potentially advantageous risk/benefit ratio may not reach the patient.

Biophysically-detailed models of the cardiac AP have emerged as tools linking *in vitro* observations with *in vivo* proarrhythmic risk. This thesis establishes a framework to integrate newly generated experimental data into the development of a novel predictive AP model.

New data were generated *ex vivo* in adult human ventricular tissue to investigate the relationship between drug-induced changes in APD, I_{Kr} inhibition, and I_{CaL} inhibition. A framework was developed to calibrate an AP model to this new data, with particular considerations for limitations on the data and on the understanding of mechanisms underlying the AP. Using this framework, a new AP model was calibrated, achieving improved predictions of drug-induced changes in APD in comparison with previous AP models.

Accurately predicting the changes in APD from *in vitro* experiments is the first step towards reliable predictions of drug-induced changes in clinically-relevant biomarkers. This work therefore contributes to a greater integration of *in vitro* experiments and *in silico* tools, and to enhanced pre-clinical predictions of the cardiac safety assessment of new compounds.

Acknowledgements

I want to thank my supervisors from the bottom of my heart for their immutable support, help and trust: Ken for initiating this splendid journey, believing in me, and taking your time to get me on board with the project, Dave for calmly and kindly challenging my ideas and advances, enabling me to become more and more of a rigorous scientist through the project, Gary for all the time and energy you took to make me grow, getting me to write scientific articles properly, learning how to link the pieces of the puzzle together, Michael for your invaluable expertise, inspiring storytelling skills and contagious passion for making scientific challenges so lively, and Liudmila for getting me to better communicate with a broader audience outside of my little field of expertise, for your invaluable insights into the experimental data that gave me a few eureka moments, and for your support through the different stages of the project.

When I am looking back at where I started, I am thinking "what a great journey", and I know it would have never been possible without your passion, patience, expertise and support. I am deeply grateful for having had you as supervisors on that DPhil journey.

I also want to deeply thank Thierry for making this journey possible and for believing in me.

My family was the founding rock of the whole story: Patrick and Magdalena always happy to get out of your way to cherish me at home (besides creating the perfect environment for me to grow up into a scientist), Alexandre and Raphael in particular for making sure I did not forget to play video games from time to time, Paul for the countless times we jumped off a plane together on our way to Legendary, Dominique, Valérie, Julie and Mélanie for the refreshing télétravail experience. Un énorme merci à Hubert & Jacqueline pour la bulle d'air qu'a toujours été Sainte Foy pour moi, me permettant de me ressourcer. Serdecznie dziękuję Markowi, Marysii, Maji i Adamowi za wsparcie, radosne dyskusje, i pierś z indyka z morelami.

I also want to thank my friends for being there along the road, so that my mental health was always taken care of. Particular thanks go to Alexandre, Anastasia, Annabell, Apo, Arthur, Carl, Carlo, Caro, Davide, Élise, Jasmin, Laura, Leanna, Louis, Luana, Lydia, Marius, Max, $(\text{Nadim})^2$, Nico, Nicolo, Ora, Petro, Sarah, Simon, Tino, Tom, Victor, Xavier, Yassine.

With all of you, I felt at home in Basel, Besançon, Casablanca, Lyon, Montbéliard, Mouans-Sartoux, Paris, Strasbourg, Turku, and Warszawa, so I could always give full energy to my work.

Contents

1 Introduction

Research question

During the healthy normal activity of a cardiac muscle cell, ions are constantly exchanged across the cell membrane, thus generating ionic currents. The interplay of the various ionic currents leads to changes in the transmembrane voltage, called the "action potential" (AP).

Several small molecule drugs, including drugs not targeting the heart, have been found to perturb the electrophysiological activity of the cardiac muscle. In particular, drugs inhibiting the rapid delayed rectifier K^+ current (I_{Kr}) are likely to prolong the AP duration (APD) in ventricular cardiomyocytes, which leads to prolongation of the QT interval on the electrocardiogram (ECG). I_{Kr} inhibition and QT prolongation are not dangerous *per se*, but they promote the risk of Torsades de Pointes (TdP), a deadly heart rhythm disorder. Pre-clinical and clinical guidelines for cardiac safety assessment of drug candidates therefore use a compound's potency to inhibit I_{Kr}, typically measured *in vitro* in patch-clamp experiments, and to prolong QT, respectively, as metrics to predict the compound's TdP risk. These guidelines have prevented drugs with unacceptable risk/benefit ratio from reaching the market, but they have also led to many false positives in the past, which has prevented some potentially safe compounds from being explored for therapeutic use.

In particular, concomitant inhibition of the L-type Ca^{2+} current (I_{CaL}) mitigates the delaying of the ventricular repolarisation induced by the blockade of I_{Kr}. Because of the counterbalancing effects of I_{Kr} inhibition (a pre-clinical guideline endpoint) and I_{CaL}

inhibition, drug candidates might be incorrectly deemed proarrhythmic, based on the current guidelines. Although this counterbalancing effect of I_{Kr} and I_{CaL} has frequently been mentioned in the literature, many open questions remain concerning the quantitative relationship between APD, I_{Kr} inhibition, and I_{CaL} inhibition. It therefore remains the case that no *in silico* biophysically-detailed AP model has been trained and validated to predict changes in repolarisation time induced by simultaneous inhibition of I_{Kr} and I_{CaL}.

The objective of this DPhil thesis is to develop an AP model to predict the changes in APD induced by the simultaneous acute inhibition of I_{Kr} and/or I_{CaL}, as measured *in vitro*.

This DPhil establishes a framework to integrate newly generated experimental AP data in the development of a novel predictive AP model. The development of this model touches several underlying questions, that will be answered in the thesis: How should we define quality control for AP data used in model training and validation? How do experimental drug-induced changes in APD measured *ex vivo* in adult human ventricular trabeculae compare with the predictions of human ventricular AP models? What literature model is the most promising for use as a base model for model development? What is the impact of model structure on the model calibration process? What model predictivity can be achieved after model calibration to the new AP data? Is it possible to capture inter-individual variations with the calibrated model? What parameters of the new AP model should be calibrated against the experimental data, and how should this calibration be performed?

After answering these questions, the model developed during this DPhil project predicts the repolarisation time response to inhibition of I_{Kr} and I_{CaL} at a cellular level. This constitutes the first step towards an *in silico* framework capable of integrating *in vitro* data into accurate predictions of the QT effect of drug candidates.

Detailed approach

Chapter 2: Background

This thesis combines *in silico* modelling with systems biology. The interested reader can find an introduction to aspects of these domains that are relevant to this DPhil in Chapter 2. There, the physiology of the heart and cardiomyocyte function are detailed,

together with how biophysically-detailed models of the AP have been developed. In the last section, different aspects of model calibration that are relevant to the work presented in this DPhil thesis are introduced.

Chapter 3: A parameter representing missing charge should be considered when calibrating action potential models

The contents of this Chapter were published in Frontiers in Physiology in April 2022 (Barral *et al.*, 2022b).

Chapter 3 introduces a parameter important to model calibration, which, in the canonical way of expressing the transmembrane voltage V in AP models, is hidden. The conservation of charge principle imposes an algebraic constraint on the system of ordinary differential equations (ODEs) that constitute an AP model. This constraint binds V to intracellular and extracellular ionic concentrations, thus making it possible to express V algebraically. This constraint is characterised by the constant net concentration of intracellular electrical charge attributed to non-modelled charge-carrying species, denoted Γ_0. Changing the expression of V to its algebraic form makes Γ_0 appear explicitly in the model and improves the numerical accuracy of the solutions. Γ_0 is also shown to be identifiable, suggesting that calibrating Γ_0 enables better calibration of AP models.

Chapter 4: Analysis and curation of adult human ventricular action potential data recorded under drug treatment

Part of the work included in Chapter 4 was presented at the Computing in Cardiology 2022 conference, and published as a proceedings article under the title "Normalisation of Action Potential Data Recorded with Sharp Electrodes Maximises Its Utility for Model Development" (Barral *et al.*, 2022a).

Chapter 4 introduces the experimental data that were used in this DPhil project. The AP data used for model calibration in this DPhil project were generated by AnaBios Corporation. The AP data were recorded *ex vivo* with the sharp electrode technique in adult human ventricular trabeculae exposed to various drugs. Bioanalytics of the tested adult human ventricular trabeculae were performed to measure the exact exposure of the tissues to tested drugs. *In vitro* measurements of drug inhibition of I_{Kr} and I_{CaL} were also performed to calculate the inhibitory effect of drugs used in the *ex vivo* experiments.

Chapter 4 also describes how the AP data were processed. In particular, recording artefacts generated by movements of the recording electrode were identified. To mitigate this, a normalisation strategy was devised, and a synthetic study was used to verify that normalisation did not significantly affect model parameterisation.

Chapter 5: Comparison of in silico predictions of action potential duration in response to inhibition of I_{Kr} and I_{CaL} with new human experimental data

A journal article combining the contents of Chapter 4 and Chapter 5 is being prepared for journal publication.

Biophysically-detailed AP models have been developed to integrate mechanistic knowledge about the mechanisms underlying the AP, and have been used to predict response to perturbations. In Chapter 5, drug-induced changes in APD predicted by AP models are compared with the experimental data from Chapter 4. The inhibition of ionic currents by drug perturbations tested *in vitro* was used as input to AP model simulations to generate predictions of drug-induced APD changes. Predictions were made with 11 human ventricular AP models from the literature, and compared with experimental observations.

Models based on the O'Hara *et al.* (2011) (ORd) model exhibited correct reproduction for the drugs affecting selectively I_{Kr} or I_{CaL}, but I_{CaL} inhibition had little mitigating effect on the APD prolongation induced by I_{Kr} inhibition. In contrast, models based on the Ten Tusscher & Panfilov (2006) (TP) and the Grandi *et al.* (2010) (GPB) models accurately reproduced the APD response to mixed ion channel blockers, but exhibited low sensitivity to selective I_{Kr} inhibition. The TP and GPB models reformulated by Mann *et al.* (2016) (TP-M and GPB-M, respectively) exhibited an improved sensitivity to I_{Kr} inhibition while retaining the mixed effects of I_{Kr} and I_{CaL} inhibition on APD. After qualitative and quantitative comparison of model predictions with experimental data, the TP and the GPB-M models were found to be the most promising base models for the development of an AP model trained and validated for the prediction of APD changes induced by inhibition of I_{Kr} and/or I_{CaL}.

Chapter 6: Goodness-of-fit versus model predictivity, or parameters that could versus should be calibrated

Preliminary methods and results of Chapter 6 were presented in a poster at the Cardiac Physiome 2021 Conference in November 2021. The contents of Chapter 6 are being prepared for journal publication.

The *ex vivo* data introduced in Chapter 4 were generated from different individuals. With the objective of developing individual-specific AP models in the following Chapter, Chapter 6 consists of three parts. In each part, a different aspect of the calibration of individual-specific AP models is investigated: prior knowledge on inter-individual variability, adequate selection of parameters to individualise, and the impact of model discrepancy on this selection. The inter-individual variability in model parameters was estimated from publicly available RNA sequencing data. Using "synthetic" data generated with different AP models, we investigated the influence of the set of individualised parameters on model predictions with and without model discrepancy. In this process, the variability and/or uncertainty in non-individualised parameters was incorporated into the model calibration process. Without model discrepancy, the more parameters that were individualised, the higher the model predictivity (provided that the parameters were identifiable). With model discrepancy, parameter identifiability and model predictivity were reduced. Finally, maximal model predictivity was achieved without individualising all the identifiable parameters: all parameters that *could* be individualised *should not necessarily* be individualised.

Chapter 7: Calibration of a human ventricular action potential model for prediction of changes in action potential duration induced by acute inhibition of $\mathbf{I_{Kr}}$ and $\mathbf{I_{CaL}}$

The contents of Chapter 7 are being prepared for journal publication.

Chapter 7 combines the previous pieces of work together to calibrate a new AP model to the *ex vivo* data. The new AP model was constructed based on the GPB-M model, in which the I_{Kr} component was changed to the model developed by Lei *et al.* (2019), and in which intracellular ionic concentrations are dynamically modelled allowing for the voltage to be written in its algebraic form. The *ex vivo* data were separated

into independent training and validation datasets. At first, the training dataset was treated as if it was obtained from a single generic individual. Training the new AP model with this approach therefore produced the model for a generic individual, denoted Gen-NP. The Gen-NP model was then re-used as a first guess for the training of individual-specific versions of the new AP model. Individualised parameters were selected with consideration for the findings presented in Chapter 6. By training an individual-specific model for each individual included in the training dataset, a collection of individual-specific models, denoted Col-NP, was created. APD changes induced by I_{Kr} and/or I_{CaL} inhibition predicted by the Gen-NP model and by Col-NP were finally compared with the validation dataset. The most accurate predictions were obtained with the Gen-NP model, which also exhibited improved predictivity compared with existing AP models studied in Chapter 5: the Gen-NP model predicted more accurately the effects of selective I_{Kr} and selective I_{CaL} inhibition, as well as the mitigation of I_{Kr} inhibition by I_{CaL} inhibition. Yet, further improvements will be needed before predictions by the Gen-NP model can replace *in vitro* or *in vivo* experiments reliably.

2 Background

2.1 Introduction

This Chapter introduces the background, concepts, and techniques that are used in the rest of this DPhil thesis. It contains four sections that provide the reader with background about the physiology of the mechanisms that are modelled in this work, an introduction to *in silico* tools used for cardiac safety assessment of drug candidates, and a detailed introduction and discussion of the framework for training and validation of computational models like the model developed in Chapter 7.

Section 2.2 introduces general background about heart physiology. Section 2.3 introduces the physiology of action potentials (APs) and mechanisms leading to their formation, from the molecular to the cellular scale. The historical evolution of *in silico* models for human ventricular AP is reviewed in the following Section 2.4. Finally, different aspects of AP model development are discussed in Section 2.5.

2.2 Heart physiology

2.2.1 Circulation

The heart is the vital organ that ensures the supply of oxygen and nutrients to the body, by maintaining blood circulation. The human cardiovascular system is presented in Figure 2.1. The heart is split into two sides (left and right) that pump the blood into two circuits (systemic and pulmonary, respectively). Low oxygen blood is pumped by the

right side of the heart towards the pulmonary circuit, so that the blood is oxygenated in the lungs. After that, the blood comes back to the left side of the heart. From there, the blood is distributed to the various organs and tissues. Low oxygen blood comes back to the right side of the heart, and the cycle can be repeated.

Each side of the heart is separated into two compartments by valves which ensure a unidirectional blood flow. The two sides of the heart have the same cyclic functioning principle. At first, the ventricles filled with blood contract, thus ejecting it into the arteries towards the pulmonary and systemic circuits. The ventricles remain contracted for a while to ensure a sufficient amount of blood is ejected. Note that the left ventricular muscle faces a higher mechanical load, and it is therefore larger and thicker.

After contracting, the ventricles relax and the ventricular pressure decreases. When the ventricular pressure becomes lower than the atrial pressure, the blood flows from the atria to refill the ventricles. The atria then contract to completely refill the ventricles, so that the heart is prepared for the next beat.

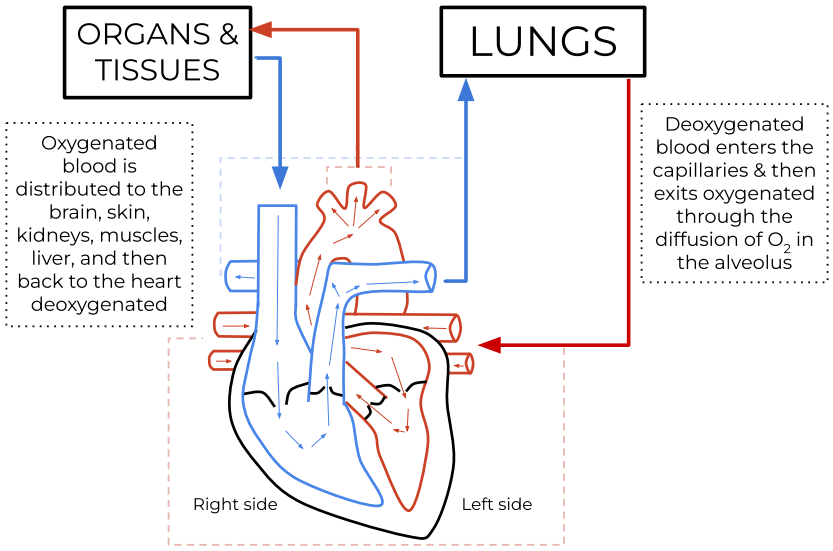

Figure 2.1: Schematic representation of the cardiovascular system and of the human heart, seen by a coronal section (Santilla, 2022).

2.2.2 The electrical activity of the heart

The cyclic functioning of the heart is governed by its electrical activity. The conduction network (Figure 2.2A) propagates an electrical signal, triggering contraction throughout the heart tissue. This activity can be visualised with electrocardiograms (ECG), which can be recorded non-invasively in patients. A typical ECG is sketched in Figure 2.2B.

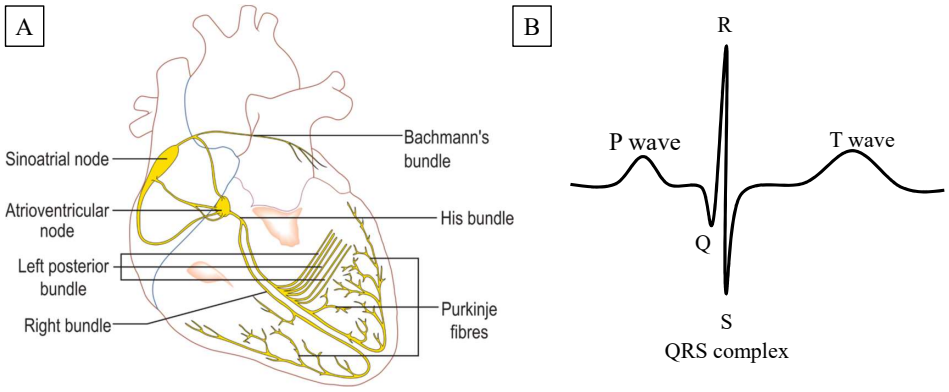

Figure 2.2: Schematic representation of the conduction system of the heart (**A**) (Madhero88, 2010), and sketch of a typical electrocardiogram (ECG) (**B**).

Under typical healthy conditions, the P wave corresponds to the propagation of the electrical signal to the atria, which subsequently contract. Then, the QRS complex is observed when the signal propagates through the wall separating the ventricles then spreads over them, while the atria return to resting state. After the QRS complex, ventricles remain contracted until the T wave, so that blood is expelled towards the body. Finally, the T wave is observed when the ventricles return to their resting state to prepare for the next beat. The QT interval on the ECG therefore characterises the time it takes for ventricles to return to resting state.

2.3 Electrophysiology of the cell

Living cells are surrounded by a membrane composed of a phospholipid bi-layer, forming a lipophilic medium which is mostly impermeable to charged species like ions (Gorter & Grendel, 1925). Transmembrane proteins called “ion channels” act as selectively permeable pores which enable the flow of ions across the membrane (Bean *et al.*, 1969). Ions can also be transported through the cell membrane actively via “ion pumps” or

passively via "ion exchangers" (Zaza & Rosen, 2000). Hence, the membrane acts as a filter that actively selects the ions that enter or exit the cell.

Various types of cardiac cells are needed to build the complex structure and activity of the heart, and electrophysiological properties vary between cell types. The work presented in this DPhil thesis focuses on the ventricular cardiac muscle cell (cardiomyocyte) which is the cell type central to heart contraction. In the rest of this DPhil thesis, unless stated otherwise, the "cell" refers to *the human ventricular cardiomyocyte.*

The ventricular muscle is constituted of three main layers with different expressions of ion channels, pumps, and exchangers (Antzelevitch, 2007): the epicardium (external layer), the myocardium, and the endocardium (internal layer). It is worth mentioning that muscular bundles called "trabeculae" project from the inner surface of the ventricles (Moore & Agur, 2007), as illustrated in Figure 2.3. Trabeculae contribute to heart contractility and (most importantly for this DPhil) they constitute relatively easily accessible endocardial cardiomyocyte fibres that can be used to investigate the cardiomyocyte electrophysiology, as in Chapter 4.

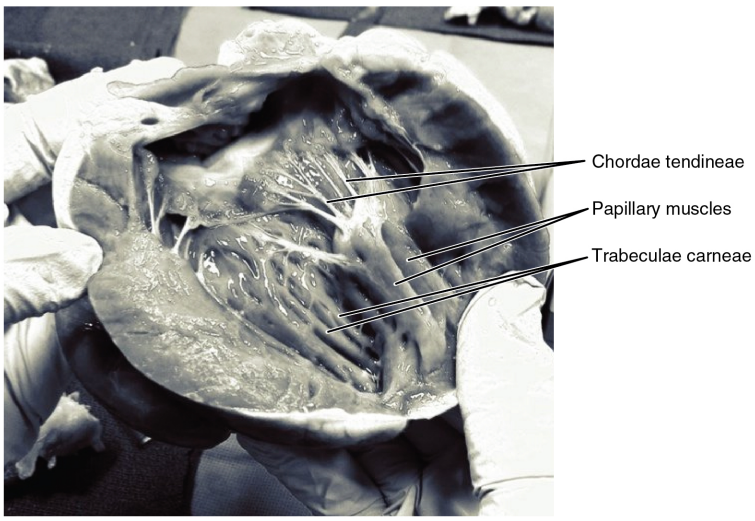

Figure 2.3: Frontal section of the interior of the heart showing the papillary muscles, chordae tendineae, and trabeculae carnae (OpenStax College, 2010).

2.3.1 The action potential

At the cellular scale, the electrical signal propagates as what is called the "action potential" (AP), which is the result of the interplay of several ionic currents. A typical human

ventricular AP and the major underlying ionic currents are shown in Figure 2.4.

The transmembrane voltage V can be modelled as voltage across an ideal capacitor, with electrical charges carried across the cell membrane by ionic currents (Hodgkin & Huxley, 1952):

$$\frac{\mathrm{d}V}{\mathrm{d}t} = \frac{1}{C_\mathrm{m}} \times I_\mathrm{total}, \tag{2.1}$$

with C_m the membrane capacitance, and I_total the sum of all ionic currents.[1]

When the cell is stimulated periodically under normal conditions, the complex interplay of the ion channels creates a periodic voltage signal (Figure 2.4).

Phase 0: The AP starts when the cell is stimulated (by neighbouring cells or by artificial stimulation) and the opening of the Na^+ channels is triggered, thus creating the fast sodium current, I_{Na} (Hodgkin & Katz, 1949). Phase 0 is called the "depolarisation phase" as the cell loses its negative polarisation.

Phase 1: I_{Na} rapidly deactivates, and the transient outward K^+ current, I_{to}, activates to release K^+ out of the cell, thus reducing V (Gustafsson *et al.*, 1982).

Phase 2: At this moment, the L-type Ca^{2+} current, I_{CaL}, and the rapid rectifier K^+ current, I_{Kr}, activate, leading to the plateau phase. I_{CaL} is attributed to Ca^{2+} flowing through $Ca_V1.2$ ion channels (Agrawal *et al.*, 2023). $Ca_V1.2$ channels are mostly located in membrane invaginations called T-tubules, facing the sarcoplasmic reticulum (SR). The SR in an intracellular Ca^{2+} reservoir which releases Ca^{2+} into the cell when exposed to Ca^{2+}, a phenomenon called "calcium-induced calcium release". The subsequent increase in the intracellular Ca^{2+} concentration is converted into mechanical contraction of the cell, in what is known as electro-mechanical coupling (Ebashi & Endo, 1968). I_{CaL} is sensitive to Ca^{2+} and V (Catterall, 2011) and inactivates because of low V and high intracellular concentration of Ca^{2+}. For further details on Ca^{2+} handling by cardiomyocytes, refer to the review by Agrawal *et al.* (2023).

Phase 3: The repolarisation phase starts when I_{CaL} inactivates, mainly driven by I_{Kr}. I_{Kr} is mainly attributed to K^+ fluxes through channels formed mainly by $K_V11.1$, encoded by the human ether-a-go-go related gene (hERG) (Sanguinetti *et al.*, 1995; Li *et al.*, 1996).

[1] Note that C_m and I_total are usually expressed per unit of surface.

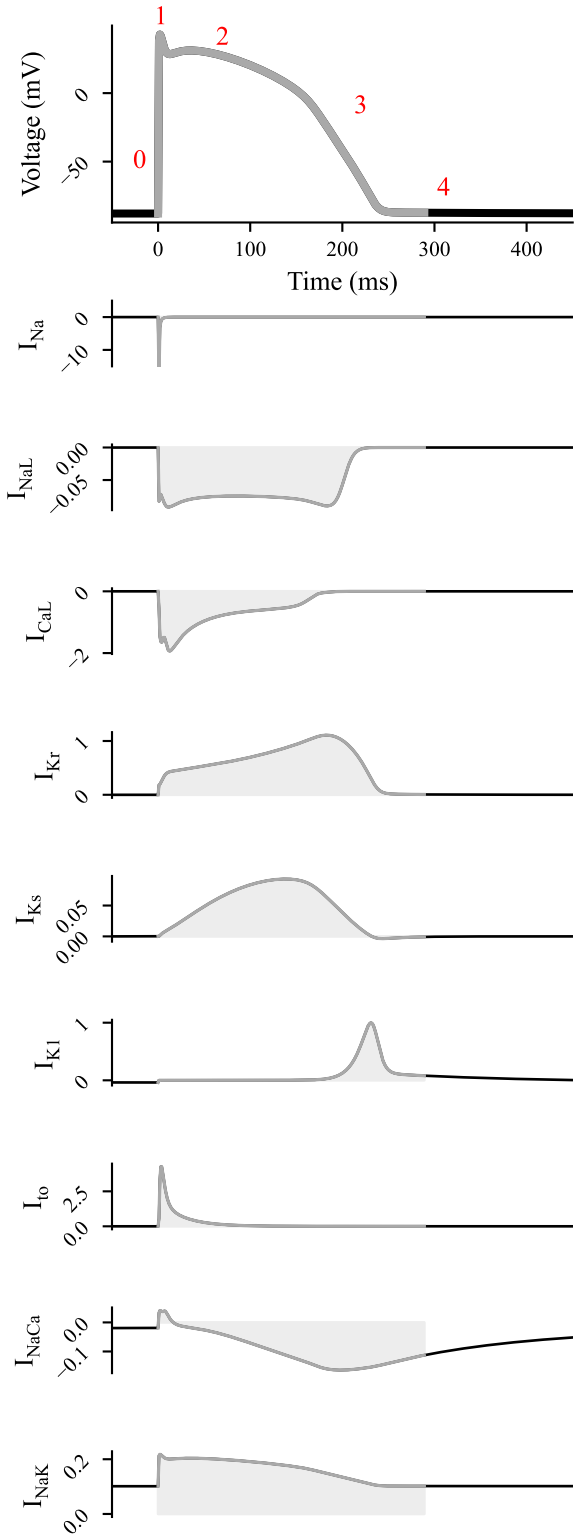

Figure 2.4: Typical ventricular AP and underlying activity of major ionic currents simulated with the Dutta *et al.* (2017) model. Currents are expressed in A/F.

Therefore, I_{Kr} is sometimes referred to as "hERG current". The repolarisation currents release K^+ to the extracellular space, bringing the cell voltage back to its resting membrane potential (RMP) of approximately $-80\,mV$. The amplitude of I_{Kr} determines the speed of the repolarisation, and therefore impacts the ventricular repolarisation time. Note that I_{Kr} is doubled with the slow rectifier K^+ current, I_{Ks}, which ensures the repolarisation when I_{Kr} is insufficient, a phenomenon called "repolarisation reserve" (Roden, 1998). The inward rectifier K^+ current, I_{K1}, ensures the final part of the repolarisation.

Phase 4: Finally, the cell stays at the RMP while the ion pumps and exchangers re-establish the ionic concentrations to prepare the next beat (Zaza & Rosen, 2000), leading in particular to the Na^+-K^+ pump current (I_{NaK}) and the Na^+-Ca^{2+} exchanger current (I_{NaCa}).

In an alternative to its derivative form (Eq. 2.1), V can be expressed algebraically as a difference of electrical charges carried by ions on both sides of the cell membrane:

$$V = \frac{1}{C_m} \times (Q_{i,\,total} - Q_{o,\,total}), \tag{2.2}$$

with $Q_{i,\,total}$ and $Q_{o,\,total}$ the total electrical charge of the intra- and extracellular spaces, respectively. The electrical charge can be computed from intra- and extracellular ionic concentrations (Varghese & Sell, 1997).

Note that Eq. 2.1 is found by differentiating Eq. 2.2: both forms are mathematically equivalent when a conservation law is applied to electrical charges (Varghese & Sell, 1997; Endresen *et al.*, 2000). The implications of using one or the other equation for V are investigated in Chapter 3.

2.3.2 Ionic currents

Ionic currents flow through ion channels, pumps, and exchangers. They are formed of complex transmembrane proteins, themselves composed of several transmembrane subunits forming a pore in their middle (Purves *et al.*, 2001). The pore is often selective to only certain ions. Depending on the spatial conformation of the ion channel, the pore is open or close, thus regulating the flow of ions through the pore. Therefore,

the ion channel is modelled as a variable resistance. Ionic currents I are canonically described with three terms:

$$I = G \times \mathcal{K}(V, \ldots) \times \mathcal{D}(V, \ldots), \tag{2.3}$$

with G the maximal conductance (or permeability) parameter, $\mathcal{K}$ a term describing the kinetics of factors influencing I, including conformational changes of the ion channel, and $\mathcal{D}$ a term describing the electrodiffusion force driving ions through the channel. G depends on the conductance of a single ion channel, as well as the number of functional ion channels in the cell membrane, therefore acting as a scaling factor for the ionic current.

Describing the kinetics of factors influencing I

The different terms in Eq. 2.3 have been given various formulations in the past to model ionic currents. The first model by Hodgkin & Huxley (1952) described ion channels as a series of gates:

$$I = G \times \prod_i gate_i \times \mathcal{D}, \tag{2.4}$$

with $gate_i$ the open fraction (between 0 and 1) of the gate i.

A few decades after Hodgkin & Huxley put the activity of ion channels into descriptive equations for the first time, Armstrong (1971) and Colquhoun (1973) proposed a description of ion channels using Markov models, in particular to describe ligands binding to ion channels. Markov models for ion channels rely on the assumption that one can describe stochastically the transitions between the conformations of the ion channel:

$$I = G \times O \times \mathcal{D}, \tag{2.5}$$

with O the fraction of open channels.

As any possible state can be added to Markov models, they offer much greater versatility (Rudy & Silva, 2006), but overly complex Markov models raise the issue of parameter unidentifiability (Horn & Vandenberg, 1984; Fink & Noble, 2009). Implications of parameter (un)identifiability are discussed in Section 2.5.3.

Describing the electrodiffusion driving force

There are important differences between intra– and extracellular concentrations of K^+, Na^+, Ca^{2+}, Cl^-, creating gradients of ionic concentrations across the cell membrane (Figure 2.5). This enables diffusion, a mechanism by which ions can cross a permeable membrane when there is a transmembrane gradient of concentrations (Nernst, 1889; Planck, 1910). Based on the concentrations in play, K^+ leave the cell, while Cl^-, Na^+ and Ca^{2+} enter the cell. Note that to preserve the transmembrane gradients of ionic concentrations in the long term, transport against the gradient is performed by ion exchangers and ion pumps.

As they are electrically charged, the diffusion of ions is impacted by V. Thus, there is a potential at which the direction of the flux of an ion A reverses: the "reversal potential", E_{rev}. E_{rev} can be computed from the Nernst equation (Nernst, 1889) as:

$$E_{rev} = \frac{RT}{zF} \ln\left(\frac{[A]_o}{[A]_i}\right), \tag{2.6}$$

with $[A]_i$ and $[A]_o$ the intra– and extracellular concentrations of A, z its valence, F the Faraday constant, R the gas constant, and T the temperature.

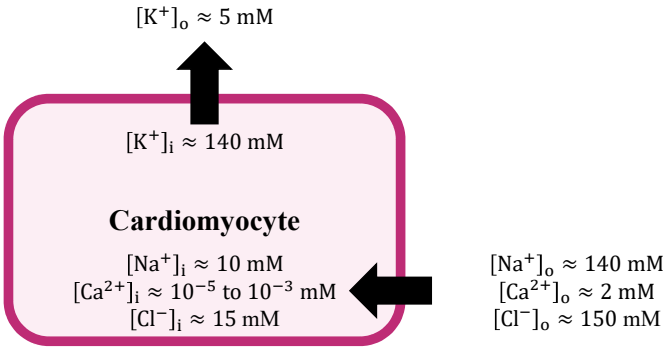

Figure 2.5: Electrochemical driving force for ionic currents. Intra- and extracellular concentrations of the three main ionic species responsible for APs in human ventricular cardiomyocytes.

Ionic concentrations in the external and internal compartments are usually modelled as uniform, thus making the electrodiffusion a 1-D problem. As ions diffuse through the cell membrane, an electrical current is created. The steady-state current is described, under the assumption of linearity of voltage in the membrane, with the Goldman-Hodgkin-Katz

(GHK) equation (Hodgkin & Katz, 1949):

$$I = G \times \mathcal{K} \times V \times \frac{[A]_{\mathrm{i}} e^{zFV/RT} - [A]_{\mathrm{o}}}{e^{zFV/RT} - 1}, \tag{2.7}$$

with I the electrical current due to the electrodiffusion of A. Note that G here corresponds to the membrane permeability to ions.

Alternatively, Ohm's law can be used:

$$I = G \times \mathcal{K} \times \Delta V, \tag{2.8}$$

with ΔV the difference between V and E_{rev}.

2.3.3 Experimental techniques for investigating the electrophysiological activity of cells

Many efforts have been put into investigating the electrophysiological activity of cells. Investigating the activity of ion channels in live cells is particularly challenging as one needs to record their activity in the least invasive manner possible.

The sharp electrode technique uses a micropipette filled with an electrolyte solution into which an electric wire is introduced. The sharp electrode is impaled into the recorded cell, either isolated or in tissue. This technique has been applied to record the AP in adult human cardiomyocytes in tissue configuration (Page *et al.*, 2016). The data presented in this DPhil thesis were recorded with this technique in human ventricular tissue *ex vivo* (Chapter 4).

The patch-clamp technique developed by Sakmann & Neher (1984) has been widely used to investigate the properties of ion channels, as its results are repeatable and reproducible (Li *et al.*, 2004). In brief, a glass pipette is brought in close proximity to the cell membrane and a seal is formed between the pipette and the membrane by suction. One electrode is inserted into the micropipette and the other electrode is immersed in the bath solution, outside of the cell, so that the voltage or current across the cell membrane (or a patch of membrane) can be recorded.

A common approach applicable with both techniques, called "voltage-clamp", is to maintain constant membrane potential allowing to measure ion currents across the

cell membrane. The protocol of applied voltage can be designed to explore various regimes of the activity of ion channels.

Note that to disentangle the different ionic currents, experiments are often carried out in non-cardiomyocyte cells engineered to express mostly a single type of ion channel (Kramer *et al.*, 2013).

A third technique consists of a microelectrode array (Thomas Jr *et al.*, 1972) in which a tissue is cultured on top of an array of electrodes. More recently, the microelectrode array concept has gained in significance, as it enables investigating electrophysiology at subcellular scale (Habib *et al.*, 2019; Hu *et al.*, 2020). Currently, there remain experimental limitations on invasiveness (Lin *et al.*, 2014), reproducibility (Hayes *et al.*, 2019) and cell adherence (Asakura *et al.*, 2015) to address in microelectrode array assays. Data from microelectrode arrays were not used in this DPhil.

2.4 Mathematical models of the human ventricular action potential

Since the seminal work of Hodgkin & Huxley (1952), the mechanisms underlying the cardiac AP have been progressively unveiled. AP models have been constructed by progressively integrating discoveries made in various sources (tissues, species) into mathematical models (Niederer *et al.*, 2009). In this section, AP models with major contribution to unraveling the human ventricular AP are presented.

The first mathematical model to represent the electrical activity of excitable cells was developed by Hodgkin & Huxley (1952). Their model represented quantitatively the electrophysiology of the squid giant axon, and reproduced its AP shape and size. This first model accounted only for three ionic currents.

Noble (1962) then extended the modelling work of Hodgkin & Huxley to Purkinje fibres. The same currents as in the Hodgkin & Huxley model were included in the Noble model, but the parameters were changed, to match with Purkinje fibres' sustained AP and pacemaker activity. This set the founding stone for the field of cardiac electrophysiology modelling.

McAllister *et al.* (1975) followed Noble's work and further detailed the functioning of Purkinje fibres, adding five currents to their model. DiFrancesco & Noble (1985) further

refined the model of the Purkinje fibre AP to consider the dynamic changes in intracellular concentrations due to ionic currents, including ionic pumps and exchangers.

Beeler & Reuter (1977) published the first model of the mammalian ventricular AP. It featured only four currents, focusing on the calcium current to reproduce the plateau phase of the AP. Luo & Rudy then developed two major models for the mammalian ventricular cardiomyocyte AP, based mainly on guinea pig data. The first Luo & Rudy (1991) model extended the work of Beeler & Reuter, remaining simple with only six ionic currents, and clamping the intracellular ionic concentrations to a fixed value. The second Luo & Rudy (1994) model, based on the first, included the dynamical changes of intracellular ionic concentrations, in particular calcium handling in the different subcellular compartments. This model was then adapted by Priebe & Beuckelmann (1998) to create a model of the *human* ventricular cardiomyocyte AP. Notably, the repolarisation current in the Priebe & Beuckelmann model was split into a fast (I_{Kr}) and a slow (I_{Ks}) component.

Bernus *et al.* (2002) introduced many simplifications to the Priebe & Beuckelmann model, such as clamping of the ionic concentrations and removal of the calcium handling component. Simulation with this model came at a minimal computational cost, which made it interesting for simulations of a cardiac tissue of interconnected cells.

The Ten Tusscher *et al.* (2004) (TNNP) and Ten Tusscher & Panfilov (2006) (TP) models were then based on the same idea of model simplification, yet keeping the dynamic modelling of intracellular concentrations and including the calcium handling component. One of the key features of the TP model is that it can reproduce alternans generation, despite its numerical simplicity. The TP model is still currently widely used as the cellular model underlying many ventricular tissue and whole-heart 3D models (Corrado *et al.*, 2021).

The Matsuoka *et al.* (2003) model added electro-mechanical coupling to the Luo & Rudy (1994) model, followed by Iyer *et al.* (2004a). However, the two models pursued two different objectives: studying electro-mechanical coupling for the former, studying arrhythmogenesis for the latter. These models were reused to construct the Asakura *et al.* (2014) model, and then the Himeno *et al.* (2015) model, with further details in the description of the calcium release-units and of calcium handling. Lately, the Bartolucci

et al. (2020) (BPS) model focused on the dependence of the calcium-induced calcium release to extracellular ionic concentrations. In particular, a new model for I_{CaL} and for the calcium release unit was used in the BPS model.

The Grandi *et al.* (2010) (GPB) model was developed to predict changes in the AP duration at 90% repolarisation (APD_{90}) induced by drugs inhibiting of repolarisation currents. The GPB model relied heavily on the TP and Iyer *et al.* (2004a) models of the human AP and on the Shannon *et al.* (2004) rabbit AP model, where Cl^- currents are described.

One year later, the O'Hara *et al.* (2011) (ORd) model was published, featuring the late sodium current (Maltsev *et al.*, 1998), I_{NaL}. The ORd model quantitatively captured APD_{90} effect of drugs inhibiting I_{Kr}, as well as early after-depolarisation (EAD) and alternans generation.

The ORd model was later recalibrated by Mann *et al.* (2016), Dutta *et al.* (2017), and Krogh-Madsen *et al.* (2017). Mann *et al.* and Krogh-Madsen *et al.* focused on the reproduction of the QT_c difference between the healthy population and patients with long QT syndrome (LQTS) type 1 and 2 who have a loss of function of I_{Ks} and I_{Kr}, respectively. Dutta *et al.* (ORd-CiPA) calibrated the ORd model to reproduce the APD_{90} response to changes in pacing frequency and to inhibition of five different ionic currents.

One of the latest human ventricular AP models was published by Tomek *et al.* (2019). This model was based on the ORd model, and includes the same Cl^- currents as the GPB model. An important feature in the Tomek *et al.* model is its calibration process, with an independent set of training and validation experimental data, that aims at improving the predictivity of the model. Following our finding that the voltage could not be written in its algebraic form in the Tomek *et al.* model because it did not conserve charge, an updated version of this model was developed to unclamp the concentrations of Cl^- and K^+ (Tomek *et al.*, 2020).

A centralised repository has been created to facilitate sharing, reuse, and further development of computational biology models (Yu *et al.*, 2011). The models used for this DPhil project were downloaded from `https://models.physiomeproject.org`.

2.4.1 Use of action potential models for cardiac safety assessment

Two guidelines, ICH S7B (ICH, 2005) and ICH E14 (ICH, 2006), guide the preclinical and clinical cardiac safety assessment of drug candidates. Pre-clinically, ICH S7B recommends to assess the propensity of drug candidates (and metabolites) to inhibit I_{Kr} *in vitro*, and to use *in vivo* animal models to predict their QT effect in humans. ICH E14 requires testing drug candidates clinically for their effects on the QT interval, corrected for heart rate (QT_c).

These guidelines succeeded at preventing proarrhythmic compounds from reaching the market (De Ponti, 2008), and updates have been made to these guidelines as arrhythmogenesis has been progressively unraveled (Lester, 2021). However, some limitations remain to this day (Vargas *et al.*, 2021). Mirams *et al.* (2011) showed for example that the proarrhythmic risk promoted by the inhibition of I_{Kr} can be mitigated by the inhibition of other currents, in particular I_{CaL}.

To try and address some of the limitations of these guidelines, the Comprehensive *in vitro* Proarrhythmia Assay (CiPA) initiative was launched (Sager *et al.*, 2014; Colatsky *et al.*, 2016). CiPA focuses on a drug's propensity to promote Torsades de Pointes (La Dessertenne, 1966), TdP, a deadly ventricular arrhythmia. Under the CiPA paradigm, new metrics classify drugs into three TdP risk categories: low, intermediate, or high risk. These risk categories are defined with 28 reference compounds (Li *et al.*, 2019). Proposed TdP risk classifications must be validated against a part of the dataset that is excluded from model training (Colatsky *et al.*, 2016), thus ensuring reliable classification of drugs into the correct risk categories. A key feature of the CiPA initiative is the integration of AP models into the cardiac safety assessment of new compounds based on their ability to inhibit ionic currents, typically measured *in vitro* in patch-clamp experiments. Different approaches have been used under the CiPA paradigm.

Dutta *et al.* (2017) used the net flux of electrical charges over an AP predicted by the ORd-CiPA model, in a metric called Q_{net}. Parikh *et al.* (2017) and Yoo *et al.* (2021) classified the drugs based on a neural network which processes AP markers simulated with the ORd-CiPA model. Gaur *et al.* (2020) developed a safety evaluation based on drug-induced changes in the repolarisation reserve.

Other TdP risk scores rely on another reference for the classification of drug-induced proarrhythmic risk (Woosley & Romer, 1999). They were designed based on occurrence of repolarisation abnormalities in populations of AP models (Passini *et al.*, 2017; Zhou *et al.*, 2020; Trovato *et al.*, 2022; Varshneya *et al.*, 2021), on simulated pseudo-ECGs (Romero *et al.*, 2018; Llopis-Lorente *et al.*, 2020), or on whole-heart simulations (Sahli-Costabal *et al.*, 2020).

All of these methods exhibit improved accuracy compared with the metric that originally inspired the ICH S7B guideline: the I_{Kr} inhibition by the drug at a concentration 30 times higher than its maximal effective free therapeutic concentration (C_{max}) (Redfern *et al.*, 2003). In particular, Q_{Net} was accepted as an example of TdP risk assessment matching the CiPA requirements (Li *et al.*, 2019).

However, with the exception of the metric of Gaur *et al.* (2020), these risk metrics cannot be measured experimentally.

The drug-induced APD_{90} change from baseline (ΔAPD_{90}) is measurable in adult human isolated muscle fibres, and it showed good agreement with drugs' effects on the ventricular repolarisation time measured on the ECG (Vicente *et al.*, 2018). Predicting the ΔAPD_{90} response to inhibition of ionic currents would therefore constitute a first step towards predicting clinically-relevant changes in ECG features from *in vitro* measurements. Therefore, in this DPhil project, we focus on the prediction of drug-induced ΔAPD_{90} using *in silico* AP models.

2.5 Calibration of new action potential models

After experimental data are collected, the next critical step in the development of new AP models is model calibration: "the process of adjusting parameters of a model to maximize the agreement between observed data and simulations" (Whittaker *et al.*, 2020). This is best done in two steps: model training and model validation. In model training, the mismatch between model outputs and experimental data is minimised. In model validation, the predictions of the trained model are compared with additional experimental data to assess model predictivity. The validation data are not used in model training and, ideally, they are qualitatively different from the training data.

To help with the calibration of new *in silico* models for cardiac safety assessment, Colatsky *et al.* (2016) and Li *et al.* (2020) provided guidance on the development of AP models and associated risk metrics under the CiPA paradigm, defining six pillars (see also Musuamba *et al.* (2021); Galappaththige *et al.* (2022)):

1. *"A defined end point consistent with the context of use";*
2. *"An unambiguous algorithm"*;
3. *"A defined domain of applicability"*;
4. *"A stringent strategy and predefined criteria to assess predictivity";*
5. *"A mechanistic interpretation";*
6. *"Appropriate uncertainty quantification".*

The six pillars of Li *et al.* guide model selection, calibration, and use. They aim at improving the confidence in model predictions by making the prediction and interpretation of the risk metric transparent and reproducible, by defining explicitly the applicability of the predictions, by ensuring the objectivity of the validation of the assessment, and by accounting for uncertainty at all steps of the predictions.

These principles were particularly important in Chapter 7 where a new AP model was developed to predict the changes in APD_{90} induced by I_{Kr} and I_{CaL} inhibition. In the rest of this section, we elaborate further on key aspects of model development that are relevant to the work presented in this DPhil thesis.

2.5.1 Model training

Bayesian inference

In the work presented in this DPhil thesis, model training relied on Bayesian inference to find parameter estimates and their uncertainty. Bayesian inference is a set of statistical inference techniques to estimate a probability distribution of parameters of a model, given observed data. It can therefore be used to also perform uncertainty quantification (Lei *et al.*, 2020). Bayesian inference is powerful by its high versatility, and can be applied even to situations where low amounts or repeats of experimental data are available (Robert, 2007).

Let us consider a process which generates an observed dataset y^*, and which is approximated with a model $\mathcal{M}$ parameterised by θ. Bayesian inference aims at determining

the "posterior" probability distribution of θ, $p(\theta|y^*)$, given the observation y^* and prior knowledge on θ, $p(\theta)$. The higher the posterior probability, the better $\mathcal{M}$ parameterised with θ is thought to approximate the true process that generated y^* (Robert, 2007). The posterior probability for θ can be computed using Bayes formula (Bayes & Price, 1763):

$$p(\theta|y^*) = \frac{p(y^*|\theta)p(\theta)}{p(y^*)}, \tag{2.9}$$

with $p(y^*|\theta)$ the likelihood, $p(\theta)$ the prior probability, and $p(y^*)$ the marginal likelihood.

The marginal likelihood $p(y^*)$ can be computed as:

$$p(y^*) = \int p(y^*|\theta)p(\theta)\, d\theta. \tag{2.10}$$

When inferring the posterior distribution of θ, the marginal likelihood would act as a constant scaling factor that does not depend on θ. Therefore, algorithms for estimating the posterior distribution can avoid computing the marginal likelihood for the sake of computational time/cost (Fourment *et al.*, 2020). Computing the marginal likelihood (also called Bayesian evidence) remains useful for model selection and hypothesis testing, as it is dependent on $\mathcal{M}$ (Llorente *et al.*, 2020).

The prior probability $p(\theta)$ is calculated from information about parameter values the user knows *a priori*. In the work presented in this DPhil thesis, the prior distribution was always non-informative, i.e., uniform over the boundaries of the search space defined by prior belief on θ.

The likelihood $p(y^*|\theta)$ is computed with the model based on user assumptions. Applied to cases investigated in this DPhil thesis, y^* consists of a noisy time-series, noted $(y_0^*, \ldots, y_N^*)$. There is noise due to minor processes neglected in the model. The noise at each time point is modelled as independent, identically distributed (i.i.d.), and normal with a fixed width σ_y and mean 0. The noise is added on top of the true signal:

$$y^* = y(\theta^*) + N(0, \sigma_y), \tag{2.11}$$

with N the normal distribution of the noise.

By construction, the residuals obtained by subtracting y from the dataset y^* should follow the distribution $N(0, \sigma_y)$. Thus, the probability at the time-point i that y_i^* was

generated by $\mathcal{M}$ with θ is given by:

$$p(y_i^*|\theta) = \frac{1}{\sqrt{2\pi\sigma_y^2}} e^{\left(\frac{y_i^* - y_i(\theta)}{\sigma_y}\right)^2}. \tag{2.12}$$

Over the whole time series of y^* with i.i.d. noise, the likelihood is therefore:

$$p(y^*|\theta) = \prod_i^N p(y_i^*|\theta) = \prod_i^N \frac{1}{\sqrt{2\pi\sigma_y^2}} e^{\left(\frac{y_i^* - y_i(\theta)}{\sigma_y}\right)^2}. \tag{2.13}$$

In practice, with numerous data points, this product would require us to multiply many small quantities which would make ℓ very sensitive to numerical error. Therefore, it is preferable to work with the log of the likelihood during numerical Bayesian inference:

$$\ell(\theta) = \ln\, p(y^*|\theta) = -\frac{N}{2} \ln 2\pi\sigma_y^2 + \sum_i^N \left(\frac{y_i^* - y_i(\theta)}{\sigma_y}\right)^2. \tag{2.14}$$

In Bayesian inference, the posterior distribution must be interpreted with respect to the prior distribution (Haugh, 2017). As is the case in this DPhil, the prior distribution can be uniform over the search space, i.e., it is "non-informative" other than by defining the search space. In this case, the posterior distribution matches the likelihood distribution (Figure 2.6A). Therefore, all information on parameters is considered to be gained from the data.

In the case where the prior distribution is not uniform, the posterior distribution with the same likelihood is attracted towards the prior distribution (Figure 2.6B). In extreme cases where observed data do not give any information on the parameters, the likelihood is uniform and the posterior distribution matches the prior distribution.

Parameter optimisation

During model training, parameter estimates are found by minimising the mismatch between model outputs and experimental observations, so that the model approximates optimally the true process. The mismatch can be quantified with a cost function, $\mathcal{C}$, that quantifies the "goodness-of-fit". For example, when estimating parameters of an AP model, an AP trace observed experimentally can be compared with the simulated V.

A classic measure for $\mathcal{C}$, which was used in this DPhil thesis, is the distance between the data, y^*, and model outputs y:

$$\mathcal{C} = \sum_i (y_i^* - y_i)^2. \tag{2.15}$$

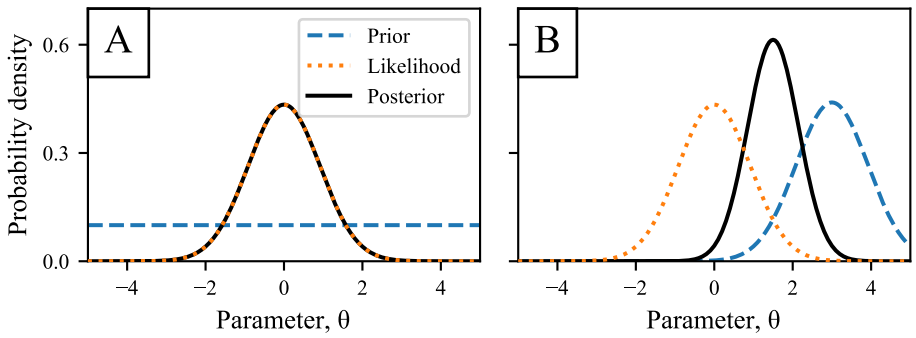

Figure 2.6: Posterior distribution computed from a uniform prior distribution (**A**) and from a Gaussian prior distribution (**B**). In both cases, the likelihood distribution is the same, but the prior distribution skews the posterior distribution towards what was known *a priori* about θ^*. In this dummy example, the marginal likelihood was assumed to be equal to 1. In the work presented in this DPhil thesis, the prior distribution was uniform over the search space (**A**).

Note that $\mathcal{C}$ is an affine transformation of the log-likelihood, ℓ, used in this work (Eq. 2.14). Minimising $\mathcal{C}$ is equivalent to maximising ℓ, and therefore to maximising the posterior probability for θ, given the non-informative prior distributions used in the present work (Figure 2.6). The estimate of θ, θ^*, is therefore defined as:

$$\theta^* = \underset{\theta}{\operatorname{argmin}}\, \mathcal{C}(\theta) = \underset{\theta}{\operatorname{argmin}} \sum_i |y_i^* - y_i(\theta)|^2. \tag{2.16}$$

Finding θ^* corresponds to solving an optimisation problem, for which various optimisation algorithms have been developed.

Many optimisation algorithms, as the ones used in this DPhil, follow an iterative process that proceeds as follows:

- One or multiple points of the parameter space are sampled;
- $\mathcal{C}$ is evaluated at the sampled point(s);
- The algorithm checks whether model outputs match sufficiently well the data for stop conditions to be met;
- Optionally, the rule for sampling the parameter space is adapted, so that $\mathcal{C}$ is more likely to be reduced at the next iteration.

In complex biological systems such as cardiac electrophysiology, model equations are high dimensional and non-linear. In cases with such high complexity, evolution-based algorithms can reasonably be used to find a good solution to the optimisation problem of Eq. 2.16, although the optimality of the solution cannot be guaranteed (Reeves (1996) and Chapter 6).

For the work presented in this DPhil thesis, the Covariance Matrix Adaptation - Evolution Strategy (CMA-ES) (Hansen *et al.*, 2003) algorithm was used. The functioning of the CMA-ES algorithm is illustrated in Figure 2.7.

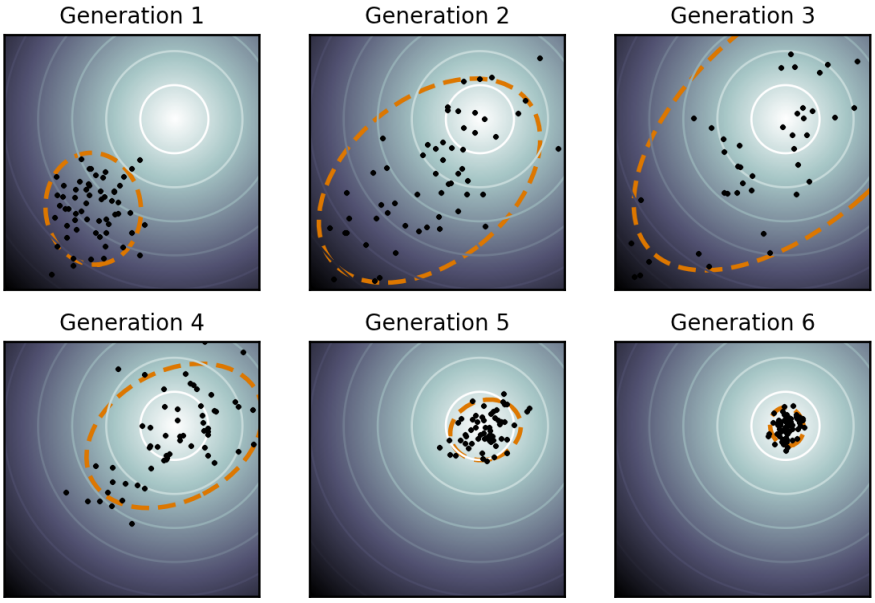

Figure 2.7: Illustration by Sentewolf of the CMA-ES algorithm developed by Hansen *et al.* (2003). At first, the search distribution (dotted orange line) is initialised with prior knowledge on the parameters of interest. From the search distribution, a population of particles (black points) is sampled. The points with the highest goodness-of-fit (towards the white region) are weighted more to direct the search distribution for the next generation. After generation 4, the adaptation of the search distribution width is crucial to explore more accurately solutions with high goodness-of-fit.

At each iteration (or generation) i, the objective function is evaluated in $\mathcal{N}$ random samples of the search space, $(\theta_{i,0}, \ldots, \theta_{i,\mathcal{N}})$, called "particles":

$$(\theta_{i,0}, \ldots, \theta_{i,\mathcal{N}}) \sim \mu_i + N(0, \Sigma_i), \tag{2.17}$$

where N is the normal distribution, and μ_i and Σ_i are the center and covariance matrix of the sampling distribution, respectively. The best performing particles of i then drive the evolution of μ_{i+1} to ensure improvement of the goodness-of-fit from generation to generation. The speed of convergence of the algorithm is facilitated by the adaptation of Σ_{i+1} that distorts the normal distribution along axes in the parameter space where $\mathcal{C}$ is more sensitive to θ.

Note that the adaptation of Σ_i needs to preserve the balance between rapid convergence of the optimisation algorithm and thorough exploration of the parameter space.

Details of the search distribution adaptation can be found on the CMA-ES tutorial published by Hansen (2016).

As investigated further in Chapter 6, the initial proposal covariance for new parameter samples, Σ_0, and the number of particles exploring the parameter space, $\mathcal{N}$, are critical for the efficiency of the exploration of the search space.

Uncertainty in parameter estimates

With optimisation algorithms, only the maximum of the likelihood is sought. Results of optimisation algorithms must therefore be complemented with other techniques to compute the uncertainty in the estimate. This is central to the 6$^{\text{th}}$ pillar of Li *et al.* (2020) for model development.

In the work presented in this DPhil thesis, two methods were used to estimate the posterior distribution of parameters.

The first method relied on the "ensemble modelling approach" (Villaverde *et al.*, 2015), used in Chapters 6 and 7, illustrated in Figure 2.8.

The affine relationship between $\mathcal{C}$ (Eq. 2.15) and the expression of ℓ used in this work (Eq. 2.14) means that many evaluations of ℓ can be calculated from evaluations of $\mathcal{C}$ made during the optimisation with the CMA-ES algorithm. These evaluations of ℓ are leveraged by the ensemble modelling approach to estimate the posterior probability distribution of θ.

With a non-informative (uniform) prior distribution as used in this work, the posterior probability distribution matches the profile of ℓ (Figure 2.6A). Under the assumption that the posterior distribution can be approximated by a normal distribution around its maximum of likelihood, the 95% confidence interval in parameter estimates corresponds to parameter values that yield a log-likelihood within a 1.92 tolerance range in ℓ around the maximum of ℓ (Villaverde *et al.*, 2019).

The second method used to estimate the uncertainty in parameter estimates in this thesis relied on Markov Chain Monte-Carlo (MCMC) algorithms applied to Bayesian inference (Van Ravenzwaaij *et al.*, 2018). Iteratively, a chain of parameter set samples is created. At each iteration, a quantity proportional to the posterior probability is evaluated in one or several points of the parameter space. Based on a comparison between

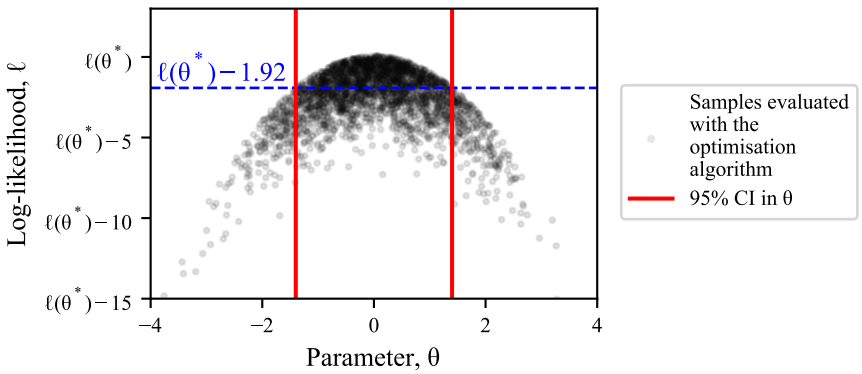

Figure 2.8: Estimation of the 95% confidence interval with the ensemble modelling approach (Villaverde *et al.*, 2019), in the case of a non-informative (uniform) prior distribution. This figure shows a sketch used for illustrative purposes only.

the posterior probabilities of the new sample and the last sample in the chain, the new sample is accepted or rejected. If the sample is accepted, the sample is appended to the chain. If it is rejected, the last accepted sample is appended again. Eventually, the rule for sampling is adapted for the next iteration.

After many iterations, the distribution of samples constituting the chain approximates the posterior probability distribution for the parameters. Different strategies have been adopted to identify when the chain has converged well enough to the posterior distribution. For example, adaptive MCMC algorithms, like the Haario-Bardenet MCMC algorithm (Johnstone, 2018) used in this DPhil, target a certain acceptance rate for which the chains are expected to match sufficiently well with the posterior distribution (Gelman *et al.*, 1997). Similarly to the CMA-ES algorithm, the adaptation of the sampling rule is key to accelerate MCMC convergence (Valderrama-Bahamóndez & Fröhlich, 2019).

The ensemble modelling approach presents the advantage that after finding the parameter estimates with the CMA-ES algorithm, no additional simulations are needed to estimate the parameter uncertainty. However, to randomly sample from the posterior distribution, additional post-processing is needed (Villaverde *et al.*, 2022). Furthermore, the posterior distribution may be poorly approximated by a normal distribution around θ^*, in which case the log-likelihood threshold used to compute the confidence interval should be revised.

In contrast, the Haario-Bardenet MCMC algorithm returns a close approximation of the posterior distribution. The main drawback with this approach is that numerous

additional simulations are needed (approximately 10,000 samples in Chapter 4) which makes this technique very computationally costly.

Leveraging the uncertainty in inputs used for simulations and the uncertainty in parameter estimates (Section 2.5.1), the uncertainty in model outputs can be computed and propagated onto the assessment of model predictivity.

Accounting for variability

Variability is inherent to biological systems, even between cells in the same tissue in the same organism (Walmsley *et al.*, 2015). In the example of cardiac AP models, different cells produce in varying amounts the proteins that form the ion channels (Schulz *et al.*, 2006). This leads to variation in the amount of functional ion channels on the cell surface, which has been modelled as variation of ion channel conductance parameters (Muszkiewicz *et al.*, 2016).

A hierarchical Bayesian framework can be used to estimate the probability distribution of parameters in a population (Lee & Mumford, 2003). In brief, the model is trained on data from several individuals at the same time. Parameters are inferred for each individual as described above. Hyperparameters are inferred on top, to describe the overarching distribution of parameters in the modelled population.

Alternatively, the population of models approach (Britton *et al.*, 2013) has been used to investigate the effects of variability on AP response to various stimuli such as drug treatment (Passini *et al.*, 2017) or adaptation to heart rate (Bartolucci *et al.*, 2020). To calibrate a population of AP models, AP models with random parameterisations are generated, and AP markers are calculated, e.g., RMP or peak voltage. The AP models producing AP markers within an experimental range are retained and finally used for predictions.

2.5.2 Model validation

Model validation compares model predictions with experimental data to assess the predictivity of the model, which is the 4^{th} pillar of Li *et al.* (2020) for model development.

The quality of the validation process is defined by the coverage of the context of use by the validation data, and by the independence of the validation data with respect to the

training data. The former is problem-specific: experiments should be designed to collect the relevant data for model development (Musuamba *et al.*, 2021). The latter spans three levels: internal, internal-external and external validation (Steyerberg & Harrell Jr, 2016).

With internal validation techniques, e.g., the leave-one-out cross validation technique, the same data are used in model training and model validation. Only limited reliability of model predictivity can be ensured with these techniques (Kubinyi, 2002; Gramatica, 2007; Steyerberg *et al.*, 2003; Mostofian & Zuckerman, 2019), but they have proved useful to test the consistency of a dataset and have been commonly used (Steyerberg & Harrell Jr, 2016).

Internal-external validation relies on a dataset generated from different experiments under the same experimental conditions. This way, the dataset is separated into training and validation datasets that ideally encompass similar populations and cover the whole context of use of the developed model. The validation data are independent from the training data, but they are generated under the same experimental conditions.

External validation corresponds to the use of validation data generated under different experimental conditions than training data. The validation data therefore evaluate the ability of the model to extrapolate from the training data, which ensures the highest reliability of model predictions (Musuamba *et al.*, 2021). For example, the strategy applied by Tomek *et al.* (2019) to separate training and validation data constitutes an external validation of the model.

To reliably assess the predictivity of the model developed in this DPhil, an external validation strategy was employed.

2.5.3 Model selection

A fundamental step in the development of a model is the selection of the mathematical representation (and therefore parameters) that will be used to describe the studied mechanisms: this is model selection (Cawley & Talbot, 2010).

The quote "Everything should be made as simple as possible, but no simpler" attributed to Einstein gives good guidance about model selection. Some tools have been developed to rationalise model selection and to quantify the trade-off between mathematical simplicity and the mechanistic comprehensiveness of a model. For example, the Bayesian Information

Criterion (BIC, Schwarz (1978)) penalises improvements in the likelihood by the number of parameters estimated from the data. However, model selection is a problem-specific question, which limits the use of such tools for model selection (Liu (2000) and Chapter 6).

Important problem-specific aspects of model selection are model discrepancy, parameter identifiability, and overfitting.

Model discrepancy

Biological systems are incredibly complex and experimental data are often very noisy (Tsimring, 2014). While mathematical models facilitate human understanding of complex biological processes, they are imperfect representations of the unknown real world mechanism (Engl *et al.*, 2009).

The imperfect knowledge of biology leads to a discrepancy between the mathematical description and the biological reality, called "model discrepancy", or "model misspecification" (Lei *et al.*, 2020). The famous quote of Box (1976) "all models are wrong, but some are useful" highlights that model discrepancy is ubiquitous in mathematical models. Still, there is hope for developing useful models.

On the example of AP models, the early models qualitatively reproduced the behaviour of Purkinje fibres and were central to the understanding of electrophysiological properties of APs (DiFrancesco & Noble, 1985). However, newer models were constantly developed because the existing models were not able to extrapolate to particular conditions, e.g., Iyer *et al.* (2004a); Grandi *et al.* (2010); O'Hara *et al.* (2011).

The latest models are mechanistically more elaborate and the equations describing ion channel conformational changes have been refined with additional experimental data (Section 2.4). Therefore, the latest models are supposedly approximating more accurately the ongoing mechanisms and model discrepancy may be reduced with the latest models. Still, many models exist for the human ventricular AP and they predict very different responses to the same perturbation, e.g. inhibition of I_{Kr} and I_{CaL} (investigated in Chapter 5). This can perhaps be explained by the fact that these models were based on different datasets, developed for different purposes, and because the processes generating the AP are still to be further understood.

It is worth noting that mechanistic models rely on analytical functions to describe biological processes and distributions: exponential, square-root, etc; Normal, Poisson, etc. Analytic functions are useful as they enable the approximation of complex non-linear dependencies with a limited number of parameters. However, biological processes may be unsuitably described with such mathematical tools, and it is important to keep in mind that equations are only approximations of what truly happens in the studied systems (Engl *et al.*, 2009).

Overfitting

A pitfall of model selection, entangled with model discrepancy, is overfitting (Bilger & Manning, 2015). Overfitted models are defined as "Models that contain more unknown parameters than can be justified by the data" (Everitt & Skrondal, 2010). It typically occurs when too many parameters are estimated during model training, and model predictivity is poor for new data, as evaluated in model validation.

A famous example of overfitting comes from the quote attributed to John Von Neumann: "With four parameters, I could fit an elephant, and with five I can make him wiggle his trunk" (Dyson, 2004). Fermi quoted his friend Von Neumann to Dyson, when Dyson came to present mathematical computations (performed with four free arbitrary parameters) that matched almost perfectly experimental data published by Fermi. Fermi pointed out that these four additional parameters do not come from physical considerations or self-consistent mathematical formalism — essential to the quantum physics models used by Dyson. Thus anything, including an elephant, could be introduced in Dyson's model with four free arbitrary parameters. In the epilogue of this anecdote, the model used by Dyson was proven to be mechanistically wrong with additional experimental data generated years later (Dyson, 2004).

To limit the risk of overfitting, Occam's razor and Einstein's rule of thumb "Everything should be made as simple as possible, but no simpler" are useful. More concretely, the theorem of Shannon (1949) for sampling gives an upper limit for the number of calibrated parameters: one needs at minimum two times more experimental points than fitted parameters. Furthermore, model validation is key to ensure that model predictivity is not

hindered by overfitting (Cawley & Talbot, 2010). Finally, careful verification of parameter identifiability also contributes to reduce the risk of overfitting (Whittaker *et al.*, 2020).

Parameter identifiability

Identifiability is a property of a model and its observable outputs in a particular experimental setting, so that it produces identical outputs if and only if the parameter values are identical (Cole, 2020). *Identifiable parameters* are these parameters for which a single estimate can be inferred from a given dataset.

Identifiability of parameters is crucial to assess during model development. It ensures that meaningful parameter values can be recovered from the training data, and that predictions of the model will be reliable (Whittaker *et al.*, 2020). Conversely, when a model is unidentifiable, optimal outputs can be achieved with different parameterisations, so parameter estimates are less accurate and/or incorrect, and model predictivity is limited (Fink *et al.*, 2011).

Two types of (un)identifiability can be distinguished: structural and practical (Raue *et al.*, 2009), illustrated in Figure 2.9.

When the parameters are structurally unidentifiable, the optimal goodness-of-fit can be achieved with different combinations of parameters and unique parameter estimates cannot be found.

It may happen that despite the model parameters being structurally identifiable with a unique set of parameters returning maximal goodness of fit, the parameters are not identifiable in practice: parameters are practically unidentifiable. The parameters are estimated based on the information obtained from the training data. Due to limited data quality and/or quantity, situations arise where the confidence interval in parameters is unacceptably (or even sometimes infinitely) wide. In Bayesian terms, even though a single parameter value with maximal likelihood can be found, the posterior probability distribution cannot be constrained to a satisfactorily narrow region of the parameter space.

Practically identifiable parameters (by definition) are those that can be correctly estimated with a finite and satisfactorily small uncertainty. Note the subjective aspect of practical identifiability, previously discussed by Wieland *et al.* (2021).

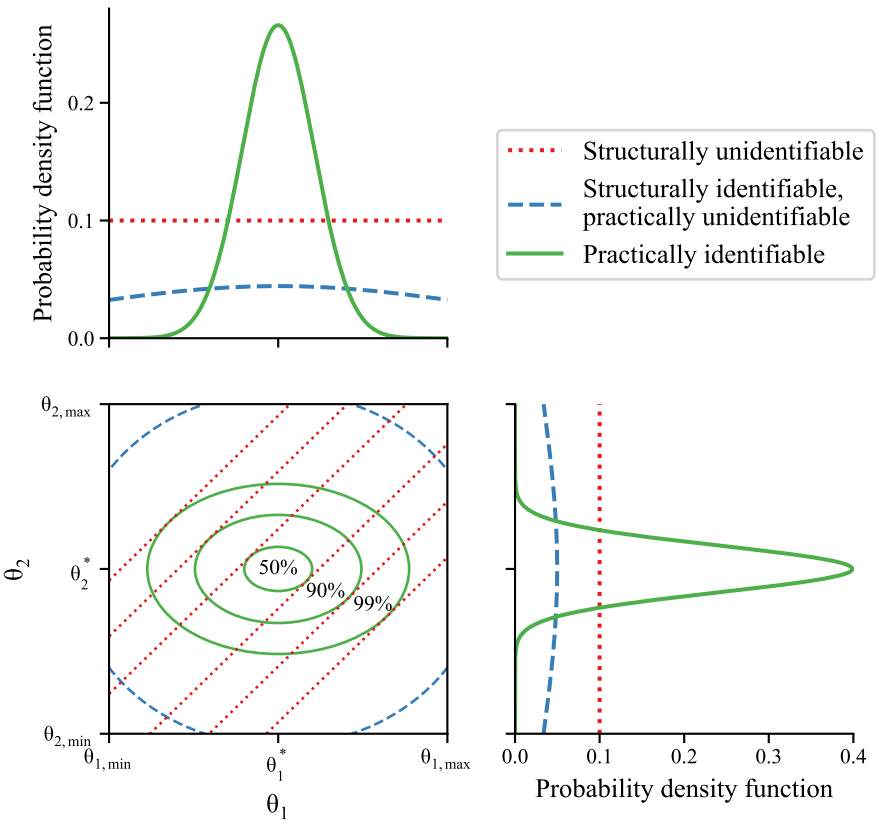

Figure 2.9: Different types of parameter identifiability. Distributions of θ_1 and θ_2 in different scenarios are plotted in the diagonal subplots. The contour plot highlights the 50%, 90% and 99% confidence intervals of the joint distribution of (θ_1, θ_2). If the optimal goodness-of-fit is achieved with different combinations of θ_1 and θ_2, the parameters are structurally unidentifiable (**red dotted line**). The optimal goodness-of-fit may be achieved with a single value (θ_1^*, θ_2^*) but the uncertainty in parameters is unacceptably large: the parameters are structurally identifiable but practically unidentifiable (**blue dashed line**). When θ_1 and θ_2 are both estimated with small uncertainty, the parameters are practically identifiable (**solid green line**). This figure shows sketches used for illustrative purposes only.

The redundancy in biological systems is an important limitation to identifiability of biophysically-detailed models (Tononi *et al.*, 1999). Strategies to alleviate unidentifiability can focus on the data or on model selection. With the former strategies, data of higher quality or under additional conditions can be generated (Dokos & Lovell, 2004; Syed *et al.*, 2005; Groenendaal *et al.*, 2015). With the latter strategies, the number of calibrated parameters can be reduced and model equations can be updated to integrate more advanced understanding of the system (Wieland *et al.*, 2021). Note that overfitting should be avoided when integrating additional mechanisms into a model.

Computational cost

In very complex simulations, the computational cost can make some models practically impossible to train or to use. In 3D multi-scale models of cardiac AP propagation, millions of cells are simulated at the same time. Despite being less physiologically-detailed, simpler cellular models are practically more usable in such complex simulations. Computational cost is for example the main reason why the Ten Tusscher & Panfilov (2006) model is the most used model in 3D multi-scale models of cardiac AP propagation (Corrado *et al.*, 2021). For the work presented in this DPhil thesis, the computational cost of AP models was also an important bottleneck for model training (Chapters 6 and 7).

In conclusion, the selected model should offer the most advantageous trade-off between the comprehensive and accurate representation of mechanisms, identifiability given experimental limitations on available data, and practical usability.

2.6 Summary

In Chapter 2, the concepts essential to the work presented in this DPhil thesis have been introduced. The normal function of the heart was introduced (Section 2.2) and linked with the cellular activity in the heart tissue, focusing on the ventricular AP (Section 2.3). Previous mathematical models of the human ventricular AP and their use for cardiac safety prediction were discussed in Section 2.4. Finally, key aspects of model calibration were discussed in Section 2.5. Concepts introduced in Section 2.5 were applied to the example of the calibration of AP models, for this is relevant to this DPhil thesis.

In Section 2.3.1, two equivalent equations for the transmembrane voltage in AP models (Eq. 2.1–2.2) were introduced. In Chapter 3, the implications on AP simulations and on the calibration of AP models of using either equation are investigated.

3

A parameter representing missing charge should be considered when calibrating action potential models

Preamble

The equation for the transmembrane voltage can be written as a derivative or an algebraic form (Section 2.3.1). Using the algebraic form requires the introduction of a new parameter, that we denote Γ_0, which represents the net concentration of all charged ionic species that influence membrane voltage but are not considered in the model. Although previous studies have examined the impact of Γ_0 on long-term stability and drift in model predictions, there has been little examination of its effects on model predictions, particularly when a model is refitted to new data. In this Chapter we illustrate how Γ_0 affects important physiological properties such as action potential (AP) duration (APD) restitution, and examine the effects of (in)correctly specifying Γ_0 during model calibration.

The work presented in this Chapter was published in Frontiers in Physiology (Barral et al., 2022b). For this article, I carried out the research and wrote the manuscript. The Chapter contains only minor notation and typestting changes.

3.1 Introduction

Since the seminal work by Hodgkin & Huxley (1952), mathematical models of electrophysiology have been developed for many different cell types, including neurons, cardiomyocytes, gastric smooth muscle cells, and many more (Noble, 1962; Dodge & Cooley, 1973; Corrias & Buist, 2007). Differences in ionic concentrations across cell membranes lead to a transmembrane voltage (V). The evolution of V over time is usually calculated in mathematical models by numerically integrating the effects of the ionic currents passing through the membrane. Since the late 90's, several authors have showed that V can also be computed directly from intra- and extracellular concentrations of charges, using a conservation principle in the models (Varghese & Sell, 1997; Guan *et al.*, 1997; Endresen *et al.*, 2000; Hund *et al.*, 2001; Jacquemet, 2007; Livshitz & Rudy, 2009; Pan *et al.*, 2018). In this work, we further investigate the implications of using this second expression for V in terms of numerical stability, we highlight its impact on electrophysiological predictions, and we discuss the benefits of this approach in model calibration.

First, in this section we present a brief overview of relevant work that leads to different ways of computing the voltage in AP models, based on a conservation of charge principle hidden in the equations, and we show how this conservation of charge relates to the model's steady state. Section 2 then highlights how the accuracy of solutions is improved by using the algebraic voltage expression. In Section 3, we show that model outputs are sensitive to the net concentration of charge across the cell membrane, which varies because of high variability and/or uncertainty in initial concentrations. Finally, in Section 4 we show that Γ_0, a parameter characterising the relationship between V and the intra- and extracellular concentrations of charges, can be inferred from experimental data to produce the desired steady-state behaviour of the AP model — despite being challenging to estimate experimentally.

In this Chapter, we explore the consequences of writing V algebraically using the Ten Tusscher & Panfilov (2006) (TP) model of the human ventricular AP and the O'Hara *et al.* (2011) model reformulated by Dutta *et al.* (2017) (ORd-CiPA). However, our findings apply to any model that tracks the intracellular concentrations of charge-carriers, i.e., the majority of modern electrophysiology models.

3.1.1 Membrane voltage and ionic concentrations in AP models

Major variables in AP models include V, channel and pump/transporter state variables and, in later models, concentrations of ions, buffers, and signalling molecules. The relationship between these variables, grouped together in a vector $\mathbf{X}$, is expressed as a system of ordinary differential equations (ODEs) of the form

$$\frac{\mathrm{d}\mathbf{X}}{\mathrm{d}t} = f(\mathbf{X}),$$
$$\mathbf{X} = \{V, \mathbf{C}, \mathbf{g}\},$$

where the vector function $f(\mathbf{X})$ describes the rate of change of $\mathbf{X}$, which can be subdivided into V, the ionic concentrations $\mathbf{C}$, and all other state variables $\mathbf{g}$. The first equation in f is usually the one that defines the rate of change in V, using an ideal capacitor equation:

$$\frac{\mathrm{d}V}{\mathrm{d}t} = -\frac{1}{C_\mathrm{m}} \sum_{j=1}^{N} I_j(\mathbf{X}), \tag{3.1}$$

where C_m is the membrane capacitance (usually in pF), and I_j are the N different ionic currents flowing across the cell membrane (in pA). Note that the currents depend non-linearly on voltage, concentrations, and time, so that all the state variables are coupled together in a non-linear system.

The earliest AP models (e.g. Hodgkin & Huxley, 1952; Noble, 1962; McAllister *et al.*, 1975) approximated intracellular concentrations as constants, arguing that the relatively small ionic currents would not alter concentrations significantly. This assumption holds well for the K^+ and Na^+ currents included in these models, which have relatively large internal concentrations that do not show significant variations during a single AP. In addition, these small changes could build up when simulating longer time spans, but this was computationally infeasible at the time. However, after the discovery of Ca^{2+} currents in the 1960s, it was quickly realised that $[Ca^{2+}]_\mathrm{i}$ could vary by orders of magnitude during a single AP, which necessitated the inclusion of time-varying $[Ca^{2+}]_\mathrm{i}$ in models as early as the model by Beeler & Reuter (1977).

Later, DiFrancesco & Noble (1985) proposed a model where the current-induced changes in $[Ca^{2+}]_\mathrm{i}$, $[K^+]_\mathrm{i}$, and $[Na^+]_\mathrm{i}$ were tracked over time, along with the extracellular concentration of K^+ close to the cell membrane. This revolutionised the understanding

of major features of cardiac electrophysiology (Dibb *et al.*, 2015). Many subsequent AP models have retained the dynamic description for *intracellular* concentrations (although $[K^+]_i$ is sometimes held constant) and extended it with concentrations in intracellular compartments such as the sarcoplasmic reticulum (SR, e.g. Noble *et al.*, 1991; Wilders *et al.*, 1991; Luo & Rudy, 1994) and other species (e.g. chloride in Tomek *et al.*, 2020). Variations in extracellular concentrations over the course of the AP proved less popular but are still present e.g. in some models of atrial (Hilgemann & Noble, 1987; Lindblad *et al.*, 1996; Nygren *et al.*, 1998) and sino-atrial (Demir *et al.*, 1994; Dokos *et al.*, 1996; Lovell *et al.*, 2004; Pohl *et al.*, 2016) APs. Even though extracellular concentrations do vary in practice (e.g. under ischemic conditions), their variations due to ionic currents are often neglected in AP models because ions are constantly exchanged with the vascular buffer which limits their temporal variation in the extracellular space (Dokos *et al.*, 1996) and reduces the accumulation of ions in the extracellular space.

3.1.2 Algebraic expressions for V

A study by Varghese & Sell (1997) showed that models in which all membrane currents are assigned to a charge-carrying species, and in which the intracellular ionic concentrations vary accordingly, will implicitly satisfy a *conservation of charge* principle. As a result, V can be computed algebraically as a function of the concentrations, so that the ODE for V (Eq. 3.1) is redundant. Applying the approach of Varghese & Sell to the Luo & Rudy (1994) model as an example, we obtain

$$V = \frac{\mathcal{V}_i F}{C_m}\left([Na^+]_i + [K^+]_i + 2[Ca^{2+}]_i + 2\frac{\mathcal{V}_{JSR}}{\mathcal{V}_i}[Ca^{2+}]_{JSR} + 2\frac{\mathcal{V}_{NSR}}{\mathcal{V}_i}[Ca^{2+}]_{NSR}\right) + V_0, \quad (3.2)$$

where V_0 is an integration constant in units of mV (called C_0 in the original publication), $\mathcal{V}_{JSR}$ and $\mathcal{V}_{NSR}$ are the volumes of the junctional (JSR) and network (NSR) sarcoplasmic reticulum compartments of the cell, respectively, and $[Ca^{2+}]_{JSR}$ and $[Ca^{2+}]_{NSR}$ are the concentrations of Ca^{2+} in these compartments. Hund *et al.* (2001) used a similar expression for V but moved the integration constant within the brackets, thereby turning it into a concentration instead of a voltage. Using C_0 to represent the concentration, the two representations are related by $V_0 = -\frac{\mathcal{V}_i F}{C_m} C_0$.

Endresen *et al.* (2000) proposed an expression very similar to that of Varghese & Sell but with a stronger assumption: that all charges contributing to V are carried by K^+, Na^+, and Ca^{2+}. This assumption leads to

$$V_0 = -\frac{\mathcal{V}_i F}{C_m}\Big([K^+]_o + [Na^+]_o + 2[Ca^{2+}]_o\Big), \tag{3.3}$$

where $[X]_o$ is the extracellular concentration of species X. In other words, V is simply proportional to the difference between total intracellular and extracellular concentrations of these three species. Endresen *et al.* acknowledged that their approach omitted anions, but justified this with the observation that the total concentrations of anions are approximately the same inside and outside the cell and that most currents are carried by cations. However, this framework would still need to be extended for models which include Cl^-, e.g. Hund & Rudy (2004); Grandi *et al.* (2010); Tomek *et al.* (2020): Eqs. 3.2 & 3.3 can be combined and generalised to any number of modelled species and compartments:

$$V = \frac{\mathcal{V}_i F}{C_m}\left(\sum_A \sum_k z_A [A]_{\text{total},k} \frac{\mathcal{V}_k}{\mathcal{V}_i} - \sum_A z_A [A]_o\right), \tag{3.4}$$

where A represents each charged species in the model, z_A its valence, $\mathcal{V}_k$ is the volume of the compartment k, and the index k is over all intracellular compartments (e.g. $k = i$ might correspond to the cytosol). Eq. 3.4 therefore accommodates further electrically charged species such as chloride, provided that the model keeps track of changes in their intracellular concentrations.

Note that the total concentration of any ion A in the compartment k is denoted here as $[A]_{\text{total},k}$. Some models include buffering of ions which alters free ionic concentrations, but since binding to buffers does not cause current flow through the membrane it should not change V. The $[A]_{\text{total}}$ notation in Eq. 3.4 serves as a reminder that the total concentration carried by A is given by the sum of any buffered and free concentrations. For example, in many models $[Ca^{2+}]_{\text{total,i}}$ is not equal to $[Ca^{2+}]_i$. This can make derivation of an algebraic-V form more complicated than in the examples above.

Various other charge-carriers — ions, compounds and charged proteins — are known to be present at different concentrations on either side of the membrane, but are omitted from models. If these omitted charge carriers lead to a net transmembrane voltage, then

an extra parameter is needed to account for the contribution of their charge imbalance to V. For example, the Hund & Rudy (2004) dog AP model includes Cl^- ions so that an extra offset parameter would be needed to compensate the strong imbalance between intracellular ($\sim 20\,\text{mM}$) and extracellular ($\sim 100\,\text{mM}$) concentrations of Cl^-, or there would be huge voltages using Eq. 3.4.

In this model, chloride co-transporters change intracellular K^+, Na^+ and Cl^- concentrations but do not induce any ionic current or change voltage as they transport pairs of oppositely charged ions. The balanced effect of these co-transporters does not need special treatment in the equations above as long as both co-transported ionic species are accounted for.

We can modify Eq. 3.4 to explicitly allow for transmembrane imbalance of species that are not included in the model:

$$V = \frac{\mathcal{V}_\text{i} F}{C_\text{m}} \left(\sum_A \sum_k z_A [A]_{\text{total},k} \frac{\mathcal{V}_k}{\mathcal{V}_\text{i}} - \sum_A z_A [A]_\text{o} \right) + \Delta V. \tag{3.5}$$

Here, ΔV corresponds to the transmembrane potential due to the difference in charge of *all* un-modelled species on either side of the membrane. As the contribution of these species to V is not modelled as varying, ΔV remains constant through the simulations. Equivalently, we can express the offset constant as a concentration that we denote Γ_0:

$$V = \frac{\mathcal{V}_\text{i} F}{C_\text{m}} \left(\sum_A \sum_k z_A [A]_{\text{tot},k} \frac{\mathcal{V}_k}{\mathcal{V}_\text{i}} - \sum_A z_A [A]_\text{o} + \Gamma_0 \right), \tag{3.6}$$

where

$$\Gamma_0 = \mathcal{V}_\text{i} F \Delta V / C_\text{m}. \tag{3.7}$$

Expressing the offset as a concentration rather than voltage may help in assessing whether the values implicitly attributed to Γ_0 by ODE models could be realistic. If positive, Γ_0 could be interpreted as the net concentration of 1+ charged intracellular ions carried by species omitted in the model (or equivalently the net extracellular concentration of 1− charged ions), and if negative it could be interpreted as a net intracellular concentration of 1− charged omitted ions. In reality it will reflect the sum of concentrations of a wide range of intra and extracellular un-modelled charged species. The smaller the magnitude of Γ_0, the smaller the transmembrane imbalance of charge carried by un-modelled species. As a

consequence, a value of $\Gamma_0 = 0\,\text{mM}$ does not necessarily imply that no charge is missing in the model; but it does imply that any missing external charge is balanced exactly by an internal missing charge. Thus, the value of Γ_0 must be interpreted in the light of which charged species are included in each model. Throughout this Chapter, we will use the Γ_0 symbol to represent these missing charges, but the results hold equally well for its mathematically equivalent representation as voltage (Endresen *et al.*, 2000), concentration of charge (Hund *et al.*, 2001), or electrical charge (Jacquemet, 2007). Further detail on these expressions and their interpretation is provided in Section A.2 in the Appendix.

A value for Γ_0 can be found by substituting in the initial conditions for the concentrations and the initial value of V from the ODE formulation. This highlights an important point: models that express V in derivative form "hide" the value of this model parameter *within their initial conditions*. So when a set of initial conditions is chosen, perhaps arbitrarily from within the bounds of physiological realism, a hidden assumption is made about the (im)balance of un-modelled charges in the cell. As we will show in this Chapter, this net imbalance in un-modelled charge, captured by Γ_0, is a key parameter in determining the behaviour of AP models.

3.1.3 Γ_0 and stable behaviour

In Figure 3.1 we show the stable behaviour of the ORd-CiPA model when paced for a long time at 1 Hz. The solution converges to a pattern in which all variables in the system follow the same trajectory (to within numerical simulation tolerances) every time a stimulus is applied. The resulting periodic orbit in the state variable space (as shown in Figure 3.1E) is called a "stable limit cycle" in the study of dynamical systems, but is often referred to as a "steady state" for shorthand in electrophysiology modelling.

Figure 3.1 also shows how a change in pacing to 2 Hz results in a transient shift to a new limit cycle. Similar transients to different limit cycles will also occur when other parameters in the model are changed (e.g. when drug block alters maximal ion channel conductances, or when a change in extracellular concentrations is applied).

In physiological terms, a model at a limit cycle has settled to a stable behaviour where each ionic concentration is in a dynamic equilibrium — any depletion/accumulation

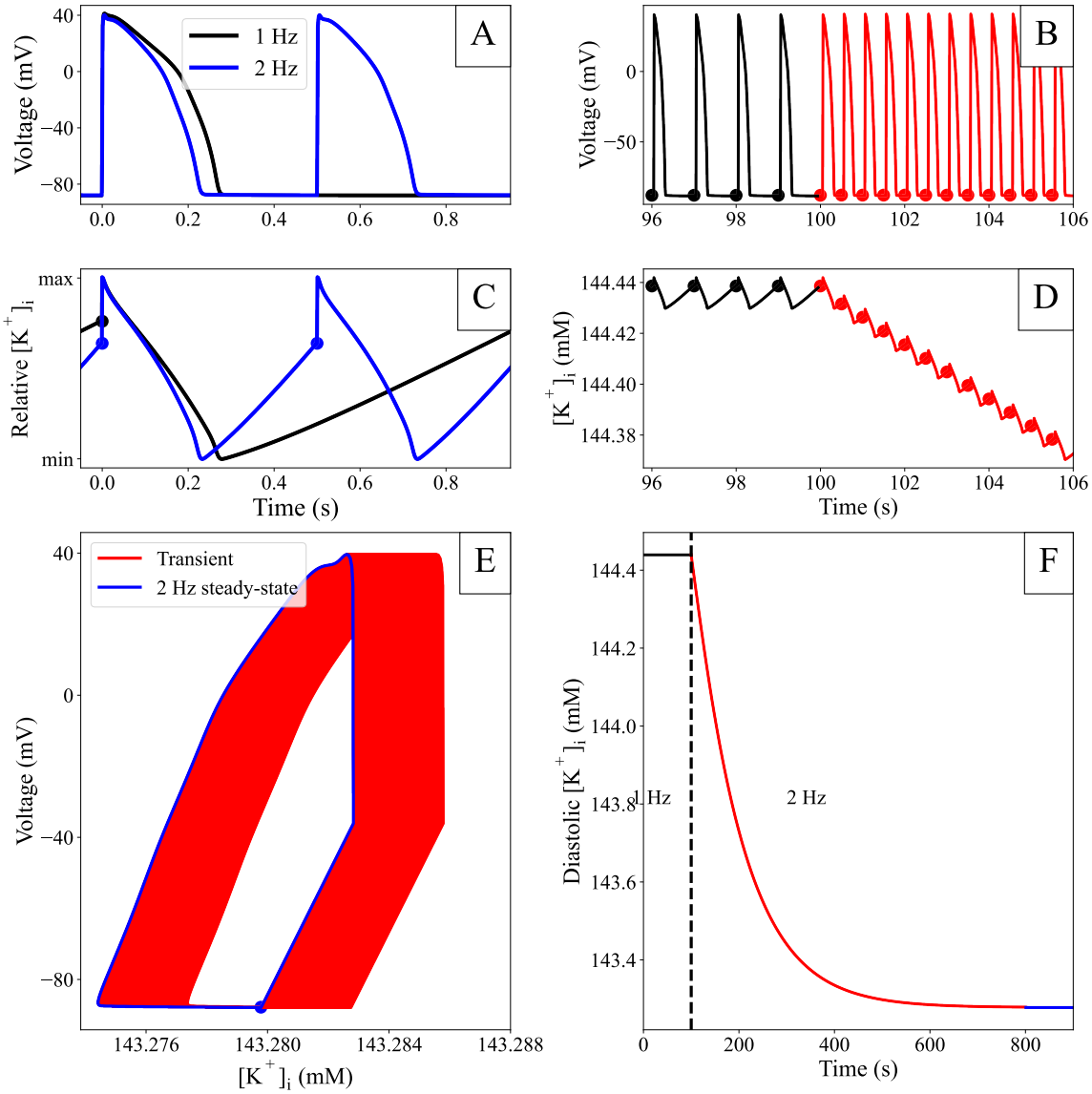

Figure 3.1: Example of a limit cycle in the ORd-CiPA model (Dutta *et al.*, 2017), using the initial conditions from the published CellML model. The simulation methods are detailed in Section 3.2.1. **A:** Comparison of paced steady-state APs with 1 Hz and 2 Hz pacing. **B:** Adaptation of the voltage profile when the pacing rate is suddenly changed from 1 Hz to 2 Hz. The dots plotted on the traces correspond to the end of the diastolic phase in each AP. **C:** Comparison of periodic steady-state $[K^+]_i$ variations during the AP with 1 Hz and 2 Hz pacing. The values are normalised for easier comparison. **D:** Adaptation of $[K^+]_i$ after the sudden change to 2 Hz shown in panel B. **E:** V and $[K^+]_i$ during the transient adaptation phase where the model converges towards its periodic steady state. Data are shown from the 500^{th} pace onward. After a slow drift of $[K^+]_i$ over time, a limit cycle (in blue) is reached where the patterns from consecutive APs overlap. **F:** Evolution of diastolic intracellular potassium (measured at the time points denoted with dots in B and D) after a change in pacing rate. A limit cycle is reached after approximately 1600 2 Hz paces.

due to ions flowing down concentration gradients is restored before the next pace by pumps and exchangers (see Figure 3.1C).

Convergence to a stable limit cycle of the same period as the pacing (a 'period-1' orbit) is not guaranteed: some models' variables may simply keep drifting (perhaps reaching unrealistic levels); exhibit more complex behaviour such as alternans (a stable 'period-2' limit cycle in which we arrive back at the same state after two stimuli periods rather than one); or even chaotic behaviour (Qu, 2011). If pacing is stopped altogether, model variables may converge to stable values — a "stable steady state". In models that exhibit automaticity, a limit cycle can be reached without any periodic forcing applied by a stimulus current. In this Chapter, we will use either "limit cycle" or "periodic steady state" when referring to stable limit cycles, and "quiescent steady state" when referring to stable steady states without any periodic forcing by a stimulus current.

Many published models do not exhibit a periodic steady state. Hund *et al.* (2001); Jacquemet (2007) showed that models where variables drift can often be 'fixed' to produce periodic steady states by ensuring that all currents through the membrane, including the stimulus current, are taken into account in the concentration updates, i.e. by ensuring that charge is conserved (Pan *et al.*, 2018).

Even when a model does have a periodic steady state, if V is written as a redundant ODE the charge represented by Γ_0 is defined by the initial conditions. As a result, arbitrarily varying initial conditions in the presence of this redundant ODE alters the parameterisation of the model (changes the amount of charge in the system), and any quiescent steady states or limit cycles are altered accordingly. In other words, when a redundant ODE is included there can be no unique periodic steady state, but it will vary depending on the initial conditions. Conversely, when the redundant ODE is removed there is often a unique stable limit cycle or quiescent steady state; that is, the same quiescent steady state or limit cycle is reached for *any* initial conditions.

Some authors such as Livshitz & Rudy (2009) have gone a step further, and suggested that uniqueness of limit cycles/quiescent steady states is guaranteed once conservation of charge is met. An analysis by Jacquemet (2007), however, shows that more than one stable quiescent steady state can exist for a charge-conserving model with a given

value of Γ_0. Examining the atrial model by Nygren *et al.* (1998), Jacquemet found that for some values of Γ_0 the model had a stable steady state where V is polarised at rest (-60 to $-90\,\mathrm{mV}$), a stable steady state where the cell is depolarised to about $-30\,\mathrm{mV}$, and an unstable periodic steady state where the model displays automaticity. In the course of this study we also found examples of more than one stable limit cycle in other analytic-V models, which are discussed below.

Although undoubtedly important for reproducible modelling, it is reasonable to question the physiological relevance of quiescent steady states and limit cycles. Convergence to a perfect limit cycle seems unlikely to occur in real cells, as channel activity and other chemical processes are inherently stochastic and will perturb each orbit differently. The idea of a limit cycle, however, overlaps well with biological concepts of homeostasis and robustness. Even though the cell's environment is constantly altering to some degree, it would be ideal for a cell to exist in close proximity to a stable limit cycle such that small stochastic perturbations converge back to the same behaviour — at least while energetic demands are met.

3.2 Impact of the algebraic voltage formulation on numerical solutions

3.2.1 Models and simulation

CellML files for the TP and ORd-CiPA models were obtained from the Physiome Model Repository (Yu *et al.*, 2011). The TP model has epi-, endo- and myocardial variants; where not stated otherwise we used the epicardial variant in this Chapter. The units in the obtained CellML files for TP had to be corrected before the algebraic-V_m form could be applied, as described in Section A.1 in the Appendix. The algebraic-V forms of the TP and ORd-CiPA models were derived, and model variants that employ this form were created for comparison with the original derivative-V form. A detailed overview of the conversion of a model to its algebraic-V form is given in Section A.3 in the Appendix, along with a guide to performing this translation in other models.

Simulations were performed using Myokit (Clerx *et al.*, 2016) which imported the CellML models, and using solver tolerances stated in the section below. Unless stated

otherwise, figures were created after 2000 pre-pacing stimuli at a frequency of 1 Hz. In the TP model, the stimulus current was modelled as a K^+ current of amplitude -52 A/F lasting 0.5 ms. In the ORd-CiPA model, the stimulus current was also attributed to K^+ ions, its amplitude was set at -50 A/F, and its duration at 1 ms.

All the Python scripts, CellML and Myokit models used for this Chapter are available in a GitHub repository at https://github.com/CardiacModelling/Gamma_0.

3.2.2 Accuracy of solutions

Simulations in Myokit are performed using the CVODES software package (Hindmarsh *et al.*, 2005) to numerically integrate the differential equations. CVODES has two "tolerance" settings that control the accuracy of the numerical solutions (Cohen *et al.*, 1996). To visualise the influence of solver tolerance on AP simulations and find suitable tolerances to use in this Chapter, simulations were run for 2000 paces with the ORd-CiPA model in its derivative-V form, using a coarse setting (10^{-6} and 10^{-4} for absolute and relative tolerance, respectively) and a fine setting (10^{-8} and 10^{-6}). The resting membrane potential (RMP) was measured as the V 1 ms before application of the stimulus, and plotted for the final 1750 paces in Figure 3.2.

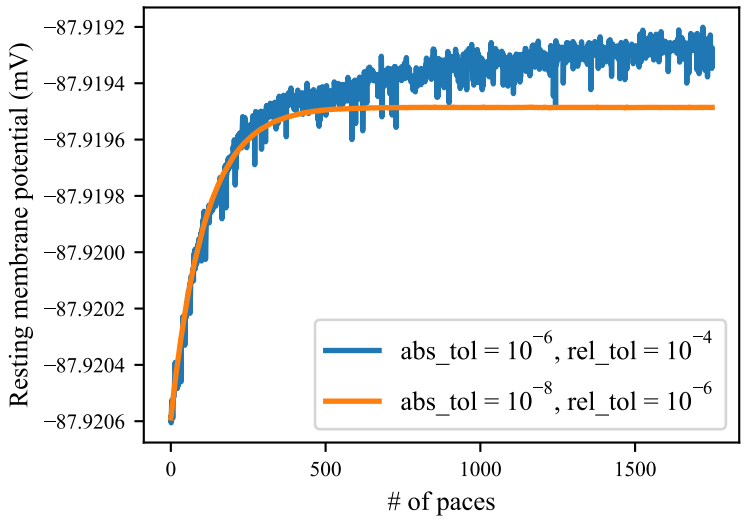

Figure 3.2: Evolution of resting membrane potential (RMP) in a simulation with the derivative-V ORd-CiPA model, starting from the published initial conditions. 2000 paces were simulated, we are showing paces 250 onwards to examine the behaviour close to periodic steady state. A slight drift is observed when using a coarse solver tolerance, but this disappears when tolerances are tightened.

As expected, using coarse tolerances results in (a small) numerical error in the solution, but the figure also shows a slight drift in V, even after 1000 paces. When tightening the solver tolerance the numerical noise is significantly reduced, and V stabilises after around 700 paces. The other state variables show a similar pattern, as can be seen for $[K^+]_i$ in Section A.4 in the Appendix.

To further investigate the long term stability of the solutions, 3000 paces were simulated with the ORd-CiPA and TP models, in both the derivative and the algebraic-V forms. Since, with fine tolerances, the system had stabilised after 2000 paces (see Figure 3.2), the variation in the state variables after 2000 paces could safely be attributed to numerical error and not to electrophysiological phenomena. We quantified this variation by measuring the standard deviation in the final 1000 paces in $[K^+]_i$, the state variable that had the highest absolute value and largest variations over successive paces (Section A.4 in the Appendix). This standard deviation was evaluated for several solver tolerances in both the derivative and algebraic-V forms of the models and shown in Figure 3.3.

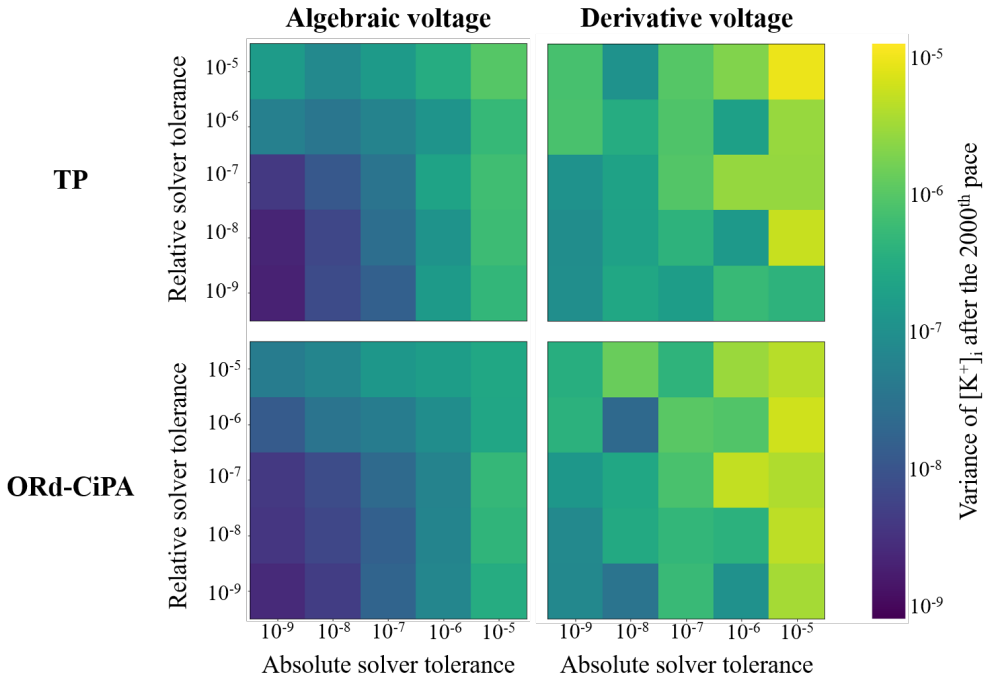

Figure 3.3: Numerical stability of $[K^+]_i$ in the TP and ORd-CiPA models, comparing the derivative and algebraic-V forms. The colour corresponds to the standard deviation of $[K^+]_i$ between the 2000^{th} and 3000^{th} pace. The darker the colour, the lower the variance, and the more stable the simulation.

For both models, numerical solutions appear less stable when using the derivative-V form (Eq. 3.1). We believe this is because the intracellular ionic concentrations and V are updated without the numerical method having any knowledge of Γ_0. This can lead to numerical errors that break conservation of charge, effectively introducing variations in Γ_0, and allowing the periodic steady state of the system to change. By contrast, when explicitly incorporating the algebraic constraint on V (Eq. 3.6) and fixing Γ_0, conservation of charge is guaranteed, so that the periodic steady state stays the same and the stability of the solution is improved.

For the remainder of this Chapter, we therefore used the algebraic-V form and absolute and relative solver tolerances of 10^{-8} and 10^{-6}, respectively.

3.2.3 Computation time

We also investigated whether computation time was affected by switching to the algebraic-V form of the model. One might have expected an improvement in simulation time due to a smaller and better conditioned system with the redundant ODE removed (avoiding a singular Jacobian as Varghese & Sell (1997) suggested), but there was no significant (if any) change in computation time (Figure A.5 in the Appendix).

3.3 Physiological impact of Γ_0

3.3.1 Γ_0, $[K^+]_i$ and $[Na^+]_i$ in human ventricular AP models

The algebraic-V form of the model (Eq. 3.6) gives the voltage in terms of the total intra- and extra-cellular ionic concentrations. The impact of variations in these parameters and variables across ventricular models was investigated by computing Γ_0 for several literature models using the published initial conditions. This work could be carried out only for models which obey the conservation of charge principle. The results are shown in Table 3.1 which reports Γ_0 (Eq. 3.6), the corresponding C_0 as defined by Endresen *et al.*, and the corresponding voltage offset ΔV for each of the investigated models.

These parameters contain information about the difference between the un-modelled intra- and extracellular charged species (e.g. H^+, Mg^{2+}, cations, phosphates, proteins). In the TP Epi model, for example, the intra- and extra-cellular charges of these missing

species are responsible for a voltage offset of 18.2 V. In the ORd-CiPA model, the voltage offset is of −126.8 V.

The Tomek *et al.* (2020) model (an update of the 2019 version to conserve charge) has a very high Γ_0 constant due to the inclusion of chloride ions, for which there is a very large difference between intra- and extracellular concentrations. In the Ten Tusscher *et al.* (2004) model, the epicardial and endocardial versions were assumed to have the same initial conditions, so their missing charge concentrations are the same. The epi/endo variants of the TP model have minor differences in the initial conditions and buffered Ca^{2+}concentrations. As a result, there are slight differences in Γ_0 between the various versions of the TP model.

Model	C_0 (mM)	Γ_0 (mM)	ΔV (mV)	Included ions
Trovato *et al.* (2020)	195.3377	−46.3377	-1.0605×10^6	K^+, Na^+, Ca^{2+}
Stewart *et al.* (2009)	147.2641	2.1359	1.8273×10^4	K^+, Na^+, Ca^{2+}
Ten Tusscher *et al.* (2004) Epi/Endo	150.5207	−1.1207	-9.5878×10^3	K^+, Na^+, Ca^{2+}
Ten Tusscher & Panfilov (2006)(TP) Epi	147.2683	2.1317	1.8237×10^4	K^+, Na^+, Ca^{2+}
Ten Tusscher & Panfilov (2006) (TP) Endo	150.5427	−1.1427	-9.776×10^3	K^+, Na^+, Ca^{2+}
Iyer *et al.* (2004b)	135.7501	10.2499	1.6659×10^5	K^+, Na^+, Ca^{2+}
O'Hara *et al.* (2011) Endo	156.8010	−7.8010	-1.2680×10^5	K^+, Na^+, Ca^{2+}
O'Hara *et al.* (2011) Epi	156.8022	−7.8022	-1.2682×10^5	K^+, Na^+, Ca^{2+}
Dutta *et al.* (2017) (ORd-CiPA) Endo	156.8011	−7.8011	-1.2680×10^5	K^+, Na^+, Ca^{2+}
Tomek *et al.* (2020) Epi	135.7563	−137.1563	-2.2294×10^6	K^+, Na^+, Ca^{2+}, Cl^-
Tomek *et al.* (2020) Endo	135.7555	−137.1555	-2.2294×10^6	K^+, Na^+, Ca^{2+}, Cl^-

Table 3.1: The integration constant for a range of human AP models, written as C_0 (Hund *et al.*, 2001) — see Section 3.1.2 —, net un-modelled species concentration Γ_0 (Eq. 3.6), and voltage offset ΔV (Eq. 3.5). The Trovato *et al.* (2020) and Stewart *et al.* (2009) models are Purkinje fibre models, while the remaining models represent ventricular cells.

It remains to be seen whether the Γ_0 value (net concentration of un-modelled ionic species) is biologically as variable as the values it has been implicitly assigned within models, or whether this simply reflects lack of information on real concentrations and subsequent uncertainty in what initial conditions should be used.

Comparing the magnitudes of Γ_0 and ΔV in Table 3.1 shows that a 20 mV variation one might observe in resting potential between models corresponds to Γ_0 variations of approximately 0.002 mM, much smaller than the variation in the offset constants between models. So what we observe is not influenced much by the precise value of the initial condition for the RMP (this is the same reason initial gating variable values have negligible effects) but instead by how the various possible initial concentrations

cause longer term system behaviour to change via altered Nernst potential (or GHK flux equations) and resulting currents, as well as any explicit concentration-dependence in gating kinetics. So the impact of initial RMP on Γ_0 can be neglected in comparison to that of initial concentrations (RMP is also much easier to measure to within a few millivolts in experiments). As a consequence, variation of the initial voltage used to compute Γ_0 from Eq. 3.6 was neglected in this study and the initial voltage as published in the original models was used to compute Γ_0 in simulations of the sections below.

3.3.2 Γ_0 and ranges of K^+ and Na^+

In this section, we estimate the variability of Γ_0 from literature and observe how this variability might impact the AP predicted by the model. The values that can be taken by Γ_0 are, for a large part, dictated by the uncertainty in intracellular concentrations in intact myocytes. Extracellular concentrations are fixed parameters in most AP models that are more reliably estimated (at least in in-vitro experiments); we therefore investigate the effect of only the initial conditions of intracellular state variables on long-term model behaviour.

A literature search was carried out to find the range of intracellular K^+ and Na^+ concentrations observed experimentally in human cardiomyocytes and/or used in simulations. The contribution of Ca^{2+} to total intracellular charge at the end of the resting phase of the AP is much smaller, so its variation can be neglected compared to K^+ and Na^+, and Γ_0 variation between the models is mainly due to different intra- and extra-cellular K^+ and Na^+. The intracellular concentrations of K^+ and Na^+ used in previous cardiac AP models are reported in Figure 3.4, for a range of tissues and species based on the annotated CellML models at `https://github.com/Chaste/cellml` that were studied in Cooper *et al.* (2015).

In human ventricular cardiomyocytes the intracellular sodium concentration ($[Na^+]_i$) was found to range experimentally from 4 mM to 16 mM (Bers *et al.*, 2003). Fry *et al.* (1986) determined experimentally that the intracellular potassium concentration ($[K^+]_i$) is 113 ± 6 mM in rat cardiomyocytes. We did not find direct experimental measurements of $[K^+]_i$ in ventricular human cardiomyocytes in the literature. Also, experimental measurements of intracellular ionic concentrations in intact cardiomyocytes were all

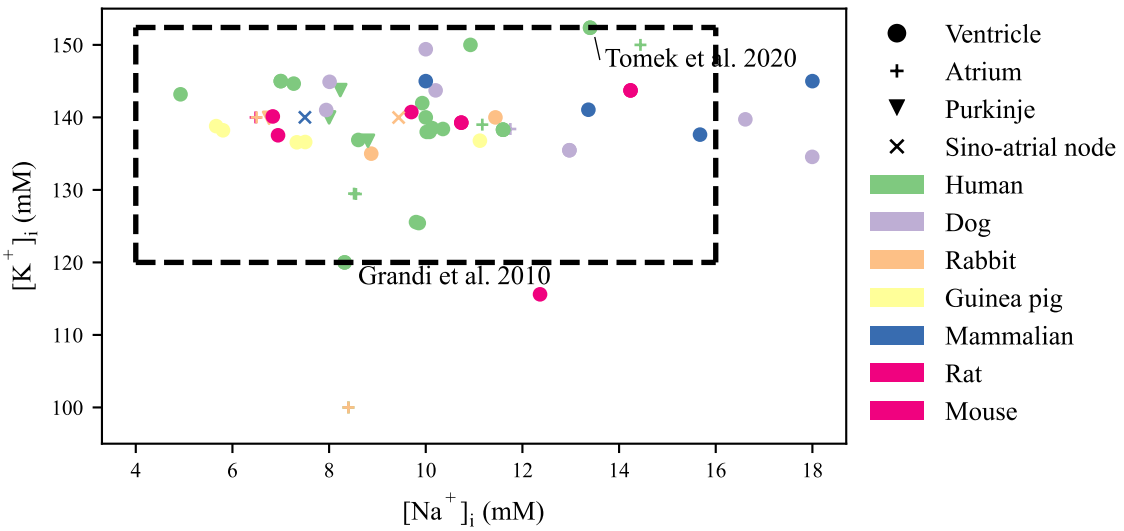

Figure 3.4: Initial concentrations published for cardiac AP models, for a range of species and tissues. **Green:** human, **Purple:** canine, **Orange:** rabbit, **Yellow:** Guinea pig, **Blue:** mammalian, **Pink:** murine. The dotted box highlights the extreme values of intracellular concentrations, estimated from the work of Bers *et al.* (2003) for Na^+ and from the Grandi *et al.* (2010) and the Tomek *et al.* (2020) models for K^+.

performed in the quiescent configuration. We therefore used initial values for $[K^+]_i$ from human ventricular AP models as a measure of uncertainty in $[K^+]_i$, which ranged from **120 mM** in the Grandi *et al.* (2010) model to **152mM** in the Tomek *et al.* (2020) model. With these estimated ranges for $[K^+]_i$ and $[Na^+]_i$, the range for their sum varies by 44 mM. This major uncertainty in intracellular concentrations produces the high variability of Γ_0 between models that is observed in Table 3.1.

The extreme K^+ and Na^+ concentrations from Figure 3.4 were used to initialise $[K^+]_i$ and $[Na^+]_i$ in simulations to observe the effect of such variations on the limit cycle AP. The K^+ concentration was initialised at 120 mM and 152 mM in the two models, whilst the initial Na^+ concentration was initialised at 4 mM and 16 mM, respectively. Γ_0 was computed from Eq. 3.6 and initial voltage was set to its published value (−84.9 mV for the TP model, −88 mV for the ORd-CiPA model). Γ_0 computed with the lowest and highest total concentration of intracellular ions yielded $\Gamma_0 = 23.6$ mM and $\Gamma_0 = -20.4$ mM in the TP model, respectively. Γ_0 computed with the lowest and highest total concentration of intracellular ions yielded $\Gamma_0 = 20.9$ mM and $\Gamma_0 = -24.4$ mM in the ORd-CiPA model, respectively.

In simulations in following sections where the value of Γ_0 is imposed by the user, the initial intracellular concentrations must be changed to satisfy the algebraic constraint of Eq. 3.6 and leave the initial voltage unchanged. Otherwise, the high variations of Γ_0 reported in Table 3.1 would lead to voltage offsets of up to several kilovolts. $[K^+]_i$ was therefore adjusted with Eq. 3.6 so that the initial voltage remains untouched and consistent with the required value of Γ_0. Alternatively, $[Na^+]_i$ could be adjusted; but the degree of variation of Γ_0 could lead to negative values of $[Na^+]_i$ so we adjust K^+ instead.

The ORd-CiPA model has more ionic variables than the TP model: variables were added for the concentrations of sodium and potassium in a subspace, denoted $[Na^+]_{SS}$ and $[K^+]_{SS}$. At the limit cycle, the difference between diastolic concentrations of ions in the subspace and in the intracellular compartment were observed to be smaller than 0.1 mM, even when initial conditions were set to very different values (results not shown). Furthermore, there is no physical structure delimiting the subspace from the bulk intracellular space. Thus, $[K^+]_{SS}$ and $[Na^+]_{SS}$ are very close $[K^+]_i$ and $[Na^+]_i$ at the end of the resting phase of the AP, i.e. when state variables are initialised in simulations. To avoid introducing big differentials in $K^+$and Na^+concentrations between the subspace and the bulk cytosol compartment in simulations where the user introduced changes to initial conditions for $[K^+]_i$ and $[Na^+]_i$, the initial conditions of $[Na^+]_{SS}$ and $[K^+]_{SS}$ were set to the same values as $[Na^+]_i$ and $[K^+]_i$ respectively.

The limit cycle APs, as observed after 2000 paces, are shown in Figure 3.5. The difference in Γ_0 induces important changes in the limit cycle AP, especially for the TP model. For instance when simulated with a very low Γ_0 value, the TP model does not have a physiological AP: the cell does not depolarise. In the ORd-CiPA model, the RMP is particularly impacted, decreasing from -82 mV for $\Gamma_0 = -24.4$ mM to -88 mV for $\Gamma_0 = 20.9$ mM. This shows that Γ_0 variations have a strong impact on the model output, which is investigated further below.

3.3.3 Effect of Γ_0 on steady states

Several authors have asserted that Γ_0 (or an equivalent) defines the steady states of various models, both under paced and unpaced conditions (Hund *et al.*, 2001; Jacquemet,

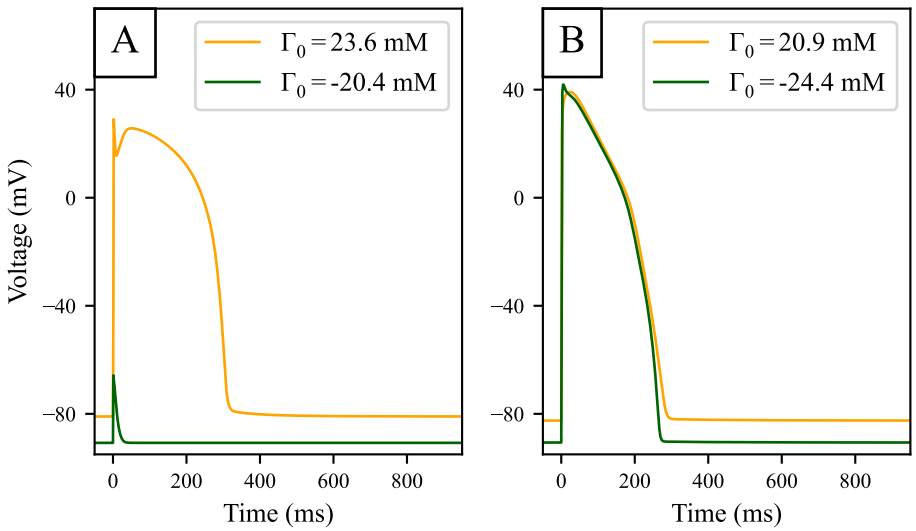

Figure 3.5: Limit cycle APs for extreme initial conditions for the TP model (**A**) and for the ORd-CiPA 2017 model (**B**). Extreme Γ_0 values covering approximately 44 mM are computed from the extreme $[K^+]_i$ and $[Na^+]_i$ observed in human ventricular models, as reported in Figure 3.4.

2007; Livshitz & Rudy, 2009; Pan *et al.*, 2018). Here we investigate the steady states and limit cycles reached by the TP and ORd-CiPA models for initial conditions that sample the range of physiologically-plausible Γ_0 values (Section 3.3.2).

The range of experimental concentrations determined in the previous section was sampled at 10 linearly spaced Γ_0 values. For each Γ_0 value, the $[Na^+]_i$ range was sampled linearly at 10 points. The initial $[Ca^{2+}]_i$ was varied from 0.5 to 1.5 times its originally published value, also with 10 sampling points, giving a total of 100 samples for each Γ_0 value. The remaining Ca^{2+} concentrations were initialised to a random value ranging from 0.5 to 1.5 times their published initial value. The initial value for $[K^+]_i$ was computed using Eq. 3.6 to match with the initial voltage of the published model. Due to the linear relationship between the ionic concentrations in Eq. 3.6, a hyperplane in the state variable space can be found for each Γ_0 value. The initial values of the remaining state variables (gating variables) were taken randomly within the range 0 to 1, and the sum of the Markov states in the I_{Kr} compartment of the ORd-CiPA model was kept equal to 1. The quiescent steady state was reached after 4000s without pacing and the limit cycle was recorded after 2000s of steady 1 Hz pacing, and the values of the state variables at the end of the diastole were recorded.

The quiescent steady state and the 1 Hz limit cycle diastolic intracellular concentrations are shown in Figure 3.6. For each Γ_0 value, all the simulations converged to the same quiescent or periodic steady state. The steady states that can be reached by the models for the various Γ_0 values align on these plots.

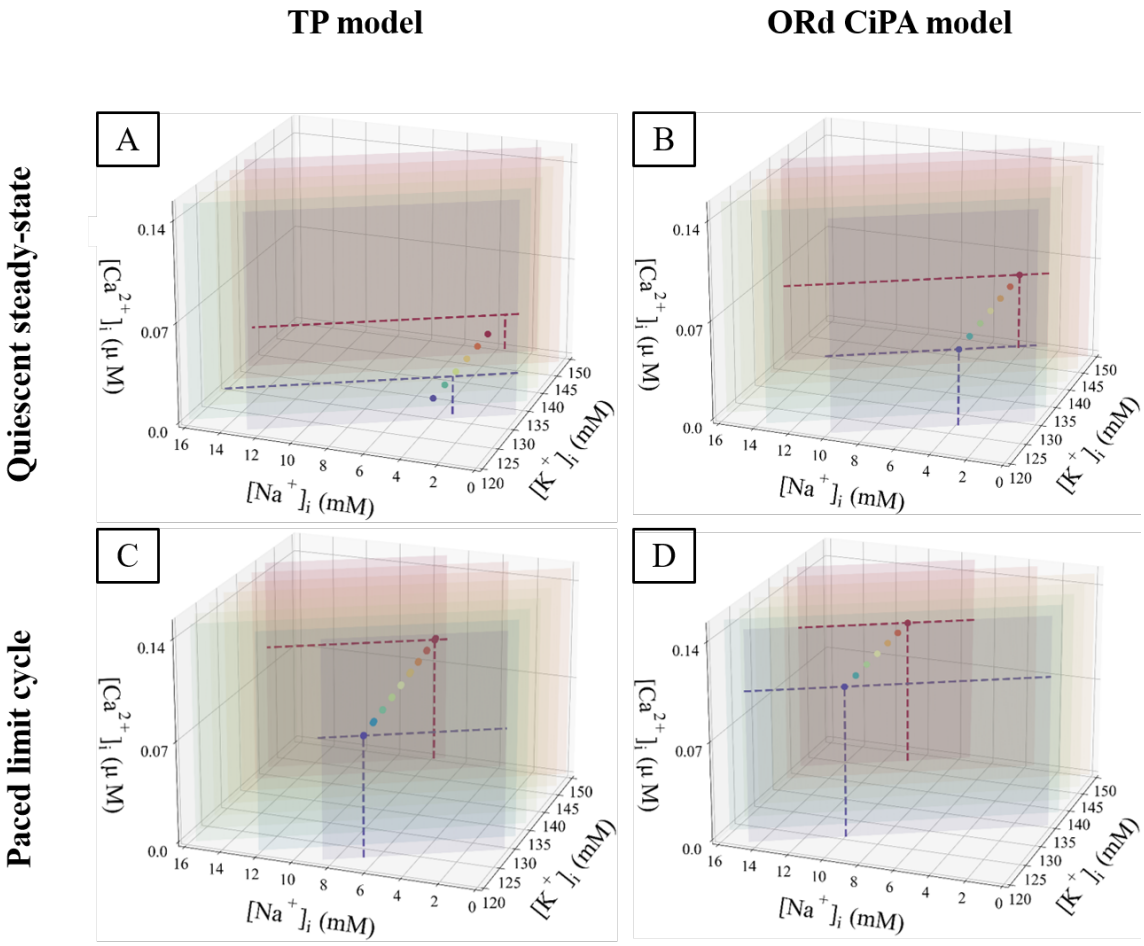

Figure 3.6: Plot of the quiescent steady state and limit cycle values for $[Na^+]_i$, $[K^+]_i$and $[Ca^{2+}]_i$. **A:** TP model at a quiescent steady state. **B:** ORd-CiPA model at a quiescent steady state. **C:** TP model in a limit cycle. **D:** ORd-CiPA model in a limit cycle. Each plane has initial conditions satisfying Eq. 3.6 with the same fixed Γ_0 value. 100 combinations of initial conditions are sampled from each plane to cover the physiological range of concentrations. These initial conditions are used in simulations to reach the (**top row**) quiescent steady state and the (**bottom row**) paced limit cycle. The steady state and limit cycle concentrations are plotted as points (with dashed projections along the associated Γ_0 plane), with the colour matching the plane from which the initial conditions were sampled. For clarity, the planes for which the quiescent steady state is out of the range reported in Section 3.3.2, are not shown.

Note how some of the points in Figure 3.6A appear to move outside the Γ_0 plane. Only $[K^+]_i$, $[Na^+]_i$, and $[Ca^{2+}]_i$ are plotted to allow a 3D visualisation of the quiescent steady states and limit cycles. Thus, major changes in other concentrations, which are

not shown in the figure, shift the steady states. Although the steady state variables appear outside of the initial Γ_0 plane in this lower dimensional representation, Γ_0 was correctly preserved throughout the simulations.

For both models, regardless of the initial conditions used for the state variables, a unique quiescent steady state and a unique 1 Hz limit cycle were observed for each value of Γ_0. Thus, the solution of the model under quiescence and for prolonged regular pacing is defined by the value of Γ_0. This observation is consistent with the studies mentioned previously, with constants equivalent to Γ_0. As a conclusion, Γ_0 can be used as a single model parameter to summarise the intracellular concentrations in these models at these pacing conditions and parameter values. Moreover, the initial conditions for the gating variables did not impact the limit cycle or steady-state outputs, so their initial conditions were not altered in further simulations. When calibrating an AP model based on its limit cycle or steady state outputs, it appears sufficient to establish the correct value of Γ_0, regardless of how K^+, Na^+ and Ca^{2+} concentrations and gating variables are individually initialised as long as they remain physiologically plausible. Thus, when exploring values of Γ_0 in a derivative-V model the changes could be attributed to a single intracellular concentration (K^+ for example) without loss of generality.

3.3.4 Model predictions are sensitive to Γ_0

The influence of Γ_0 on the limit cycle outputs and on the restitution portrait of the AP duration (APD) was evaluated in the TP and ORd-CiPA models. The models' outputs were recorded with Γ_0 values varying by 30 mM. Intracellular concentrations were initialised so that Eq. 3.6 was satisfied with the initial voltage set to its published value. The state variables other than intracellular concentrations were initialised to their originally published initial values. 2000 paces were simulated to approach the limit cycle. The currents which showed the highest sensitivity to Γ_0 change, the inward rectifier potassium current (I_{K1}) and the sodium potassium exchanger current (I_{NaK}), were recorded at 1 Hz pacing, together with V.

The APD restitution portrait at limit cycle was investigated using the Cardiac Electrophysiology Web Lab (`https://scrambler.cs.ox.ac.uk/`) (Cooper *et al.*, 2016;

Daly *et al.*, 2018). There, the models were loaded as CellML files, using the public protocol "Steady State Restitution". In this protocol, 2000 paces are applied (bringing models close to their limit cycles) at various pacing periods ranging from 250 ms to 2000 ms. Two consecutive APs are then recorded, and their APD at 90% repolarisation (APD_{90}) is measured. The limit cycle outputs at 1 Hz and the restitution plots are shown in Figure 3.7.

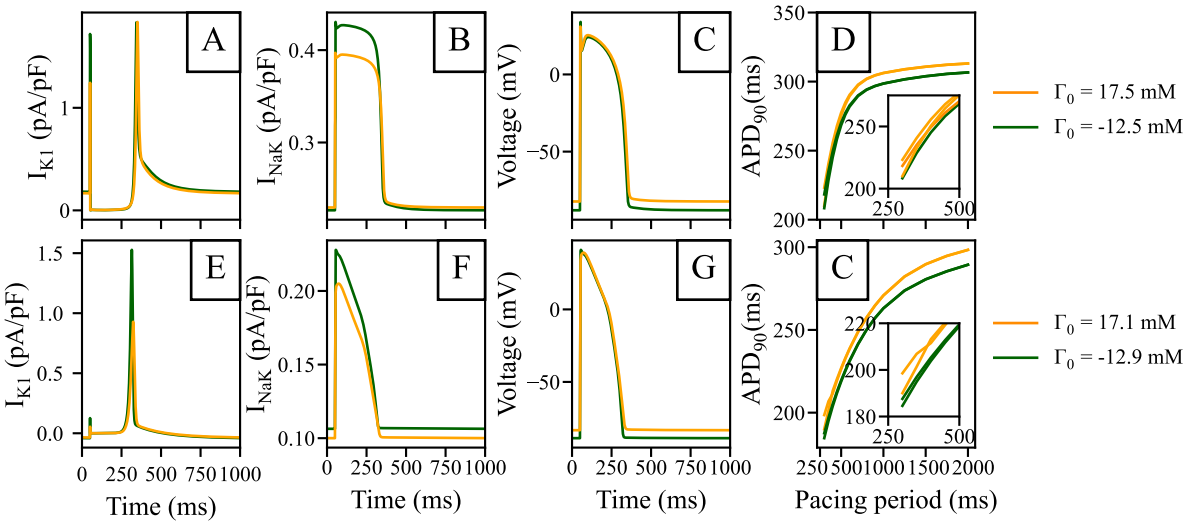

Figure 3.7: Comparison of model predictions in the periodic steady state outputs for the extreme values of Γ_0 computed from Section 3.3.2. Data are shown for the TP (**top row**) and ORd-CiPA models (**bottom row**). **A** and **E:** I_{K1}. **B** and **F:** I_{NaK}. **C** and **G:** AP. **D** and **H:** Limit cycle restitution portraits showing APD_{90} variation with the pacing period. The insets show pacing cycle lengths of 500 ms and shorter.

Γ_0 variations impacted the I_{K1} current particularly strongly in both models, with faster I_{K1} activation kinetics for lower Γ_0 values, see Figure 3.7A and E. In addition, peak I_{K1} is decreased by 45% when increasing Γ_0 by 30 mM in the ORd-CiPA model. I_{NaK} is also shown to be sensitive to Γ_0, see Figure 3.7B and F. When using a low Γ_0 value, I_{NaK} is reduced by approximately 15% in both the TP and the ORd-CiPA models. The consequences for the simulated AP are important, see Figure 3.7C and G. When looking at the resting membrane potential (RMP) and the APD_{90} for example, RMP is increased from −88 mV to −82 mV for the TP model, and from −88 mV to −83 mV in the ORd-CiPA model when increasing Γ_0 by 30 mM. APD_{90} is increased from 299 ms to 306 ms for the TP model, and is increased from 265 ms to 273 ms in the ORd-CiPA model, when increasing Γ_0 by 30 mM.

Figures 3.7D and H show that Γ_0 has an effect on the APD_{90} steady state restitution portraits. The observed APD_{90} bifurcation is particularly important as it is characteristic of *alternans*. Note that when stable alternans occurs, the limit cycle no longer follows the trajectory of the state variables over a single pacing period, but over two consecutive pacing periods.

There is a bifurcation of APD_{90} for pacing periods at 700 ms for the TP model and at 400 ms for the ORd-CiPA model. The pacing periods generating this bifurcation appear to be independent of Γ_0. However, the steepness of the restitution slope as well as the size of the bifurcation depend on Γ_0, especially in the ORd-CiPA model. In the studied models, higher values of Γ_0 generate wider bifurcations in the APD_{90} restitution portrait. The impact of Γ_0 on characteristics of the alternans predicted by the TP and ORd-CiPA models shows the need to carefully consider the value of Γ_0 used in AP models.

3.4 Calibration of AP models and Γ_0

The dependency of model outputs to Γ_0 observed in Figure 3.7 is also expected have an impact when fitting parameter values to whole traces of V, or their derived biomarkers. Indeed, if Γ_0 is fixed to a value that incorrectly summarises the experimental concentrations under which the data were generated, we might expect a fitting process to return parameter values which are skewed away from their correct values. A fitting of the ORd-CiPA model to synthetic (simulated) data was performed to examine this effect.

The synthetic datasets used in model training were generated by running the ORd-CiPA model for 2000 pre-paces (1 Hz pacing), and recording the 2001^{st} AP, with one data point per 0.05 ms. No noise was added. The "true" scaling parameters for conductances were then 'forgotten' and re-calibrated to the synthetic AP data, as in Johnstone *et al.* (2016). The parameters used for the simulations are expressed as: $g_{\text{simulation}} = \theta \times g_{\text{original}}$, with $g_{\text{simulation}}$ the value of the conductance used for the simulation, θ the scaling factor, and g_{original} the original value of the conductance parameter. Thus, a scaling factor of $\theta = 1$ corresponds to the conductance used in the original published model (the true value in this synthetic study).

Three cases were explored. In the first case, the initial conditions are unaltered (assumed to be known/exactly correct), therefore the value of Γ_0 during the fitting is set to the true value, i.e. the one used for synthetic data generation. In the second case, the model is fitted with a fixed and incorrect Γ_0 value computed from initial concentrations and voltage published for the TP model, a different but still plausible value. In the third case, fitting is the same as the second case, but Γ_0 is added to the set of parameters to be fitted, which allows compensation for discrepancy in the initial intracellular ion concentrations provided by the user. In terms of Figure 3.6 this allows flexibility in the plane upon which intracellular concentrations will settle. The initial conditions used when fitting are reported in Table 3.2.

Case	Γ_0	**Initial conditions for** $[K^+]_i$	**Initial conditions for other concentrations**
Data generation	−7.801	144.6 mM	ORd-CiPA
#1 Fixed & "correct" Γ_0	−7.801	144.6 mM	ORd-CiPA
#2 Fixed & "wrong" Γ_0	−1.562	135.4 mM	TP
#3 Fitted Γ_0	Fitted	135.4 mM	TP

Table 3.2: Initial conditions used in the various fittings of the ORd-CiPA model to synthetic data.

When using initial concentrations from the TP model, calcium concentrations, $[Na^+]_i$ and $[K^+]_i$ were set to the values published by Ten Tusscher & Panfilov (2006). $[K^+]_{SS}$ and $[Na^+]_{SS}$ were initially set to the same value as $[K^+]_i$ and $[Na^+]_i$. In the ORd-CiPA model, the SR is split into two sub-compartments while the TP model has only one SR compartment. Therefore $[Ca^{2+}]_{NSR}$ and $[Ca^{2+}]_{JSR}$ were initialised at the same concentration published by Ten Tusscher & Panfilov for $[Ca^{2+}]_{SR}$.

The optimisation problem was defined as the minimisation of the sum of square errors between the synthetic data and the fitted model AP. The fitting algorithm uses the PINTS Python package (Clerx *et al.*, 2019), to run the Covariance Matrix Adaptation-Evolution Strategy (CMA-ES, Hansen *et al.* (2003)). The scaling factor parameters $\theta_{CaL}, \theta_{Kr}, \theta_{Ks}, \theta_{Na}, \theta_{NaL}$ of the ORd-CiPA model were fitted. The initial guesses for scaling factors were taken from the range 0.2 to 5, while the boundaries were set to 0.1 to 10. The CMA-ES hyperparameter Σ_0, the initial proposal covariance for new parameter samples, was set to 0.1 along the diagonal and zero otherwise.

Case	Γ_0 (mM)	Diastolic $[K^+]_i$ at limit cycle	θ_{CaL}	θ_{Kr}	θ_{Ks}	θ_{Na}	θ_{NaL}	APD_{90} baseline	APD_{90} with 50% I_{Kr} block
Data generation	−7.801	**144.4**	**1**	**1**	**1**	**1**	**1**	**266 ms**	**369 ms**
#1 Fixed & 'correct' Γ_0	−7.801	144.4	1.000	1.000	1.000	1.000	1.000	266 ms	369 ms
#2 Fixed & 'wrong' Γ_0	−1.562	138.6	0.760	1.187	0.522	1.129	1.585	265 ms	383 ms
#3 Fitted Γ_0	−7.801	144.4	1.000	1.000	1.000	1.000	1.000	266 ms	369 ms

Table 3.3: Parameters retrieved from fittings in the investigated cases. The fitting process with an incorrect Γ_0 value yields incorrect values for model parameters. Such a model suffers from poor predictive power. This can be corrected by fitting Γ_0 together with the other model parameters.

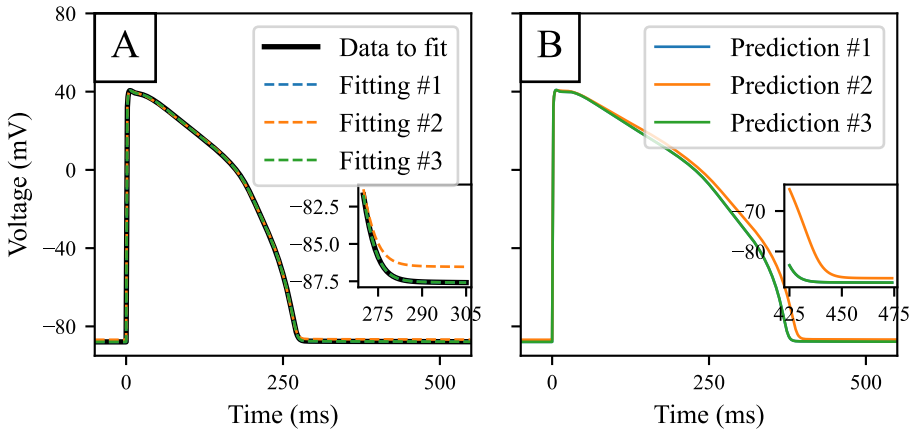

Figure 3.8: Predicted APs for the ORd-CiPA model fitted to synthetic data. **A:** Comparison of the synthetic data with APs obtained from optimal parameterisations in the different fitting cases. **B:** Prediction of response of the model to 50% block of I_{Kr}. Predictions of model with parameter fittings #1, #3 and the true parameters set overlay.

The value of scaling parameters retrieved by the three fittings are compared in Table 3.3, and the corresponding APs are shown in Figure 3.8. In the case of the first fitting with the correct Γ_0, the true parameter values are retrieved as expected due to these model parameters being identifiable. In the case of the second fitting with a discrepancy in Γ_0, the model cannot converge to the right limit cycle. The optimal AP is still very similar to the synthetic data, the only difference being a small shift in the resting membrane potential, as seen in Figure 3.8A. However, the discrepancy in ionic concentrations is compensated by a shift in the retrieved scaling parameters, especially for g_{Ks} (0.522) and g_{NaL} (1.585). This impacts the response of the model to perturbation: for example 50% block of I_{Kr} as shown in Figure 3.8B, where we see a 14 ms difference in the predicted APD_{90} which would be significant in many drug effect prediction settings.

In the third case, the true values for all scaling parameters could be recovered.

The fact that the value of Γ_0 could also be accurately found through fitting shows its identifiability as a model parameter.

3.4.1 Calibration when multiple stable limit cycles exist for a single Γ_0 value

It was shown in Section 3.3.3 that the ORd-CiPA model, with published parameters, has a unique limit cycle for any particular value of Γ_0 that has been used (implicitly) in previous models. As shown by previous studies, under certain conditions there exist multiple quiescent steady states (Guan *et al.*, 1997; Jacquemet, 2007) and/or limit cycles (Surovyatkina *et al.*, 2010) for the same value of Γ_0.

For instance, with 95% of I_{Kr}, $\Gamma_0 = -20$ mM, and 1 Hz pacing, the ORd-CiPA model has two stable limit cycle APs, shown in Figure 3.9. With the initial Na^+ concentration as originally published in the ORd-CiPA model, the limit cycle AP has an early after-depolarisation (EAD), whereas the limit cycle AP with higher initial Na^+ concentration exhibits alternans and an EAD. This is characteristic of a bifurcation of the limit cycle for the same value of Γ_0, which is investigated further in this section.

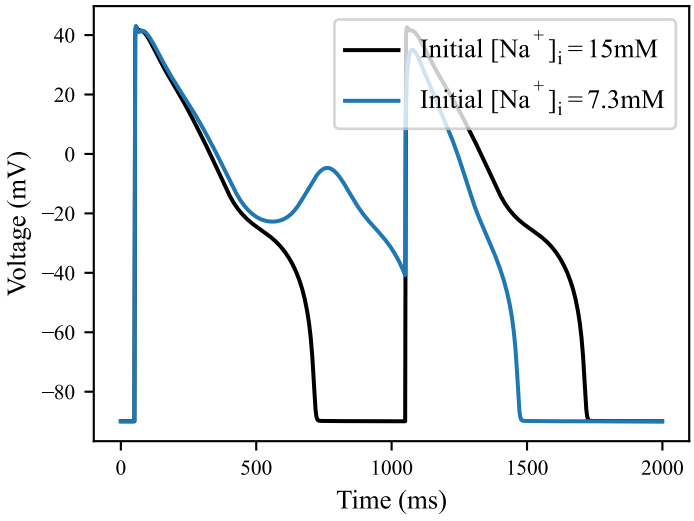

Figure 3.9: Limit cycle APs for the ORd-CiPA model with 95% of I_{Kr} reduction, generated with the same value for $\Gamma_0 = -20$ mM, but different initial $[Na^+]_i$. With the initial $[Na^+]_i$ set to 15 mM (**Black**), the limit cycle AP shows no early after-deploratisation (EAD). With a lower initial Na^+ concentration of 7.3 mM (**Blue**), the limit cycle AP exhibits alternans with an EAD.

Various conditions of I_{Kr} block (0%, 90% and 95%) were applied to the ORd-CiPA model to test for the presence of multiple limit cycles for a single value of Γ_0. As in

Section 3.3.3, the ORd-CiPA model was paced to its limit cycle for initial conditions sampling the physiological range of concentrations reported in Section 3.3.2, but variations of initial conditions were considered only for $[K^+]_i$ and $[Na^+]_i$. Given the low influence of $[Ca^{2+}]$ variations on Γ_0 value, its influence on the model outputs were neglected. Eq. 3.6 defines a linear relationship between $[Na^+]_i$ and $[K^+]_i$ and Γ_0, and therefore for a fixed value of Γ_0, the intracellular concentrations follow a line in the ($[Na^+]_i$, $[K^+]_i$) plane, if the other ionic concentrations are not changed. 10 different initial conditions were sampled for each of the 15 values of Γ_0 covering the physiological range of concentrations ($[K^+]_i$ between 120 mM and 152 mM and $[Na^+]_i$ between 4 mM and 16 mM). In cases with alternans, diastolic concentrations were read out at the end of the longer AP.

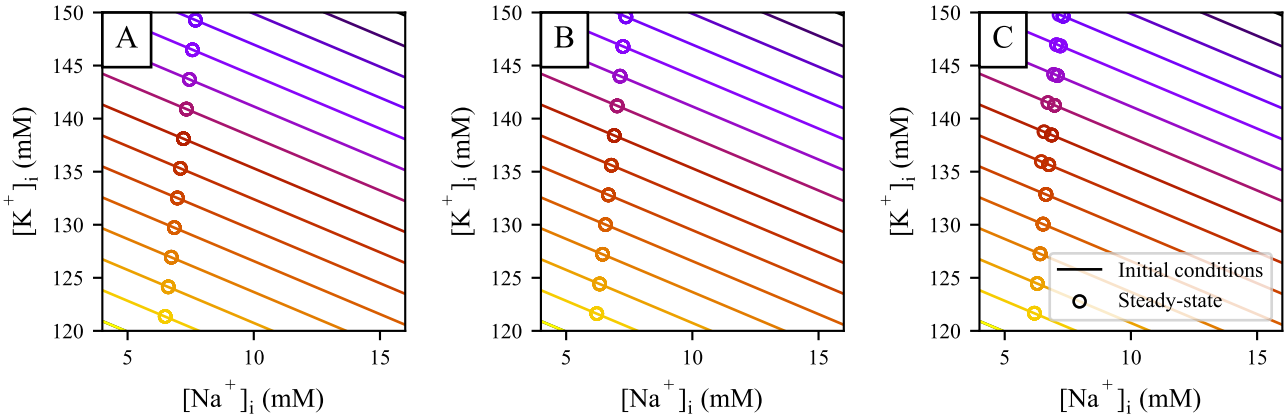

Figure 3.10: Limit cycle concentrations of $[K^+]_i$and $[Na^+]_i$ for simulations with ORd-CiPA model starting from different initial conditions. Each line corresponds to a single Γ_0 value. For each value of Γ_0, 10 combinations of $[K^+]_i$and $[Na^+]_i$ are used to sample the whole physiological range reported in Section 3.3.2. Limit cycle concentrations of the 10 combinations are marked by circles, with colour matching the initial conditions. With 90% I_{Kr} reduction, a unique limit cycle can be reached per value of Γ_0. In the case of 95% of I_{Kr} reduction, two distinct limit cycles can be observed for higher intracellular concentrations. **A:** No I_{Kr} reduction. **B:** 90% I_{Kr} reduction. **C:** 95% I_{Kr} reduction.

The limit cycle diastolic concentrations are shown as circles in Figure 3.10. For I_{Kr} block lower than 90% across the range of initial conditions we studied, the limit cycle is unique for a given value of Γ_0. In such situations, fitting Γ_0 would be sufficient to fully inform the intracellular concentrations.

In the extreme case of 95% of I_{Kr} block, a bifurcation is observed for the ORd-CiPA model — see Figure 3.10C. A second stable limit cycle appears, and intracellular concentrations converge to one or the other limit cycle value depending on their initial

conditions, despite having the same Γ_0 value. The multiple limit cycles at a fixed Γ_0 value are observed for Γ_0 values ranging from $-13\,\mathrm{mM}$ to $2\,\mathrm{mM}$ — see Figure 3.10C. In such cases, Γ_0 does not solely determine which limit cycle will be reached, and one needs to consider $[K^+]_i$ and $[Na^+]_i$ initial conditions separately.

As observed in Figure 3.10, multiple stable limit cycles can be found for the same value of Γ_0 under particular conditions. In the following, we investigate how the bifurcations of the limit cycle can impact the fitting process. Under 95% of I_{Kr} reduction, there are two stable limit cycle APs for the ORd-CiPA model for the same value of Γ_0: one with an early after-depolarisation (EAD) generated with low initial $[Na^+]_i$, and one without EADs with high initial $[Na^+]_i$ (Figure 3.9).

The synthetic data were generated with the ORd-CiPA model under 95% of I_{Kr} block, with intracellular concentrations initialised at $[Na^+]_i = 15\,\mathrm{mM}$ and $[K^+]_i = 149\,\mathrm{mM}$, corresponding to $\Gamma_0 = -20\,\mathrm{mM}$. Synthetic data showed no EAD. As seen in Figure 3.9, there is a second stable limit cycle AP, with EAD, in this configuration of the ORd-CiPA model with lower initial Na^+ concentration.

During the fitting process, the initial concentration of $Na^+$was fixed to its published value $[Na^+]_i = 7.3\,\mathrm{mM}$, and when a new value of Γ_0 was proposed by the fitting algorithm, the changes in Γ_0 were attributed to K^+ ions. As a consequence, when the "true parameters" were evaluated during the fitting process, an EAD was observed. Fitting of the ORd-CiPA model to synthetic data from the same model was performed with the same methods as in Section 3.4. The same parameters as previously were fitted (θ_{CaL}, θ_{Kr}, θ_{Ks}, θ_{Na}, θ_{NaL}, Γ_0).

Note that for $\Gamma_0 = -20\,\mathrm{mM}$, $[Na^+]_i$ can take only values between 14 mM and 16 mM for $[K^+]_i$ to remain in the physiological range (Figure 3.10). This bifurcation was selected despite the initial and limit cycle concentrations being outside the physiological range, because of the dramatic changes between the two limit cycle APs that make more visual the potential impact of multiple stable limit cycles on the parameters obtained from model calibration.

The parameters found by fitting are reported in Table 3.4. The limit cycle AP under 95% I_{Kr} reduction for the calibrated model is compared to the synthetic data

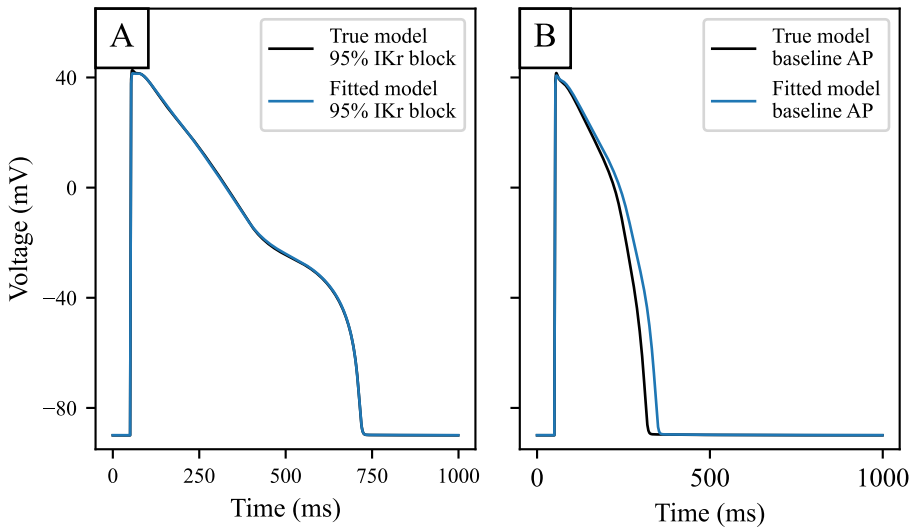

Figure 3.11: Consequence of fitting the ORd-CiPA model in case of multiple stable limit cycles for the same Γ_0 value. **A:** ORd-CiPA fitted with initial $[Na^+]_i$= 7.3 mM under 95% I_{Kr} block is able to reproduce the synthetic data generated with initial $[Na^+]_i$= 15 mM (APs superposed). **B:** predictions for no I_{Kr} block. Despite the good fit to I_{Kr} block data in Panel A, incorrect parameter values are obtained, and the prediction by the calibrated model is erroneous.

	Γ_0 (mM)	Diastolic $[K^+]_i$ (mM)	θ_{CaL}	θ_{Kr}	θ_{Ks}	θ_{Na}	θ_{NaL}	APD_{90} with 95% I_{Kr} block	APD_{90} baseline
Data generation	**-20.0**	**156.18**	**1**	**1**	**1**	**1**	**1**	**663 ms**	**264 ms**
Fitted values	-19.7	155.73	0.863	0.933	1.263	0.936	1.574	663 ms	294 ms

Table 3.4: Rescaling factors for conductance parameters retrieved from fitting to data generated under conditions where several stable limit cycles coexist for the same value of $\Gamma_0 = -20$ mM.

(Figure 3.11A) and its prediction of AP without I_{Kr} block is compared to that of the true model that generated the synthetic data in the validation case of Figure 3.11B.

The optimal values of θ_{Kr} and θ_{Na} are close to their true values, but θ_{NaL} and θ_{Ks} show considerable differences to their true values (57% and 26% increase respectively). This explains why even though the synthetic data AP are well reproduced (Figure 3.11A), the fitted model makes an incorrect prediction in the validation case with no I_{Kr} block (Figure 3.11B). The optimal value of Γ_0 is interestingly close to its true value. However, one cannot conclude from this example alone that Γ_0 value will still be correctly recovered in the case of bifurcation.

In this case with bifurcation, fitting initial conditions for both $[Na^+]_i$ and $[K^+]_i$ would be necessary to reach the correct limit cycle and obtain a correct optimal model. However,

we would not recommend fitting both $[Na^+]_i$ and $[K^+]_i$ simultaneously as a standard. In most cases, there is only one limit cycle solution for a given value of Γ_0, so that the two parameters would be unidentifiable (see Whittaker *et al.*, 2020).

3.5 Discussion

We have investigated the consequences of computing voltage in AP models directly from concentrations, using an algebraic-V formulation (Eq. 3.6). This method for computing V provides increased numerical accuracy of solutions compared to the derivative-V method. The computation time was not significantly impacted: changing to the algebraic-V form did not reduce the computational time required for AP simulations, most likely because it does not change the stiffness of the model (the main driver for the computational cost).

Γ_0 represents the net concentration of un-modelled charge. In most cases, the value of Γ_0 defines the steady-state behaviour of the model, regardless of the combination of initial values for state variables such as concentrations. Given the high variability of intracellular concentrations used in AP models, Γ_0 is also highly variable. Extreme variations of Γ_0 lead to very different steady-state behaviours and substantially impact simulation outputs, making it important to establish Γ_0 as accurately as possible.

Measurements of intracellular ionic concentrations in intact myocytes are not generally available alongside recordings of electrophysiological activity used to calibrate AP models. We showed that this issue could potentially be addressed by inferring Γ_0 from the data.

With the algebraic-V form, the algebraic constraint on the variables appears explicitly. At each time-step, this constraint is therefore rigorously applied. With the derivative-V form, the constraint is mathematically satisfied by the system — by design in AP models which satisfy the conservation of charge principle — but during the numerical integration of the equations, the constraint is not verified at each time step. Therefore, even small numerical errors appearing during integration allow the constraint to be violated. This violation of conservation of charge explains why with a coarse solver tolerance, the model does not properly converge to a limit cycle (Figure 3.2). Livshitz & Rudy (2009) noted that AP models are often mistaken for Ordinary Differential Equation (ODE) systems when they are actually Differential-Algebraic Equation (DAE) systems, i.e., ODE systems

with algebraic constraints. With the algebraic-V form, the DAE constraints appear explicitly. In theory, the differential-V and algebraic-V equations are mathematically equivalent, so modellers could use either of them as preferred (Hund *et al.*, 2001). In practice, we recommend the algebraic-V form.

Using this makes Γ_0 appear as a model parameter, highlighting the need to consider it explicitly. We propose to infer Γ_0 from the experimental data on which the model is calibrated. Endresen *et al.* (2000) wrote with the derivative-V form that "the observer tracks only the variations in the number of ions, but then an initial concentration must be guessed". Livshitz & Rudy (2009) proposed criteria for validation against experimental data and adequate comparison between dynamic models. Among these criteria, the use of "a consistent set of initial conditions for state variables (V, intracellular ion concentrations)" is recommended. Smirnov *et al.* (2020) noted that the question of initial conditions for ionic concentrations is often overlooked when fitting AP models, when they fitted the O'Hara Rudy model (O'Hara *et al.*, 2011) to AP recordings from optical mapping experiments in human ventricular wedges.

The errors induced in conductance fits when using a fixed but incorrect Γ_0 (Section 3.4) emphasise the importance of using the correct initial concentrations when fitting to AP data. An AP model calibrated using incorrect concentrations (i.e. an incorrect but plausible value for Γ_0) will be badly parameterised, with up to $\pm 50\%$ error in maximal conductance parameters, and reduced predictive power.

Our results show that Γ_0 can be fitted to compensate for errors in assumed intracellular concentrations, at least when fitting to synthetic (simulated) AP data. So we recommend inferring Γ_0 from the training data during model calibration, following the methods of Section 3.4. When using real data, discrepancy in the AP model may cause additional problems, but still the possibility for uncertainty in Γ_0 should be explicitly considered.

In this Chapter, we show that due to the conservation law: i) a consistent Γ_0 value should be used throughout the model calibration, and ii) it is sufficient to fit the value of Γ_0 to capture the input of intracellular concentrations on steady state outputs, unless bifurcations are present. The second point is supported by observations on other models reported in the literature (Hund *et al.*, 2001; Jacquemet, 2007; Livshitz & Rudy, 2009;

Pan *et al.*, 2018). For example, Smirnov *et al.* (2020) have included initial values for $[Na^+]_i$ and $[Ca^{2+}]_{SR}$ in their set of parameters to calibrate, which is similar to fitting Γ_0. However, they fitted their initial conditions independently at each pacing rate, thus changing the value of Γ_0 from one pacing rate to another.

It remains important to consider that the uniqueness of the limit cycle for a single Γ_0 value is not always guaranteed (Guan *et al.*, 1997; Jacquemet, 2007). The methods presented in Section 3.3.3 can be reused to verify that Γ_0 uniquely defines the limit cycle for a given set of experimental conditions. If the uniqueness of a limit cycle is verified, it is reasonable to fit Γ_0 alone to summarise the initial intracellular ionic concentrations. If the limit cycle bifurcates, we recommend fitting Γ_0 and the initial condition of $[Na^+]_i$. Alternatively, initial conditions for $[K^+]_i$ and $[Na^+]_i$ could be inferred.

3.5.1 Limitations

As mentioned above and in the literature (Guan *et al.*, 1997; Jacquemet, 2007), the uniqueness of the steady states for a single Γ_0 value is not always guaranteed. In cases of bifurcation, where several stable solutions exist for the model with a single value of Γ_0, Γ_0 (as well as other parameters) can be incorrectly determined. We observed in this Chapter that for the ORd-CiPA model, the limit cycle is unique in most physiologically-plausible cases. However, this property does not always hold if parameters are changed. A method to thoroughly investigate the uniqueness of the limit cycle for a given value of Γ_0 for all parameterisations of an AP model would be extremely costly computationally. Still, we have demonstrated for the ORd-CiPA model that Γ_0 is identifiable and could be correctly estimated. We observed consistent findings for Γ_0 in the TP model, which has a very different model structure to the ORd-CiPA model (data not shown). We therefore expect this behaviour to be replicated with other AP models that conserve charge.

To define the physiologically-plausible range of concentrations, we used the extreme values of $[K^+]_i$ reported in previous human ventricular AP models. Direct experimental measurements of $[K^+]_i$ would help refining this range. Moreover, $[Na^+]_i$ and $[K^+]_i$ were considered separately in our study. Simultaneous experimental measurements of $[Na^+]_i$ and $[K^+]_i$ in human ventricular cardiomyocytes would give better understanding

of correlation between these concentrations, which may further restrict the range of physiologically-plausible Γ_0 values.

When AP models are used to investigate changes in extracellular concentrations (e.g. when simulating hypo/hyperkalemia or ischaemia — pathological changes to extracellular concentrations such as $[K^+]_o$) care is needed with Eq. 3.6. In such situations, as the extracellular concentration of interest changes, opposite charges will be introduced into the same solution to maintain electrical neutrality, e.g., if we experimentally use the salt KCl to change $[K^+]_o$ we also change $[Cl^-]_o$. If one ion is accounted for in Eq. 3.6 but the "opposite ion" is not (e.g., the model does include $[K^+]_o$ but does not explicitly consider $[Cl^-]_o$) then Γ_0 will need to be adjusted by the same amount to account for this extra 'opposite' charge. If external concentrations are fixed as constants an equation of the form of Eq. 3.2 with V_0 or C_0 can be used, thus simplifying simulation procedures when extracellular concentrations are changed by the user.

3.5.2 Future work

Although this Chapter was focused on ventricular AP models, the conservation law applies to all cellular electrophysiology models including: other cardiac cell types, neurons, gastric and skeletal muscle, etc.

The extent to which intracellular concentrations are known has been somewhat overlooked (Smirnov *et al.*, 2020). This Chapter shows the importance of the correct estimation of Γ_0 when specifying concentrations. In literature models, there is significant variation between the assumed initial concentrations, and therefore variation in Γ_0 (Section 3.3.2). In articles on AP model development, we have not found any discussion of the choice of Γ_0, or equivalently the choice of the offset between concentrations and voltage in initial conditions, perhaps suggesting somewhat arbitrary choices. It remains to be seen whether Γ_0 exhibits significant physiological variation to contribute to inter-cell and/or inter-individual differences in electrophysiology, or whether it is a well-constrained biological quantity — which would be the case if the un-modelled missing ions that Γ_0 represents do not vary significantly between cells or individuals. In either case, Γ_0 strongly influences model behaviour and a concerted effort should be made to identify its

value alongside other key model parameters. The recent emergence of cell-specific models (Groenendaal *et al.*, 2015) may offer an approach to quantify Γ_0 more accurately.

3.6 Conclusion

In this Chapter, we advocate for the use of the algebraic-V form of AP models, as it improves the stability of numerical solutions by enforcing an algebraic constraint hidden in the models. Furthermore, the algebraic-V form ensures that the model conserves charge. It forces the modeller to think carefully about initial intracellular concentrations and to acknowledge their effect on model outputs. We recommend consideration of the potential discrepancy and uncertainty in intra- and extracellular concentrations of ions, as model outputs and model fitting are dependent on them. The Γ_0 value summarises these factors into one parameter which can be fitted alongside the rest of a model.

In the following Chapters, unless stated otherwise, the algebraic-V form of AP models is used. When training AP models, Γ_0 is considered as a parameter to calibrate.

In Chapter 4, experimental data used for the calibration of a new AP model are introduced. The processing of the AP data central to this DPhil thesis is described, and its impact on the calibration of Γ_0 is investigated in a synthetic exercise similar to Section 3.4.

4

Analysis and curation of adult human ventricular action potential data recorded under drug treatment

Preamble

New experimental data were generated to calibrate an action potential (AP) model that reliably predicts changes in the AP duration (APD) induced by the inhibition of the rapid delayed rectified K^+ current (I_{Kr}) and of the L-type Ca^{2+} current (I_{CaL}). APs were recorded in adult human ventricular tissue under baseline conditions and with I_{Kr} and/or I_{CaL} inhibition by drugs. Drugs were tested in vitro for their inhibitor potency for both ionic currents. Combining in vitro data with ex vivo data, the APD_{90} change from baseline could be linked with I_{Kr} and I_{CaL} inhibition.

This Chapter covers experimental data generation and handling, including in vitro measurements of the effect of nine drugs on I_{Kr} and I_{CaL}, the generation, curation, and post-processing of the AP data under drug treatment, verification that the post-processed AP data is suitable for model development, and an analysis of drug-induced changes in APD.

Experimental AP data were produced by the AnaBios Corporation in two phases (2014–2016 and 2020–2022), following the methods previously described by Page et al. (2016). Based on a preliminary analysis of the Phase 1 data, I contributed to select drugs

and concentrations used in Phase 2 experiments. I also performed the data formatting, post-processing, and analysis.

In vitro measurements of current inhibition by the tested drugs were performed by colleagues in Dr. Polonchuk's lab (F. Hoffman-La Roche Ltd., Pharma Research and Early Development, Pharmaceutical Sciences).

The work presented in this chapter was partially presented in a poster session at the Computing in Cardiology 2022 conference, and the associated proceedings article was published as Barral et al. (2022a). The ex vivo measurements of APD in human ventricular trabeculae will be submitted for journal publication together with Chapter 5.

4.1 Introduction

A major objective of this DPhil thesis is to develop an AP model predicting changes in action potential (AP) duration (APD) induced by the inhibition of the rapid delayed rectified K^+ current (I_{Kr}) and of the L-type Ca^{2+} current (I_{CaL}). In this Chapter, we describe the acquisition, curation, and analysis of experimental data used to gain understanding of the relationship between the APD, I_{Kr} inhibition, and I_{CaL} inhibition.

Because of the lack of non-invasive methods to record AP data in patients, many studies have been carried out in animals or *in vitro*. However, animals and *in vitro* systems exhibited limited agreement with adult human systems (Hackam & Redelmeier, 2006; Jiang *et al.*, 2018). In this Chapter, we use adult human ventricular tissue to investigate *ex vivo* the link between the APD and drug treatment.

Page *et al.* (2016) developed a method to record the AP in adult human ventricular tissue. This *ex vivo* method enables the recording of AP traces during several hours, while the tissue is repeatedly paced and exposed to different stimuli, such as drugs with known inhibition of ionic currents. The method of Page *et al.* was therefore selected to generate the dataset used for model calibration.

We describe in this Chapter how the *ex vivo* data were post-processed and how AP markers, e.g., the APD at 90% repolarisation (APD_{90}), were measured. We then review the data quality by testing the reproducibility of the data and by identifying recording artefacts. In particular, movements of the recording electrode may lead to artefacts in sharp

electrode experiments (Gao & Wang, 2020), which may reduce the usability of the data for model development. Therefore, normalisation of recorded APs is investigated in this Chapter as a mitigation strategy for these recording artefacts. After data quality review, we exclude data affected by recording artefacts that are not usable for model calibration.

We then refine the relationship between drug-induced changes in APD_{90} (ΔAPD_{90}) and drug treatment, using a bioanalytical analysis to measure the actual concentration of drug to which the tissues were exposed. Combining it with *in vitro* measurements of the inhibitor potency for I_{Kr} and I_{CaL} of the tested drugs, we derive the relationship between drug-induced ΔAPD_{90}, I_{Kr} inhibition, and I_{CaL} inhibition.

We visualise ΔAPD_{90} using I_{Kr} and I_{CaL} inhibition as X- and Y-axis coordinates in "2-D maps". We therefore identify and exclude outliers to finally obtain a consistent dataset, used for model development in the following Chapters.

4.2 Presentation of drugs

In this Section, we briefly introduce the nine drugs that were used throughout this and the following Chapters.

Drug	Commercial name	Indication
Chlorpromazine	Largactil (EU), Thorazine (US)	Schizophrenia
Clozapine	Clozaril, Denzapine, Zaponex	Treatment-resistant schizophrenia
Dofetilide	Tikosyn	Atrial fibrillation and flutter
Nifedipine	Adalat	Angina, hypertension
Quinidine	Cardioquin, Cin-Quin, Quinidex	Atrial fibrillation, Brugada syndrome
Thioridazine	Mellaril or Melleril	Schizophrenia, Psychosis
Verapamil	Verapamil, Isoption, Veralan	Angina, hypertension

Table 4.1: Drugs used in the experiments of this Chapter.

Chlorpromazine was developed in the 1950's by Rhône-Poulenc, and became rapidly successful as an antipsychotic drug (Baumeister, 2013). It modulates neural transmission by increasing the synthesis, release, and metabolism of catecholamines, which are important neurohormones to the stress response (Carlsson & Lindqvist, 1963).

Clozapine, commercialised under the names Clozaril, Denzapine, or Zaponex, is indicated for treatment-resistant schizophrenia (Nielsen *et al.*, 2011). Its effect is achieved by binding with the Dopamine D_2 receptor and with other neuroreceptors (Nucifora *et al.*, 2017).

Dofetilide, also known as Tikosyn, is a class III antiarrhythmic drug used to treat atrial fibrillation and flutter by inhibiting I_{Kr} (Roukoz & Saliba, 2007).

Nifedipine (Adalat) is used to treat hypertension and angina, a type of chest pain caused by reduced blood flow to the heart (Khan *et al.*, 2019). Its mechanism of action relies on I_{CaL} inhibition to promote the relaxation of muscle cells (Van Geijn *et al.*, 2005).

Quinidine is an I_{Na} inhibitor that has been known since the 19^{th} century for its antiarrhythmic effects, and which is still used to treat atrial fibrillation (Grace & Camm, 1998) and Brugada syndrome (Belhassen *et al.*, 2004).

Thioridazine was used to treat schizophrenia and psychosis until 2005, when it was withdrawn from market due to cardiac adverse events (Purhonen *et al.*, 2012). It works by blocking Dopamine D_2 receptors, thus diminishing positive symptoms of schizophrenia, e.g., hallucinations (Feinberg *et al.*, 2022). Thioridazine is metabolised by CYP2D6 to Mesoridazine (Llerena *et al.*, 2000).

Verapamil, introduced in 1962, relies on the same principle as Nifedipine by inhibiting I_{CaL} to treat angina and hypertension (Singh *et al.*, 1978).

4.3 In vitro measurements of I_{Kr} and I_{CaL} inhibition

In vitro measurements of drug-induced I_{Kr} and I_{CaL} inhibition were performed to link drugs' concentrations with fractions of I_{Kr} and I_{CaL} inhibition. With this knowledge, drug perturbations could be selected to investigate the effect of particular I_{Kr} and I_{CaL} inhibition fractions on APD_{90} later in this Chapter.

Drug effect was modelled as simple pore block, using the Hill equation (Hill, 1910). When more than one drug was used at the same time, current inhibition was computed with the Loewe independent additivity model (Jarvis & Thompson, 2013). The current

under drug treatment, I, was computed as:

$$I = \frac{1}{1 + \sum_k \left(\frac{D_k}{\mathrm{IC}_{50,k}} \right)^{h_k}} \times I(0) \tag{4.1}$$

with D_k the concentration of drug k, h_k its Hill coefficient, $\mathrm{IC}_{50,k}$ its half-maximal inhibitory concentration, and $I(0)$ the baseline ionic current without any drug exposure.

IC_{50} and h values for drug inhibition of $\mathrm{I}_{\mathrm{CaL}}$ were obtained in Chinese hamster ovary (CHO) cells (Kim & Kim, 2005) transfected with genes encoding the human cardiac $\mathrm{Ca_V}1.2$ channel in the whole-cell patch-clamp configuration (Sakmann & Neher, 1984). The datasets for inhibition of I_{Kr} were obtained in CHO cells stably expressing hERG channels, in the whole-cell patch-clamp configuration. All patch-clamp experiments reported in this chapter were performed at 37°C. More details on the methods for cell culture and electrophysiology measurements are given in Section B.1 in the Appendix.

Two voltage-clamp protocols were used to measure drug-induced $\mathrm{I}_{\mathrm{CaL}}$ inhibition: "$\mathrm{I}_{\mathrm{CaL}}$ CiPA" (Li *et al.*, 2019) and "$\mathrm{I}_{\mathrm{CaL}}$ Pharm" (Roche in-house), shown in Figure 4.1. In the $\mathrm{I}_{\mathrm{CaL}}$ Pharm protocol, the transmembrane voltage, V, was set to a resting potential of $-90\,\mathrm{mV}$, where the baseline current amplitude was recorded. $\mathrm{I}_{\mathrm{CaL}}$ was then activated with a 120 ms step to 0 mV, where the peak current was recorded.

In the $\mathrm{I}_{\mathrm{CaL}}$ CiPA protocol, V was held at $-80\,\mathrm{mV}$, where the baseline current was recorded. Then a 40 ms step to $V = 0\,\mathrm{mV}$ was applied to record the peak current. Next, V was held at $+30\,\mathrm{mV}$ for 200 ms, followed by a downward ramp to return to $-80\,\mathrm{mV}$ in 99 ms.

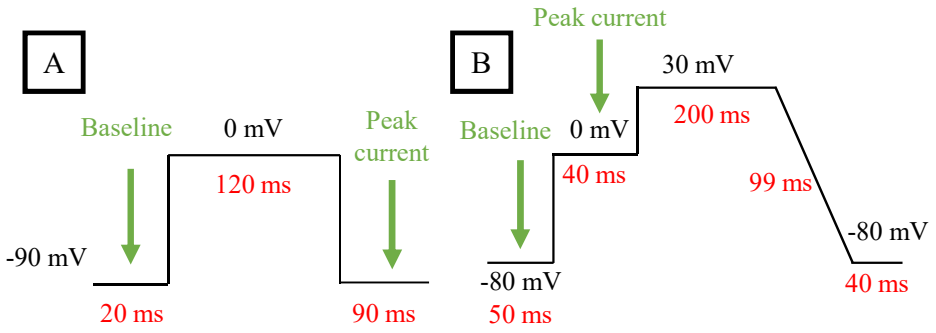

Figure 4.1: Protocols for recording peak $\mathrm{I}_{\mathrm{CaL}}$. **A:** $\mathrm{I}_{\mathrm{CaL}}$ Pharm (Roche in-house). **B:** $\mathrm{I}_{\mathrm{CaL}}$ CiPA (Li *et al.*, 2019).

Similarly, two voltage-clamp protocols were used to measure I_{Kr} inhibition, denoted "I_{Kr} CiPA" (Kramer *et al.*, 2020) and "I_{Kr} Pharm" (Roche in-house), as shown in Figure 4.2. In the I_{Kr} Pharm protocol, the resting potential was set to −80 mV. Then V was clamped to −40 mV for 100 ms, where the baseline current was recorded. V was then brought to +20 mV for 500 ms and finally to −40 mV for 500 ms, where the peak current was recorded. Afterwards, V was set back to the resting potential of −80 mV.

In the I_{Kr} CiPA protocol, V was held to a resting potential of −80 mV. $V = +40$ mV was then applied to cells for 500 ms, followed by a −1.25 mV/ms ramp that brought the voltage down to the resting potential in 96 ms. The peak current was recorded during this ramp down.

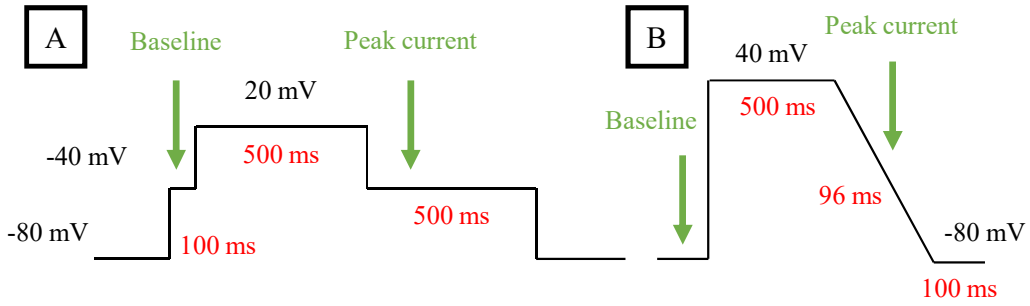

Figure 4.2: Protocols for recording peak I_{Kr}. **A:** I_{Kr} Pharm (Roche in-house). **B:** I_{Kr} CiPA (Kramer *et al.*, 2020).

The stimulation patterns were applied with a frequency of 0.1 Hz. Once the recorded peak and baseline currents were stabilised, the amplitude of the ionic current, computed as the difference between the peak and the baseline current, was recorded for 3–5 min without drug. Then, with increasing drug concentrations, the amplitude of the ionic current was recorded for 3 min. Finally, the Hill equation (Eq. 4.1) was fitted to the recorded current amplitude at each drug concentration.

Note that the recorded current amplitudes correspond to the amplitudes of ionic currents through $Ca_V1.2$ and hERG channels in CHO cells, respectively $I_{Ca_V1.2}$ and I_{hERG}. The inhibitor potency of drugs for I_{CaL} in human ventricular cardiomyocytes was assumed to be the same as for $I_{Ca_V1.2}$, and to be the same for I_{Kr} and I_{hERG}.

Between 3 and 11 repeats of each measurement were performed, and the associated Hill fits are shown in Figure 4.3 for I_{CaL} inhibition and in Figure 4.4 for I_{Kr} inhibition.

For each protocol, IC_{50} and h were taken from one repeat selected by hand to *qualitatively* match the average drug effect. The values of IC_{50} and h used for the rest of this Chapter and the rest of the DPhil project are reported in Table 4.2. Note that Dofetilide's I_{CaL} IC_{50} and Nifedipine's I_{Kr} IC_{50} were above the highest tested concentration ($> 200\,\mu$M and $> 5.2\,\mu$M, respectively). Therefore, Dofetilide and Nifedipine were modelled as selective I_{Kr} and I_{CaL} inhibitors, respectively.

Drug	**IC_{50} (h) I_{CaL} Pharm**	**IC_{50} (h) I_{CaL} CiPA**	**IC_{50} (h) I_{Kr} Pharm**	**IC_{50} (h) I_{Kr} CiPA**
Chlorpromazine	2.289 (0.88)	2.868 (0.93)	0.359 (0.84)	0.608 (0.69)
Clozapine	1.676 (0.75)	4.378 (0.93)	2.123 (1.05)	1.978 (0.94)
Dofetilide	> 200	> 200	0.029 (1.10)	0.033 (1.17)
Fluoxetine	0.994 (0.94)	0.857 (0.90)	0.712 (1.26)	0.772 (0.75)
Mesoridazine	4.056 (0.76)	3.962 (0.83)	0.503 (1)	0.565 (0.74)
Nifedipine	0.105 (0.85)	0.144 (0.72)	> 5.2	> 5.2
Quinidine	20.849 (0.63)	6.68 (1)	0.966 (1.01)	0.820 (1.43)
Thioridazine	0.497 (1.07)	0.637 (1.26)	0.171 (1)	0.154 (1.05)
Verapamil	1.381 (0.72)	0.310 (1)	0.273 (0.98)	0.570 (1.67)

Table 4.2: Inhibitor potency (IC_{50}) for I_{Kr} and I_{CaL} of drugs tested *ex vivo*, in μM. Dofetilide effect was modelled as a selective I_{Kr} inhibitor.

In the following, the "CiPA dataset" refers to using measurements of IC_{50} and h obtained with the I_{Kr} CiPA protocol and the I_{CaL} CiPA protocol. Respectively, the "Pharm dataset" refers to using measurements of IC_{50} and h obtained with the I_{Kr} Pharm protocol and the I_{CaL} Pharm protocol.

It was reported in previous studies that measurements of IC_{50} and Hill coefficients are dependent on the experimental protocol and even sometimes on the experimenter (Redfern *et al.*, 2003; Mirams *et al.*, 2011; Elkins *et al.*, 2013; Lee *et al.*, 2019). There were substantial differences between the CiPA and the Pharm datasets, the highest difference being observed for Verapamil's 4.5-fold difference in I_{CaL} IC_{50}. In other cases, the CiPA and Pharm datasets were within an acceptable 3-fold range from each other so, with similar arguments to Gomis-Tena *et al.* (2020), the Hill model (Eq. 4.1) for drug effect is reasonable for the drugs included in this study.

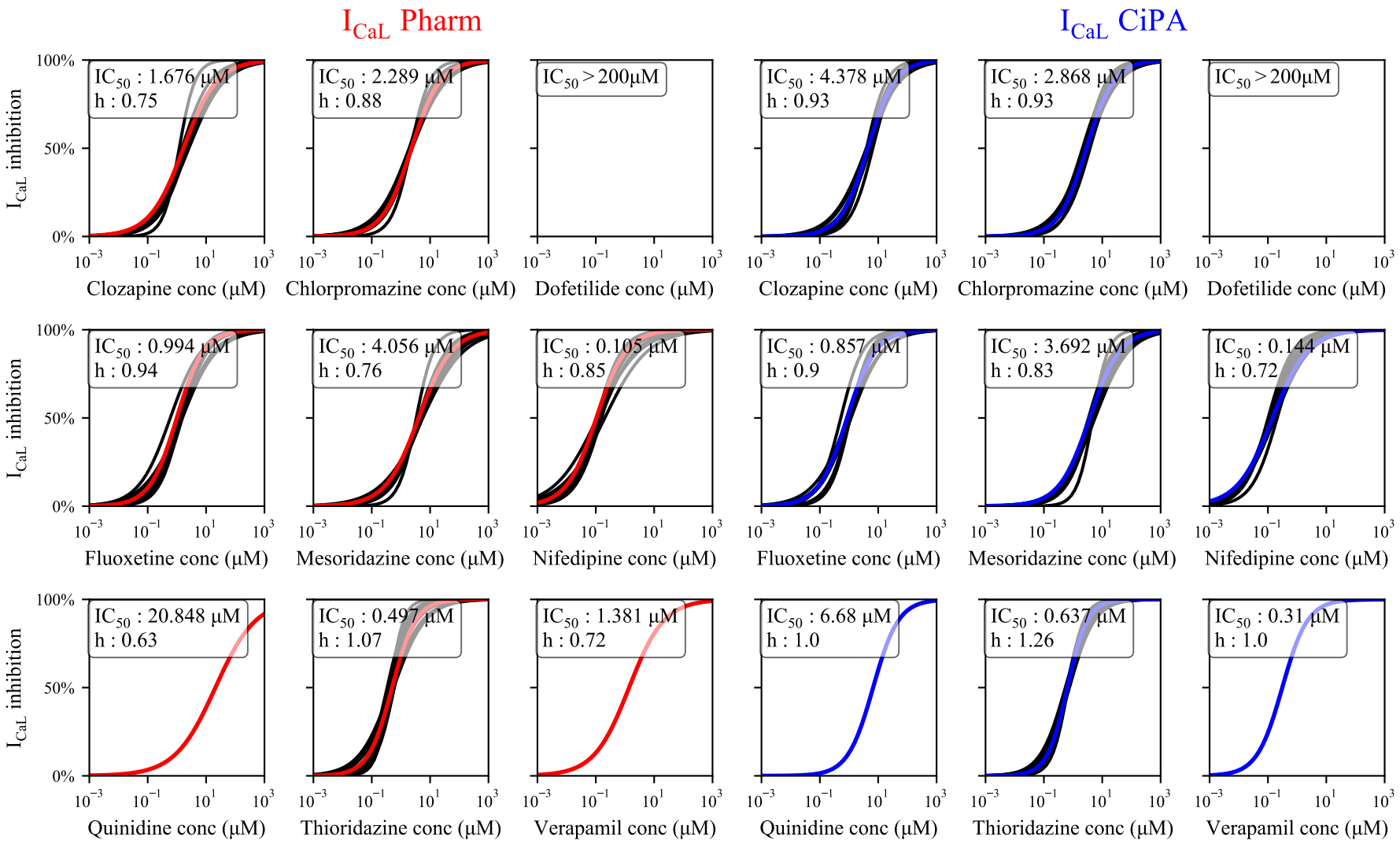

Figure 4.3: Concentration-response curves for I_{CaL} inhibition by the tested drugs, obtained for 3 to 11 repeats (**black lines**) with the I_{CaL} Pharm and I_{CaL} CiPA protocols. Qualitatively average repeats selected to compute IC_{50} and h are highlighted in **red** and **blue** for the Pharm and CiPA protocols, respectively. Dofetilide was modelled as a selective I_{Kr} inhibitor.

DRAFT Printed on May 18, 2023

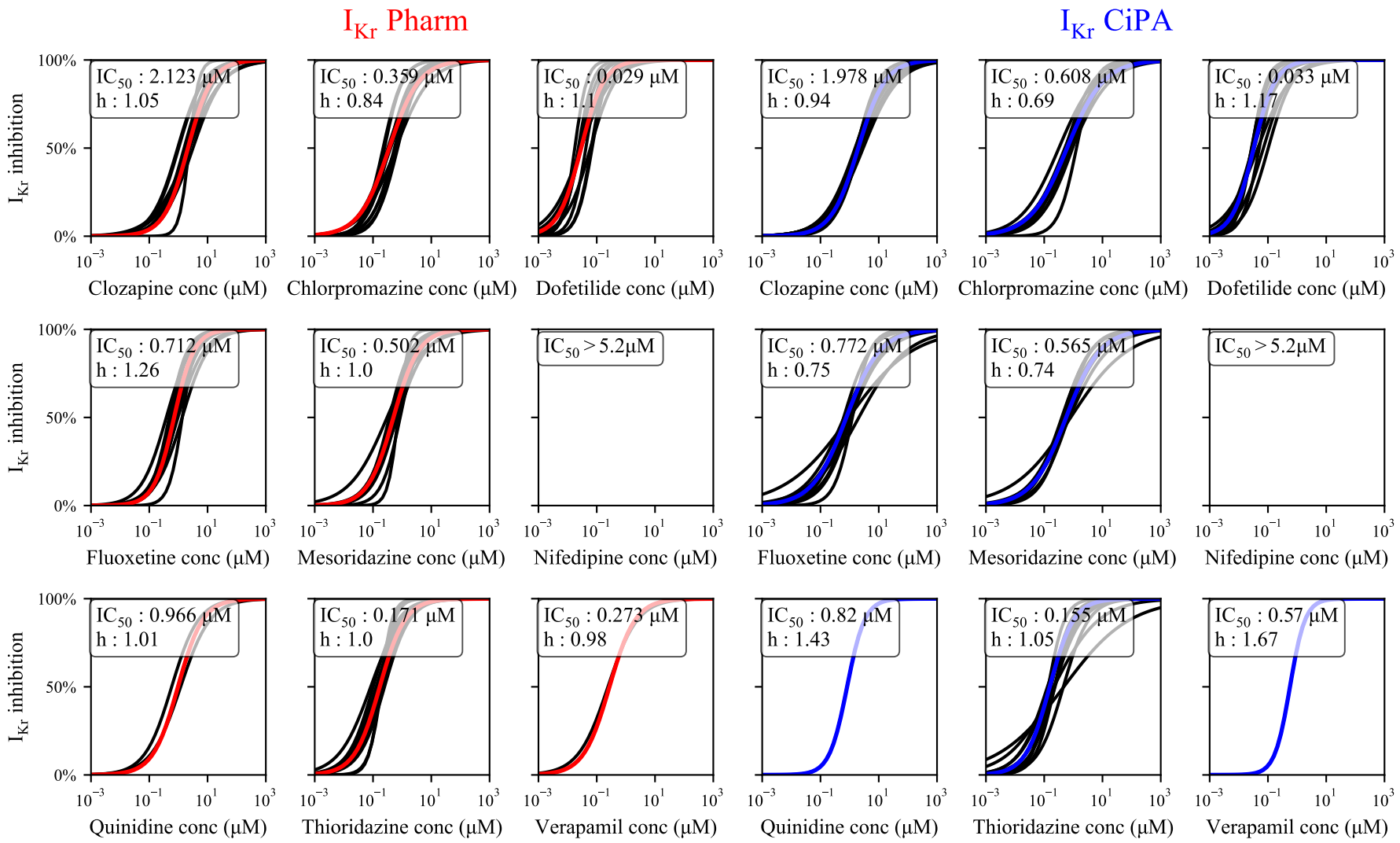

Figure 4.4: Concentration-response curves for I_{Kr} inhibition by the tested drugs, obtained for 3 to 11 repeats (**black lines**) with the I_{Kr} Pharm and I_{Kr} CiPA protocols. Qualitatively average repeats selected to compute IC_{50} and h are highlighted in **red** and **blue** for the Pharm and CiPA protocols, respectively. Nifedipine effect was modelled as a selective I_{CaL} inhibitor.

DRAFT Printed on May 18, 2023

Differences between the CiPA and Pharm datasets can be attributed to differences in the voltage-clamp protocols and also to IC_{50} uncertainty (Elkins *et al.*, 2013). However, the uncertainty in IC_{50} was not directly investigated in this DPhil.

The inhibitor potency for I_{Kr} and I_{CaL} of the drugs (Table 4.2) can be used to link drug concentrations with current inhibition, helping the selection of drug treatments (see Section 4.4 below). The *in vitro* data is also useful to derive the relationship between ΔAPD_{90}, I_{Kr} inhibition, and I_{CaL} inhibition (see Section 4.12 below).

4.4 Ex vivo action potential acquisition

AP data were acquired with the methods developed by Page *et al.* (2016). In brief, trabeculae were extracted from adult human hearts that were not suitable for transplantation, sharp electrodes were impaled in isolated cardiac muscle fibers from the trabeculae, and their electrophysiological activity was recorded at 37°C at baseline or with vehicle (solvent used to administer drugs of interest) or with drugs added. Up to three trabeculae per heart were obtained from the inner endocardial wall of the left (100 trabeculae) and right (4 trabeculae) ventricles. Each drug was applied to 4 to 15 trabeculae.

In each trabecula, the electrophysiological activity was recorded under baseline conditions, then with three increasing drug concentrations. After the last drug condition, a positive control for APD_{90} prolongation with I_{Kr} inhibition was finally performed with 100 nM Dofetilide addition.

At each drug concentration, each trabecula was paced at 1 Hz for a minimum of 25 min, until voltage recordings were stabilised for at least 2 mins. The stability of APs was assessed qualitatively by the experimenter, based on approximate measurements of the resting membrane potential (RMP), AP amplitude (APA) and APD_{90}. After reaching stable recordings, each trabecula was paced at 2 Hz for 3 min then paced again at 1 Hz for 3 min. The experimental protocol for drug administration is shown in Figure 4.5.

For more information on the experimental protocol, please refer to Page *et al.* (2016).

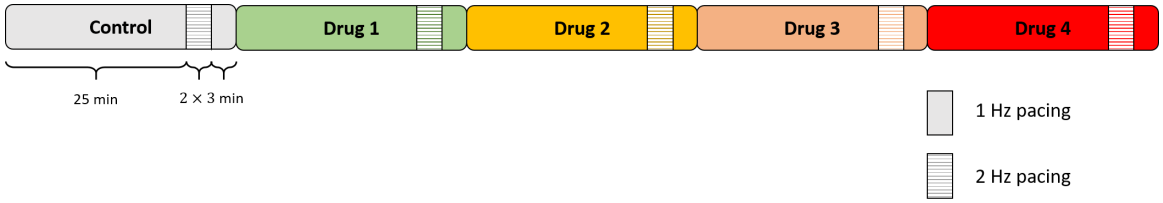

Figure 4.5: Protocol for sharp electrode recordings of the electrophysiological activity in isolated left- and right-ventricular human trabeculae. After baseline conditions, the response to three drug perturbations was recorded. After the third drug treatment, 100 nM Dofetilide was added as a positive control for APD_{90} prolongation with I_{Kr} block.

4.4.1 Selection of compounds and concentrations

Preliminary *ex vivo* data were generated in 2014–2016, prior to the work presented in this DPhil thesis. This data will be referred to as the "Phase 1" dataset. Drugs tested in Phase 1 experiments and their nominal (intended) concentrations are reported in Table 4.3. The tested drugs enabled the exploration of ΔAPD_{90} response to various combinations of I_{Kr} and I_{CaL} inhibition.

Drug	Conc #1	Conc #2	Conc #3	Conc #4	Number of trabeculae
Clozapine	0.3 μM	3 μM	30 μM	30 μM + 100 nM Dofetilide	4
Dofetilide	0.001 μM	0.01 μM	0.1 μM	0.2 μM	15
Nifedipine	0.003 μM	0.03 μM	0.3 μM	0.3 μM + 100 nM Dofetilide	4
Quinidine	0.1 μM	1 μM	10 μM	10 μM + 100 nM Dofetilide	15
Verapamil	0.01 μM	0.1 μM	1 μM	1 μM + 100 nM Dofetilide	15
DMSO (vehicle)	Rep. 1	Rep. 2	Rep. 3	100 nM Dofetilide	7

Table 4.3: Nominal drug concentrations tested *ex vivo* in Phase 1 experiments.

The list of drugs tested in Phase 2 experiments, and their nominal concentrations are reported in Table 4.4, and the induced I_{Kr} and I_{CaL} inhibition, computed with Eq. 4.1, are shown in Figure 4.6.

The compounds and concentrations tested in Phase 2 experiments were selected based on a first analysis of the Phase 1 dataset. This suggested that drugs approximately two times more potent on I_{Kr} than on I_{CaL}, e.g., Clozapine, induced small ΔAPD_{90}.

Chlorpromazine and Fluoxetine were chosen to explore I_{Kr} and I_{CaL} block conditions where APD_{90} was expected to remain approximately constant, based on Phase 1 data.

Drug	Conc #1	Conc #2	Conc #3	Conc #4	Number of trabeculae
Chlorpromazine	300 nM	1 μM	3 μM	3 μM + 100 nM Dofetilide	6
Clozapine	0.3 μM	1 μM	3 μM	3 μM + 100 nM Dofetilide	9
Dofetilide + Nifedipine	10 nM + 0 nM	10 nM + 10 nM	30 nM + 50 nM	50 nM + 150 nM	6
Fluoxetine	0.3 μM	1 μM	3 μM	3 μM + 100 nM Dofetilide	5
Nifedipine + Dofetilide	30 nM + 0 nM	30 nM + 3 nM	30 nM + 10 nM	30 nM + 100 nM	7
Mesoridazine	40 nM	250 nM	10 μM	10 μM + 100 nM Dofetilide	6
Thioridazine	12 nM	600 nM	2 μM	2 μM + 100 nM Dofetilide	5

Table 4.4: Nominal drug concentrations tested *ex vivo* in Phase 2 experiments.

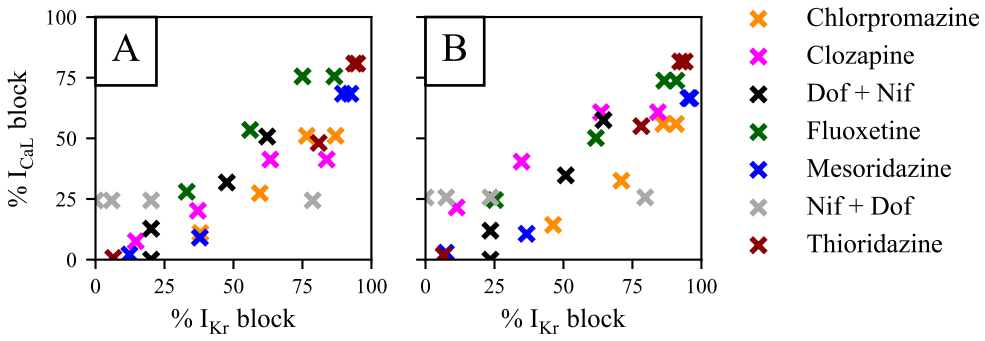

Figure 4.6: I_{Kr} and I_{CaL} block combinations achieved with the compounds and concentrations selected for Phase 2 experiments. I_{Kr} and I_{CaL} inhibition percentages were computed with IC_{50} and Hill coefficient values taken from the CiPA dataset (**A**) and from the Pharm dataset (**B**) (Table 4.2).

Thioridazine and its active metabolite Mesoridazine were selected for their mixed inhibition on I_{Kr} and I_{CaL} (Kramer *et al.* (2013) and Table 4.2). Therefore, different combinations of drug-induced inhibition of I_{Kr} and I_{CaL} could be explored, with particular emphasis on drugs with a low or intermediate pro-arrhythmic risk despite a known effect on I_{Kr}.

Finally, in order to verify that both phases gave consistent results, concentrations of Nifedipine, Dofetilide and Clozapine were selected so that at least one concentration from Phase 1 experiments was reproduced.

4.5 Ex vivo data post-processing

4.5.1 Software and data format

The raw AP data acquisition was performed by the AnaBios Corporation in `adicht` format, readable in the commercial software LabChart (https://www.adinstruments.com/products/labchart). The data were loaded and converted into Python pickle files using the `adi` Python package (https://github.com/JimHokanson/adinstruments_sdk_python). For Fourier filtering of the noise, the `numpy.fft` Python package was used.

4.5.2 Filtering

60 Hz noise due to the mains electricity was observed in the recorded voltage. A typical segment observed at the end of the APs is shown in Figure 4.7A, together with the Fourier spectrum of the whole AP (Figure 4.7B and C). To filter out the 60 Hz noise, the log-modulus and the phase of the Fourier spectrum of the AP were smoothed for each 60 Hz harmonic frequency. A representative segment and its filtering are shown in Figure 4.7 in red.

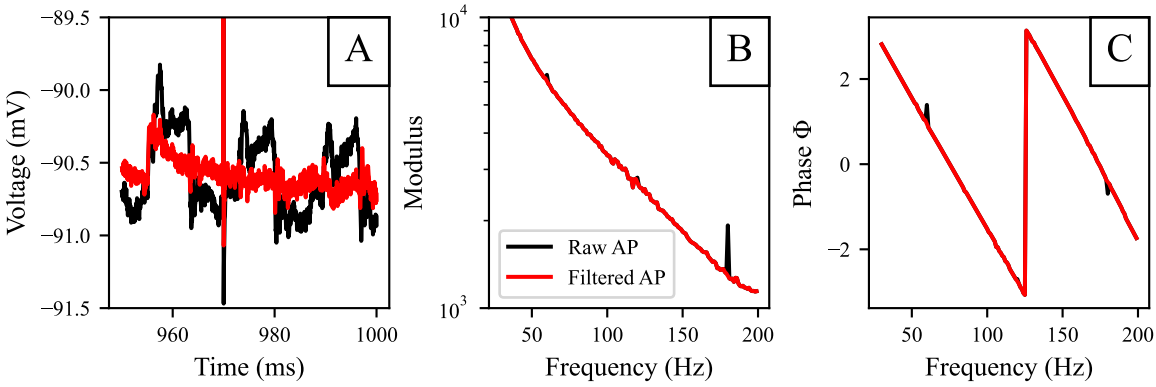

Figure 4.7: Typical 60 Hz noise, and noise filtering in the Fourier domain. **A:**Noise recorded after 25 min steady 1 Hz pacing in trabecula #2021030402. **B** Modulus (in log-scale) of the Fourier spectrum of the whole AP, zoomed on 30 Hz to 200 Hz to make 60 Hz harmonics visible. **C:** Corresponding phase of the Fourier spectrum of the whole AP.

4.5.3 Action potential markers

APs were summarised by the calculation of several markers. Upstroke time ($t_{upstroke}$) was measured for each AP as the first time point after which $V > -40$ mV was sustained for more than 50 ms. The maximal voltage reached over the course of one AP was sensitive

to noise, and successive APs — otherwise similar — exhibited substantial variability in maximal voltage. Therefore, a more robust measure for peak voltage was selected: the upper 95$^{\text{th}}$ percentile of the voltage recorded over one AP, V_{95} (Wang *et al.*, 2015). To avoid stimulus artefacts, the resting membrane potential (RMP) was measured as the average voltage between 800 ms and 900 ms after $t_{upstroke}$ at 1 Hz pacing. APA was computed as the difference between RMP and peak voltage.

APD_{90} was computed as the time after $t_{upstroke}$ needed for V to return below V_{APD} computed as:

$$V_{\text{APD}} = V_{95} - 0.9 \times (V_{95} - RMP). \tag{4.2}$$

APD_{90} was averaged over 30 consecutive APs at the end of the 25 min period of steady 1 Hz stimulation at each drug concentration.

ΔAPD_{90} was computed as the difference with APD_{90} under baseline conditions. To match more closely with guidelines for clinical safety that indicate thresholds of concern as absolute changes in the repolarisation time (ICH, 2006), ΔAPD_{90} was not normalised to baseline APD_{90} in this study. Moreover, drug-induced ΔAPD_{90} was verified to exhibit little correlation with baseline APD_{90} — see Section B.6 in the Appendix.

The recordings after 3 min of 2 Hz steady pacing had not fully stabilised in most cases, so the ΔAPD_{90} effect at 2 Hz was not investigated further in this Chapter.

4.6 Consistency from Phase 1 to Phase 2

The Phase 1 and Phase 2 *ex vivo* datasets were generated at different times in different trabeculae over a period of 8 years. The Phase 1 dataset was used to design the experiments for the generation of the Phase 2 dataset. The Phase 2 dataset reproduced some of the Phase 1 drug perturbations, and explored the ΔAPD_{90} response to other drug perturbations.

To ensure that both datasets are consistent, ΔAPD_{90} were compared. Clozapine (0.3 μM and 3 μM), Nifedipine (30 nM), and Dofetilide (10 nM) experiments were repeated in the Phase 2 dataset. ΔAPD_{90} for both datasets are shown in Figure 4.8.

No significant difference between the ΔAPD_{90} distributions obtained from both datasets could be found, indicating good reproducibility. As a result, Phase 1 and Phase 2 datasets can be safely concatenated.

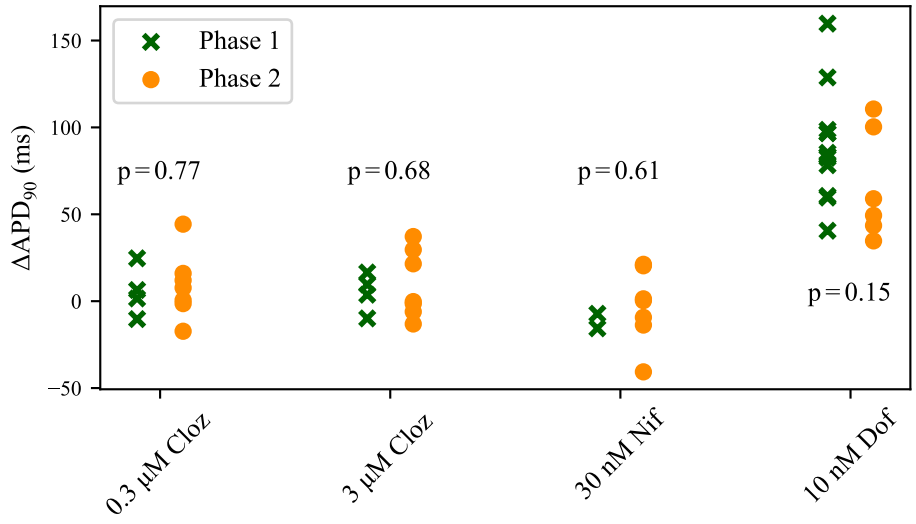

Figure 4.8: ΔAPD_{90} recorded in Phase 1 and Phase 2. *p*-values were computed with Student's t-test.

4.7 Stimulus artefact varies between trabeculae and prevents calibration of I_{Na}-related parameters

The tissues were stimulated by applying a 3 V pulse for 3 ms, which is 1.5-fold the threshold for AP generation (Page *et al.*, 2016). A stimulation artefact could be observed as a biphasic pulse before the upstroke, illustrated in Figure 4.9 for trabeculae #2021060701 and #2021052102.

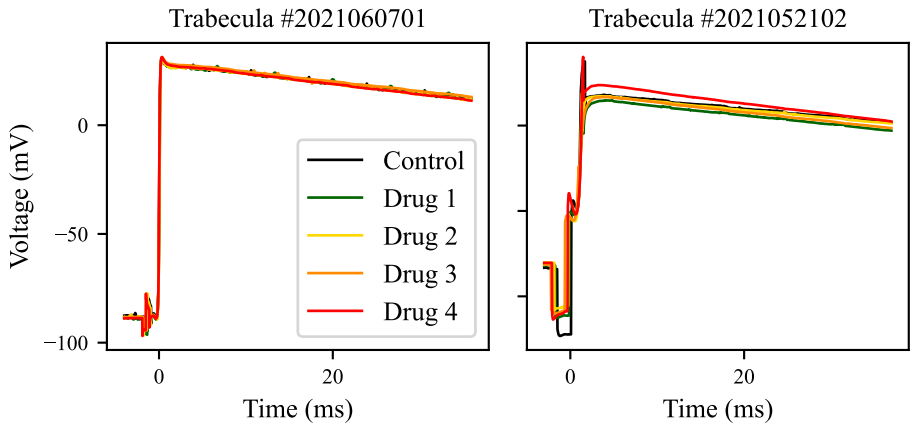

Figure 4.9: Biphasic pulses observed in trabeculae #2021060701 (**left**) and #2021052102 (**right**) after 25 mins of steady 1 Hz pacing, for each tested drug concentration (Figure 4.5).

The duration of the stimulation artefact remained unchanged in the same trabecula

throughout the whole experiment. However, the duration of the stimulation artefact varied between trabeculae (Figure 4.9). In addition, the magnitude of the artefact could vary during the experiment, as observed in the example of trabecula #2021052102.

The delay between the stimulation artefact and $t_{upstroke}$ varied between individual trabeculae, so that the artefact could interfere with the voltage recorded during the upstroke, and the data had to be discarded. To obtain a consistent dataset across all trabeculae, time points potentially affected by stimulus artefacts in any trabecula were discarded. Thus, data points around the upstroke (within $[t_{upstroke} - 100\,\text{ms}; t_{upstroke} + 5\,\text{ms}]$) were systematically excluded from model training.

In AP models, the upstroke is mainly driven by the fast sodium current I_{Na}. The contribution of I_{Na} to the AP more than 5 ms after the upstroke is close to zero (Figure 2.4). As a consequence, we do not attempt to gain any insight on I_{Na}-related parameters from such AP data.

4.8 Normalisation of voltage

4.8.1 Resting membrane potential instability can be used as marker for electrode instability

In sharp electrode experiments, the tissue is impaled by an electrode to record the intracellular voltage — for more details, see the full description of the methods by Page *et al.* (2016). Gao & Wang (2020) showed that in sharp electrode recordings of primate neurons the RMP is influenced by the position of the electrode in the cell.

In the case of the cardiac *ex vivo* tissue studied in this work, the tissue is contracting, making it even more challenging to maintain a stable electrode position. When the position changes, the electrical environment of the cell changes as well, directly impacting the recorded voltage.

When recording the *ex vivo* data, the experimenter corrected the position of the electrode every time the RMP went above −65 mV or when the electrode impalement was lost. Discontinuities in RMP were observed every time the recording electrode moved, as highlighted in trabecula #2021040101 (Figure 4.10).

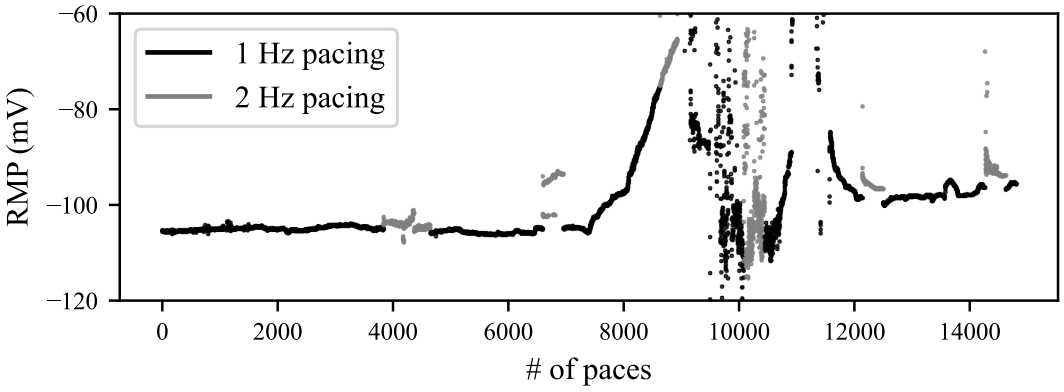

Figure 4.10: Evolution of RMP over time for the trabecula #2021040101. Until the 7500$^{\text{th}}$ pace, the RMP under 1 Hz pacing remains stable, and then the position of the electrode changes, eventually losing electrode impalement. After the 12000$^{\text{th}}$ pace, the RMP (and the recording setup) is stabilised again.

When observing the RMP evolution over time, the RMP should be ideally stable, as, for example, for trabecula #2021040101 until the 7350$^{\text{th}}$ pace (Figure 4.10). When the electrode moved, the recorded RMP changed abruptly, as observed after the 7350$^{\text{th}}$ pace. Since these changes were most likely not due to physiological changes, there is a discrepancy between the recorded voltage and the voltage driving the biophysical activity of the cell. Therefore, changes observed in APs could not be attributed exclusively to drug treatment, and further analysis was required to distinguish artefacts from drug response.

We investigated the use of RMP stability as a surrogate marker for the stability of the electrode. When discontinuities in RMP occurred or a strong sustained RMP increase was observed (moving average of RMP computed on 30 APs increase steadily by more than 5 mV/pace), the electrode was considered to have moved.

Movements of the sharp electrode induce changes in the AP that are artefacts a model should not attempt to fit. Therefore, AP data after electrode movement cannot be used in the dataset for model training. Electrode movement happened on many occasions in most trabeculae, thus limiting the usability of the AP data.

4.8.2 Normalised action potential data were not perturbed by electrode movement

APD_{90} and AP shape were not sensitive to electrode movement in most cases, while APA and RMP changes induced by electrode movements were inversely correlated.

These changes suggested that electrode movement induced a linear transformation of the recorded voltage. We therefore hypothesised that the normalised voltage (V_{norm}) calculated *per AP* as:

$$V_{\text{norm}} = \frac{V - RMP}{V_{95} - RMP} \tag{4.3}$$

would not be impacted by the electrode movement.

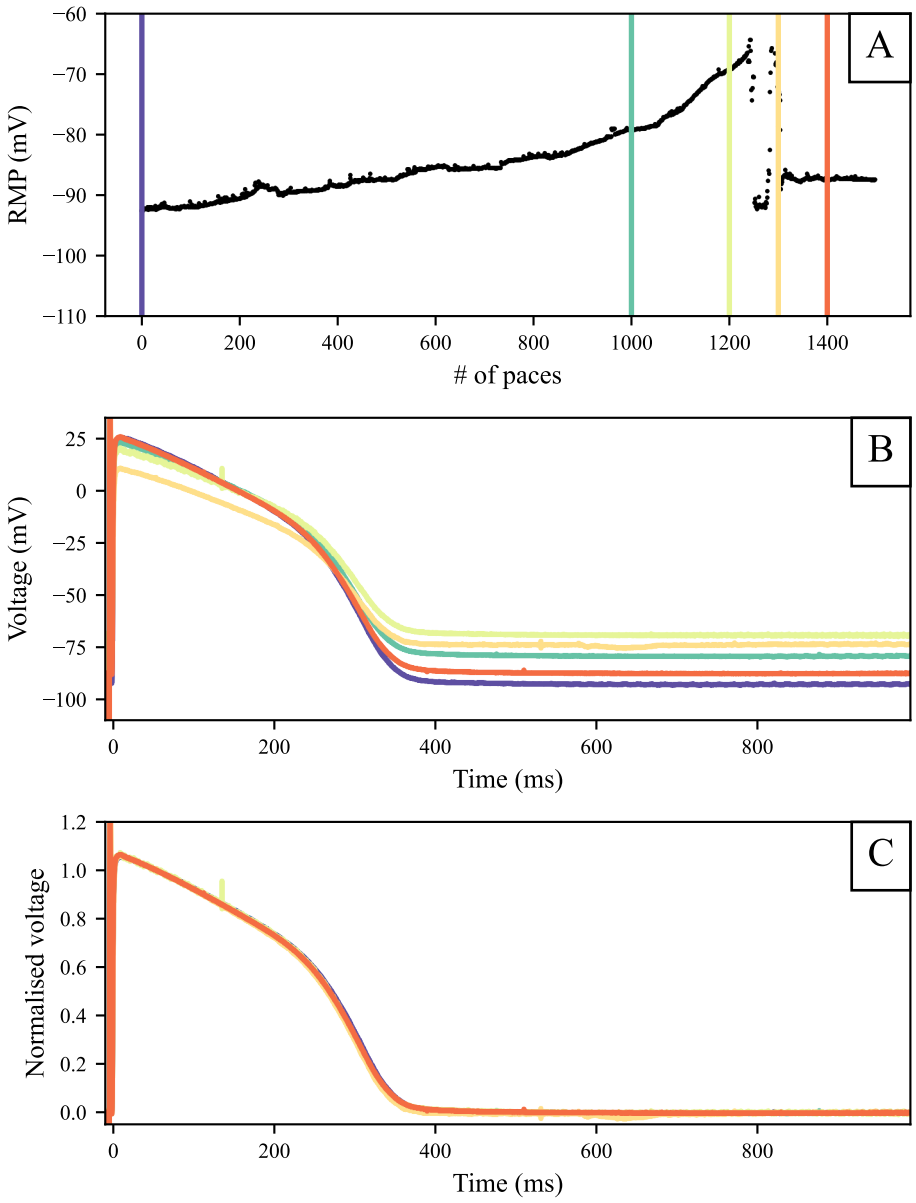

Figure 4.11: The normalised AP is unaffected by electrode movement. **A:** Evolution of the RMP. **B:** Non-normalised APs at times indicated by the coloured bars in **A**. **C:** Normalised APs at the same times.

For example, the RMP, the AP, and the normalised AP of trabecula #2021070301 observed during 25 min of steady 1 Hz pacing with 0.3 μM Clozapine is shown in Figure 4.11. After the 1250$^{\text{th}}$ pace, the electrode impalement was lost (Figure 4.11A), and the experimenter adjusted the electrode position. Because of the electrode movement, it is unclear if differences between the AP at the beginning of drug infusion (purple) and the AP at the end of drug infusion (orange) are due to drug effect or electrode movement (Figure 4.11B).

On the other hand, the AP data normalised with Eq. 4.3 was not impacted by electrode movements (Figure 4.11C). Normalisation therefore mitigates recording artefacts induced by electrode movement and makes the data before and after the electrode movement consistent. Thus, our hypothesis is that discontinuity in the recorded RMP can be attributed solely to changes in the setup, while the electrophysiological activity of the cell remains unaltered at the moment of the spike in RMP.

Furthermore, normalised AP data can be used to verify that the data before and after discontinuities in the RMP are consistent. When no perturbation of the normalised AP data was observed, the electrophysiological activity of the cell was considered as preserved and the normalised AP data were deemed usable for model training.

4.8.3 Impact of the normalisation of the training action potential data on model calibration

The purpose of the experimental data presented here is to be used for training and validation of an AP model to predict the ΔAPD_{90} response to acute inhibition of I_{Kr} and I_{CaL}. These two currents are mostly active during the plateau and repolarisation phases of the AP (Figure 2.4 in Chapter 2). This suggests there will be no strong sensitivity of RMP and peak voltage to I_{Kr} and I_{CaL} inhibition. The effects of I_{Kr} and I_{CaL} inhibition on the AP are mostly expected to impact the plateau duration and the speed of repolarisation, which are preserved in normalised AP data. Therefore, it was hypothesised that normalised AP data could be used for model calibration in the scope of this DPhil project, and this hypothesis is tested in this section.

The loss of precision in parameter estimation induced by normalisation of the AP data was estimated in a *synthetic* study. AP data were generated with a known AP

model, the epicardial variant of the Ten Tusscher & Panfilov (2006) model (TP), called the "true" model in this section. The TP model was reformulated in its algebraic-V form to make the net intracellular concentration of un-modelled charge, Γ_0, appear explicitly (Chapter 3). Parameters of the TP model were estimated from the synthetic AP data, both non-normalised and normalised, to mimic the model calibration described in following Chapters. Parameter estimates were then compared with parameter values from the true model, called "true parameter values".

The TP model was downloaded in CellML format from the Physiome repository (`https://models.physiomeproject.org/electrophysiology`), then imported and solved with `myokit` 1.33.7 (Clerx *et al.*, 2016), which uses SUNDIALS for model solving (Hindmarsh *et al.*, 2005). Absolute and relative solver tolerance were both set to 10^{-9}. APs were simulated with the TP model, steadily paced at 1 Hz to steady-state for 1500 paces.

Simulations were run under four conditions with inhibition of I_{Kr} and I_{CaL}: 0% I_{Kr}/0% I_{CaL}, 25% I_{Kr}/20% I_{CaL}, 50% I_{Kr}/40% I_{CaL}, and 75% I_{Kr}/80% I_{CaL} inhibition. To mimic real experimental data, a normally-distributed ($\sigma_y = 0.1$ mV, estimated from the variation of voltage during the resting phase of the AP) independent noise was added to the simulated APs. The four resulting non-normalised and normalised APs are shown in Figure 4.12A and B, respectively.

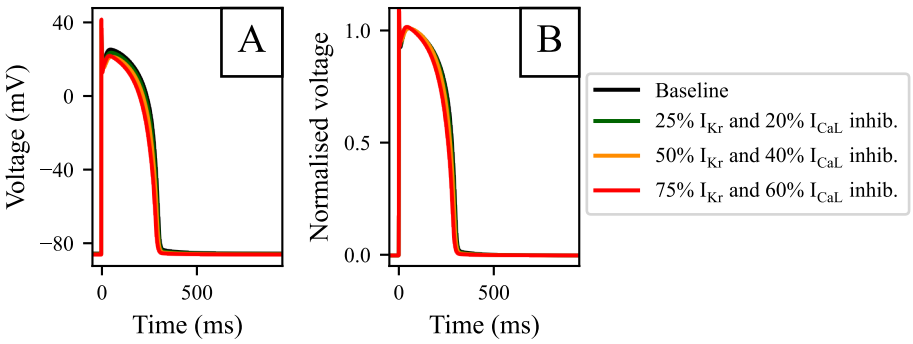

Figure 4.12: Synthetic data generated with the TP model, and used to compare models developed from normalised and non-normalised AP data. **A:** Non-normalised synthetic APs. **B:** Normalised synthetic APs.

Similarly to the model training process described in next Chapters, the vector θ composed of eight major conductance parameters of the TP model (G_{Kr}, G_{CaL}, G_{Na},

G_{NaCa}, G_{NaK}, G_{K1}, G_{Ks}, G_{to}) and of Γ_0 (see Chapter 3) was estimated from the non-normalised synthetic AP data. The process was then repeated with the normalised synthetic AP data. The (posterior) probability distribution of parameters was estimated with the Haario-Bardenet MCMC algorithm, using a non-informative prior distribution as described in Section 2.5.1. The log-likelihood ℓ was computed as:

$$\ell(\theta|y^*) = \sum_{\text{c}}^{\text{4 conditions}} \left(\frac{N}{2} \ln \frac{2\pi}{\sigma_y^2} - \frac{1}{2\sigma_y^2} \sum_{t}^{N} \left(y_{\text{c}}^*(t) - y_{\text{c}}(\theta, t) \right)^2 \right), \tag{4.4}$$

with N the number of data points, y_{c}^* the synthetic data under the inhibition condition c, and $y_{\text{c}}(\theta)$ the simulation output of the TP model parameterised with θ. N was selected to be 20,000 per inhibition condition, to match the time resolution of the *ex vivo* AP data. When using normalised synthetic data, simulated APs were normalised with Eq. 4.3.

In simulations when maximising ℓ, the effective value of the conductance parameters, G, was not directly changed. Instead, a log-scale scaling factor, $\hat{\text{g}}$, was applied to each conductance parameter, which enabled a direct comparison between conductance parameters, and enforced the positivity of G during parameter estimation (Johnstone, 2018). The effective conductance value used in simulations, G, was therefore computed as:

$$G = \bar{G} \times e^{\hat{\text{g}}}, \tag{4.5}$$

with $\bar{G}$ the true value of the conductance parameter in the TP model. Note that a scaling factor $\hat{\text{g}} = 0$ corresponds to using the true value for each conductance parameter in simulations.

10,000 iterations of the Haario-Bardenet MCMC algorithm with five independent chains were performed. After 7,000 iterations, the chains were mixed and the posterior distributions were read from the last 3,000 iterations of the five chains (Figure 4.13).

As expected, inference on normalised AP data returned wider posteriors for the rescaling factors of conductance parameters ($4 \times 10^{-4} < \sigma_{\text{normal}} < 9 \times 10^{-4}$) than on the non-normalised data ($10^{-4} < \sigma_{\text{raw}} < 6 \times 10^{-4}$). The posterior distribution of the missing charge parameter Γ_0 was 7-fold wider when inferred from normalised APs ($\sigma_{\text{normal}} = 0.05\,\text{mM}$ vs $\sigma_{\text{raw}} = 0.007\,\text{mM}$), and its mean was shifted by 0.2 mM.

The significance of these differences was assessed by comparing APD_{90} predictions resulting from the two posterior distributions. Parameterising the TP model with 500

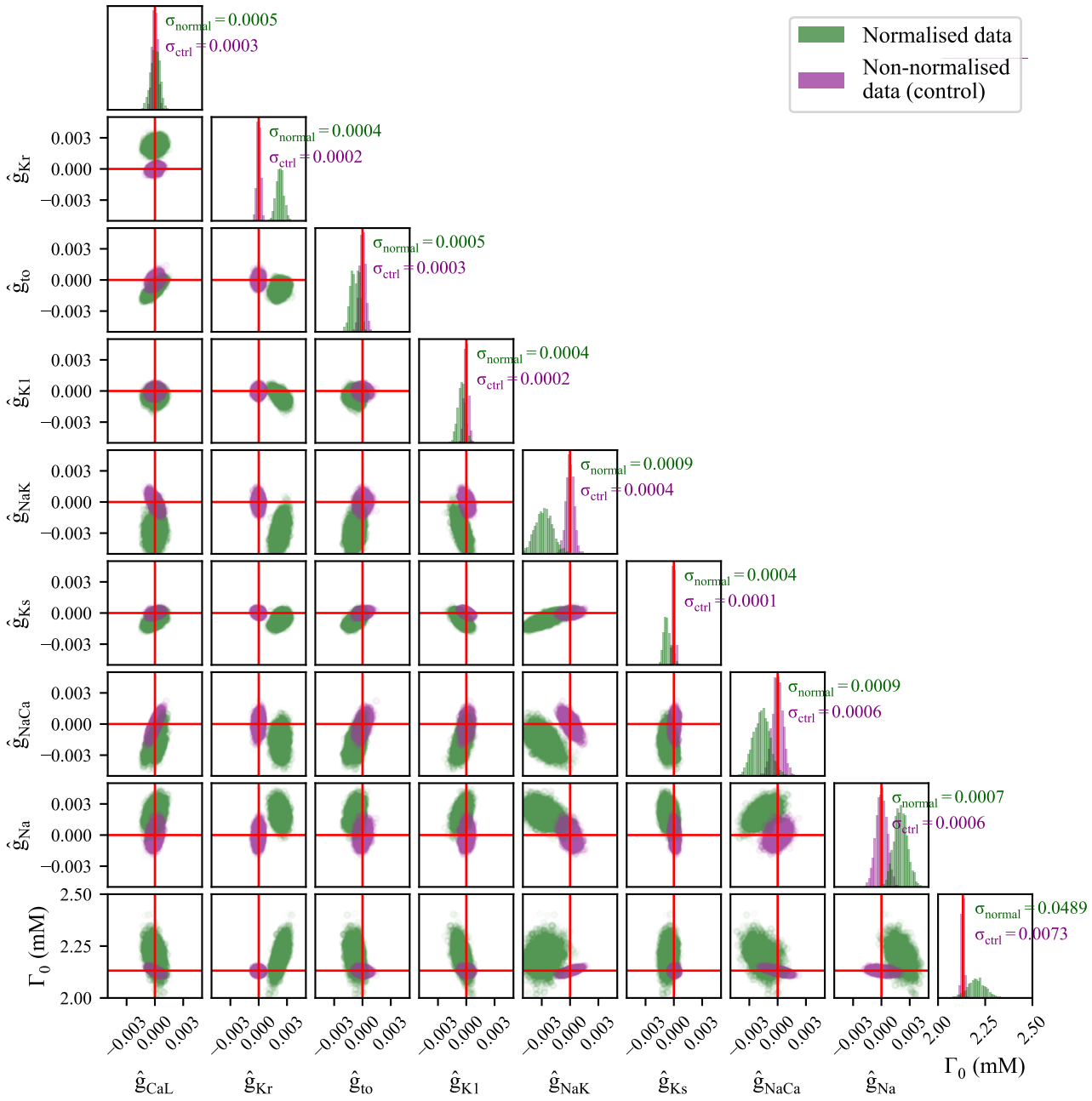

Figure 4.13: Posterior distributions of parameters inferred from the non-normalised and normalised synthetic datasets. The "true" parameter values used to generate the synthetic data are indicated by red lines. The posterior distribution inferred from non-normalised AP data (purple) is closer to the true values than the distribution inferred after the normalisation of the AP data (green).

different values of θ sampled from each posterior distribution, the AP was simulated and APD_{90} was calculated. APD_{90} predictions obtained from the two posterior distributions are shown in Figure 4.14.

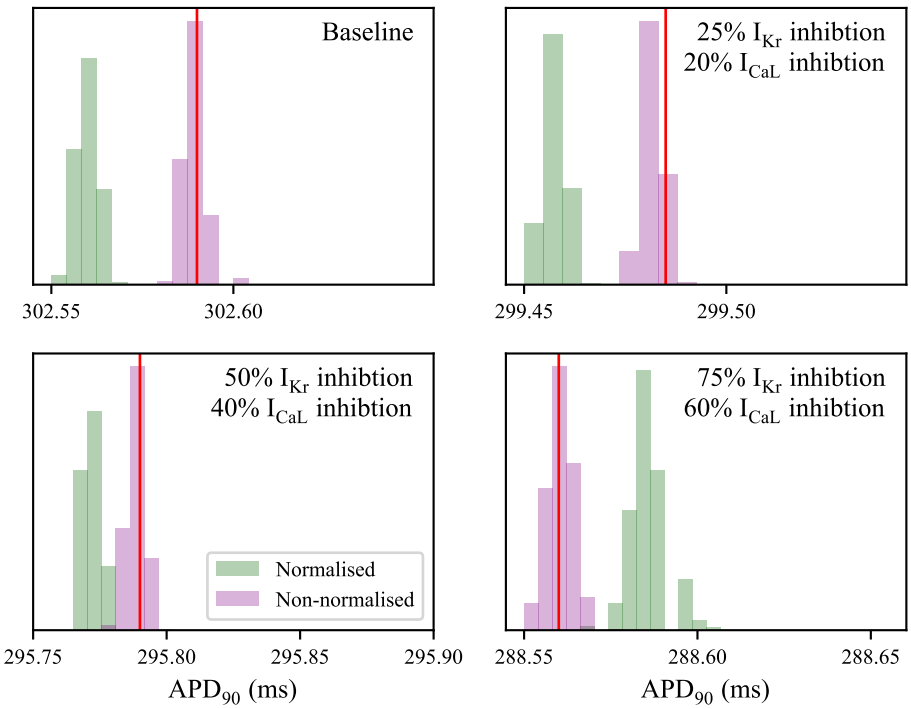

Figure 4.14: Distribution of APD_{90} predicted by 500 random samples taken from the posterior parameter distributions inferred from non-normalised and normalised synthetic datasets (Figure 4.13). APD_{90} predictions made with parameters inferred from the non-normalised datasets are closer to the true APD_{90} (red line), but errors in APD_{90} predictions made with parameters inferred from normalised AP data are small (APD_{90} error < 0.1 ms).

The errors in APD_{90} predictions introduced by the normalisation of the AP data for calibration were lower than 0.1 ms. Therefore, no noticeable differences are expected between ΔAPD_{90} predictions by AP models calibrated to normalised and non-normalised AP data. Normalisation of the AP data mitigates the experimental limitations of the sharp electrode recordings, and the normalised AP data can reasonably be used for model calibration in the following Chapters.

4.8.4 Note on consequences for model calibration

Parameters of AP models are usually not identifiable from the sole trace of an AP under baseline condition, but they are identifiable when the data for model development

is recorded under several perturbed conditions (Syed *et al.*, 2005). Therefore, the identifiability of parameters is limited by the number of successive experimental conditions in the same dataset. Regardless of the increase in dataset size, normalisation of the AP data was observed to have no significant impact on parameter estimation. By mitigating the recording artefacts and increasing the size of the usable dataset, the normalisation of the AP data therefore improves the identifiability of parameters from the *ex vivo* data in each trabecula. This also improves the feasibility of the calibration of AP models specific for each trabecula.

Calibrating a population of models to experimental ranges of variation of AP markers, e.g., RMP and APD_{90}, has been proposed as a method to estimate the inter-individual variability in ventricular electrophysiology and the uncertainty on conductance parameters in AP models (Britton *et al.*, 2013). Doing so, various random parameterisations of an AP model are created and used in simulations to compute AP markers. The parameterisations producing AP markers within the experimental ranges of AP markers are included in the population of models. The population of models is then used for predictions, e.g., of cardiac safety (Passini *et al.*, 2017). Experimental limitations on the measurements of AP markers highlighted in previous sections must be considered during the development of populations of AP models. Indeed, the variability recapitulated with populations of models calibrated on sharp electrode recordings should be disentangled from noise generated by non-biological artefacts.

4.9 Summary of data of sufficient quality

The following workflow was used to investigate whether data from each trabecula of the Phase 2 dataset was affected by the instability of the electrode:

1. Calculate the RMP and APD_{90} throughout the whole *ex vivo* experiment.
2. Search for discontinuities in the RMP evolution. If discontinuities in APD_{90} are observed at the same time, reject the data after the RMP discontinuity.
3. Observe the evolution of the normalised APs before and after each discontinuity in RMP. If the evolution of the normalised APs after the discontinuity matches with before, the discontinuity is disregarded and the data are accepted until the next discontinuity. Otherwise, the data after the discontinuity are discarded.

Optimal data quality was obtained in some trabeculae where all markers were well stabilised throughout the whole study. Trabecula #2022030802 is an illustrative example of trabecula which exhibited stable activity with stable recording. The evolution of RMP, APD_{90} and APA are shown in Figure 4.15 for this trabecula. APD_{90} can be seen to be adapting to the exposure to the drug, and is stabilised after 25 minutes of steady 1 Hz pacing (except after the addition of 100 nM Dofetilide).

In most trabeculae, the data quality was insufficient for some of the drug concentrations and were rejected (not processed). The preceding concentrations were used regardless.

In the example case of trabecula #2022030801 (Figure 4.16), the electrode impalement was lost between the 9000^{th} and the 9500^{th} pace. In this situation, it is not possible to know whether the changes in the AP recorded after the 9500^{th} pace were due to the drug effect or to electrode movement. Therefore, the data after the 9500^{th} pace cannot be used.

For the Phase 1 dataset, only the last 3 min out of 25 min of steady 1 Hz pacing were available. It was therefore impossible to carry out the comprehensive data quality assessment used for the Phase 2 dataset. Instead, the whole Phase 1 dataset was accepted for model training by default, unless obvious data quality issues were observed during a manual inspection of the recordings.

With 100 nM Dofetilide, early after-depolarisations (EADs) were observed in one trabecula and alternans was observed in another. The data for 100 nM and 200 nM Dofetilide for these two trabeculae were therefore excluded, and only the first two drug concentrations (1 nM and 10 nM Dofetilide) were used in further analyses.

The data deemed of acceptable quality are summarised in Table 4.5.

Overall, the fraction of accepted data in the Phase 2 dataset after AP normalisation is high (83%). With the exception of 30 nM and 300 nM Nifedipine, at least three repeats were usable for each drug condition. Without normalisation, 49% of the Phase 2 data would have been rejected.

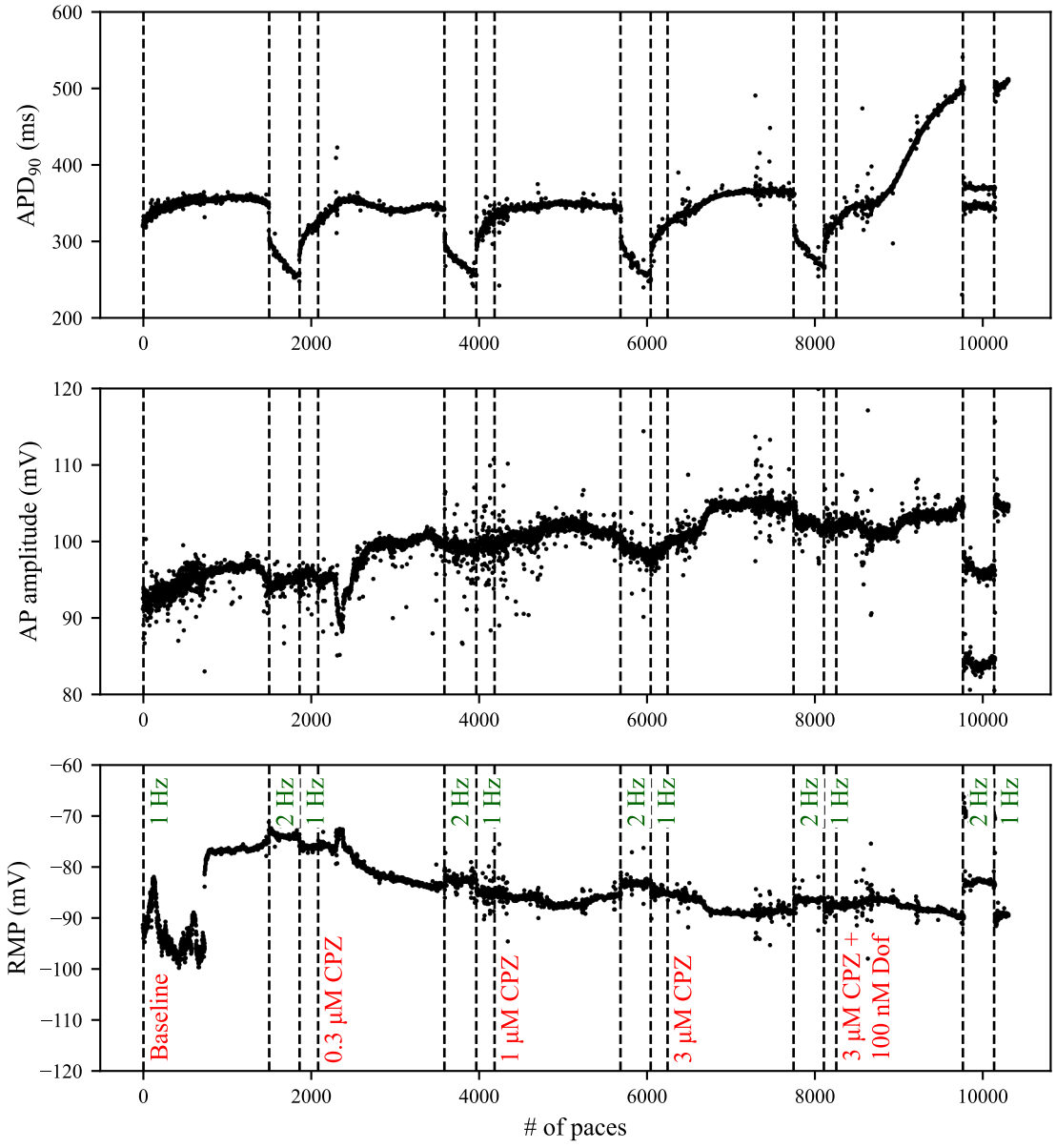

Figure 4.15: Evolution of AP markers used to evaluate data quality through the whole study, for trabecula #2022030802. All markers are stable: the electrode position is maintained stable through the study and the electrophysiological activity of the cell is perturbed only by the successive drug perturbations. Note that the baseline AP was recorded at the end of the steady 1 Hz 25 min period, therefore the discontinuity in the RMP at the 700$^{\text{th}}$ pace did not impact data usability. CPZ: Chlorpromazine. Dof: Dofetilide.

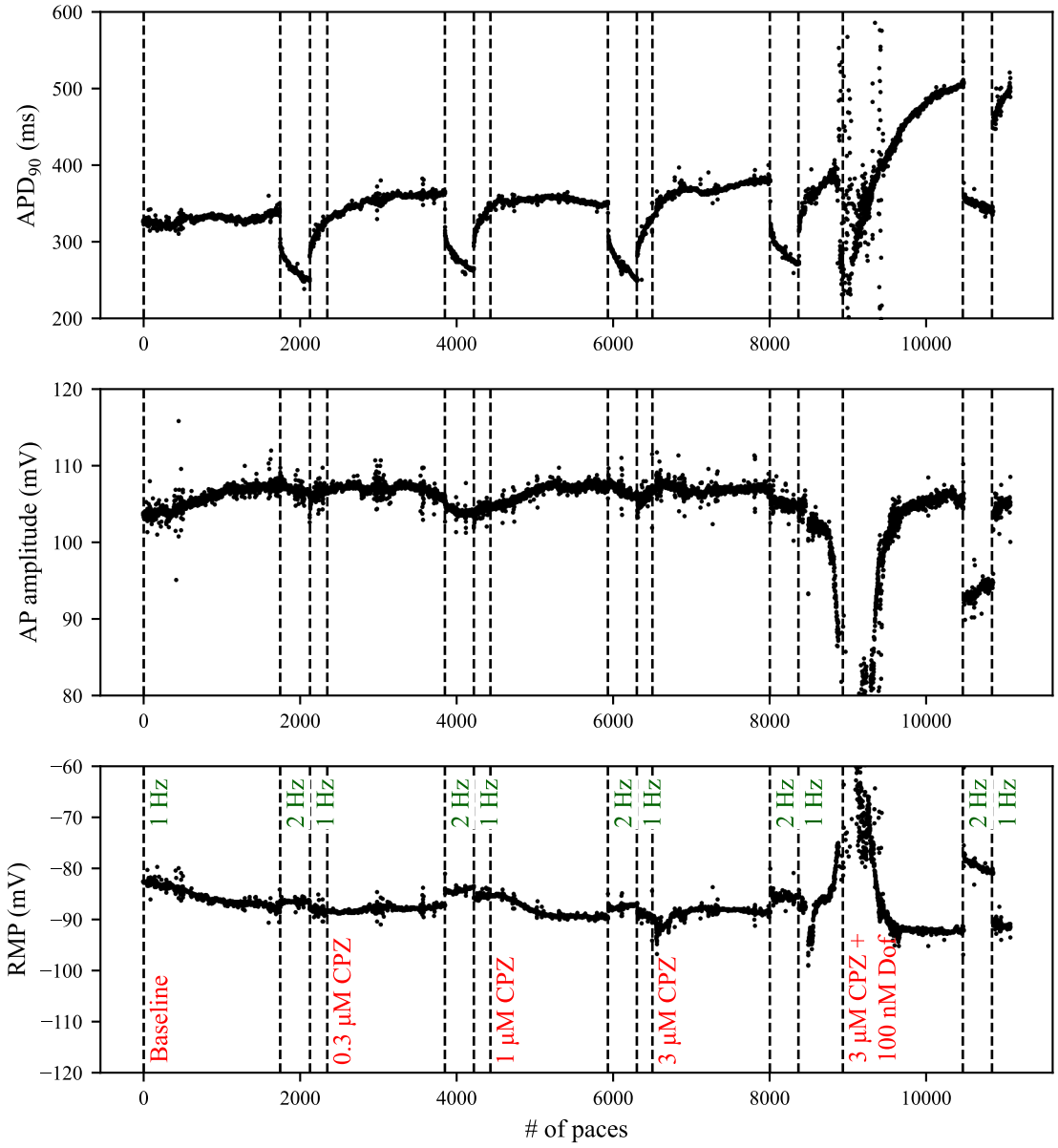

Figure 4.16: Evolution of AP markers used to evaluate data quality through the whole study, for trabecula #2022030801. The electrode impalement was lost between the 9000^{th} and the 9500^{th} pace: data for $3\,\mu$M Chlorpromazine + 100 nM Dofetilide were deemed unusable. For control and the three first experimental conditions, the electrode remained stable and data were used for model development. CPZ: Chlorpromazine. Dof: Dofetilide.

Drug	Baseline	1st conc	2nd conc	3rd conc	3rd conc + 100 nM Dof
Phase 1					
Clozapine	4/0	4/0	4/0	4/0	3/1
Dofetilide	15/0	15/0	13/2	11/4	10/5
Nifedipine	4/0	4/0	2/2	2/2	2/2
Quinidine	15/0	14/1	14/1	14/1	13/2
Verapamil	15/0	15/0	15/0	14/1	14/1
Phase 2					
Chlorpromazine	6/0	6/0	6/0	5/1	2/4
Clozapine	8/1	7/2	7/2	5/4	3/6
Dofetilide + Nifedipine	6/0	6/0	4/2	3/3	3/3
Fluoxetine	5/0	5/0	5/0	5/0	3/2
Nifedipine + Dofetilide	7/0	7/0	7/0	4/3	3/4
Mesoridazine	6/0	6/0	6/0	6/0	6/0
Thioridazine	5/0	4/1	4/1	4/1	3/2

Table 4.5: Data not affected by electrode movement for each drug condition. The data are reported as: number of records with acceptable/unacceptable quality. When sufficient quality of data was not achieved, the data were rejected.

4.10 Drug-induced ΔAPD_{90}

4.10.1 DMSO: vehicle

To be applied to trabeculae, drugs of interest (Tables 4.3–4.4) were dissolved in DMSO, used as a vehicle compound. The effect of DMSO alone was investigated in 7 trabeculae (Table 4.3). The ΔAPD_{90} measured in each trabecula exposed to DMSO is shown in Figure 4.17.

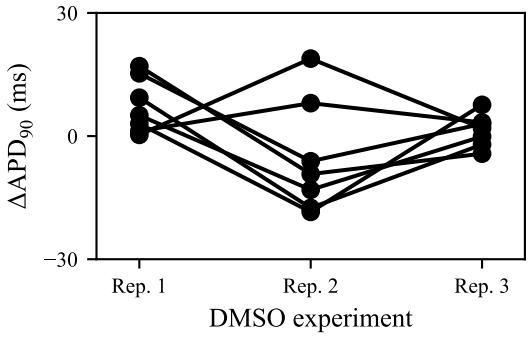

Figure 4.17: APD_{90} change observed with three repeats of DMSO (vehicle). Each line indicates the ΔAPD_{90} observed in a single trabecula.

The mean DMSO-induced ΔAPD_{90} and the standard error of the mean (SEM) computed for each repeat are reported in Table 4.6. When drugs are applied using DMSO as vehicle, their effects are entangled with those of DMSO. The SEM of DMSO-induced ΔAPD_{90} therefore corresponds to the finest possible resolution in the mean ΔAPD_{90} in this work.

Repeat	#1	#2	#3
Mean ΔAPD_{90}	+7.3 ms	−5.4 ms	+1.3 ms
ΔAPD_{90} SEM (ms)	2.4	4.9	1.4

Table 4.6: Mean and standard error of the mean(SEM) in ΔAPD_{90} observed in 7 trabeculae exposed to three consecutive repeats of exposure to DMSO.

4.10.2 Drugs of interest

APD_{90} was measured under baseline conditions (without drug) and under each perturbed condition of Table 4.3 and Table 4.4. For each drug condition c, the mean ΔAPD_{90} and its SEM were calculated across recordings of sufficient quality (Table 4.5). The results are summarised in Table 4.7.

Chlorpromazine, Clozapine, Fluoxetine, and Mesoridazine induced mixed inhibition of I_{Kr} and I_{CaL} (Table 4.2), which generated little to no changes in APD_{90}. For such perturbations, the effects of I_{Kr} and I_{CaL} inhibition on the APD_{90} compensated each other.

Verapamil, also exhibiting mixed effects on I_{Kr} and I_{CaL}, substantially shortened the APD_{90} (−15 ms to −20 ms in average) with high variability in the APD_{90} response (up to 35 ms).

Substantial variability of baseline APD_{90} was observed in trabeculae tested with Mesoridazine, Clozapine, and Nifedipine (60 ms, 44 ms, and 55 ms respectively), but this did not lead to particularly high variability in drug-induced ΔAPD_{90}. The SEM of ΔAPD_{90} response was below 7 ms, 9 ms, and 6 ms for Mesoridazine, Clozapine, and Nifedipine, respectively. Fluoxetine-induced ΔAPD_{90} also exhibited low SEM, below 7 ms. In contrast, Dofetilide induced the most variable ΔAPD_{90}, with up to 33 ms SEM for 200 nM Dofetilide. Note that differences in actual drug concentrations were observed between trabeculae exposed to the same nominal drug concentration (Table 4.7). These differences likely contributed to the variability in ΔAPD_{90}.

Drug	**Mean baseline APD_{90} (SD), in ms**	**Nominal drug conc (μM)**	**Mean ΔAPD_{90} (SEM), in ms**
Chlorpromazine	299 (36)	0.3	+9 (10)
		1	+18 (8)
		3	+24 (11)
		3 + 0.1 μM Dof	+135 (32)
Clozapine	324 (51)	0.3	+8 (5)
		1	+10 (7)
		3	+10 (7)
		30	+15 (9)
		3 + 0.1 μM Dof	+148 (30)
		30 + 0.1 μM Dof	+129 (28)
Dofetilide	317 (51)	0.001	+20 (5)
		0.01	+82 (8)
		0.1	+256 (21)
		0.2	+318 (33)
Dofetilide + Nifedipine	342 (25)	0.01 + 0.03	+87 (20)
		0.03 + 0.05	+147 (41)
		0.05 + 0.15	+170 (46)
Fluoxetine	271 (36)	0.3	+10 (4)
		1	+6 (7)
		3	−2 (5)
		3 + 0.1 μM Dof	+174 (25)
Mesoridazine	334 (60)	0.04	−2 (7)
		0.25	+2 (4)
		10	+21 (2)
		10 + 0.1 μM Dof	+70 (7)
Nifedipine	336 (55)	0.003	+7 (4)
		0.03	−5 (6)
		0.3	−24 (6)
		0.3 + 0.1 μM Dof	+172 (26)
Nifedipine + Dofetilide	372 (33)	0.03 + 0.003	+14 (7)
		0.03 + 0.01	+80 (10)
		0.03 + 0.1	+234 (51)
Quinidine	302 (53)	0.1	+6 (5)
		1	+8 (5)
		10	+37 (7)
		10 + 0.1 μM Dof	+174 (18)
Thioridazine	307 (48)	0.012	+15 (9)
		0.6	+16 (20)
		2	+6 (14)
		2 + 0.1 μM Dof	+83 (41)
Verapamil	349 (61)	0.01	−15 (4)
		0.1	−19 (5)
		1	−20 (10)
		1 + 0.1 μM Dof	+180 (14)

Table 4.7: Experimental data for average APD_{90} baseline and APD_{90} change with drug exposure. SEM: standard error of the mean. SD: standard deviation.

Dofetilide induced a substantial prolongation of APD_{90} in all trabeculae, regardless of exposure to another drug beforehand. 100 nM Dofetilide prolonged APD_{90} by 70 ± 7 ms when combined with 10 μM Mesoridazine, and up to 256 ± 21 ms when applied alone.

4.11 Comparison of nominal and actual drug concentrations

To refine the relationship between ΔAPD_{90} and drug treatments investigated in the previous section, the actual drug concentrations to which trabeculae were exposed was measured.

In Phase 2 experiments (2020–2022), a bioanalytical analysis of the bath solution was performed, at the end of each 25 min steady 1 Hz pacing period. The sample analysis was performed according to the operating procedure for sample preparation for Liquid Chromatography with tandem mass spectrometry (LC-MS/MS) analysis in a bioanalytical laboratory. For data gathered in Phase 1 (2014–2016), actual drug concentrations were not measured, therefore nominal drug concentrations were used (Table 4.3). For each drug condition tested *ex vivo*, the nominal concentrations were compared with the actual measured concentrations in Table 4.8.

Overall, actual concentrations were lower than nominal concentrations. Mesoridazine actual concentrations were approximately 20% lower than the nominal concentrations, Fluoxetine 40% lower, Chlorpromazine 60% lower, with substantial variations. This can be explained by some loss of compound due to its stickiness to various surfaces of the experimental machinery.

On the other hand, Dofetilide was administered at higher doses than planned. In the extreme case, the Dofetilide actual concentration reached up to 144 nM for a nominal concentration of 100 nM. The second concentration of Clozapine (1 μM nominal concentration) was also overachieved, with up to 2.6 μM measured in trabecula #2021070301. No mechanistic explanation was satisfactory for such a high Clozapine concentration, and human error during solution preparation and/or bioanalytical analysis cannot be ruled out.

Using the actual drug concentration in Eq. 4.1 when available, the relationship between ΔAPD_{90}, I_{Kr} inhibition, and I_{CaL} inhibition can be investigated as accurately as possible.

Drug 1	Nominal conc (μM)	Actual conc (μM)	Drug 2	Nominal conc (μM)	Actual conc (μM)
Chlorpromazine	0.3	0.097(0.055, 0.162)	Dofetilide	0	BLQ
	1	0.361 (0.226, 0.453)		0	BLQ
	3	1.404 (1.137, 1.635)		0	BLQ
	3	1.404 (1.137, 1.635)		0.1	0.116 (0.091, 0.131)
Clozapine	0.3	0.288 (0.248, 0.334)	Dofetilide	0	BLQ
	1	1.525 (0.958, 2.605)		0	BLQ
	3	2.689 (2.425, 3.375)		0	BLQ
	3	2.689 (2.425, 3.375)		0.1	0.083 (0.078, 0.089)
Dofetilide	0.01	0.009 (0.009, 0.009)	Nifedipine	0	BLQ
	0.01	0.009 (0.009, 0.010)		0.01	0.010 (0.009, 0.011)
	0.03	0.027 (0.024, 0.028)		0.05	0.058 (0.052, 0.065)
	0.05	0.047 (0.042, 0.048)		0.15	0.167 (0.143, 0.177)
	0	BLQ		0.03	0.030 (0.026, 0.038)
	0.003	0.003 (0.002, 0.003)		0.03	0.030 (0.027, 0.037)
	0.01	0.009 (0.008, 0.013)		0.03	0.030 (0.028, 0.034)
	0.1	0.085 (0.082, 0.091)		0.03	0.030 (0.027, 0.035)
Fluoxetine	0.3	0.152 (0.119, 0.176)	Dofetilide	0	BLQ
	1	0.594 (0.506, 0.722)		0	BLQ
	3	1.688 (1.085, 2.125)		0	BLQ
	3	1.688 (1.085, 2.125)		0.1	0.108 (0.106, 0.111)
Mesoridazine	0.040	0.033 (0.028, 0.035)	Dofetilide	0	BLQ
	0.25	0.233 (0.202, 0.254)		0	BLQ
	10	7.933 (7.33, 8.065)		0	BLQ
	10	7.933 (7.33, 8.065)		0.1	0.108 (0.105, 0.110)
Thioridazine	0.012	0.002 (0.001, 0.003)	Dofetilide	0	BLQ
	0.6	0.248 (0.203, 0.313)		0	BLQ
	2	0.835 (0.653, 0.908)		0	BLQ
	2	0.835 (0.653, 0.908)		0.1	0.116 (0.098, 0.144)

Table 4.8: Comparison of nominal and actual measured concentrations after bioanalytical analysis of the trabeculae tested in Phase 2 experiments. Values are reported as: Mean (minimum, maximum). BLQ: below limit of quantification.

4.12 Qualitative visualisation of ΔAPD_{90} as a function of I_{Kr} and I_{CaL} inhibition

In this section, we present a qualitative visualisation of the relationship between ΔAPD_{90} and I_{Kr} and I_{CaL} inhibition. ΔAPD_{90} was reported on a 2-D map, using I_{Kr} and I_{CaL} inhibition as X- and Y-axis coordinates, respectively.

One data point was reported per nominal drug concentration. Coordinates (I_{Kr} and I_{CaL} inhibition) were computed with Eq. 4.1, using *in vitro* data (Table 4.2) and the average drug concentration across trabeculae exposed to the same nominal drug

concentration. When available, the actual drug concentration in the bath solution was used (Table 4.8). Otherwise, the nominal drug concentration was used (Tables 4.3–4.4).

The drug-induced ΔAPD_{90} was also averaged across trabeculae exposed to the same nominal drug concentration. ΔAPD_{90} was reported following a colour-map covering extreme values observed for ΔAPD_{90}.

Next, a quadratic surface of ΔAPD_{90} as a function of I_{Kr} and I_{CaL} inhibition was fitted through the *ex vivo* data points (Section B.4 in the Appendix). The quadratic surface was finally plotted in the background, with the same colour code as for experimental data points. Note that combinations of inhibition of I_{Kr} and/or I_{CaL} for which no change in APD_{90} were observed/predicted ($|\Delta APD_{90}| \leq 1$ ms) were plotted as white pixels, thus highlighting a "0 ms line".

Figure 4.18 visualises how the map of ΔAPD_{90} prediction was generated.

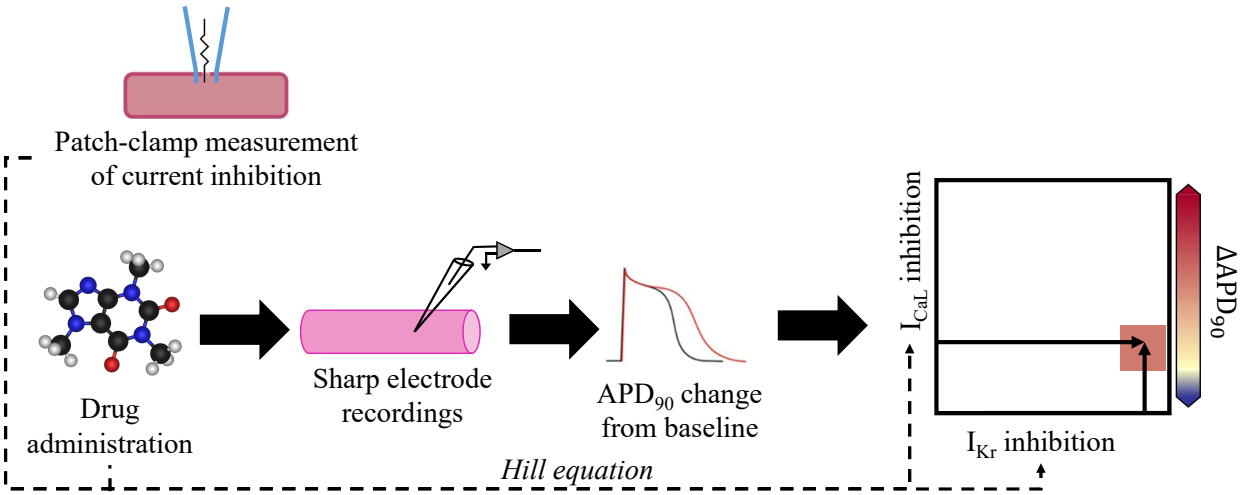

Figure 4.18: Schematic of methods used to plot ΔAPD_{90} 2-D maps. Drug-induced ΔAPD_{90} is measured experimentally with sharp electrodes. The inhibition of I_{Kr} and I_{CaL} by the drug at the tested concentration is computed with the Hill equation (Eq. 4.1) and IC_{50} data (Table 4.2). The corresponding point is then added to the 2-D map, with ΔAPD_{90} reported with the colour-map.

2-D maps of ΔAPD_{90} are shown in Figure 4.19 using the Pharm dataset (I_{Kr} Pharm and I_{CaL} Pharm protocols) and the CiPA dataset (I_{Kr} CiPA and I_{CaL} CiPA protocols) for drug-induced I_{Kr} and I_{CaL} inhibition.

Points corresponding to situations where Dofetilide was administered on top of another drug — all with large prolongation of APD_{90} — did not produce a map consistent with the remaining points. In particular, combinations of Nifedipine and Dofetilide induced

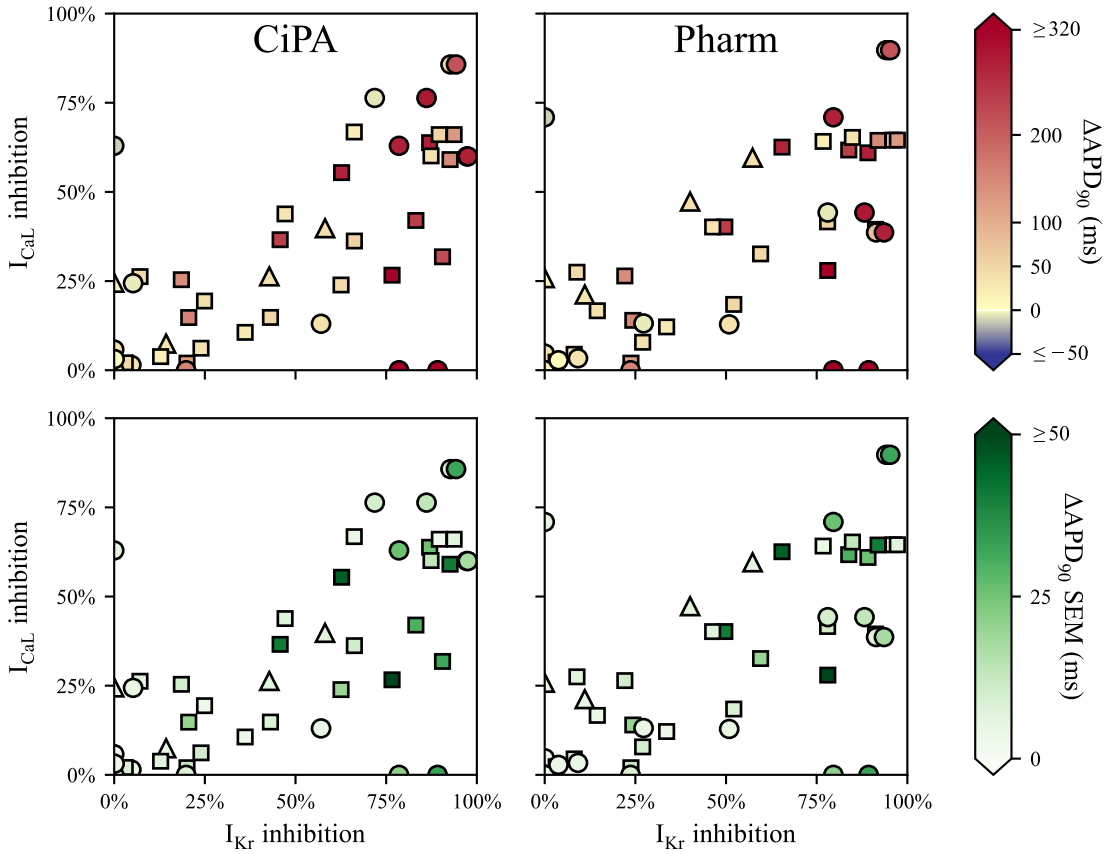

Figure 4.19: Experimental ΔAPD_{90} measured *ex vivo* under various drug treatments in human ventricular trabeculae, as a function of I_{Kr} and I_{CaL} inhibition. I_{Kr} and I_{CaL} inhibition were computed using the Hill equation (Eq. 4.1), with the CiPA (left) and Pharm (right) datasets reported in Table 4.2. The bottom panels report the SEM in ΔAPD_{90}. When actual drug concentrations were measured for all trabeculae tested with the same nominal drug concentration, the data point was plotted as a **square**. When actual drug concentrations were measured only for some trabeculae tested with the same nominal drug concentration, the data point was plotted as a **triangle**. When only nominal concentrations were available, the data point was plotted as a **circle**.

a visibly higher prolongation of APD_{90} than other drugs inducing a similar inhibition of I_{Kr} and I_{CaL}. For instance, in the Phase 2 dataset, trabeculae exposed to 30 nM Nifedipine + 10 nM Dofetilide (17–20% I_{Kr}/23–24% I_{CaL}inhibition) exhibited marked APD_{90} prolongation ($+80 \pm 10$ ms), while trabeculae exposed to 0.3 μM Chlorpromazine induced no significant APD_{90} prolongation ($+9 \pm 10$ ms), despite inhibiting more I_{Kr} (22–25%) and less I_{CaL} (4–6%).

To correct for the missing mechanisms that would explain such differences, the inhibition of I_{Kr} and I_{CaL} by multiple drugs would need to be investigated. Data obtained

from trabeculae exposed to two drugs simultaneously could not be used in the same dataset as the rest of the data otherwise. As this topic was out of the scope of this DPhil project, **the data used for model development was limited to normalised AP data obtained in trabeculae exposed to a single drug**.

4.13 Final dataset for model calibration

The findings of previous sections can be used to obtain a dataset usable for model calibration. By normalising V (Eq. 4.3) and excluding data of insufficient quality, we ensure that the data were not affected by movements of the electrode (Table 4.5). By excluding data obtained with two concomitant drugs, the consistency of the dataset is improved (Section 4.10). As a result, the final dataset deemed usable for model calibration is summarised in Table 4.9.

Drug	Baseline	1st conc	2nd conc	3rd conc	3rd conc + 100 nM Dof
Phase 1					
Clozapine	4/0	4/0	4/0	4/0	0/4
Dofetilide	15/0	15/0	13/2	11/4	10/5
Nifedipine	4/0	4/0	2/2	2/2	0/4
Quinidine	15/0	14/1	14/1	14/1	0/15
Verapamil	15/0	15/0	15/0	14/1	0/15
Phase 2					
Chlorpromazine	6/0	6/0	6/0	5/1	0/6
Clozapine	8/1	7/2	7/2	5/4	0/9
Dofetilide + Nifedipine	6/0	6/0	0/6	0/6	0/6
Fluoxetine	5/0	5/0	5/0	5/0	0/5
Nifedipine + Dofetilide	7/0	7/0	0/7	0/7	0/7
Mesoridazine	6/0	6/0	6/0	6/0	0/6
Thioridazine	5/0	4/1	4/1	4/1	0/5

Table 4.9: Final data usable for model calibration. The data is reported as: number of usable/unusable records for model development. When electrode instability affected the normalised AP or when two drugs were applied at the same time, the data were excluded.

The ΔAPD_{90} data included in the final dataset were plotted in a 2-D map as a function of I_{Kr} and I_{CaL} inhibition, shown in Figure 4.20.

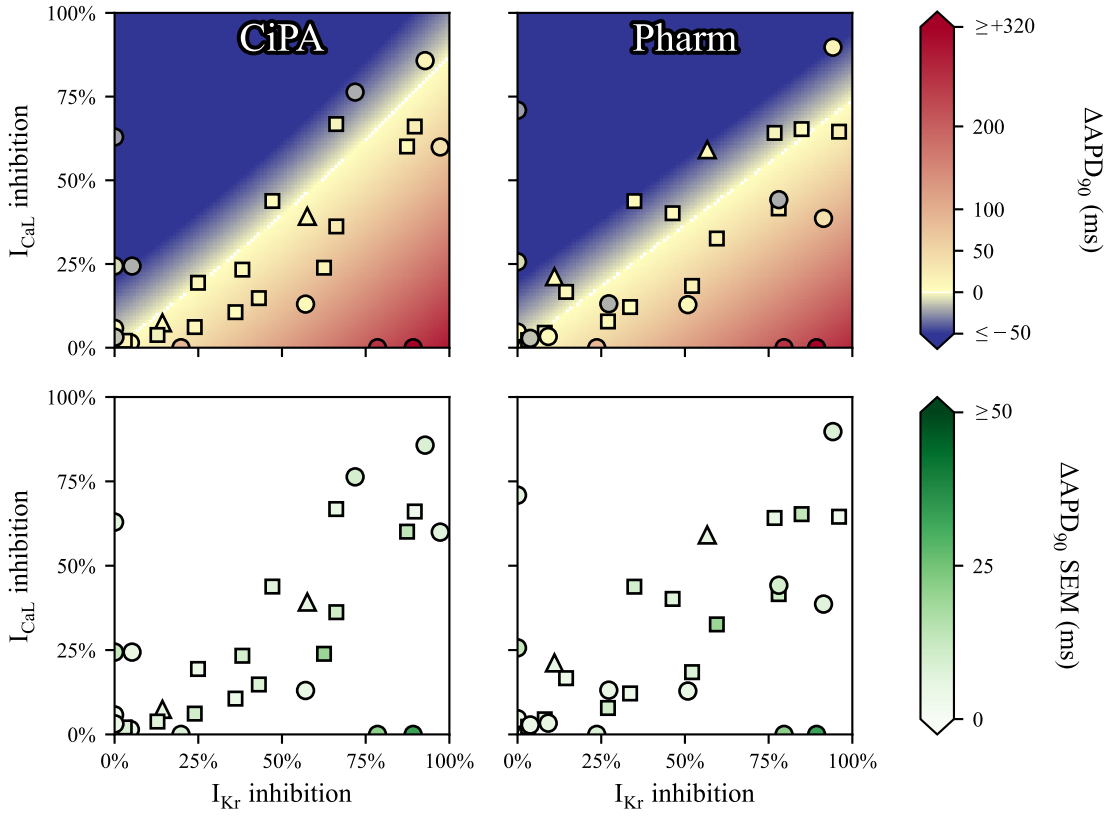

Figure 4.20: ΔAPD_{90} measured *ex vivo* (Table 4.7) as a function of I_{Kr} and I_{CaL} inhibition in the final dataset used for model calibration. A quadratic surface approximating the data points is plotted in the background (Section B.4 in the Appendix). I_{Kr} and I_{CaL} inhibition were computed using the Hill equation (Eq. 4.1), with the CiPA (left) and Pharm (right) datasets reported in Table 4.2. The bottom panels report the SEM in ΔAPD_{90}. When actual drug concentrations were measured for all trabeculae tested with the same nominal drug concentration, the data point was plotted as a **square**. When actual drug concentrations were measured only for some trabeculae tested with the same nominal drug concentration, the data point was plotted as a **triangle**. When only nominal concentrations were available, the data point was plotted as a **circle**.

With increasing I_{CaL} inhibition, the mean APD_{90} was shortened (the colour on the 2-D map tends towards dark blue colours). On the other hand, the more I_{Kr} was inhibited, the more APD_{90} was prolonged. I_{Kr} and I_{CaL} inhibition differed from one dataset to another, with the CiPA dataset being more sensitive to inhibition of I_{CaL} than the Pharm dataset.

When the inhibition of I_{Kr} and I_{CaL} was computed with the Pharm dataset, Verapamil effect on APD_{90} was not always consistent with the effects of other drugs. The biggest outlier from the surface is observed with 1 μM Verapamil, where it induced $\Delta APD_{90}= -20 \pm 10$ ms at 1 μM, with 78% I_{Kr} and 44% I_{CaL} inhibition, while 3 μM Clozapine induced $\Delta APD_{90}= 10 \pm 7$ ms with 57% I_{Kr} and 59% I_{CaL} inhibition. Nevertheless, both

datasets yield qualitatively similar results.

These results are consistent with the data used by O'Hara *et al.* (2011) to validate the predictions of their model for APD_{90} response to 70% I_{Kr} inhibition ($+154 \pm 70$ ms in guinea pig cardiomyocytes (Sanguinetti & Jurkiewicz, 1990)) and to 90% I_{CaL} inhibition (-58 ± 29 ms in rat cardiomyocytes (Walsh *et al.*, 2007)). For additional comparison, Hortigon-Vinagre *et al.* (2016) found that 30 nM and 300 nM Nifedipine shortened APD_{90} by 10% and 50%, respectively, in human induced pluripotent stem cells derived into cardiomyocytes (hiPSC-CMs).

For trabeculae used in Phase 2 experiments, the actual drug concentrations in the bath solution were measured, and differences were observed with the nominal concentrations (Table 4.8). Using the nominal drug concentrations instead of the actual drug concentrations for plotting the Phase 2 data did not impact the qualitative interpretation of the above results (Section B.5 in the Appendix). This supports the use of the Phase 1 and Phase 2 datasets in a single consistent dataset.

4.14 Study limitations

The AP data required normalisation to mitigate the movements of the recording electrode. Therefore, drug effects on any AP marker impacted by AP normalisation cannot be retrieved from sharp electrode recordings in cardiac tissue. For example, a population of models (Britton *et al.*, 2013) constructed with these markers recorded with sharp electrodes would suffer from limited reliability.

Furthermore, parameter inference was not impacted by normalisation of the AP data, when AP data were available for multiple conditions with I_{Kr} and I_{CaL} inhibition (Section 4.8.3). If other drug perturbations are investigated, e.g., inhibition of the sodium-calcium exchanger current (I_{NaCa}) that is mainly impacting the RMP, information lost in the normalisation of the AP data may impair the estimation of parameters.

No model discrepancy was included in the synthetic study of Section 4.8.3. Model discrepancy is expected to be introduced when calibrating any AP model to the real data, which hinders parameter estimation (Lei *et al.*, 2020). The normalisation of the AP data may therefore impact differently the calibration of a model to real data. Therefore,

assessing the identifiability of parameters and estimating their uncertainty will be necessary, when calibrating any AP model to the real normalised AP data.

Substantial variations of APD_{90} are expected to be only due to recording artefacts combined with potential DMSO effects (Figure 4.17). This suggests that the uncertainty in drug-induced ΔAPD_{90} calculated for each individual should account for DMSO effect. Yet, the standard error of the mean ΔAPD_{90} was low for the effect of DMSO (Table 4.6), thus supporting that ΔAPD_{90} averaged over several trabeculae would be reliable. Furthermore, drug-induced ΔAPD_{90} could be corrected for DMSO effects in future analyses (Section B.7 in the Appendix). However, normalised whole AP traces, used for model training in Chapter 7, cannot be corrected for the effect of DMSO. To make a consistent use of the *ex vivo* data across all Chapters, no corrections for the effect of DMSO were made in this DPhil thesis.

Substantial beat-to-beat (or in our data "pace-to-pace") APD_{90} variability (> 10 ms) under steady stimulation under baseline conditions was also observed in some trabeculae. In this work, APD_{90} was averaged over the last 30 APs of steady 1 Hz pacing, therefore neglecting the pace-to-pace variability in APD_{90}. In future work, the pace-to-pace variability in APD_{90} could be used to recalculate the uncertainty in APD_{90} measurements. Furthermore, beat-to-beat APD_{90} variability can be used as a proarrhythmic risk marker (Thomsen *et al.*, 2004; Sampedro-Puente *et al.*, 2019), and the drug effect on pace-to-pace variability in APD_{90} could be investigated in future work.

During *ex vivo* experiments, tissues were stimulated with bi-phasic pulses of 3 V for 3 ms, i.e., 1.5 times more than the minimal stimulus for AP initiation (Page *et al.*, 2016). Any effect of the drugs on the fast sodium current (I_{Na}) was therefore hidden with this protocol, because the trabeculae depolarised in response to the stimulus rather than the sodium current. As a consequence, sodium channel block was not taken into account, even though some of the drugs used exhibit inhibition of I_{Na} at the tested concentrations (Clozapine, Quinidine and Thioridazine in particular (Mirams *et al.*, 2011; Kramer *et al.*, 2013; Crumb Jr *et al.*, 2016; Li *et al.*, 2019)). In constructing the 2D maps we have also assumed the drugs do not act on any other ion channels, pumps or exchangers, and that conductance block fully represents the electrophysiological effects of the drugs.

The experiments lasted less than 3 h in total, with 25 min steady 1 Hz pacing under each drug treatment. Therefore, only acute I_{Kr} and I_{CaL} inhibition was investigated *ex vivo*. Similarly, only acute inhibitory effects of drugs were tested *in vitro*.

In reality there may be some other ion channel effects and kinetics of drug binding (state-dependent binding, etc.) that play a role which could explain why some drugs in similar locations on the map exhibit slightly different APD effects on the trabeculae and different effects in the clinic. For example, Chlorpromazine is a weak inhibitor of the Na^+–K^+ pump current (Van Dyke & Scharschmidt, 1987). Also, the effect of Dofetilide is more accurately described by taking into account the drug binding kinetics to the hERG channel (Milnes *et al.*, 2010). Also, long-term drug effects are not captured in this study, e.g., Thioridazine promotes the degradation of hERG channels, and increases I_{CaL} density via reactive oxygen species-mediated activation of CaMKII (Liu *et al.*, 2020).

In this Chapter, we tried two different approaches to inhibit simultaneously I_{Kr} and I_{CaL}, by applying 1) a single multi-ion current inhibitor or 2) a selective I_{Kr} inhibitor and a selective I_{CaL} inhibitor at the same time. The APD_{90} data presented in this Chapter exhibited a major inconsistency between these two approaches (Figure 4.19). Other drugs combined with Dofetilide yielded unexpectedly high prolongation of APD_{90}. Further investigation of the interaction between tested drugs and Dofetilide would be required to integrate best this data to the dataset used for model development. It is likely that the Loewe independent additivity model used to compute current inhibition by concomitant drugs (Eq. 4.1) may not be adequate. To maintain the focus of this DPhil project, the mechanism of interaction between tested drugs and Dofetilide inhibition of I_{Kr} and I_{CaL} was not investigated further. The data recorded with exposure to two concomitant drugs was not used in the following chapters.

Our new experimental APD_{90} data were obtained in ventricular trabeculae taken only from endocardial tissues. Predictions of myocardial repolarisation time with only one myocardial cell type omit transmural dispersion of repolarisation (Antzelevitch, 2007). Further investigation with mid-wall and epicardial tissue would enable a more complete evaluation of the response of cardiac safety markers to I_{Kr} and I_{CaL} changes. Alternatively,

in silico models could be used to translate results obtained from endocardial tissue into mid-wall and epicardial response to drug effects.

4.15 Summary

In this Chapter, new experimental data that can be used for the calibration of a new AP model were introduced. In Section 4.3, the inhibitor potency for I_{Kr} and I_{CaL} of nine drugs was investigated *in vitro* in voltage-clamp patch-clamp experiments.

The acquisition of AP data *ex vivo* in adult human ventricular trabeculae with the sharp electrode technique under baseline and drug treatment (Tables 4.3–4.4) was described in Section 4.4. The AP data were then post-processed to filter noise and calculate AP markers (Section 4.5). Next, data quality was checked to 1) verify the reproducibility of the experimental data generated in two separate phases (Section 4.6), 2) exclude data points affected by stimulus artefacts (Section 4.7), and 3) identify a strategy to mitigate experimental limitations imposed by movements of the sharp electrode (Section 4.8). Importantly, it was verified in a synthetic exercise that the mitigation strategy, normalisation of the voltage (Eq. 4.3), does not hinder parameter estimation (Section 4.8.3).

A bioanalytical analysis of the bath solution was performed to measure the actual drug concentrations to which the trabeculae were exposed (Section 4.11), finding substantial differences between actual and nominal drug concentrations (Table 4.8). With the actual drug concentrations and *in vitro* data (Table 4.2), the fraction of drug-induced inhibition of I_{Kr} and I_{CaL} can be calculated as accurately as possible (Eq. 4.1).

Combined with the *in vitro* data, drug-induced ΔAPD_{90} was linked with drug-induced inhibition of I_{Kr} and I_{CaL} (Section 4.10). A major inconsistency was observed between ΔAPD_{90} induced by a single drug and ΔAPD_{90} induced by two concomitant drugs (Figure 4.19). As drug-drug interactions modelling is out of the scope of the present DPhil thesis, the data generated with two concomitant drugs were excluded from the final dataset. The final dataset was reported in Table 4.9 and visualised in Figure 4.20.

The new experimental AP data introduced in this Chapter provide quantitative understanding of the relationship between APD_{90} and I_{Kr} and I_{CaL} inhibition in adult

human ventricular cardiac muscle. Whole traces of APs, although normalised, were observed with several drug perturbations tested in the same individual and can be used for model calibration in a following Chapter. Furthermore, the experimental data for ΔAPD_{90} introduced in this Chapter can be used to evaluate the performance of existing *in silico* AP models for prediction of response I_{Kr} and I_{CaL} inhibition, which is the purpose of Chapter 5.

Acknowledgements

Patch-clamp experiments were carried out internally in Roche by Evgenia Gissinger and Fabian Häusermann, in Dr. Liudmila Polonchuk's lab (F. Hoffmann-La Roche Ltd., Pharma Research and Early Development, Pharmaceutical Sciences).

5

Comparison of in silico predictions of action potential duration in response to inhibition of I_{Kr} and I_{CaL} with new human experimental data

Preamble

The proarrhythmic risk associated with drug candidates, in particular risk of Torsades de Pointes (TdP), is thoroughly investigated in pre-clinical and clinical phases of drug development. Inhibition of the rapid delayed rectifier K^+ current (I_{Kr}) can prolong the action potential (AP) duration (APD), and is reflected in prolongation of the electrocardiogram QT interval, used as a clinical risk factor for TdP. Previous studies have shown that although existing guidelines have successfully prevented compounds with unfavorable TdP risk/benefit ratio from reaching the market, the I_{Kr}-centric approach has limited specificity for drugs concurrently affecting other ionic currents, in particular the L-type Ca^{2+} current (I_{CaL}). Biophysically-detailed mathematical AP models are in silico tools that could address these limitations. In particular, some AP models have been developed to integrate multi-ion channel effects on the AP and other biomarkers. However, no systematic comparison has been carried out between experimental drug-induced APD versus predictions by AP models. In Chapter 4, new in vitro and ex vivo data for APD under various conditions with drug-induced I_{Kr} and I_{CaL} inhibition was acquired, processed, and analysed. In this Chapter, we input in vitro measurements of drug inhibition of I_{Kr} and

I_{CaL} from patch-clamp experiments into AP models to assess how well they recapitulate drug-induced APD changes observed experimentally.

The contents of this Chapter will be submitted for journal publication together with ex vivo measurements of APD in human ventricular trabeculae from Chapter 4.

5.1 Introduction

The rapid delayed rectifier K^+ current (I_{Kr}) is a major ionic current contributing to the repolarisation of ventricular cardiomyocytes. Inhibition of I_{Kr} can prolong the action potential (AP) duration (APD) and the QT interval (Redfern *et al.*, 2003). Many drugs inhibiting I_{Kr} have been shown to increase the risk of occurrence of Torsades de Pointes (TdP), a potentially lethal arrhythmia (Redfern *et al.*, 2003; Li & Ramos, 2017). In the 1990s, several drugs were withdrawn from the market because of undetected TdP risk, and regulatory bodies established the guidelines ICH S7B and ICH E14 to prevent the development of new compounds with unacceptable pro-arrhythmic risk (ICH, 2005, 2006). According to the pre-clinical guideline ICH S7B (ICH, 2005), the ability of compounds to inhibit I_{Kr} must be tested *in vitro*, and a safety margin has been suggested such that drugs should have a half-maximal inhibitory concentration (IC_{50}) of over 30 times their maximal free therapeutic plasma concentration, C_{max}, (Redfern *et al.*, 2003). *In silico* mathematical electrophysiology models describing the formation of the AP from the underlying ionic currents (AP models) were included in a refinement of TdP risk assessment, under the Comprehensive *in vitro* Proarrhythmia Assay (CiPA) initiative (Colatsky *et al.*, 2016).

AP models can improve the limited specificity of the I_{Kr}-centric guidelines by accounting for simultaneous inhibition of multiple ionic currents in AP models (Li *et al.*, 2017). In particular, inhibition of the L-type Ca^{2+} current (I_{CaL}) mitigates the arrhythmogenicity of I_{Kr} inhibitors (Mirams *et al.*, 2011), partially explaining why some potent I_{Kr} inhibitors such as Verapamil do not promote TdP risk. Yet, AP model predictions for APD induced by simultaneous inhibition of I_{Kr} and I_{CaL} have not been validated against human data.

In this Chapter, we compare the predictions of 11 *in silico* AP models with the new *ex vivo* human data described in Chapter 4. We use *in vitro* data from automated patch-clamp screening in expression systems (Section 4.3) to calculate percentage block

of I_{Kr} and/or I_{CaL} induced by nine compounds (Chlorpromazine, Clozapine, Dofetilide, Fluoxetine, Mesoridazine, Nifedipine, Quinidine, Thioridazine, Verapamil). This is then used for inputs into the simulations for prediction of the APD at 90% repolarisation (APD_{90}). Next, predictions of APD_{90} change from baseline (ΔAPD_{90}) are validated against the *ex vivo* data. We carry out this study using both *in vitro* datasets produced following two different protocols (CiPA and Pharm, Table 4.2). Finally, we compare the *ex vivo* data with the net charge carried by ionic currents, (Q_{net}), used as a predictive metric of TdP risk by e.g., Dutta *et al.* (2017) and Li *et al.* (2019).

Given that ΔAPD_{90} induced by I_{Kr} and I_{CaL} inhibition are linked to QT changes (Johannesen *et al.*, 2014), this study is a crucial first step towards the development of a mechanistic predictive model of QT change induced by I_{Kr} and I_{CaL} inhibition.

5.2 Methods

5.2.1 Ex vivo action potential data

AP data were obtained *ex vivo* from cardiac trabeculae extracted from the inner endocardial wall of donor hearts with the sharp electrode technique (Chapter 4). Only drug conditions tested experimentally with a single drug were included in this Chapter (Section 4.10). The selected drugs and concentrations are reported in Table 5.1. Inhibitor potency for I_{Kr} and I_{CaL} are shown in Table 4.2.

The dataset was generated from experiments undertaken in two distinct phases. In Phase 2, a bioanalytical analysis of the bath solution was performed to measure the exact drug concentration, at the end of each 25 min steady 1 Hz pacing period (Section 4.11). In Phase 1, measurements were not available so the nominal concentrations were used (Table 4.3).

5.2.2 Simulations of APD_{90} with *in silico* action potential models

Selected Models

We selected six main models representative of recent efforts to model the human ventricular AP: Ten Tusscher *et al.* (2004) (TNNP), Ten Tusscher & Panfilov (2006) (TP), Grandi *et al.* (2010) (GPB), O'Hara *et al.* (2011) (ORd), Tomek *et al.* (2020) (ToR-ORd), and Bartolucci *et al.* (2020) (BPS). Since their release, five new parameterisations and variants

Drug	1st conc (μM)	2nd conc (μM)	3rd conc (μM)	4th conc (μM)	Number of trabeculae
Chlorpromazine	0.3	1	3		6
Clozapine	0.3	1	3		7
Clozapine	0.3	3	30		4
Dofetilide	0.001	0.01	0.1	0.2	15
Fluoxetine	0.3	1	3		5
Mesoridazine	0.04	0.25	10		6
Nifedipine	0.003	0.03	0.3		4
Quinidine	0.1	1	10		15
Thioridazine	0.012	0.6	2		4
Verapamil	0.01	0.1	1		15

Table 5.1: Drugs tested in *ex vivo* experiments that were used for the present Chapter, and corresponding nominal concentrations.

of these models have been published. Dutta *et al.* (2017) replaced the I_{Kr} component of the ORd model with a 6 state Markov model (Li *et al.*, 2017) and rescaled the maximal conductances of five ionic currents (I_{Kr}, I_{CaL}, I_{K1}, I_{Ks}, I_{NaL}). The GPB, TP and ORd models were rescaled by Mann *et al.* (2016) to capture the effects of I_{Kr} and I_{Ks} inhibition and to reproduce APD_{90} features observed in long QT Syndrome (LQTS) populations. Mann *et al.* added a late sodium component to their versions of the GPB and TP models, based on the ORd model. Krogh-Madsen *et al.* (2017) proposed a version of the ORd model with rescaled maximal conductance parameters for six ionic currents (I_{Kr}, I_{CaL}, I_{Ks}, I_{NaCa}, I_{NaK}, I_{NaL}) to capture populations with long QT syndrome, which was also included in the present study. All these variant models were included in the present study and are summarised in Table 5.2.

To maximise consistency with the trabeculae measurements, the endocardial variant of the AP models was used.

Computational tools

AP models were downloaded from the Physiome Model Repository (Yu *et al.*, 2011) in CellML format. Simulations were performed using Myokit 1.33.7 (Clerx *et al.*, 2016) and CVODE 5.7.0 (Hindmarsh *et al.*, 2005). Absolute and relative solver tolerance for

Model	Reference	Model structure
BPS*	(Bartolucci *et al.*, 2020)	ORd + I_{CaL}
GPB10*	(Grandi *et al.*, 2010)	GPB
GPB-M	(Mann *et al.*, 2016)	GPB + ORd I_{NaL}
ORd*	(O'Hara *et al.*, 2011)	ORd
ORd-CiPA*	(Dutta *et al.*, 2017)	ORd + I_{Kr}
ORd-KM	(Krogh-Madsen *et al.*, 2017)	ORd
ORd-M	(Mann *et al.*, 2016)	ORd
ToR-ORd20*	(Tomek *et al.*, 2020)	ToR-ORd
TNNP	(Ten Tusscher *et al.*, 2004)	TNNP
TP*	(Ten Tusscher & Panfilov, 2006)	TP
TP-M	(Mann *et al.*, 2016)	TP + ORd 2011 NaL

Table 5.2: Selected AP models. The * symbol indicates when the endocardial variant of the model was selected among different versions developed by the authors of the model.

CVODE were both set to 10^{-10} to ensure numerical accuracy of the solutions. Note that with the TNNP and TP models, singularities at 0 mV and −60 mV sometimes triggered numerical errors, in which case the absolute and relative solver tolerance were loosened to 10^{-9}. In the TNNP model, a numerical singularity for $V = 0$ mV was corrected for the component of I_{CaL} described with a Goldman-Hodgkin-Katz flux-style equation.

Action potential simulations

1 Hz steady pacing was applied in line with the *ex vivo* experiments. Stimulus current width, amplitude, and responsible ions (for instance K^+, see Chapter 3) were not changed from the published CellML model. We simulated 1500 s to reach a steady-state response to 1 Hz pacing. In all models, the convergence to steady-state was achieved with 1500 pre-paces (results not shown). The 1501st AP was then recorded with time resolution of 0.05 ms, matching the resolution of the *ex vivo* data and allowing for precise estimation of APD_{90}.

When computing 2-D maps of ΔAPD_{90} as a function of I_{Kr} and I_{CaL} inhibition, default internal and external concentrations from the CellML files were used (Section 5.3.1). When comparing quantitative model predictions with trabeculae recordings (Section 5.3.2), external concentrations of K^+, Na^+, and Ca^{2+} were set to 4 mM, 148.35 mM, and

1.8 mM respectively, matching concentrations in the external solution used experimentally (Page *et al.*, 2016).

The steady-state APs simulated with the included models are shown in Figure 5.1 for visual comparison. Note that the TNNP model does not predict a physiological AP with external ionic concentrations matching concentrations in the external solution used for *ex vivo* experiments. Therefore, predictions with the TNNP model were not quantitatively compared with the *ex vivo* data.

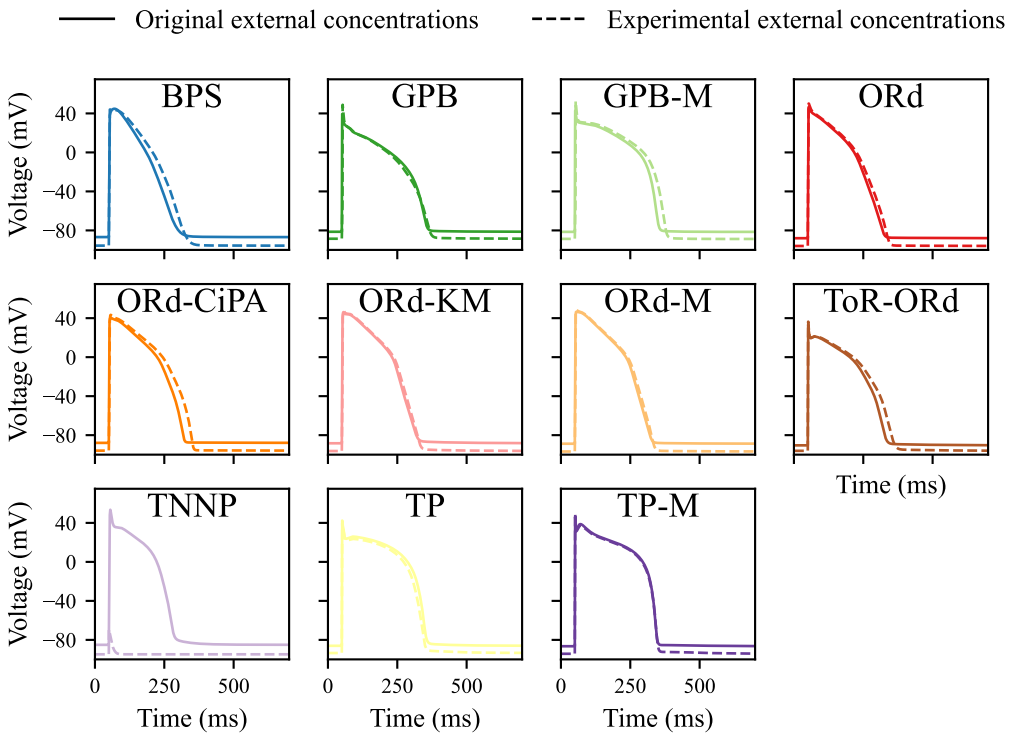

Figure 5.1: Steady-state 1 Hz AP simulated with the AP models included in this study. External concentrations were set to experimental values (**dashed line**) or left to their values in the original CellML model (**solid line**).

Drug effects were modelled as simple pore block, with the reduction of the current computed using the Hill equation (Hill, 1910):

$$I(D) = \frac{1}{1 + \left(\frac{D}{\mathrm{IC50}}\right)^{h}} \times I(0), \tag{5.1}$$

with $I(D)$ the current with drug inhibition, D the drug concentration, h the Hill coefficient, IC_{50} the half-maximal inhibitory drug concentration, and $I(0)$ the ionic current without drug.

5.2.3 Comparison of model predictions with experiments

Qualitative comparison with 2-D maps of ΔAPD_{90} versus current inhibition

With each model, we simulated APs under $101 \times 101 = 10,201$ combinations of I_{Kr} and I_{CaL} inhibition, ranging from 0% to 100% inhibition. ΔAPD_{90} was computed for each I_{Kr}/I_{CaL} inhibition combination. ΔAPD_{90} was plotted as a function of I_{Kr} and I_{CaL} inhibition used as X- and Y-axis coordinates, respectively, as a "2-D map".

ΔAPD_{90} was shown using a colour-map that was kept consistent across all the models and which covered the experimental range of drug-induced ΔAPD_{90}. Combinations of I_{Kr} and/or I_{CaL} inhibition for which no change in APD_{90} were observed/predicted ($|\Delta APD_{90}| \leq 1$ ms) were plotted as white pixels, thus highlighting a "0 ms line".

Figure 5.2 shows how the 2-D maps were generated.

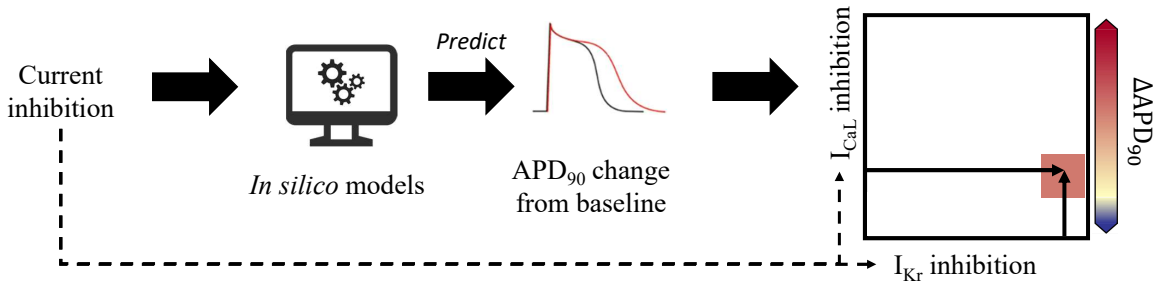

Figure 5.2: Schematic of methods used to plot ΔAPD_{90} 2-D maps. Simulated ΔAPD_{90} was computed from the *in silico* AP model run for 1500 paces, using I_{Kr} and/or I_{CaL} inhibition as input for the model. The corresponding point was then added to the 2-D map, with ΔAPD_{90} reported with the colour-map.

The 2-D map of predicted ΔAPD_{90} was then visually compared with a quadratic surface fitted through *ex vivo* data points (Figure 4.20).

Quantitative metric for model predictivity

To quantitatively compare ΔAPD_{90} measurements and predictions, we designed an error measure, E.

For each tested drug perturbation, k, tested in sharp electrode experiments, the corresponding levels of I_{Kr} and I_{CaL} inhibition were computed from the *in vitro* data (Table 4.2) and the drug concentration. When available, the mean measured drug concentration in the bath solution across trabeculae was used (Table 4.8); otherwise, the nominal drug concentration was used (Table 5.1).

The computed drug-induced I_{Kr} and I_{CaL} inhibition was then used as input for the AP models to predict the ΔAPD_{90} response to the drug perturbation k ($\Delta APD_{90,sim,k}$). Finally, to account for the variability in experimental ΔAPD_{90} response, the error in ΔAPD_{90} prediction was scaled by the inverse of the standard error of the mean ΔAPD_{90} measured experimentally. The error measure, E, used to quantify the predictive power of *in silico* AP models was defined as:

$$E = \sum_{k}^{K} \left| \frac{\Delta APD_{90,sim,k} - \overline{\Delta} APD_{90,exp,k}}{\sigma_{M,exp,k}} \right|, \tag{5.2}$$

with $\overline{\Delta} APD_{90,exp,k}$ the mean experimental ΔAPD_{90} for the drug perturbation k measured over 30 consecutive APs, averaged over the tested trabeculae, and $\sigma_{M,exp,k}$ the standard error of the mean experimental ΔAPD_{90} across the trabeculae tested with k. The values of $\overline{\Delta} APD_{90,exp,k}$ and $\sigma_{M,exp,k}$ were reported previously in Table 4.7. Indices k span all concentrations of the nine drugs (Figure 5.5A) or of a single drug (Figures 5.5B and C).

5.3 Results

5.3.1 2-D maps of ΔAPD_{90} predicted by literature AP models

The 2-D maps of ΔAPD_{90} prediction for all 11 models and model variants are shown in Figure 5.3 together with the quadratic surfaces fitted through experimental data points. The steeper the slope of the 0 ms line, the more the gradient of ΔAPD_{90} aligns with the X-axis, hence the model is more sensitive to I_{Kr} reduction. Similarly, the more horizontal the 0 ms line, the more the gradient of ΔAPD_{90} aligns with the Y-axis, and the model is more sensitive to I_{CaL} reduction.

A clear distinction was observed between models similar to the ORd model which were most sensitive to I_{Kr} block, and models similar to the TP model which were more sensitive to I_{CaL} block than I_{Kr} block. On 2-D maps for the BPS, ORd, ORd-CiPA, ORd-KM, ORd-M, and ToR-ORd models, the 0 ms line was mostly vertical, and the map was nearly 1-D along the X-axis. These ORd-like models exhibited little mitigation of I_{Kr} block-induced ΔAPD_{90} by I_{CaL} block. These results are consistent with previous observations (Mirams *et al.*, 2014).

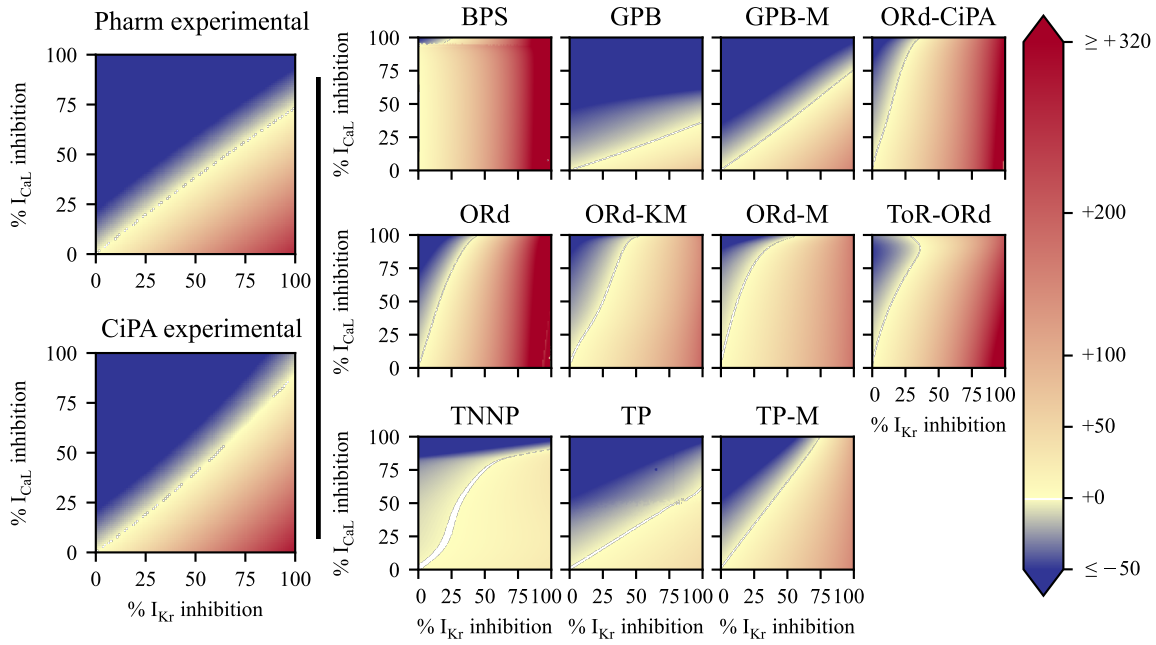

Figure 5.3: Left: Surfaces fitted through experimental data points. **Right:** 2-D maps of predicted APD_{90} change from baseline after I_{CaL} and I_{Kr} inhibition. The colour scale indicates shortening of APD_{90} (i.e., $\Delta APD_{90} < 0$ ms) for colours towards dark blue, and APD_{90} prolongation (i.e., $\Delta APD_{90} > 0$ ms) for colours towards red. ΔAPD_{90} values below −50 ms and above +320 ms were set to dark blue and red, respectively, for better visualisation. For I_{Kr} and I_{CaL} inhibition leading to $-1\,\text{ms} < \Delta APD_{90} < +1\,\text{ms}$, the pixel is coloured in white.

In the most extreme case, the BPS model, nearly no mitigation of I_{Kr} block by I_{CaL} block was observed, and the 0 ms line was vertical. In this model, I_{CaL} inhibition even prolonged the APD_{90}: 5% I_{Kr} and 80% I_{CaL} inhibition yielded $\Delta APD_{90} = +9$ ms, while 5% I_{Kr} and I_{CaL} inhibition 85% produced a ΔAPD_{90} of +11 ms. As a consequence, APD_{90} changes predicted by the BPS model were not a monotonic function of I_{Kr} and I_{CaL} inhibition. Initially, I_{CaL} inhibition prolonged APD_{90}, but with more than 91% I_{CaL} inhibition, the morphology of the AP changed considerably and APD_{90} decreased drastically. The mechanistic reason for this behaviour remains to be investigated.

ToR-ORd also exhibited an unexpected non-monotonic 2-D map: for 35% I_{Kr} and 90% I_{CaL} inhibition, the ToR-ORd model predicts no change in APD_{90}; for further I_{CaL} inhibition it predicts an increase of APD_{90}. The mechanism appears to be that for such reduced I_{CaL}, the concentration of calcium in the subspace compartment shrinks, and

therefore the calcium-activated Cl^- current ($I_{(Ca)Cl}$) cannot be activated. $I_{(Ca)Cl}$ acts as a repolarisation current, and its reduction prolongs the APD_{90}. With 90% inhibition of I_{CaL}, the effect of further reduction of I_{CaL} on the APD_{90} is therefore overshadowed by the reduction of $I_{(Ca)Cl}$, thus leading to the counter-intuitive APD_{90} prolongation.

The TP-like models (TP, TP-M, GPB, and GPB-M) models predicted similar 0 ms lines, which were almost linear with slopes between 0.5 and 1.3. The original TP and GPB models exhibited much lower sensitivities of APD_{90} to I_{Kr}-only inhibition ($\Delta APD_{90} \leq +48$ ms and +51 ms for the TP and GPB models, respectively), than observed experimentally with 200 nM Dofetilide ($\Delta APD_{90} = +318 \pm 33$ ms). The addition of I_{NaL} and rescaling of the TP and GPB models by Mann *et al.* (2016) increased their sensitivity to I_{Kr} reduction: the TP-M and GPB-M models predicted $\Delta APD_{90} = +154$ ms and +144 ms with 100% inhibition of I_{Kr} respectively.

The TNNP model behaves noticeably differently from the TP and other models, as its 0 ms line is in an "S" shape, and nearly no prolongation of APD_{90} was observed even with 100% I_{Kr} block ($\Delta APD_{90} < +30$ ms).

Visually comparing model predictions to *ex vivo* data, the relatively simple relationships predicted by the TP-M and GPB-M models appear closest to the truth. This is investigated quantitatively in the next section.

5.3.2 Comparison of in-silico prediction of ΔAPD_{90} with *ex vivo* data

A quantitative comparison of ΔAPD_{90} predictions and the new *ex vivo* trabeculae data is shown in Figure 5.4. Here, the error in ΔAPD_{90} is presented as a multiple of the experimental standard error of the mean ΔAPD_{90}, σ_M, thus making it a direct visualisation of the contribution to the error measure, E (Eq. 5.2), of each drug perturbation. Note that extracellular ionic concentrations were set to match concentrations in the external solution used in *ex vivo* experiments.

ORd-like models performed similarly in predicting the experimental ΔAPD_{90}, consistently with their 2-D maps being similar (Figure 5.3). Predictions of response to selective I_{Kr} and selective I_{CaL} inhibitors by the ORd-CiPA and ToR-ORd models in particular

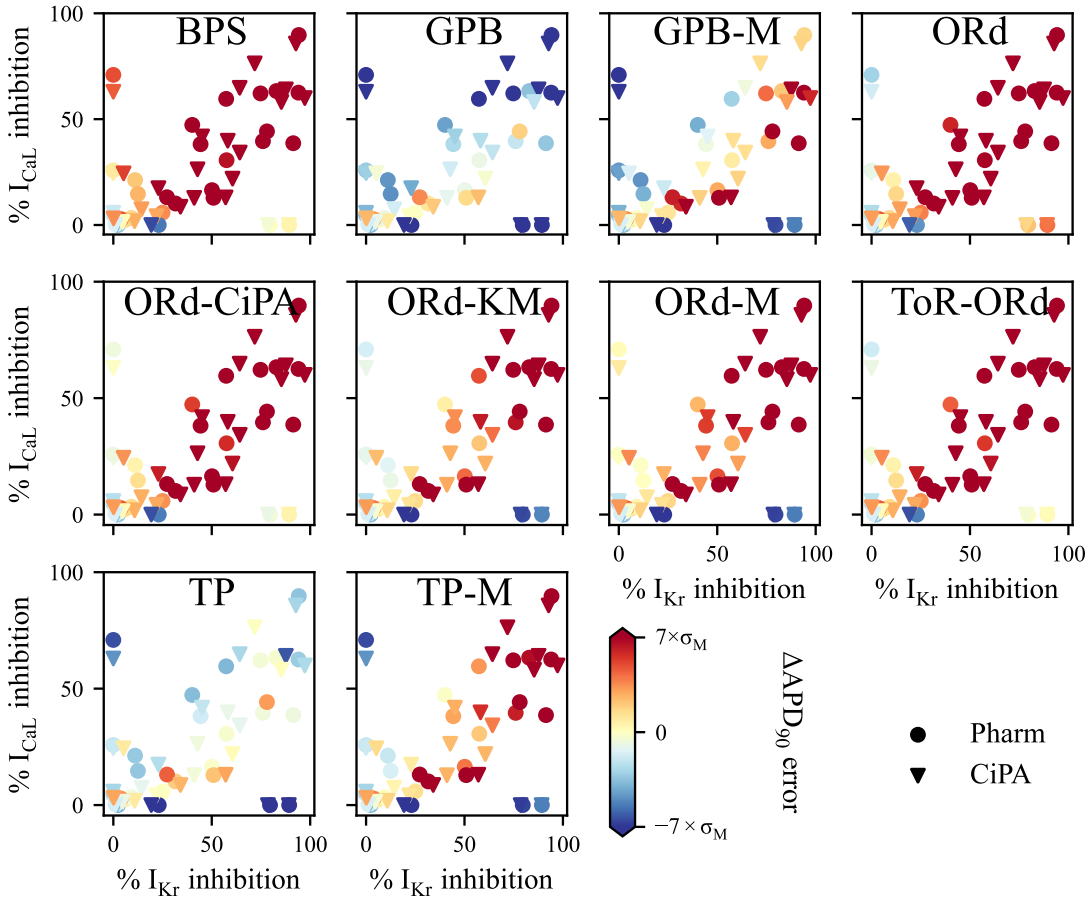

Figure 5.4: Comparison of *in silico* prediction of ΔAPD_{90} response to I_{Kr} and/or I_{CaL} inhibition with *ex vivo* data. CiPA (**triangle**) and Pharm (**circle**) datasets for IC_{50} values used to compute drug perturbation are available in Table 4.2. σ_M denotes here the experimental standard error of the mean ΔAPD_{90} response to each drug perturbation.

were largely correct (light colours). However, the ORd-like models overpredicted the prolongation of APD_{90} induced by mixed inhibitions of I_{Kr} and I_{CaL} (dark red).

The TP-like models underpredicted the ΔAPD_{90} response to inhibition of I_{Kr} alone (blue), but they provided good predictions of the ΔAPD_{90} effects of mixed I_{Kr} and I_{CaL} inhibition. The GPB model predicted excessive APD_{90} shortening after more than 50% I_{CaL} inhibition, but its predictions for mixed effects of I_{Kr} and I_{CaL} were otherwise within $3 \times \sigma_M$ of the mean experimental ΔAPD_{90}. The GPB-M and TP-M models performed differently depending on the IC_{50} dataset, but in both cases, they overpredicted APD_{90} prolongation by mixed inhibitions of I_{Kr} and I_{CaL}.

Figure 5.5A compares E (Eq. 5.2) for all 11 models, computed using the CiPA and Pharm datasets. In Figures 5.5B and C, values of E are detailed for each drug.

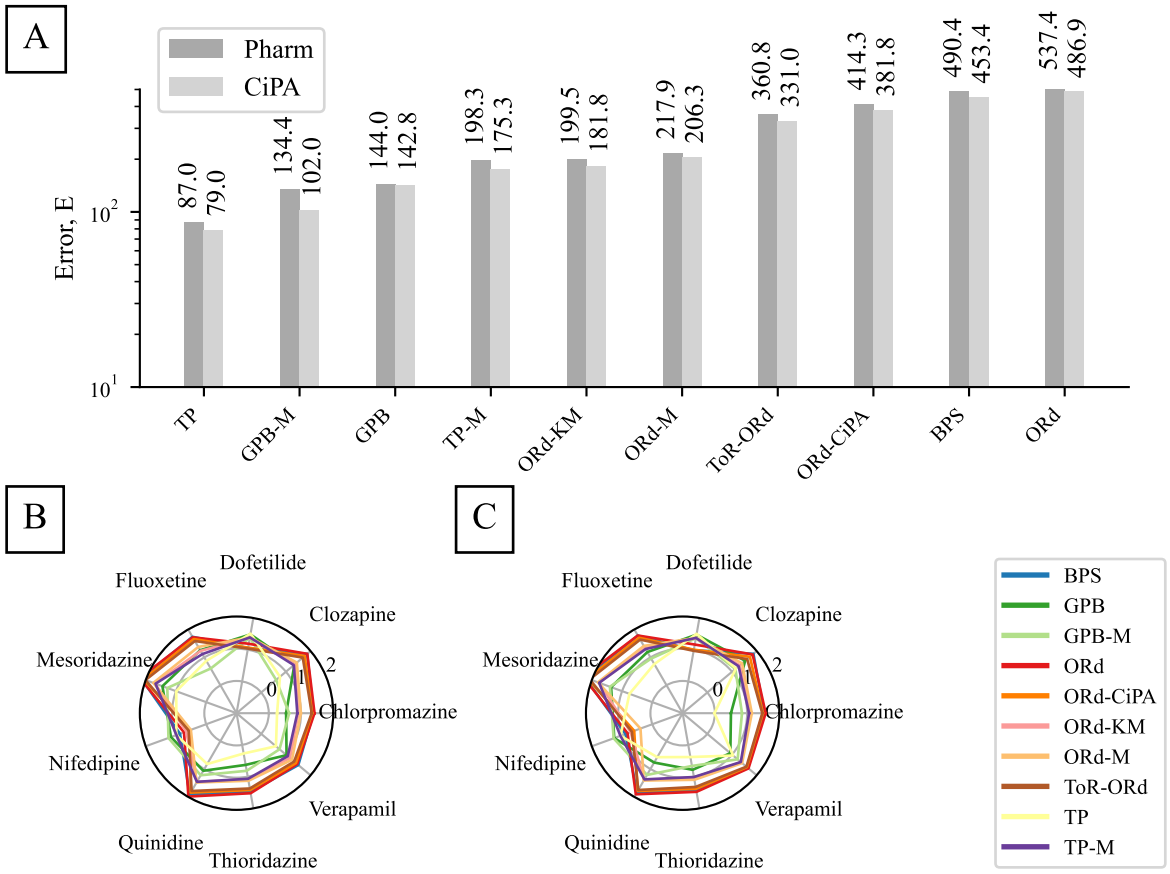

Figure 5.5: Comparison of the abilities of human ventricular AP models to reproduce the APD_{90} response to I_{Kr} and I_{CaL} inhibition observed *ex vivo*. The lower the error measure (Eq. 5.2), the more accurate the model predictions. **A:** The error measure was summed over all the drugs used in this study, when using the CiPA and Pharm protocols to compute the reduction of ionic currents by drugs. For each model, two bar plots were plotted, to compare the predictive power of models with the Pharm (left bar) and the CiPA (right bar) datasets. **B and C:** Detail of the error measures associated with each of the drugs using the CiPA and Pharm datasets, respectively, for each model. The $\log_{10}$ of the error measure is plotted along the radial-axis.

The lowest E was found for the TP model: $E = 79.0$ and 87.0 using the CiPA and Pharm datasets, respecitvely. Low values of E were found with the TP model for all drugs with a mixed effect. Indeed, the largest E values for the TP model were found for Dofetilide (24.2–31.2) and Nifedipine (8.3–9.8). All TP-like models yielded similarly high E for Dofetilide and Nifedipine, consistent with Figure 5.4, where the largest values of E were found for selective current inhibition.

For the TP and GPB models, E computed using the two datasets did not show large differences. By contrast, the models reformulated by Mann *et al.* and the ORd-like models exhibited stronger dependency on the dataset used to evaluate the drug perturbation. In

the extreme case of the ORd-CiPA model, a difference of 32.5 was observed: $E = 381.8$ vs $E = 414.3$ with the CiPA and Pharm datasets, respectively.

The ORd-like models all performed similarly, with relatively low errors for Dofetilide and Nifedipine, but high errors for the remaining drugs (up to 193.1 for Mesoridazine as predicted by the ORd model with the Pharm dataset). The ORd-like models reproduce the APD_{90} response to inhibition of I_{Kr} alone or I_{CaL} alone well, but do not capture the mitigation of I_{Kr} inhibition effect by I_{CaL} inhibition.

Importantly, a model which would predict $\Delta APD_{90} = 0\,\text{ms}$ over the whole 2-D map would yield an error measure $E = 59.0$ and would supposedly outperform the predictions of all literature models. However, this would not capture known mechanisms of APD_{90} prolongation by inhibiting only I_{Kr} and APD_{90} shortening by inhibiting only I_{CaL}. This bias is attributed to the selection of a majority of drugs that exert mixed inhibition of I_{Kr} and I_{CaL}, inducing low to no change in APD_{90}.

5.3.3 The TdP risk metric Q_{net} as a function of I_{Kr} and I_{CaL} inhibition

The CiPA initiative was established with the objective of developing an *in silico* model classifying drugs into three TdP risk categories (low, intermediate, high risk), providing a more specific safety assessment than the I_{Kr}-centric guideline (Sager *et al.*, 2014). One popular candidate, Q_{net}, relies on the net charge flux over the repolarisation phase of one AP computed with the ORd-CiPA model (Li *et al.*, 2019). Q_{net} is defined as the integral of the total net current over one AP at 0.5 Hz pacing after 1000 pre-paces defined as:

$$Q_{net} = \int_{0\,\text{ms}}^{2000\,\text{ms}} (I_{Kr} + I_{CaL} + I_{Ks} + I_{NaL} + I_{K1} + I_{to})\, dt. \tag{5.3}$$

In this section, we compare Q_{net} as a function of I_{Kr} and I_{CaL} inhibition with experimental ΔAPD_{90} measurements.

As with the AP models, Q_{net} was computed with the ORd-CiPA model for $101 \times 101 = 10,201$ combinations of I_{Kr} and I_{CaL} inhibition. The reduction of I_{Kr} was modelled by applying a multiplying factor to the maximal conductance of I_{Kr}, as in Section 5.2.3, although in the original methods of Li *et al.*, the I_{Kr} inhibition by drugs is modelled with the dynamic hERG binding model (Li *et al.*, 2017). Note that Li *et al.* classified compounds into the TdP risk categories based on the average Q_{net} computed at 1–4

times their maximal effective free therapeutic concentration. Nevertheless, a qualitative interpretation of the 2-D map remains possible.

Pixels of the 2-D map were colored based on the TdP risk category corresponding to Q_{net} obtained with the ORd-CiPA model after inhibition of the ionic currents. As in (Li *et al.*, 2019), Q_{net} values greater than $0.0671\,\mu C.\mu F^{-1}$ were classified as low risk (green), Q_{net} between $0.0581\,\mu C.\mu F^{-1}$ and $0.0671\,\mu C.\mu F^{-1}$ as intermediate risk (blue), and Q_{net} lower than $0.0581\,\mu C.\mu F^{-1}$ as high risk.

The resulting 2-D map is shown in Figure 5.6.

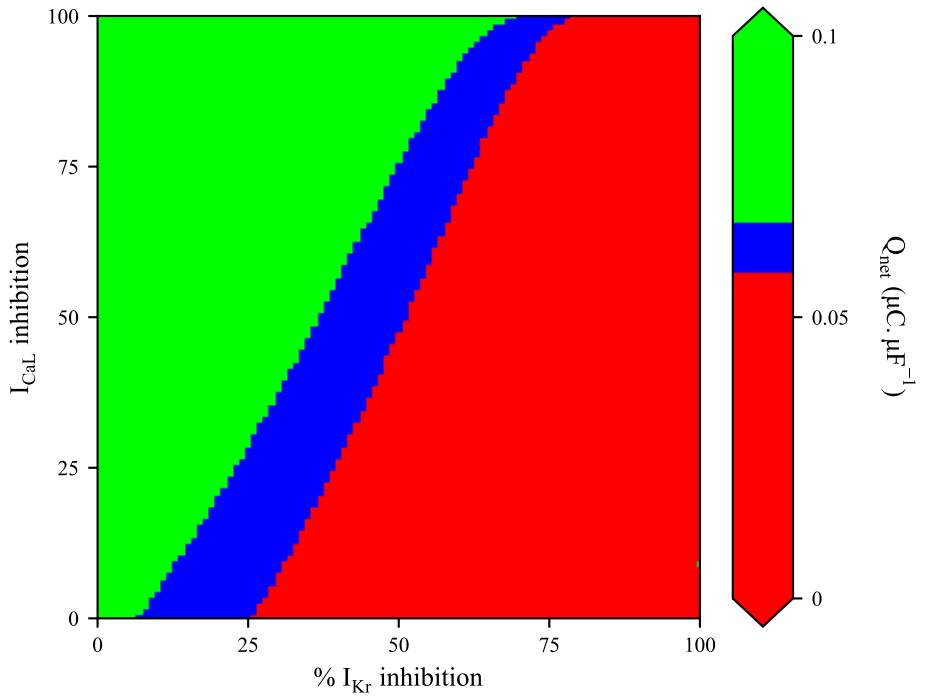

Figure 5.6: Q_{net} computed with the ORd-CiPA model, for various combinations of I_{Kr} and/or I_{CaL} inhibition. The green, blue and red regions correspond to the low, intermediate and high TdP risk categories, with the thresholds defined by Li *et al.* (2019). Note that I_{Kr} inhibition was computed as plain reduction of the maximal conductance of I_{Kr} (Section 5.2.3) instead of the dynamic hERG binding model used in the original study (Li *et al.*, 2019).

Interestingly, the decrease in Q_{net} (increase in TdP risk) induced by I_{Kr} inhibition is mitigated by I_{CaL} inhibition, with a higher sensitivity to I_{CaL} inhibition than ΔAPD_{90} predicted by the ORd-CiPA model. For example, 50% I_{Kr} inhibition and 75% I_{CaL} inhibition yields a Q_{net} value classified into the low TdP risk category, while the predicted ΔAPD_{90} is $+73\,ms$.

The shape of the 2-D map of Q_{net} is similar to that of the 2-D map of ΔAPD_{90} predicted by the TP-M model (Figure 5.3). Furthermore, qualitatively similar mitigation of I_{Kr} inhibition by I_{CaL} inhibition was observed between Q_{net} predictions and ΔAPD_{90} observed experimentally (Figure 4.20).

5.4 Discussion

5.4.1 Main findings

The predictions of ΔAPD_{90} by 11 literature AP models were computed for 10,201 combinations of I_{Kr} and I_{CaL} inhibition between 0% and 100%, and plotted on 2-D maps for visual comparison of the model predictions. Models were shown to fall into distinct categories with respect to their ΔAPD_{90} predictions: TP-like and ORd-like. The TP-like models exhibited less sensitivity of APD_{90} to I_{Kr} reduction ($\Delta APD_{90} < +150$ ms for 100% I_{Kr} inhibition) than ORd-like models ($\Delta APD_{90} > +200$ ms for 100% I_{Kr} inhibition). The TNNP model exhibited the lowest sensitivity to I_{Kr} inhibition ($\Delta APD_{90} < +30$ ms).

The model predictions were then compared with *ex vivo* ΔAPD_{90} measurements after exposure to I_{Kr} and I_{CaL} inhibitors. To compare the predictions (based on percentage of I_{Kr} and I_{CaL} inhibition) with the *ex vivo* data (based on drug concentrations) we calculated the half-maximal inhibitory concentrations and Hill coefficients characterising the tested drugs using two datasets: CiPA and Pharm. Despite some minor differences in IC_{50} values, the results with both datasets are mostly in alignment.

Predictions of ΔAPD_{90} by the TP-like models were closer to the experimental values for mixed inhibition of I_{Kr} and I_{CaL} but were less accurate for selective I_{Kr} and selective I_{CaL} inhibitors. Overall, the error measure for ΔAPD_{90} prediction was lower for TP-like models, the lowest error being obtained for predictions by the TP model with the Pharm dataset.

Mann *et al.* (2016) showed that rescaling maximal conductance parameters of the TP and GPB models and adding a component for I_{NaL} increases substantially their sensitivity to I_{Kr} reduction while preserving the compensating effects on ΔAPD_{90} of inhibition of I_{Kr} and I_{CaL}. As a conclusion, the TP and GPB-M models are most promising as base models for prediction of ΔAPD_{90} response to I_{Kr} and/or I_{CaL} inhibition, and subsequent QT changes.

5.4.2 Model differences

Several models used in this comparative study were trained or validated against previous experimental data for APD_{90} prolongation after I_{Kr} inhibition (O'Hara *et al.*, 2011; Grandi *et al.*, 2010; Tomek *et al.*, 2020; Mann *et al.*, 2016; Krogh-Madsen *et al.*, 2017; Bartolucci *et al.*, 2020). Experimental data on APD_{90} shortening with selective I_{CaL} reduction was included in the development of the BPS, ORd and ToR-ORd models. As we might therefore expect, ΔAPD_{90} predictions by these models are in qualitative agreement with the experimental APD_{90} response to selective I_{Kr} and selective I_{CaL} inhibitors (Section 5.3.2).

For instance, ΔAPD_{90} predictions of the ORd model were validated in response to 70% I_{Kr} inhibition in guinea pig (Sanguinetti & Jurkiewicz, 1990) and to 90% I_{CaL} inhibition in rats (Walsh *et al.*, 2007). ΔAPD_{90} predictions of the GPB model were validated against 100% I_{Kr} inhibition data in isolated human cardiomyocytes (Jost *et al.*, 2008). Models by Mann *et al.* (2016) were calibrated so that their ΔAPD_{90} predictions match with clinical QT data observed in long QT syndrome (LQTS) patients that included a subpopulation with 50% I_{Kr} reduction.

The ORd-like models predictions of ΔAPD_{90} in the case of simultaneous I_{Kr} and I_{CaL} inhibition had not been checked. They fail to reproduce experimental observations and predict I_{Kr}-inhibition dominated prolongation of APD_{90} where *ex vivo* data show mitigation by I_{CaL} inhibition. This shows the importance of the strict definition of the context of use of AP models and matching criteria for model validation (Li *et al.*, 2020). For instance, the ORd-CiPA model with its marker Q_{net} was validated for the classification of drugs into TdP risk categories defined under the CiPA paradigm (Li *et al.*, 2019), but it fails to accurately predict changes in AP morphology after simultaneous inhibition of I_{Kr} and I_{CaL}. With similar arguments, the BPS model was validated for APD_{90} response to 100% I_{CaL} inhibition, but it cannot be used to predict the APD_{90} response to milder inhibition of I_{CaL}.

The TP model was not trained on or validated against data for APD_{90} response to current reduction, but it interestingly yielded a low error measure ($E = 79.0$–87.0). However, the TP model was not able to accurately reproduce the substantial APD_{90} increase induced by 100 nM Dof (+26 ms predicted vs $+256 \pm 67$ ms experimentally). This

is partially explained by the maximal conductance of the slow delayed rectifier K^+ current (I_{Ks}) which is between 20 and 350 times higher in the TP model ($0.392\,mS{\cdot}\mu F^{-1}$) than in the ORd-like models (from $0.0011\,mS{\cdot}\mu F^{-1}$ in ToR-ORd to $0.0196\,mS{\cdot}\mu F^{-1}$ in ORd-M). Given the important contribution of I_{Ks} to the AP in the TP model, this model therefore has more repolarisation reserve (Roden, 1998) than ORd-like models, and the predicted ΔAPD_{90} is limited even under 100% I_{Kr} inhibition as I_{Ks} takes over.

The fact that we observe surprising behaviour is problematic for the reuse of cardiac AP models in new situations such as studies of drug block. Our work points to the need for a more rigorous examination of what behaviours each model exhibits and a careful description of their capabilities. To that end, Cooper *et al.* (2016) have developed the Cardiac Electrophysiology Web Lab where the behaviour of any model that is available in CellML format can be examined under a wide range of experimental protocols.

5.4.3 ΔAPD_{90} as a marker for proarrhythmic risk prediction

Passini *et al.* (2017) compared ΔAPD_{90} with occurrence of repolarisation abnormalities (RAs) to classify a drug's TdP risk, both metrics being predicted with parameter samples based on the ORd model (81% and 89% accuracy based on ΔAPD_{90} and occurrence of RAs, respectively). Our results concur with the conclusion that a TdP risk metric based on ΔAPD_{90} predictions of the ORd model would be inaccurate, because these predictions were incorrect for drugs inhibiting simultaneously I_{Kr} and I_{CaL} (Figures 5.3 and 5.5). However, accurate ΔAPD_{90} predictions may still be useful for TdP risk assessment.

Quinidine- and Verapamil-induced ΔAPD_{90} is consistent with their effects on QT_c and JT_{peak} intervals on the ECG (Johannesen *et al.*, 2014). This suggests that drug-induced ΔAPD_{90} at cellular level is in good agreement with organ-level markers for cardiac safety. Our new *ex vivo* data suggest that, with sufficient I_{CaL} inhibition, compounds at concentrations even higher than their I_{Kr} IC_{50} can leave APD_{90} (and therefore the QT and JT_{peak} intervals) unchanged, at least under the assumption that the compound affects the electrophysiology of cardiomyocytes only through independent I_{Kr} and I_{CaL} inhibition. Such situations correspond to differences between the ICH S7B (high risk associated with blockade of I_{Kr}) and ICH E14 (low proarrhythmic risk associated with

no change in QT interval) guidelines, hence potentially explaining false positives in pre-clinical proarrhythmic risk assessment (Vargas *et al.*, 2021). Reliably identifying which combinations of inhibition of I_{Kr} and I_{CaL} do not prolong APD_{90}, and how this relates to ECG intervals, would open the way to the development of compounds that would be incorrectly deemed proarrhythmic with a hERG-centric safety assessment. For instance, De Ponti (2008) reported that new chemical entities, selected for their physico-chemical properties and/or affinity for a therapeutic target, inhibited I_{Kr} in 60% of all cases, usually leading to their development being discontinued. This vast number of abandoned chemical entities may well have included useful compounds with an inhibitory effect on I_{CaL} that mitigated their TdP risk. It should be borne in mind that in the development of such drugs, the effect on blood pressure and myocardial contractility induced by I_{CaL} inhibition would still require attention.

A 2-D map similar to the ΔAPD_{90} maps for the 11 models was computed for Q_{net} (Li *et al.*, 2019). The region on the Q_{net} 2-D map corresponding to the low TdP risk category exhibited qualitative agreement with the combinations of I_{Kr} and/or I_{CaL} leading to $\Delta APD_{90} < 0$ ms experimentally, computed from the CiPA dataset. This supports the idea that ΔAPD_{90} is relevant to predict the cardiac safety of drugs inhibiting I_{Kr} and I_{CaL}.

The CiPA methodology relies on a reference set of 12 training and 16 validation drugs (Li *et al.*, 2020), classified into 3 TdP risk categories based on empirical expertise (Colatsky *et al.*, 2016). Other lists of reference compounds exist, with different TdP risk classification criteria (Woosley & Romer, 1999; Redfern *et al.*, 2003), and have been used to develop TdP risk prediction models (Romero *et al.*, 2018; Llopis-Lorente *et al.*, 2020; Sahli-Costabal *et al.*, 2020). Future work could compare Q_{net}- and ΔAPD_{90}-based classification of these reference lists. Agreements and disagreements between the different measures could lead to valuable new insights.

5.4.4 Study limitations

The tested compounds were assumed to only affect I_{Kr} and I_{CaL}, although literature data suggests that they may affect other ionic currents as well (Van Dyke & Scharschmidt, 1987; Zhang & Hancox, 2002; Kramer *et al.*, 2013; Crumb Jr *et al.*, 2016; Li *et al.*,

2019; Barthmes, 2021). Furthermore, the kinetics of drug binding to ion channels may require a more complex model than the simple Hill equation (Eq. 5.1) used in this work (Milnes *et al.*, 2010). Refining these modelling assumptions with additional data would enable better integration of the *in vitro* measurements into *in silico* predictions of the response to drug perturbations.

Most of the data were generated with drugs that have mixed inhibitory effects on I_{Kr} and I_{CaL}: Chlorpromazine, Clozapine, Mesoridazine, Quinidine, Thirodazine and Verapamil. By design, the experimental ΔAPD_{90} response to these selected drugs was often close to 0 ms despite I_{Kr} block. With such data, we emphasised the borderline cases of APD_{90} prolongation, which are more important and frequent in drug development. Therefore the error measure, E, favours models that reproduce the little prolongation of APD_{90} in response to mixed I_{Kr} and I_{CaL} inhibition. In the extreme case, an AP model predicting ΔAPD_{90}=0 ms for all combinations of I_{Kr} and I_{CaL} inhibition would score only 59.0, thus outperforming all the AP models considered in this study. Therefore, E as defined in Eq. 5.2 only enables limited comparison of the models. The 2-D maps of ΔAPD_{90} prediction (Figure 5.3) and of prediction errors (Figure 5.4) should be combined with E (Eq. 5.2) to enable the evaluation of the performance of the models and identification of the most promising base models for further development.

Concentration measurements were available only for half of the tested trabeculae. *Ex vivo* ΔAPD_{90} data points were relocated to different positions, as drug concentrations in the bath solution were usually lower than the nominal concentrations (Table 4.8). Therefore, E computed for the predictions of each *in silico* AP model (Eq. 5.2) was changed. Yet, small differences were observed in the fitted quadratic surface in Chapter 4, and the comparison with AP model predictions yielded similar results (Section C.1 in the Appendix). Therefore, the use of nominal concentrations instead of measured drug concentrations in the bath solution did not impact the interpretation of the present results.

5.5 Conclusion

This Chapter evaluates how *in silico* AP models capture the effects of I_{Kr} and I_{CaL} inhibition on changes in APD_{90}. The predictions of the ORd-like models matched the

experimental APD_{90} response to single-current inhibition, but showed strong deviation from ΔAPD_{90} induced by simultaneous inhibition of I_{Kr} and I_{CaL}. In contrast, TP-like models reproduced the APD_{90} response to concomitant inhibition well, while their predictions of response to single-current inhibition were incorrect. There is room for improvement of predictions of drug-induced ΔAPD_{90}, and of subsequent QT changes, by AP models. Mann *et al.* (2016) showed for example that the low sensitivity of TP-like and GPB-like models to inhibition of I_{Kr} can be improved.

An AP model that accurately predicts drug-induced effects on APD_{90}, in particular the response to multi-ion channel inhibition, would greatly assist the integration of *in vitro* experiments and *in silico* tools in the pharmaceutical industry, leading to enhanced pre-clinical predictions of the cardiac safety assessment of new compounds which tend to exhibit mixed I_{Kr} and I_{CaL} inhibition. To construct and calibrate such an AP model, the TP and the GPB-M models seem reasonable starting points, given their qualitative agreement with experimental ΔAPD_{90} data and low error measure.

Using the normalised whole AP traces acquired in each trabecula, trabecula-specific models could be calibrated to the *ex vivo* data — this is the purpose of Chapter 7. However, before calibrating trabecula-specific models, which parameters to calibrate should be carefully selected, as discussed in Chapter 6. In particular, the impact of model discrepancy on parameter selection will be investigated, showing that, for optimal model predictions, not all parameters that can be calibrated should necessarily be calibrated.

Acknowledgements

We thank Dr. Bartolucci and Dr. Severi for their help in implementing the Bartolucci *et al.* (2020) model.

6

Goodness-of-fit versus model predictivity, or parameters that could versus should be calibrated

Preamble

Novel action potential (AP) data were generated ex vivo in different human ventricular trabeculae under conditions with drug-induced inhibition of the rapid delayed rectifier K^+ current (I_{Kr}) and of the L-type Ca^{2+} current (I_{CaL}), as described in Chapter 4. In Chapter 5 it was shown that no AP model reproduces the resulting changes in the AP duration (APD) accurately. In principle, AP models can be used to integrate in vitro measurements into predictions of AP response and subsequent cardiac safety, but this requires careful model calibration. The new ex vivo data could be used to calibrate trabecula-specific models, but the question of which parameters to calibrate arises. In this Chapter, we investigate different aspects of the calibration of individual-specific models, with and without model discrepancy, using the example of an AP model calibrated to predict individual-specific APD changes induced by I_{Kr} and I_{CaL} inhibition.

A manuscript based on the contents of this Chapter is being prepared for journal submission.

6.1 Introduction

Electrophysiological parameters can vary from cell to cell, notably the level of expression of genes encoding ion channels (Schulz *et al.*, 2006) and the size/capacitance of each cell. AP models that do not include these variations are likely to predict an individual's response to a perturbation incorrectly, so there is a need for individual-specific models (Groenendaal *et al.*, 2015). Inter-individual variability (IIV) can be estimated with populations of models by identifying a range of parameter values that produce model outputs within a range of experimental observations, e.g., Britton *et al.* (2017). Alternatively, cell-specific models can be directly calibrated to data of individual cells, e.g., Groenendaal *et al.* (2015).

With the objective of calibrating trabecula-specific models to Chapter 4 data in Chapter 7, the objective of the present Chapter is to investigate pitfalls to avoid when individualising an AP model to AP data recorded in a given trabecula.

Here, we identify three important aspects of the calibration of individual-specific AP models: inter-individual parameter variation, the choice of parameters to calibrate, and the need to consider model discrepancy during the calibration of (individual-specific) models. This Chapter is composed of three parts that address each aspect separately.

6.1.1 Aspect I: Inter-individual variability impacts action potential model outputs, and can be estimated from RNA sequencing data

In AP models, a maximal conductance (or permeability) parameter is associated with each ionic current and acts as a scaling factor (Eq. 2.3). This parameter is directly proportional to the number of functional ion channels of a particular type that are present in the membrane of a particular cell, which is itself linked with the expression of the associated ion channel genes (Schulz *et al.*, 2006). Although these expression levels are known to vary from cell to cell, and to fluctuate over time, AP models are commonly formulated with a single, fixed set of parameter values for the maximal conductances.

In this study, we use experimental RNA sequencing data (RNA-Seq) available in the GTEx Portal to estimate the IIV in ion channel expression, with the "individuals" corresponding to tissue samples from different donors. This IIV is then used as a proxy for the IIV in conductance parameters. By running AP simulations with conductance

parameter values representing this variability in mRNA expression, we then estimate the resulting variability in model outputs.

6.1.2 Aspect II: Selection of parameters to individualise to maximise model predictivity

During the development of individual-specific AP models, only a small number of parameters in a model are typically individualised (e.g., maximal conductances), with the remainder (e.g., those controlling ion channel kinetics) assumed to be fixed. This raises questions concerning the *achievable* and the *required* "level of individualisation" necessary to ensure reliable and accurate predictions (Clerx, 2018; Galappaththige *et al.*, 2022). In other words, "what parameters can be individualised?" and "what parameters should be individualised?".

Various methods have been developed to verify which parameters *can* be individualised based on their *practical identifiability*, i.e., assessing whether there is an acceptable uncertainty in model parameter estimates found by the calibration to a given dataset (Whittaker *et al.*, 2020), and these have been previously applied to cardiac AP models (Groenendaal *et al.*, 2015; Johnstone *et al.*, 2016; Nieto Ramos *et al.*, 2022). The parameters which *should* be individualised to maximise model predictivity are more rarely discussed. In particular, a subtle counterpart to the selection of parameters which should be individualised is the impact of not individualising the remaining parameters (Figure 6.1). The risk of omitting the variability in these non-individualised parameters during model calibration is to underestimate the uncertainty in model predictions (Galappaththige *et al.*, 2022).

In this study, we develop a method to select parameters that *can* and *should* be individualised, accounting for "parametric variability" (Kennedy & O'Hagan, 2001), that is, the variability in parameters that are (incorrectly) assumed to be fixed during model calibration (Figure 6.1C).

To do so, we use "synthetic AP data" generated from a published model. This approach allows us to study realistic situations but where the ground truth is known (Whittaker *et al.*, 2020). The model is trained by finding estimates of the individualised parameters using a range of values for the non-individualised parameters. The uncertainty

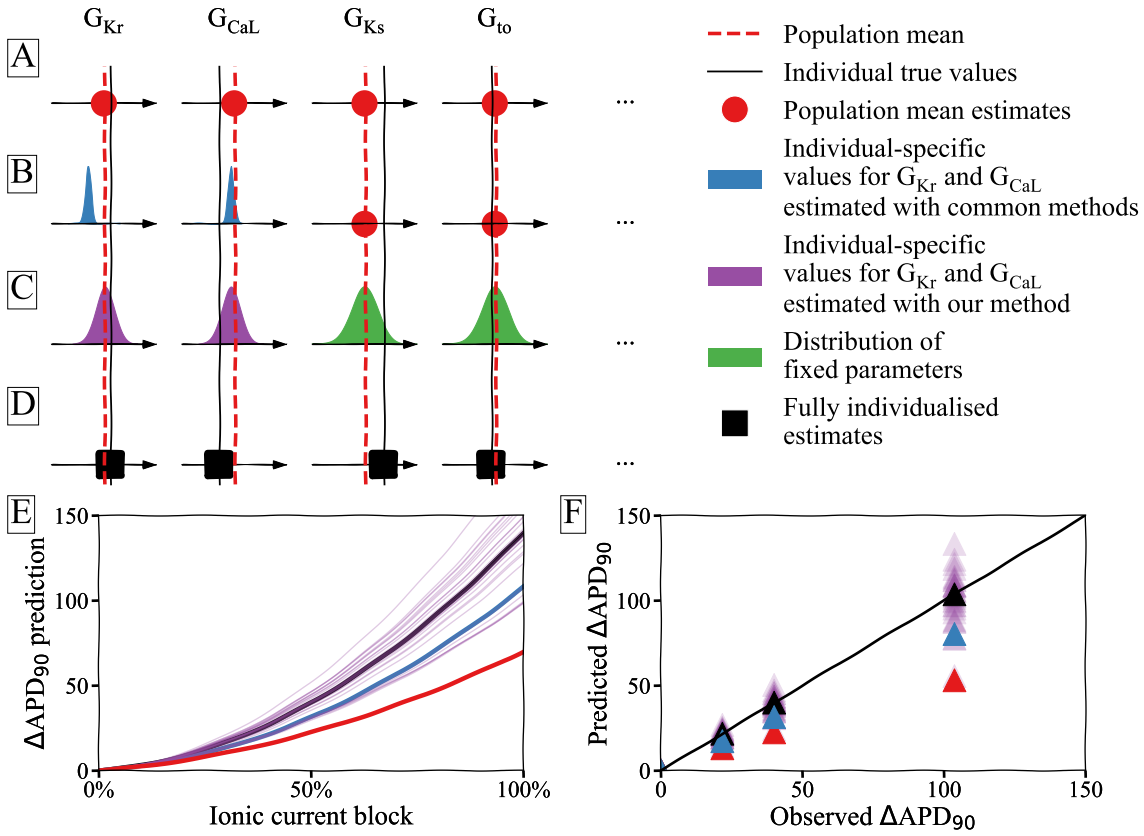

Figure 6.1: **A:** In a non-individualised model, generic parameter values represent the whole population **(red circles)**. **B:** Individuals differ from the mean, as partially captured by individualising G_{Kr} and G_{CaL} **(blue distributions)**. In this example, individual-specific parameter estimates are obtained under the assumption that non-individualised parameter values (for G_{Ks}, G_{to}, and other conductance parameters) are correct. **C:** In this study, prior knowledge on the variability in G_{Ks}, G_{to}, and other conductance parameters is included **(green distributions)** when individualising G_{Kr} and G_{CaL} **(purple distributions)**. **D:** When the correct parameters are individualised to their correct values **(black squares)**, the model captures the individual's features of interest perfectly. However, sufficient data to individualise all parameters are rarely available, so that the case of panel C merits investigation. **E:** Hypothetical predictions of ΔAPD_{90} response to ionic current inhibition, for the hypothetical models described in panels A–D, using matching colours. **F:** Comparison of ΔAPD_{90} observations in the individual of interest with predictions for the model individualised as described in panels A–D, using matching colours. Predictions of the correct individual-specific model are on the 1:1 line **(in black)**. Note that all panels show sketches, for illustrative purposes only.

induced in individualised parameters is thereby estimated, and its impact on model predictions is evaluated in a model validation step. By comparing the predictions of the model at increasing levels of individualisation, we identify the parameters that *should* be individualised to achieve the maximal predictivity.

Finally, we compare our method with the Bayesian Information Criterion (BIC) (Schwarz, 1978), which has been used to address similar questions (Neath & Cavanaugh, 2012).

6.1.3 Aspect III: Model discrepancy limits the accuracy of parameter estimation and thereby model predictivity

The considerable diversity in existing models for adult human ventricular APs suggests that the biophysical principles governing the ionic currents are still not fully understood (Agrawal *et al.*, 2023), and that their mathematical representations are in fact imperfect despite the considerable efforts put into their modelling. For example, in the O'Hara *et al.* (2011) model reformulated by Dutta *et al.* (2017) (ORd-CiPA), the kinetic term ($\mathcal{K}$ in Eq. 2.3) of I_{Kr} is described using a 6-state Markov model, whilst the Ten Tusscher & Panfilov (2006) (TP) model describes it with two voltage-dependent gating variables using the Hodgkin-Huxley formalism.

"Model discrepancy" (or "model misspecification") arises (Lei *et al.*, 2020) in situations where model outputs cannot be matched with the real mechanism underlying experimental data for any set of parameter values (see Figure 6.2). So whilst a model is tailored to an individual, this can be done with an incorrect mechanism and/or parameters, leading to a poorly-predictive individual-specific model. Model discrepancy therefore limits the predictivity of models (Whittaker *et al.*, 2020), and should be considered when developing individual-specific AP models.

In this study, we use simulation studies with multiple cardiac AP models to investigate how model discrepancy may limit the development of individual-specific models in real world cases. We use simulation results from the Grandi *et al.* (2010) (GPB) and the ORd-CiPA models to generate synthetic AP datasets, under various conditions of I_{Kr} and I_{CaL} inhibition. We then calibrate the TP model to each dataset separately. In doing

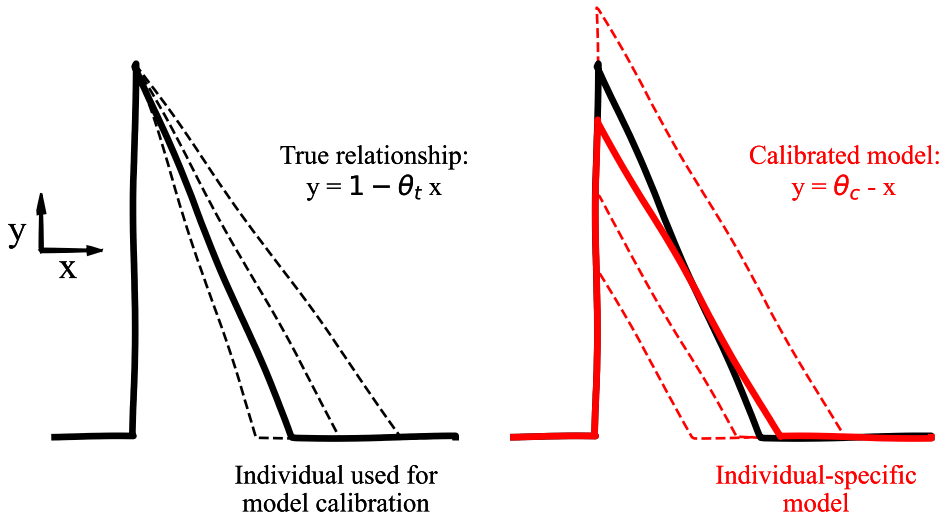

Figure 6.2: Sketch illustrating model discrepancy with models of "triangle APs". The true relationship between x and y allows different slopes for different individuals **(black dashed lines)**, and data for model calibration are obtained from a particular individual **(solid black line)**. In the calibrated model with model discrepancy, the slope is erroneously fixed to 1 but the maximal height of the triangle AP (θ_c) is variable (**dashed red lines**). The model is individualised by finding the value for θ_c which minimises the mismatch between the data and model outputs **(solid red line)**.

so, we are able to investigate the influence of model discrepancy on the predictivity of a calibrated AP model, and on the selection of the optimal set of parameters to individualise.

6.2 Part I: Inter-individual variability impacts action potential model outputs, and can be estimated from RNA sequencing data

RNA sequencing (RNA-Seq) is a technique to measure the expression of genes encoding selected proteins. In this section, we use RNA-Seq of genes associated with ion channels, pumps, and exchangers to estimate the IIV in the associated conductance parameters (Schulz *et al.*, 2006). We then feed the IIV in parameters into the TP model to estimate the IIV in AP features, such as APD_{90} under baseline conditions and with inhibition of selected ionic currents.

6.2.1 Methods

Estimation of individual-specific conductance parameters from RNA sequencing data

In the GTEx portal, RNA-Seq data for level of gene expression (in log of protein transcripts per million mapped reads, pTPM) are reported for aliquots of the left anterior ventricle taken from 303 donors with no evidence of disease. The Transcript pTPM dataset was downloaded from the GTEx Analysis v7 (https://www.gtexportal.org/home/datasets) and processed following the ReCount2 protocol (Collado-Torres *et al.*, 2017). RNA-Seq data processing was performed by colleagues in Roche.

In RNA-Seq experiments, the level of expression may be impacted by variations in input samples, RNA extraction, reverse transcription, and other factors (Dheda *et al.*, 2004). To address these limitations, the RNA-Seq data were normalised using a *housekeeping gene*. We used YWHAZ encoding 14-3-3 protein zeta/delta, which has been shown to be stably expressed in left ventricle cardiomyocytes (Molina *et al.*, 2018).

Published values for conductance parameters were assumed to correspond to the mean level of expression of the corresponding gene (Schulz *et al.*, 2006). The value of the conductance (or permeability) parameter in an individual i (G_i) was therefore obtained by multiplying the original value for the conductance parameter ($\bar{G}$) by the relative abundance of the RNA transcripts, normalised to the relative level of expression of YWHAZ:

$$G_i = \bar{G} \times \frac{\mathcal{G}_i}{\mu_{\mathcal{G}}} \times \frac{\mu_{\mathcal{H}}}{\mathcal{H}_i} = \bar{G} \times e^{\hat{\mathrm{g}}_i}, \tag{6.1}$$

with $\mathcal{G}_i$ the level of expression of the gene associated with the ionic current (in pTPM) in the individual i and $\mu_{\mathcal{G}}$ its mean across the 303 samples, $\mathcal{H}_i$ the level of expression of the housekeeping gene YWHAZ (in pTPM) in the individual i and $\mu_{\mathcal{H}}$ its mean across the 303 samples, and $\hat{\mathrm{g}}_i$ the (log-transformed) scaling factor corresponding to i. Formulating the scaling in terms of the log-transformed factor $\hat{\mathrm{g}}$ applied to $\bar{G}$ facilitates the comparison between conductance parameters of different ionic currents in Figure 6.3 further down.

To estimate $\hat{\mathrm{g}}$ for each current, the level of expression of the gene encoding the α-subunit of the corresponding ion channel, pump, or exchanger was used where possible. For the transient outward K^+ current (I_{to}), the genes KCND3, KCND2 and KCNA4

were considered, but KCND2 and KCNA4 exhibited low levels of expression, close to the limit of quantification. Therefore, variations of G_{to} were estimated from the RNA-Seq data for KCND3. Note that KCND3 has been associated with a fast component of I_{to} (Frank-Hansen *et al.*, 2005), but the TP model does not distinguish between fast and slow components of I_{to}.

Data for genes corresponding to 8 ionic currents were available in the RNA-Seq dataset (Table 6.1). In the present work, IIV was considered only in the conductance parameters of these 8 currents, which we call "adjustable" parameters in the following.[1] The contribution to the AP of these currents is discussed in Section 2.3.1.

Individual-specific values for the 8 adjustable conductance parameters were estimated to create 303 "digital twins".

Note that the expression "digital twin" usually encompasses "a physical entity, a virtual counterpart, and the data connections in between" (Jones *et al.*, 2020). In this work, the data connection between the donors and their virtual counterparts (the vectors of parameters, Φ, derived from the RNA-Seq data) was missing. To emphasise that the Φ were used to model real donors, the denomination of "digital twins" was used nevertheless.

Current	I_{Kr}	I_{CaL}	I_{Ks}	I_{K1}	I_{Na}	I_{NaCa}	I_{NaK}	I_{to}
Primary gene	KCNH2	CACN1A1	KCNQ1	KCNJ2	SCN5A	SLC8A1	ATP1A1	KCND3
Parameter	G_{Kr}	G_{CaL}	G_{Ks}	G_{K1}	G_{Na}	G_{NaCa}	G_{NaK}	G_{to}

Table 6.1: List of genes used to estimate the IIV in parameters of the TP model. The 8 parameters in this table are referred to as "adjustable" conductance parameters.

Inter-individual variability simulated with the TP model

The variability in APs resulting from the IIV in conductance parameters was simulated with the TP model. The epicardial variant of the the TP model (Ten Tusscher & Panfilov, 2006) was downloaded from the Physiome Model Repository (Yu *et al.*, 2011) in CellML

[1] I_{CaL}, I_{NaCa}, and I_{NaK} are characterised by permeability parameters in the TP model, respectively expressed in cm/s, A/F, and A/F, in contrast with the remaining ionic currents characterised by conductance parameters expressed in mS/μF. The permeability parameters G_{CaL}, G_{NaCa}, and G_{NaK} serve as scaling constants for the associated currents in the same way as the conductance parameters. The scaling of permeability parameters will therefore be undertaken identically to the conductance parameters in the following.

format. The voltage equation of the TP model was rewritten in its algebraic form to make explicit the algebraic constraint on the ionic concentrations resulting from the conservation of charge principle (Chapter 3).

Simulations were run with the Python package Myokit 1.33.7 (Clerx *et al.*, 2016) using CVODE 5.7.0 (Hindmarsh *et al.*, 2005). Absolute and relative solver tolerances were both set to 10^{-8}.

The model was paced with steady 1 Hz frequency, with the stimulus currents as defined in the CellML models: -52 A/F for 1 ms. For each simulation, 500 pre-paces were simulated to bring the TP model close to its limit cycle (see Section D.1 in the Appendix). After pre-pacing, simulated APs were recorded at a resolution of 0.05 ms, matching the resolution of the *ex vivo* data (Chapter 4).

Inhibition of I_{Kr} and I_{CaL} was modelled as the application of an *additional* scaling factor to the ionic current, ranging between 1 (no inhibition) and 0 (100% inhibition):

$$I_{inhib} = (1 - f) \times I_{baseline}, \tag{6.2}$$

with f the fraction of inhibition, $I_{baseline}$ and I_{inhib} the ionic current under baseline (no inhibition) and inhibited conditions, respectively.

APs were simulated using the individual-specific values for conductance parameters estimated from the RNA-Seq data for the 303 digital twins (Eq. 6.1), under baseline and 90% I_{Kr} inhibition conditions. Three AP markers were extracted from APs simulated under baseline conditions, namely the APD_{90}, the resting membrane potential (RMP) and the peak voltage (V_{peak}). They were used to identify models for digital twins yielding pathological and non-pathological APs. Criteria for non-pathological APs were defined as follows:

$$\begin{aligned} 200 \text{ ms} \leq APD_{90} \leq 500 \text{ ms}, \\ RMP \leq -65 \text{ mV}, \\ V_{peak} \geq 0 \text{ mV}. \end{aligned} \tag{6.3}$$

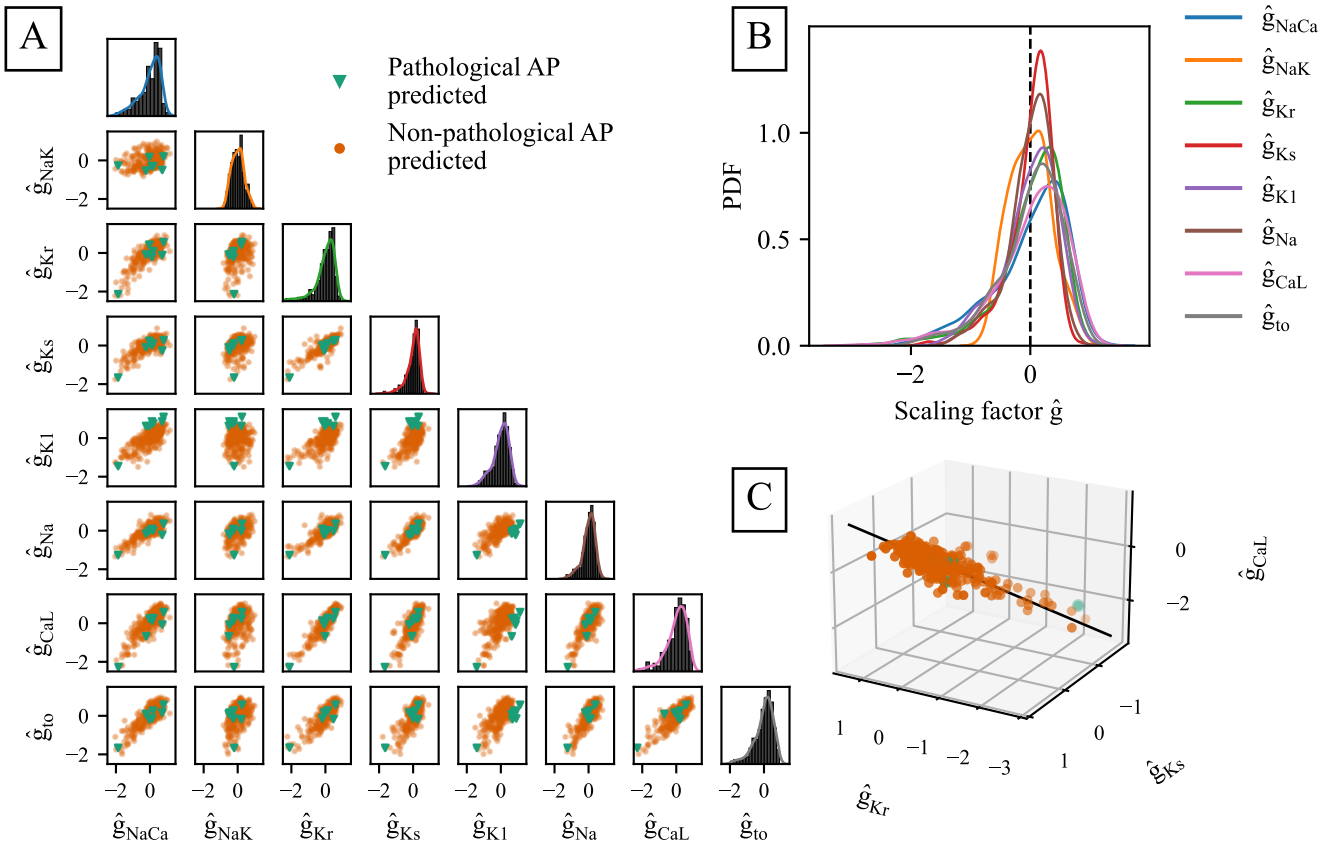

Figure 6.3: IIV in scaling parameters, estimated from RNA-Seq data. **A:** Diagonal subplots show the distribution of the scaling factors, $\hat{g}$. Non-diagonal subplots show the pairwise correlations between $\hat{g}$ associated with different currents. Each point corresponds to the log-transformed scaling factor for one of the 303 digital twins. **B:** Kernel density estimates of the distributions of scaling factors compared in a single plot. The digital twins $\Phi_{\text{data},1}$ and $\Phi_{\text{data},2}$ will be used in Part II of this Chapter.

6.2.2 Results

The values of $\hat{g}$ calculated for each of the digital twins are shown in Figure 6.3.

In Figure 6.3A, the pairwise plot of $\hat{g}$ is shown and $\hat{g}_{\text{NaCa}}$, $\hat{g}_{\text{Kr}}$, $\hat{g}_{\text{Ks}}$, $\hat{g}_{\text{K1}}$, $\hat{g}_{\text{Na}}$, $\hat{g}_{\text{CaL}}$, and $\hat{g}_{\text{to}}$ were correlated to one another. The distributions of scaling factors for the individual maximal conductance parameters are compared in Figure 6.3B. They exhibited notable similarities, and the scaling factors for all 8 currents were within $[e^{-2.5};e^{+1.5}]$, i.e., within a factor [0.08;4.48] of the original value.

The APs simulated under baseline and 90% I_{Kr} inhibition for each of the 303 digital twins are shown in Figure 6.4.

Predicted baseline APs (Figure 6.4A) varied considerably between the digital twins.

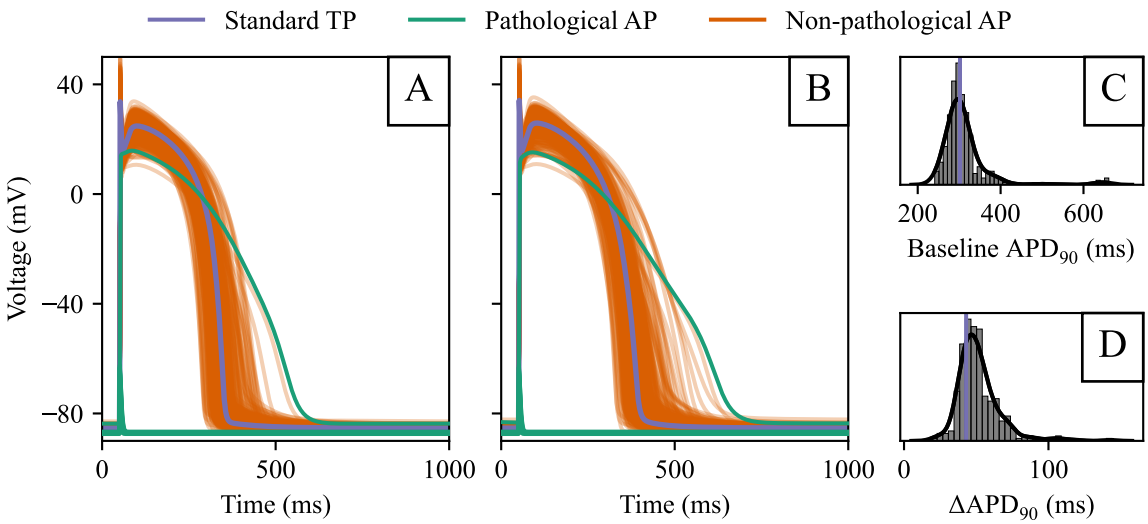

Figure 6.4: APs simulated with the models for the 303 digital twins. Criteria for pathological APs are given in Eq. 6.3. In **purple**, outputs of the standard TP model for reference. **A:** Baseline APs. **B:** APs simulated with 90% I_{Kr} inhibition. **C:** Distribution of the predicted baseline APD_{90}. **D:** Distribution of the predicted APD_{90} change from baseline (ΔAPD_{90}) induced by 90% I_{Kr} inhibition.

The upper and lower 95th percentiles of predicted baseline APD_{90} were 261 ms and 390 ms, respectively, and the median of predicted baseline APD_{90} was 303 ms (Figure 6.4C). The standard deviation of the baseline APD_{90} was 33 ms.

Despite the substantial variability in model outputs, the models for 296 out of 303 digital twins predicted non-pathological APs (Eq. 6.3). Scaling factors of the models for the 7 digital twins predicting pathological APs (Figure 6.3A) were not obvious outliers, but they correspond to extreme $\hat{g}_{K1}$ values. The models for these 7 digital twins were excluded in the following.

With 90% I_{Kr} inhibition, the simulated APs for the 303 digital twins were visibly more spread than under baseline conditions (Figure 6.4B). Indeed, ΔAPD_{90} predictions vary between the digital twins (Figure 6.4D), with the upper and lower 95th percentiles of predicted ΔAPD_{90} being +36 ms and +74 ms, respectively.

6.2.3 Discussion

In clinical drug safety testing, a 5 ms mean prolongation of the ventricular repolarisation time is considered significant (ICH, 2006). Because changes in ventricular APD_{90} are

linked with changes in the ventricular repolarisation time (Johannesen *et al.*, 2014), our results show that the IIV in response to I_{Kr} inhibition represents a significant variation that supports the need for individual-specific AP models.

Furthermore, if not all conductance parameters can be individualised, which is often the case, the variability in non-individualised parameters introduces parametric variability into the calibration of individual-specific models (Figure 6.1). The impact of the parametric variability on the model calibration process is investigated in Part II, using the IIV estimated from RNA-Seq.

6.3 Part II: Selection of parameters to individualise to maximise model predictivity

Individual-specific AP models are particularly useful in examining the consequences of IIV in conductance parameters, estimated in Part I. When developing individual-specific models, choices are made concerning the parameters that are individualised. In Part II, we investigate the impact of these choices on the calibration of an individual-specific model.

We consider the case where AP data were collected in a random individual corresponding to one of the digital twins created in Part I, that we denote $\Phi_{\text{data},1}$ (Figure 6.3A). We calibrate an individual-specific version of the TP model to $\Phi_{\text{data},1}$ data, to predict the APD_{90} response of $\Phi_{\text{data},1}$ to inhibition of I_{Kr} and I_{CaL}. Different sets of parameters are individualised to $\Phi_{\text{data},1}$ data, and the predictivity is assessed for each of these attempts at calibrating a $\Phi_{\text{data},1}$-specific model. By comparing the predictivity obtained with different sets, the best set of parameters to individualise for $\Phi_{\text{data},1}$ is identified. We then compare this method with an existing tool commonly used to select parameters to calibrate, the Bayesian Information Criterion (BIC, Schwarz (1978)).

Here, we assume that the adjustable parameters (and only them) can vary between individuals. The adjustable parameters that are not individualised, called "non-individualised" parameters, may therefore be fixed to "incorrect" values that do not correspond to $\Phi_{\text{data},1}$ during model calibration. To account for this potential error, parametric variability is introduced during the calibration of the $\Phi_{\text{data},1}$-specific model. This is done by fixing

non-individualised parameters to values taken from 30 random digital twins, denoted Φ_1 through Φ_{30}, that cover the range of variation estimated in Part I.

Finally, we investigate whether parametric variability has the same impact on the calibration to data from different individuals. To do so, we repeat this work using a dataset generated in another individual, $\Phi_{\text{data,2}}$ (Figure 6.3A).

6.3.1 Synthetic dataset for $\Phi_{\text{data,1}}$

Table 6.2 summarises the scaling factors, $\hat{g}$ (Eq. 6.1), corresponding to $\Phi_{\text{data,1}}$. The model for $\Phi_{\text{data,1}}$ is created by applying these $\hat{g}$ to the TP model. Note that $\Phi_{\text{data,1}}$ was selected by hand for its scaling factors close to the mode of the distribution of $\hat{g}$ across digital twins (Figure 6.3).

Parameter	$\hat{g}_{\text{Kr}}$	$\hat{g}_{\text{CaL}}$	$\hat{g}_{\text{Ks}}$	$\hat{g}_{\text{K1}}$	$\hat{g}_{\text{Na}}$	$\hat{g}_{\text{NaCa}}$	$\hat{g}_{\text{NaK}}$	$\hat{g}_{\text{to}}$
$\Phi_{\text{data,1}}$	0.41	0.89	−0.13	0.05	0.07	0.66	0.01	0.20

Table 6.2: The scaling factors, $\hat{g}$ (Eq. 6.1), corresponding to $\Phi_{\text{data,1}}$ are applied to conductance parameters of the TP model to generate the $\Phi_{\text{data,1}}$ synthetic dataset.

The *synthetic training and validation* data for $\Phi_{\text{data,1}}$, shown in Figure 6.5, were obtained by simulating the response of the model for $\Phi_{\text{data,1}}$ to various conditions of I_{Kr} and I_{CaL} inhibition.

The *synthetic training* data were generated by simulating 9 consecutive APs after pre-pacing under four conditions with I_{Kr} and I_{CaL} inhibition (Figure 6.5A). This gives a total of $4 \times 9 \times 20{,}000 = 720{,}000$ data points. To mimic realistic experimental conditions, a typical Gaussian noise ($\sigma_y = 0.1$ mV) was added to the synthetic training data (Chapter 4).

The *synthetic validation* data (Figure 6.5B) consist of ΔAPD_{90} values simulated using 55 conditions of I_{Kr} and I_{CaL} inhibition, plus the baseline conditions of no current inhibition. To cover the appearance of alternans, two consecutive APs were simulated, and the one with the longest APD_{90} was used.

6.3.2 Overview of the methods to select parameters to individualise

Using these synthetic data, the impact of the set of individualised parameters on the calibration of the TP model to individual data can be investigated, whilst knowing the model that represents the ground truth for this exercise. An overview of the methods

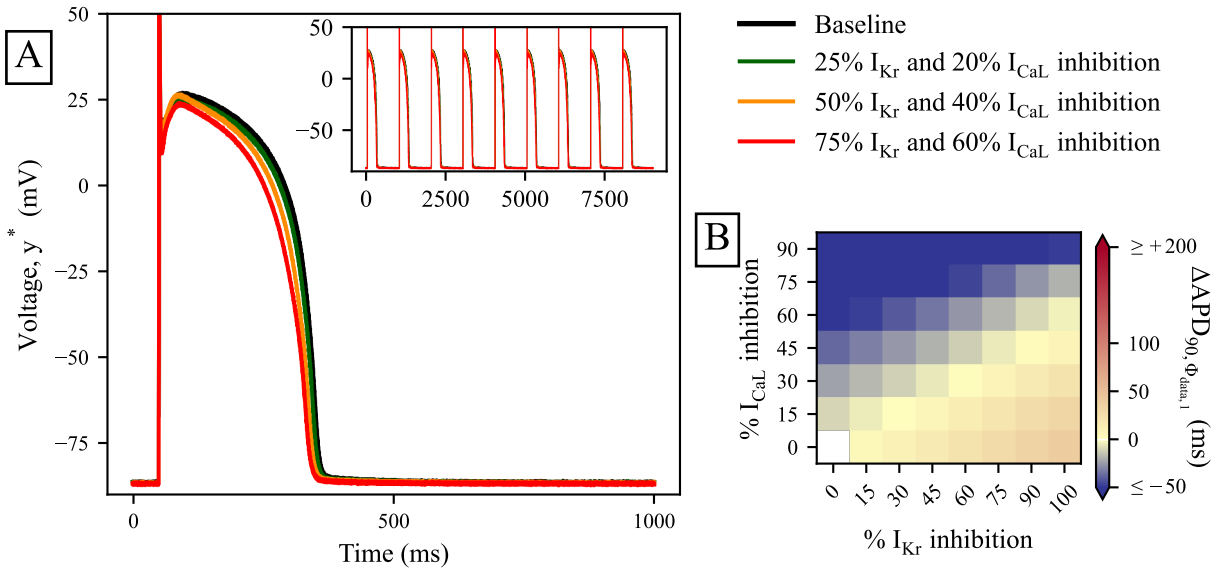

Figure 6.5: Synthetic data generated with the model for $\Phi_{data,1}$. **A:** Synthetic training data simulated under four conditions of I_{Kr} and I_{CaL} inhibition. Insets show the 9 APs constituting the synthetic training data. **B:** Synthetic validation data consisting of ΔAPD_{90} simulated under 56 conditions of I_{Kr} and I_{CaL} inhibition.

used in Part II to assess the predictivity of the TP model calibrated to $\Phi_{data,1}$ data is described in Algorithm 1, and details are provided in the following.

Algorithm 1 Pseudo-code for assessing the predictive power of the TP model calibrated to $\Phi_{data,1}$ data.

Input: Set of parameters to individualise

1: **for** i in 1:30 **do**
2: Fix the non-individualised parameters to their value taken from Φ_i ▷ *Introduce the parametric variability*
3: Estimate the individualised parameters to fit $\Phi_{data,1}$ data by minimising the cost function, $\mathcal{C}$ ▷ *Model training*
4: Compute the signed distance, ϵ, between ΔAPD_{90} predictions and $\Phi_{data,1}$ data under 55 conditions with I_{Kr} and I_{CaL} inhibition ▷ *Model validation*
5: **end for**
6: Compute predictivity metrics ($\mathcal{W}$ and $\mathcal{P}$) from the distribution of ϵ over the 30 Φ ▷ *Model predictivity assessment*

6.3.3 Steps 1–3: Impact of parametric variability on estimates of $G_{\mathbf{Kr}}$ and $G_{\mathbf{CaL}}$

Methods

As per Section 6.1.2 in the Introduction, we describe in this section how individual-specific versions of the TP model are calibrated to individual data, whilst ranges of values are used for the non-individualised parameters.

First, we describe steps 1–3 of Algorithm 1, when G_{Kr} and G_{CaL} were individualised. The remaining adjustable conductance parameters (G_{Ks}, G_{K1}, G_{Na}, G_{NaCa}, G_{NaK}, and G_{to}) were initially fixed to values taken from Φ_1. Therefore, the six non-individualised parameters took (incorrect) values that differ from $\Phi_{\mathrm{data},1}$.

The cost function $\mathcal{C}$ that was minimised during model training was defined as the sum of squared errors between the synthetic training AP data (y^*, Figure 6.5A) and the voltage simulated using four training conditions of $\mathrm{I_{Kr}}$ and $\mathrm{I_{CaL}}$ inhibition c (y_c):

$$\mathcal{C}(\theta) = \sum_{c}^{4\ \mathrm{cond}} \sum_{t} \left(y_c(\theta, t) - y_c^*(t)\right)^2, \tag{6.4}$$

with $y_c(\theta)$ the voltage simulated with the TP model parameterised with θ, and t being time-steps at 0.05 ms resolution.

The estimate of (G_{Kr}, G_{CaL}), θ^*, was found with the optimisation algorithm Covariance Matrix Adaptation-Evolution Strategy (CMA-ES) (Hansen, 2016), implemented in the `PINTS` Python package (Clerx *et al.*, 2019).

The search space for θ was constrained to $-4 < \hat{\mathrm{g}} < +4$, corresponding to multiplying factors for G within [0.02–55] (see Section D.2 in the Appendix).

To increase the confidence that parameter estimates correspond to the global minimum of $\mathcal{C}$, parameter estimation was repeated 10 times from random starting points. Further details on testing parameter identifiability and selection of hyperparameters for tuning the CMA-ES algorithm are provided in Section D.3 in the Appendix.

For reduced values of $\mathrm{I_{Kr}}$ and $\mathrm{I_{CaL}}$ in the TP model, periodic AP patterns of various periods (up to 20 paces and more) were sometimes observed as limit cycles — we called this phenomenon "multi-AP alternans". This phenomenon can lead to chaotic behaviour of the TP model which prevents the correct estimation of individualised parameters.

Therefore, a constraint was added to avoid alternans during model training: $\mathcal{C} = +\infty$ was attributed to parameters leading to alternans. More details on multi-AP alternans and chaotic behaviour of the TP model are provided in Section D.4 in the Appendix.

Repeating the above methods with Φ_2–Φ_{30} instead of Φ_1, a total of 30 estimates for G_{Kr} and G_{CaL} were found and 30 adjusted parameterisations of the TP model were created. The variability between the parameter estimates was used as a proxy for the uncertainty in individualised parameters induced by the parametric variability.

Note that a constraint was set to select only digital twins which generated a physiological AP under baseline conditions (Figure 6.4). Importantly, the digital twins Φ were all different from $\Phi_{\text{data},1}$ and $\Phi_{\text{data},2}$. There were therefore $303 - 7 - 2 = 294$ eligible digital twins. 30 out of 294 digital twins were used as a trade-off between lowering the computational cost and finely covering the ranges of values that non-individualised parameters can take, as investigated in Section D.5 in the Appendix.

Results

The individualised scaling factors $\hat{g}_{\text{Kr}}$ and $\hat{g}_{\text{CaL}}$ corresponding to the estimates of G_{Kr} and G_{CaL} for the 30 adjusted parameterisations of the TP model are shown in Figure 6.6A.

The individualised scaling factors $\hat{g}_{\text{Kr}}$ and $\hat{g}_{\text{CaL}}$ are weakly anti-correlated ($r^2 = 0.26$) and are sensitive to the values for non-individualised parameters. Estimates of G_{Kr} and G_{CaL} are relatively far from values in $\Phi_{\text{data},1}$, in comparison with the size of the search space ($-2.5 < \hat{g} < 2.5$). The uncertainty in estimates of G_{Kr} and G_{CaL} can be estimated as the standard deviation of the individualised scaling factors: $\sigma_{\text{CaL}} = 0.33$ and $\sigma_{\text{Kr}} = 0.58$, respectively. Wide ranges for the scaling factors are also obtained: $\hat{g}_{\text{CaL}} \in [-0.55; +0.62]$ and $\hat{g}_{\text{Kr}} \in [-2.15; +0.87]$. Therefore, it appears that the parametric variability in the 6 non-individualised conductance parameters induces substantial uncertainty and error in estimates of G_{Kr} and G_{CaL}.

The uncertainty in estimates of G_{Kr} and G_{CaL} propagates to the AP simulated under baseline conditions (Figure 6.6B). APD_{90} under baseline conditions predicted by the adjusted parameterisations of the TP model varies between 295 ms and 328 ms.

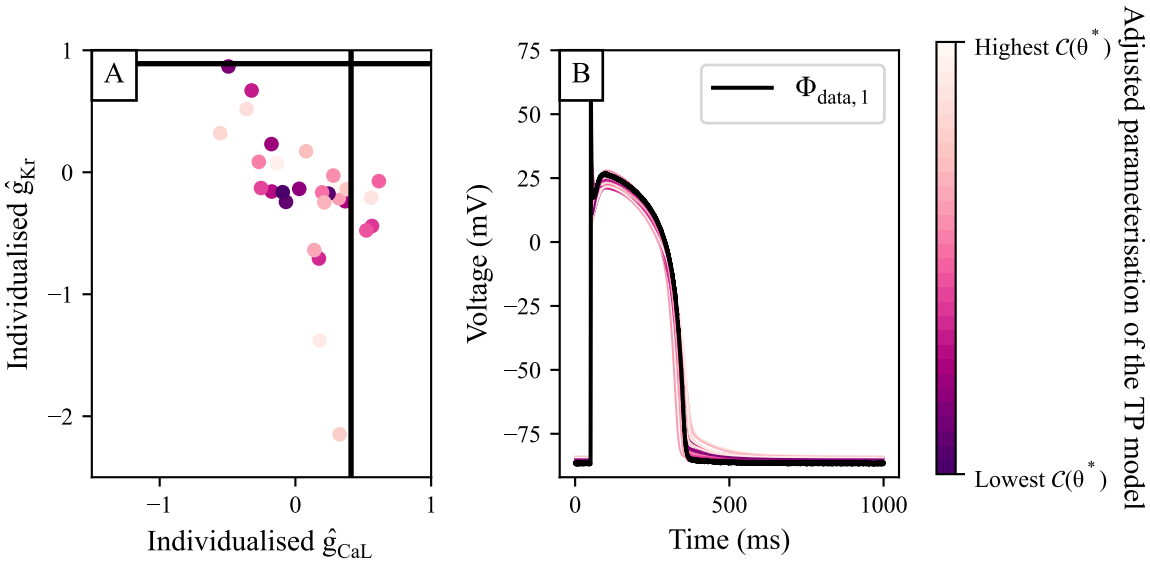

Figure 6.6: Results of model training on $\Phi_{\text{data},1}$ data, individualising G_{Kr} and G_{CaL} with 30 different values for non-individualised parameters (Algorithm 1, step 3). Each colour corresponds to one of the 30 adjusted parameterisations of the TP model. The darker the line, the lower the minimal cost $\mathcal{C}(\theta^*)$. **A:** Individualised scaling factors $\hat{g}_{\text{Kr}}$ and $\hat{g}_{\text{CaL}}$ corresponding to estimates of G_{Kr} and G_{CaL}, respectively. Black lines highlight the values in $\Phi_{\text{data},1}$. **B:** Simulated APs under baseline conditions.

$\mathcal{C}(\theta^*)$ varied between 7.8×10^5 mV^2 and 5.8×10^7 mV^2. Thus, the parametric variability also impacted the achievable goodness-of-fit.

In Figure 6.6, the colour scale indicates $\mathcal{C}(\theta^*)$ for each adjusted parameterisation of the TP model: results for the adjusted parameterisations of the TP model yielding lower $\mathcal{C}(\theta^*)$ are plotted with darker colours. There is no obvious pattern in the parameter estimates: lower $\mathcal{C}(\theta^*)$ is not directly associated with parameter estimates closer to $\Phi_{\text{data},1}$.

6.3.4 Steps 4–6: Impact of parametric variability on model predictivity, with individualised G_{Kr} and G_{CaL}

Methods

Next, the 30 adjusted parameterisations of the TP model were validated, by comparing their ΔAPD_{90} predictions with the synthetic validation data for $\Phi_{\text{data},1}$ (Figure 6.5B).

Simulations were performed under 56 conditions of I_{Kr} and I_{CaL} inhibition (Figure 6.5B), and the ΔAPD_{90} was calculated. Only 55 out of 56 conditions were used for model validation, because ΔAPD_{90} under baseline conditions is 0 ms by definition. Under each of these 55 conditions c, the signed distance between the synthetic validation

data ($\Delta\text{APD}_{90,\ c,\ \Phi_{\text{data},1}}$) and the ΔAPD_{90} prediction by the adjusted parameterisation of the TP model i ($\Delta\text{APD}_{90,\ c,\ i}$) was computed as:

$$\epsilon_{i,c} = \Delta\text{APD}_{90,\ c,\ i} - \Delta\text{APD}_{90,\ \text{c},\ \Phi_{\text{data},1}}. \tag{6.5}$$

Note that any $\epsilon < 0\,\text{ms}$ indicates that ΔAPD_{90} was underpredicted by the adjusted parameterisation of the TP model.

Since $i \in [1;30]$ and $c \in [1;55]$, a total of $30 \times 55 = 1650$ measures of ϵ were obtained. The variability in ϵ was used as a proxy for the uncertainty in model predictions induced by the parametric variability. Two metrics for model predictivity were based on the distribution of ϵ, the width of the central 95 percentiles of the distribution of ϵ ($\mathcal{W}$) for the variability in ϵ:

$$\mathcal{W} = P_{97.5\%}(\epsilon) - P_{2.5\%}(\epsilon), \tag{6.6}$$

and the proportion of cases in which $|\epsilon| < 10\,\text{ms}$ ($\mathcal{P}$) for the precision of predictions:

$$\mathcal{P} = \frac{1}{1650} \times \Big|\{\epsilon, |\epsilon| < 10\ \text{ms}\}\Big|. \tag{6.7}$$

Results

The uncertainty in parameter estimates (Figure 6.6A) propagates to the predictions of ΔAPD_{90} under 55 validation conditions of I_{Kr} and I_{CaL} inhibition (Figure 6.5B). The distribution of ϵ is shown in Figure 6.7.

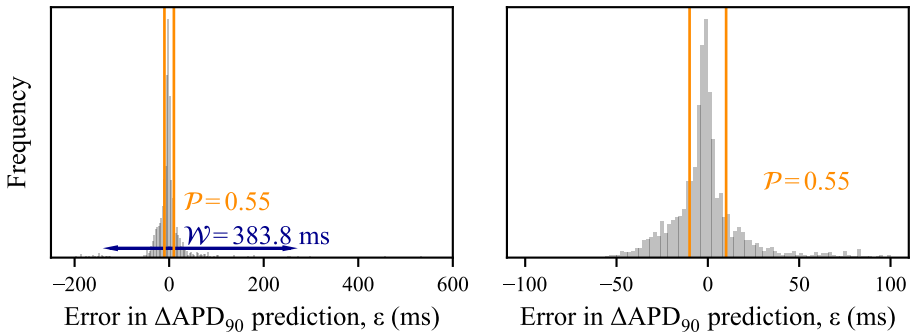

Figure 6.7: Distribution of ϵ after individualising G_{Kr}, and G_{CaL}. The metrics for model predictivity $\mathcal{W}$ (Eq. 6.6) and $\mathcal{P}$ (Eq. 6.7) are highlighted in **blue** and **orange**, respectively. The right panel is a zoom into $-100\,\text{ms} < \epsilon < +100\,\text{ms}$

The distribution of ϵ is narrow with $\mathcal{P} = 0.55$, but $\mathcal{W} = 383.8\,\text{ms}$ highlights that ΔAPD_{90} predictions remain highly uncertain. In particular, conditions of high I_{CaL} inhibition lead to very negative ΔAPD_{90} responses of the model for $\Phi_{\text{data},1}$, which could not always be reproduced by the adjusted parameterisations of the TP model. This leads to extreme values for ϵ, sometimes higher than $+300\,\text{ms}$. Therefore, ΔAPD_{90} predictions after individualisation of G_{Kr} and G_{CaL} are highly uncertain and have low precision.

For each of the 30 adjusted parameterisations of the TP model, the mean $|\epsilon|$ is plotted against $\mathcal{C}(\theta^*)$ in Figure 6.8. Note that the colour labelling associated with each adjusted parameterisation of the TP model is consistent with Figure 6.6.

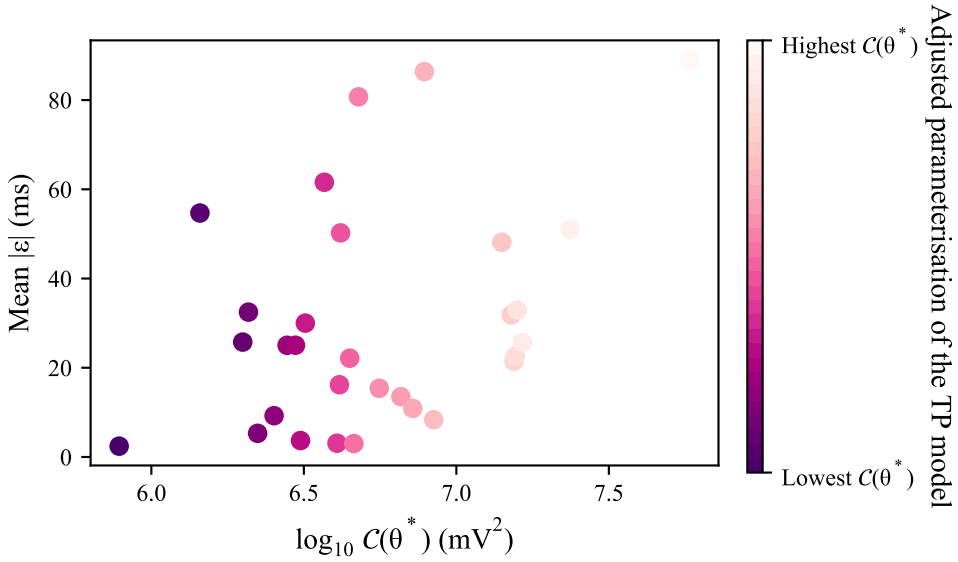

Figure 6.8: Comparison of the mean absolute error in ΔAPD_{90} prediction ($|\epsilon|$) with the goodness-of-fit (Eq. 6.4), for each of the 30 adjusted parameterisations of the TP model. Each colour corresponds to one of the 30 adjusted parameterisations of the TP model, matching colours of Figure 6.6. The darker the point, the lower the minimal cost $\mathcal{C}(\theta^*)$.

The mean $|\epsilon|$ was only weakly correlated with the goodness-of-fit ($r^2 < 0.2$). The weak correlation suggests that with parametric variability during model training, the model with the best goodness-of-fit is not necessarily the most predictive.

6.3.5 Iterative increase of the set of individualised parameters

Methods

To identify the best set of parameters to individualise, Algorithm 1 was repeated with increasing numbers of individualised parameters. The number of individualised parameters

was increased to 3, then 4, ..., up to 8 (Table 6.1), as described in Algorithm 2.

Algorithm 2 Pseudo-code for the iterative extension of the set of individualised parameters.

Start: Initialise the set of individualised parameters to $G_{\text{ind}} = (G_{\text{Kr}}, G_{\text{CaL}})$

1: **for** each adjustable conductance parameter G_{test} not in G_{ind} **do**
2: Calibrate the model by running Algorithm 1 on $(G_{\text{test}} \cap G_{\text{ind}})$
3: Compute $\mathcal{W}$ (Eq. 6.6) and $\mathcal{P}$ (Eq. 6.7)
4: **end for**
5: Add the best G_{test} that minimises $\mathcal{W}$ to G_{ind}
6: Repeat steps 1–5 until all parameters are included in G_{ind}

Every time the set of individualised parameters was increased, the set of parameters that previously yielded the lowest $\mathcal{W}$ (Eq. 6.6) was included, and the remaining adjustable conductances were tested in turn. For instance, with 3 individualised parameters, G_{Kr} and G_{CaL} were individualised, and there were 6 possible parameters for G_{test}: G_{Ks}, G_{K1}, G_{Na}, G_{NaCa}, G_{NaK}, G_{to}. Therefore, Algorithm 1 was repeated six times with 3 individualised parameters (G_{Kr}, G_{CaL}, and G_{test}). The set of 3 individualised parameters which yielded the lowest $\mathcal{W}$ was noted (G_{Kr}, G_{CaL}, G_{3rd}).

Five sets of 4 parameters were then individualised: G_{Kr}, G_{CaL}, G_{3rd}, G_{test}. The set of individualised parameters was iteratively increased following the same logic. Hence, four sets of 5 parameters, three sets of 6 parameters, two sets of 7 parameters, and one set of 8 parameters were individualised. In total, Algorithm 1 was repeated with 21 different sets of individualised parameters, and the set of individualised parameters which yielded the lowest $\mathcal{W}$ was selected as the optimal set of parameters to individualise.

Note that $\mathcal{W}$ was selected rather than $\mathcal{P}$ to guide the selection of parameters to individualise, to penalise extreme errors in ΔAPD_{90} predictions.

Comparison of $\mathcal{W}$ and $\mathcal{P}$ with the Bayesian Information Criterion, for guiding the selection of parameters to individualise

The Bayesian Information Criterion (BIC, Schwarz (1978)) is a popular tool to select how many parameters to optimise. Applied to the context of this work, the BIC is given by:

$$\text{BIC} = -2\ell(\theta^*|y^*) + n_p \ln N, \tag{6.8}$$

with n_p the number of individualised parameters, N the total number of points in the training data ($4 \times 9 \times 20{,}000 = 720{,}000$), θ^* the optimal parameters minimising $\mathcal{C}$ (Eq. 6.4), and ℓ the log-likelihood function.

In the present case where the noise at each time point followed independent and identically distributed Gaussian distributions of width σ_y, ℓ was computed as:

$$\begin{aligned}\ell(\theta^*|y^*) &= -\frac{N}{2}\ln 2\pi - N\ln\sigma_y - \frac{1}{2\sigma_y^2}\sum_{t=0}^{N}\left(y(\theta^*,t) - y^*(t)\right)^2 \\ &= -\frac{N}{2}\ln 2\pi - N\ln\sigma_y - \frac{1}{2\sigma_y^2}\mathcal{C}(\theta^*).\end{aligned} \tag{6.9}$$

The BIC was computed for the 30 adjusted parameterisations of the TP model. The average BIC was then compared with $\mathcal{W}$ and $\mathcal{P}$ for guiding the selection of parameters to individualise.

Results

$\mathcal{W}$ (Eq. 6.6) and $\mathcal{P}$ (Eq. 6.7), and the mean BIC (Eq. 6.8) with increasing sets of individualised parameters are reported in Table 6.3.

Overall, $\mathcal{P}$ converges towards 1 and $\mathcal{W}$ converges towards 0 ms. Therefore, the precision of predictions of ΔAPD_{90} response to I_{Kr} and I_{CaL} inhibition increases. When the 8 adjustable conductance parameters are individualised, the parameter estimates match the parameter values in $\Phi_{\text{data},1}$, and the very low errors in model predictions can be attributed to noise. This was expected, as all 8 adjustable conductance parameters were identifiable (Section D.3 in the Appendix) with no model discrepancy.

The BIC also decreases with increasing sets of individualised parameters, suggesting that the optimisation problem is solved more accurately with more individualised parameters, and that overfitting did not occur (Schwarz, 1978). This coincides with the convergence of $\mathcal{W}$ towards 0 ms and $\mathcal{P}$ towards 1, to conclude that all adjustable conductance parameters should be individualised to maximise the predictivity of the individual-specific model.

Nevertheless, divergences can be observed between the evolution of the BIC and that of the model predictivity. For example, the best set of 5 parameters to individualise based on the lowest BIC is G_{Kr}, G_{CaL}, G_{to}, G_{Ks}, and G_{NaK} (BIC$= 1.23 \times 10^8$).

Individualised (G_{Kr}, G_{CaL})						
$\mathcal{W}$ (ms)	383.8					
$\mathcal{P}$	0.55					
Mean BIC ($\times 10^8$)	8.75					
Individualised (G_{Kr}, G_{CaL}) +	G_{Na}	G_{K1}	G_{Ks}	G_{NaCa}	G_{NaK}	$\mathbf{G_{to}}$
$\mathcal{W}$ (ms)	299.3	175.3	429.0	376.9	331.2	**111.6**
$\mathcal{P}$	0.57	0.68	0.82	0.67	0.67	**0.60**
Mean BIC ($\times 10^8$)	6.74	5.23	4.31	6.32	5.23	**7.17**
Individualised (G_{Kr}, G_{CaL}, G_{to}) +	G_{Na}	G_{K1}	$\mathbf{G_{Ks}}$	G_{NaCa}	G_{NaK}	
$\mathcal{W}$ (ms)	90.9	45.4	**34.8**	94.3	80.7	
$\mathcal{P}$	0.62	0.75	**0.86**	0.67	0.71	
Mean BIC ($\times 10^8$)	5.80	4.22	**3.26**	4.99	4.37	
Individualised (G_{Kr}, G_{CaL}, G_{to}, G_{Ks}) +	G_{Na}	$\mathbf{G_{K1}}$		G_{NaCa}	G_{NaK}	
$\mathcal{W}$ (ms)	37.3	**15.7**		47.6	35.9	
$\mathcal{P}$	0.88	**0.97**		0.88	0.92	
Mean BIC ($\times 10^8$)	2.78	**2.08**		2.28	1.23	
Individualised (G_{Kr}, G_{CaL}, G_{to}, G_{Ks}, G_{K1}) +	G_{Na}			G_{NaCa}	$\mathbf{G_{NaK}}$	
$\mathcal{W}$ (ms)	15.2			20.4	**13.4**	
$\mathcal{P}$	0.97			0.96	**0.97**	
Mean BIC ($\times 10^8$)	1.67			1.33	**0.47**	
Individualised (G_{Kr}, G_{CaL}, G_{to}, G_{Ks}, G_{K1}, G_{NaK}) +	G_{Na}			$\mathbf{G_{NaCa}}$		
$\mathcal{W}$ (ms)	8.3			**6.6**		
$\mathcal{P}$	0.99			**0.99**		
Mean BIC ($\times 10^8$)	0.23			**0.21**		
Individualised (G_{Kr}, G_{CaL}, G_{to}, G_{Ks}, G_{K1}, G_{NaK}, G_{NaCa}) +	$\mathbf{G_{Na}}$					
$\mathcal{W}$ (ms)	**0.6**					
$\mathcal{P}$	**1.00**					
Mean BIC ($\times 10^8$)	**−0.04**					

Table 6.3: Evolution of $\mathcal{W}$ (Eq. 6.6), $\mathcal{P}$ (Eq. 6.7), and of the BIC (Eq. 6.8). For a given number of individualised parameters, values in bold indicate the set of individualised parameters which yields the lowest $\mathcal{W}$.

Yet, this set of individualised parameters produces less precise and more uncertain ΔAPD_{90} predictions ($\mathcal{P} = 0.92$ and $\mathcal{W} = 35.9\,ms$) than G_{Kr}, G_{CaL}, G_{to}, G_{Ks}, and G_{K1} ($\mathcal{P} = 0.97$ and $\mathcal{W} = 15.7\,ms$).

Similarly, $\mathcal{W}$ and $\mathcal{P}$ do not always evolve in the same direction. For example, individualising G_{Kr}, G_{CaL}, and G_{Ks} produces more precise ΔAPD_{90} predictions than individualising only G_{Kr} and G_{CaL} ($\mathcal{P}$ increases from 0.55 to 0.82). Yet, the uncertainty in ϵ increases from $\mathcal{W} = 384\,ms$ to $\mathcal{W} = 429\,ms$.

6.3.6 Repeat with synthetic data for another individual

Methods

To check whether the optimal set of parameters to individualise is also individual-specific, previous steps were repeated for a second digital twin, $\Phi_{\text{data},2}$. $\Phi_{\text{data},2}$ was chosen by hand to be reasonably close to the mode of the distribution of conductance parameters yet distinct from $\Phi_{\text{data},1}$ (Figure 6.3A). Table 6.4 lists the scaling factors $\hat{g}$ (Eq. 6.1) in $\Phi_{\text{data},2}$.

Parameter	$\hat{g}_{Kr}$	$\hat{g}_{CaL}$	$\hat{g}_{Ks}$	$\hat{g}_{K1}$	$\hat{g}_{Na}$	$\hat{g}_{NaCa}$	$\hat{g}_{NaK}$	$\hat{g}_{to}$
$\Phi_{\text{data},2}$	0.61	−0.03	0.57	0.12	0.37	0.23	0.81	0.50

Table 6.4: Scaling factors $\hat{g}$ (Eq. 6.1) applied to the conductance parameters of the TP model to create the model for $\Phi_{\text{data},2}$.

The $\Phi_{\text{data},2}$ synthetic data, generated following the same methods as for $\Phi_{\text{data},1}$ data, are shown in Figure 6.9.

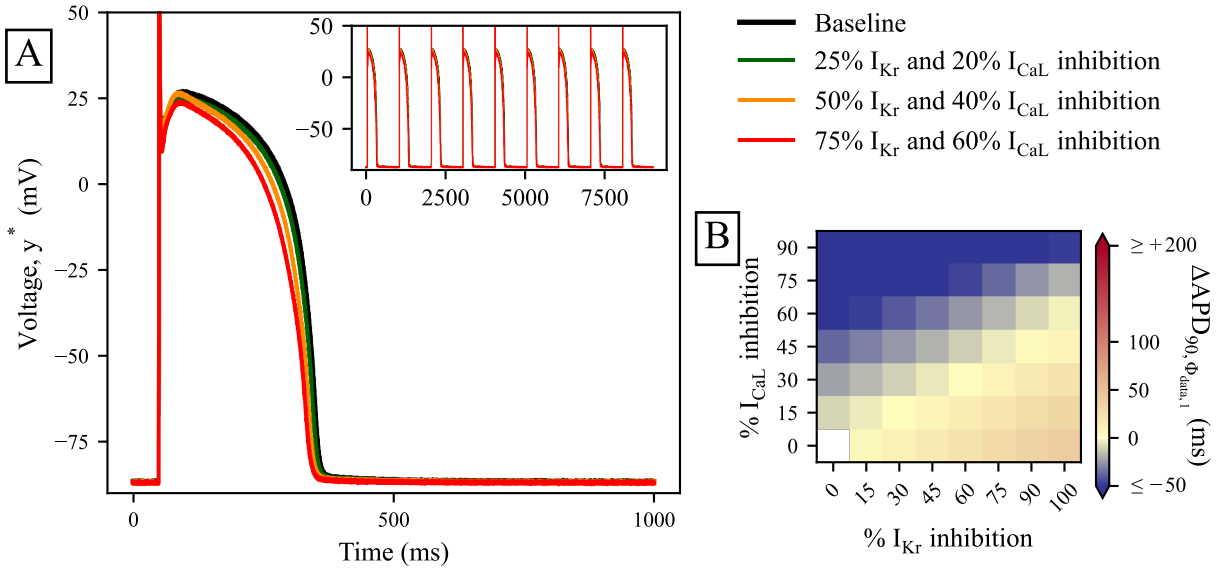

Figure 6.9: Synthetic data generated with the model for $\Phi_{\text{data},2}$. **A:** Synthetic training data simulated under 4 conditions of I_{Kr} and I_{CaL} inhibition. Insets show the 9 APs constituting the synthetic training data. **B:** Synthetic validation data consisting of ΔAPD_{90} simulated under 56 conditions of I_{Kr} and I_{CaL} inhibition.

Results

The evolution of $\mathcal{W}$ and $\mathcal{P}$ are reported in Table 6.5, and compared with the results obtained with $\Phi_{\text{data},1}$ data.

Individual	Number of individualised parameters	2	3	4	5	6	7	8
$\Phi_{\mathbf{data,1}}$	Added parameter	(G_{Kr}, G_{CaL})	G_{to}	G_{Ks}	G_{K1}	G_{NaK}	G_{NaCa}	G_{Na}
	$\mathcal{W}$ (ms)	383.7	111.6	34.8	15.7	13.4	6.6	0.6
	$\mathcal{P}$	0.55	0.60	0.86	0.97	0.97	0.99	1.00
	Mean BIC	9×10^8	7×10^8	3×10^8	2×10^8	5×10^7	2×10^7	-4×10^5
$\Phi_{\mathbf{data,2}}$	Added parameter	(G_{Kr}, G_{CaL})	G_{Ks}	G_{NaK}	G_{to}	G_{K1}	G_{NaCa}	G_{Na}
	$\mathcal{W}$ (ms)	193	138.3	99.3	87.6	80.7	8.0	0.4
	$\mathcal{P}$	0.26	0.50	0.68	0.69	0.75	0.99	1.00
	Mean BIC	4×10^9	2×10^9	1×10^9	9×10^8	4×10^8	4×10^7	-4×10^5

Table 6.5: Evolution of $\mathcal{W}$ (Eq. 6.6), of $\mathcal{P}$ (Eq. 6.7), and of the BIC (Eq. 6.8) after individualising increasing sets of parameters in model calibration to $\Phi_{\mathrm{data,1}}$ data and to $\Phi_{\mathrm{data,2}}$ data. The sets of individualised parameters reported here yield the lowest $\mathcal{W}$ for a given number of individualised parameters (corresponding to the results bolded in Table 6.3).

Using $\Phi_{\mathrm{data,2}}$ data, as previously observed with $\Phi_{\mathrm{data,1}}$ data, $\mathcal{W}$ converges towards 0 ms and $\mathcal{P}$ converges towards 1 with increasing sets of individualised parameters. However, considerably different predictivities can be achieved with the same sets of individualised parameters calibrated to $\Phi_{\mathrm{data,1}}$ data or to $\Phi_{\mathrm{data,2}}$ data. For example, individualising G_{Kr}, G_{CaL}, and G_{Ks} with $\Phi_{\mathrm{data,2}}$ data leads to considerably less uncertain predictions ($\mathcal{W} =$ 138.3 ms) than individualising the same parameters with $\Phi_{\mathrm{data,1}}$ data ($\mathcal{W} = 429.0$ ms). Also, individualising four parameters, predictions are more precise for $\Phi_{\mathrm{data,1}}$ than for $\Phi_{\mathrm{data,2}}$: $\mathcal{P} = 0.86$, $\mathcal{W} = 34.8$ ms for $\Phi_{\mathrm{data,1}}$ versus $\mathcal{P} = 0.68$, $\mathcal{W} = 99.3$ ms for $\Phi_{\mathrm{data,2}}$.

The evolution of the mean BIC with increasing sets of individualised parameters can be compared with that of the predictivity metrics $\mathcal{W}$ and $\mathcal{P}$. With both $\Phi_{\mathrm{data,1}}$ data and $\Phi_{\mathrm{data,2}}$ data, the BIC decreases with the addition of parameters to the set of individualised parameters.

6.3.7 Discussion

With the method introduced in Part II (Algorithm 1), the parametric variability propagates to model training and then to model predictions. An important finding is that with uncertainty or variability in non-individualised parameters, the predictivity of the individual-specific model was only weakly correlated with its goodness-of-fit (Figure 6.8). Therefore, the BIC and other metrics based on goodness-of-fit guide less reliably the

selection of parameters to individualise than model predictivity assessment during the model validation process.

When the 8 adjustable conductance parameters of the TP model were individualised, parameter estimates matched the parameter values used in the models for $\Phi_{\text{data},1}$ and $\Phi_{\text{data},2}$, and no error in ΔAPD_{90} predictions was observed (Table 6.5). Without model discrepancy, the BIC and predictivity metrics are in agreement on the conclusion that individualising a bigger set of parameters is desirable, provided the parameters are identifiable. Reciprocally, selecting too few parameters to individualise limits substantially the predictive power of the individual-specific model. In other words, all the parameters that *can* be individualised *should* be individualised.

With two different digital twins, we investigated the impact of the set of individualised parameters on model calibration to data for two different individuals. The iterative increase of the set of parameters to optimise was different when calibrating the TP model to $\Phi_{\text{data},1}$ data and to $\Phi_{\text{data},2}$ data. This suggests that the optimal set of individualised parameters likely depends on each individual if all the adjustable parameters cannot be individualised. Note that the work could not be reproduced with more individuals because of the high computational cost of the study (total CPU time for Part II: ∼20,000 days).

The methods introduced in Part II can be reused with synthetic data generated with models that differ from the TP model, thereby introducing model discrepancy into the model calibration process. Doing so in Part III, we investigate the importance of the identification of parameters that *can* be individualised, and those that *should* be individualised when model discrepancy is present.

6.4 Part III: Model discrepancy limits the accuracy of parameter estimation and thereby model predictivity

The three AP models that are used in this work are: the TP model, the Grandi *et al.* (2010) (GPB) model, and the O'Hara *et al.* (2011) model reformulated by Dutta *et al.* (2017) (ORd-CiPA). Many differences exist between these AP models, such as the inclusion of different ionic currents or different handling of intracellular ionic concentrations. Therefore, when the TP model is calibrated to individual synthetic data generated with the GPB

and ORd-CiPA models, these differences introduce model discrepancy into the model calibration process (Lei *et al.*, 2020). In this section, we leverage this discrepancy to investigate the impact of model discrepancy on the parameters that *can* and *should* be individualised, when working with a known ground truth.

Firstly, synthetic data are generated with the ORd-CiPA model, and the identifiability of 8 conductance parameters of the TP model (Table 6.1) is tested, allowing us to investigate how model discrepancy impacts parameters that can be individualised.

Secondly, the TP model is calibrated to synthetic data generated with the GPB model, following the same methods as in Part II. That is, increasing sets of parameters are individualised, so that we investigate how model discrepancy impacts parameters that should be individualised.

6.4.1 Methods

Synthetic dataset

Simulations with the GPB and the ORd-CiPA models followed similar methods as described in Section 6.2.1. The only differences in methods were:

- The stimulus current was set to $-50\,\mathrm{A/F}$ for 0.5 ms and $-50\,\mathrm{A/F}$ for 1 ms in the GPB and ORd-CiPA models, respectively, and repeated with a 1 Hz frequency for 500 pre-paces and 1500 pre-paces with the GPB and ORd-CiPA models, respectively;
- The voltage equation in the GPB model could not be changed to its algebraic form, because the intracellular concentrations of K^+ and Cl^- are clamped in this model (see Chapter 3).

Synthetic datasets were generated with the GPB and ORd-CiPA models, following the same methods as described in Part II, and are shown in Figure 6.10.

Testing the identifiability of the TP parameters with the ORd-CiPA data

The identifiability of the 8 adjustable conductance parameters of the TP model (Table 6.1) was tested with the ORd-CiPA data. Parameter estimates that minimise $\mathcal{C}$ (Eq. 6.4) were obtained with the methods described in Part II.

Parameter identifiability was tested with five different values (7, 10, 14, 24, 48) for the CMA-ES hyperparameter corresponding to the number of particles used to explore the parameter space, denoted $\mathcal{N}$ (Figure 2.7). For each value of $\mathcal{N}$, 100 repeats of

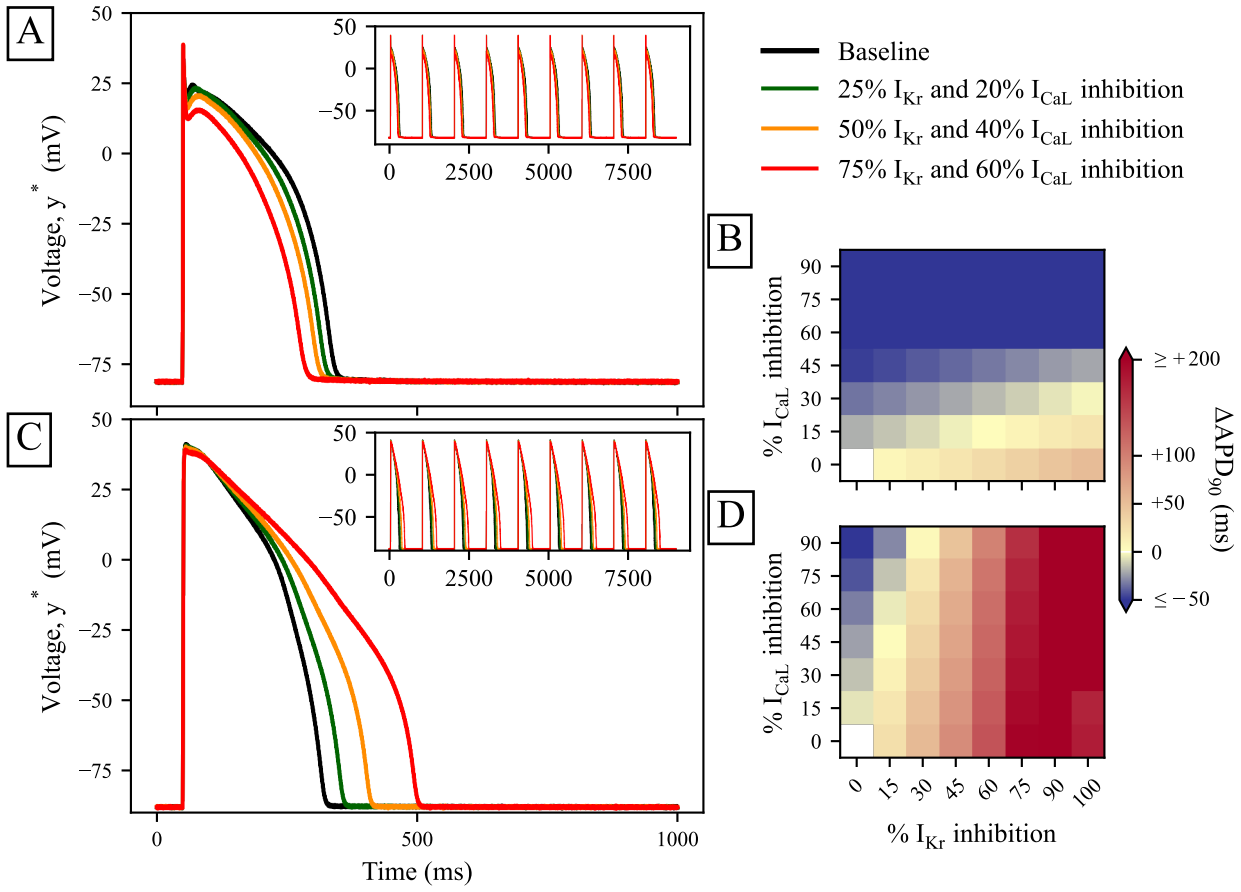

Figure 6.10: Synthetic data generated with the GPB and ORd-CiPA models. **A and C:** Synthetic training data simulated under 4 conditions of I_{Kr} and I_{CaL} inhibition with the GPB and ORd-CiPA models, respectively. Insets show the 9 APs constituting the synthetic training data. **B and D:** Synthetic validation data consisting of ΔAPD_{90} simulated under 56 conditions of I_{Kr} and I_{CaL} inhibition with the GPB and ORd-CiPA models, respectively. I_{Kr} and I_{CaL} inhibition conditions used for model calibration are the same as in Figures 6.5–6.9B.

the model training were performed. The global minimum of $\mathcal{C}$ was assumed to be found with the parameter estimates that yielded the lowest $\mathcal{C}$ across the total 500 repeats of the model training.

Calibration of the TP model to the GPB data

The optimal set of parameters to individualise in individual-specific versions of the TP model calibrated to the GPB data was selected with the same methods as in Part II. The only differences in the methods were for model training:

- wider boundaries for the search space ($-8 < \hat{g} < +5$) were used, to account for the important differences in conductance parameters between the different AP models in the literature (Table D.1 in the Appendix);

- changes were introduced in the hyperparameters used to tune the CMA-ES algorithm to ensure the reproducibility of model training, as reported in Section D.3 in the Appendix.

6.4.2 Results

Testing the identifiability of the TP parameters with the ORd-CiPA data

In this section, 8 conductance parameters of the TP model (Table 6.1) were individualised. No parametric variability was therefore introduced into the model training process, and the only differences between the repeats of the model training presented in this section are different values of $\mathcal{N}$ and random starting points for the exploration of the search space by the CMA-ES algorithm.

The global optimum ($\mathcal{C} = 2.21 \times 10^6\,\mathrm{mV}^2$) was found in only 11/500 repeats of the model training. In 175/500 repeats, a local optimum ($\mathcal{C} = 2.39 \times 10^6\,\mathrm{mV}^2$), that we call the "frequent optimum", was found. The number of repeats of the model training in which the two optima were found is reported in Table 6.6.

Particles used to explore the parameter space ($\mathcal{N}$)	**7**	**10**	**14**	**24**	**48**
Repeats of the training process finding the global optimum	8/100	0/100	2/100	1/100	0/100
Repeats of the training process finding the frequent optimum	19/100	30/100	35/100	44/100	47/100

Table 6.6: Results of model training, when individualising all the adjustable conductance parameters (Table 6.1) of the TP model to the ORd-CiPA data.

The higher the value of $\mathcal{N}$, the less likely it became that the estimates of the individualised parameters coincided with the global optimum. Instead, with increasing numbers of particles, individualised parameters were increasingly likely to coincide with the frequent optimum of $\mathcal{C}$. In the best case ($\mathcal{N} = 7$), the global optimum was found in 8/100 repeats. Yet, 19 repeats of the training process found the frequent optimum. With $\mathcal{N} = 48$, the global and frequent optima were found 0 and 47 times, respectively.

During model training, $\mathcal{C}$ was evaluated at numerous points of the parameter space. This information can be used to visualise the surface of $\mathcal{C}$ over the search space (Villaverde *et al.*, 2015). $\mathcal{C}$ is plotted against samples of the parameter space tested during the 500 repeats of the model training in Figure 6.11.

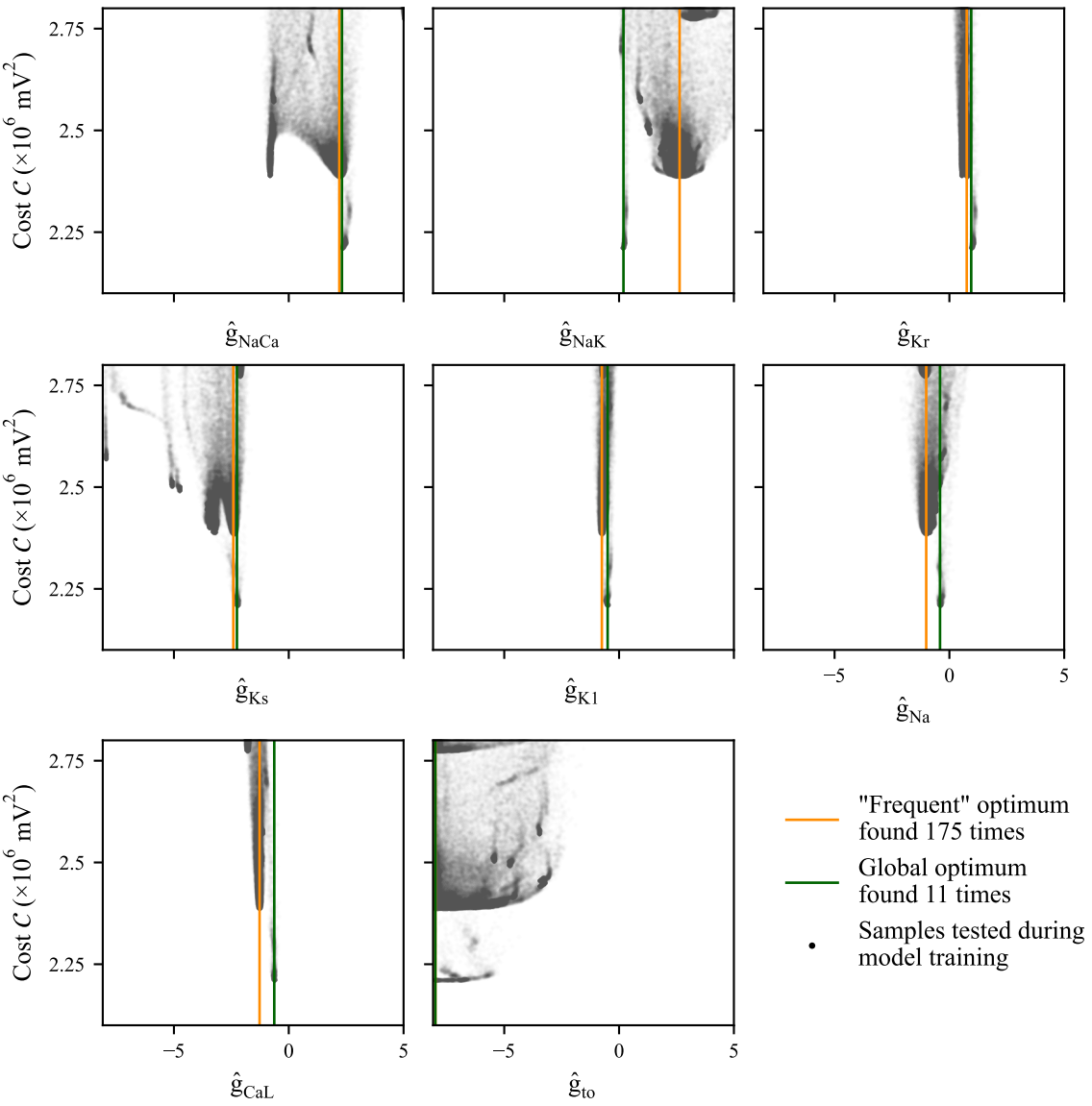

Figure 6.11: Visualisation of the surface of $\mathcal{C}$ over the search space, based on the multiple evaluations of $\mathcal{C}$ during model training. Each point corresponds to the evaluation of $\mathcal{C}$ at one point of the search space sampled during model training.

Minima of $\mathcal{C}$ are visible in Figure 6.11 as the bottom of the curved shapes. The global optimum is located in a region of the parameter space corresponding to a very narrow "funnel". Therefore, at the global optimum, the uncertainty in the optimal parameter values is low and all the adjustable conductance parameters are practically identifiable (Raue *et al.*, 2009).

In contrast, the frequent optimum is located in a region of the parameters space corresponding to a much wider "funnel", particularly visible for $\hat{g}_{NaCa}$, $\hat{g}_{NaK}$, and $\hat{g}_{Na}$.

The CMA-ES algorithm is therefore more likely to be "trapped" into the region surrounding the frequent optimum when exploring the parameter space. This effect is exacerbated by the comparable goodness-of-fit obtained for the global and the frequent optima.

Another local minimum of $\mathcal{C}$ ($\mathcal{C} = 2.388 \times 10^6\,\mathrm{mV}^2$) is close to the frequent optimum ($\mathcal{C} = 2.385 \times 10^6\,\mathrm{mV}^2$) with similar parameter estimates, except for $\hat{g}_{\mathrm{NaCa}}$ and $\hat{g}_{\mathrm{Ks}}$. This third optimum was found in 48/500 repeats, i.e., more than 4 times more frequently than the global optimum in total.

Repeating the process to select the optimal set of parameters to individualise in the TP model as in Part II would require numerous repeats of the training process to ensure that the optimum found during model training corresponds to the global optimum. This is not feasible within reasonable computational cost. Therefore, the identifiability of the 8 adjustable conductance parameters of the TP model (Table 6.1) is limited in practice. In other words, the number of parameters that *can* be individualised in practice is reduced when calibrating the TP model to the ORd-CiPA data.

ϵ was computed using 55 validation conditions of $\mathrm{I_{Kr}}$ and $\mathrm{I_{CaL}}$ inhibition, with the adjusted parameterisations of the TP model corresponding to the global optimum and to the frequent optimum (Figure 6.12). Low ϵ was observed under validation conditions that are similar to the training conditions (mixed $\mathrm{I_{Kr}}$ and $\mathrm{I_{CaL}}$ inhibition), but with the remaining conditions of $\mathrm{I_{Kr}}$ and $\mathrm{I_{CaL}}$ inhibition, ϵ was higher than 10 ms.

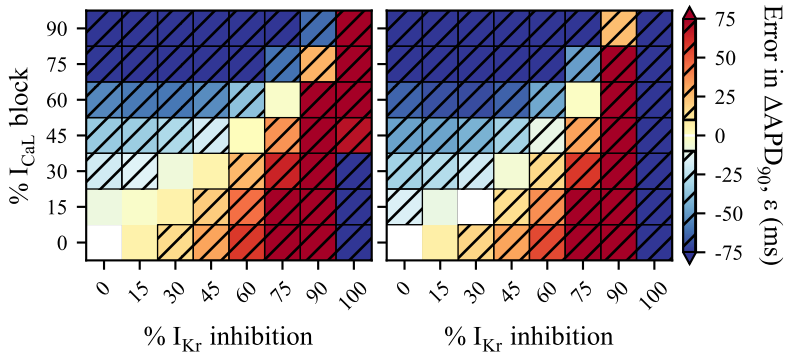

Figure 6.12: ϵ computed under 55 conditions of $\mathrm{I_{Kr}}$ and $\mathrm{I_{CaL}}$ inhibition by the adjusted parameterisation of the TP model corresponding to the global optimum (**left**) and to the frequent optimum (**right**) of $\mathcal{C}$.

Using the global and frequent optima, the precision of ΔAPD_{90} prediction was very low ($\mathcal{P} = 0.16$ and $\mathcal{P} = 0.11$, respectively) and the uncertainty in ϵ was high ($\mathcal{W} = 189.4\,ms$ and $\mathcal{W} = 143.4\,ms$, respectively). It is worth noting that the lowest $\mathcal{W}$ was achieved with the frequent optimum, i.e., with a suboptimal goodness-of-fit.

Calibration of the TP model to the GPB data

Individual-specific versions of the TP model were calibrated to the GPB data with increasing sets of individualised parameters, following the same methods as in Part II. $\mathcal{W}$ (Eq. 6.6), $\mathcal{P}$ (Eq. 6.7), and the mean BIC (Eq. 6.8) are reported in Table 6.7.

Similarly to Part II, the mean BIC (Eq. 6.8) always decreases with increasing numbers of individualised parameters. Similarly to Part II, for a given number of individualised parameters, the individualisation of parameters yielding the lowest BIC does not always make the most predictive model.

In contrast with Part II, the predictivity achieved after calibration with model discrepancy is much lower. $\mathcal{W}$ does not converge towards 0 ms and $\mathcal{P}$ does not converge towards 1. At best, individualising only 5 parameters (G_{Kr}, G_{CaL}, G_{Na}, G_{NaK}, G_{Ks}) yields the lowest uncertainty in ϵ ($\mathcal{W} = 106.9\,ms$), and individualising 8 parameters yields the most precise ΔAPD_{90} predictions ($\mathcal{P} = 0.40$).

Furthermore, with model discrepancy, increasing the set of individualised parameters does not always improve model predictions. Individualising 6 parameters (G_{Kr}, G_{CaL}, G_{Na}, G_{NaK}, G_{Ks}, G_{to}) yields more precise ΔAPD_{90} predictions ($\mathcal{P} = 0.34$) and lower uncertainty in ϵ ($\mathcal{W} = 116.4\,ms$) than individualising 7 parameters ($\mathcal{W} \in [128.6; 152.4]\,ms$ and $\mathcal{P} \in [0.24; 0.32]$). Adding the last parameter (G_{NaCa}) to the set of individualised parameters improves $\mathcal{P}$, which reaches its maximum ($\mathcal{P} = 0.40$), but $\mathcal{W}$ is further increased ($\mathcal{W} = 168.7\,ms$).

The cumulative density function (CDF) of ϵ was computed for the adjusted parameterisations of the TP model developed in the present section. For a given number of individualised parameters, the set of individualised parameters yielding the lowest $\mathcal{W}$ (highlighted in bold font in Table 6.7) was used to compute the CDF of ϵ. Results are shown in Figure 6.13.

Individualised (G_{Kr}, G_{CaL})						
$\mathcal{W}$ (ms)	588.5					
$\mathcal{P}$	0.16					
Mean BIC ($\times 10^{11}$)	2.74					
Individualised (G_{Kr}, G_{CaL}) +	$\mathbf{G_{Na}}$	G_{K1}	G_{Ks}	G_{NaCa}	G_{NaK}	G_{to}
$\mathcal{W}$ (ms)	**172.5**	210.1	181.8	428.5	396.3	192.5
$\mathcal{P}$	**0.19**	0.20	0.18	0.21	0.24	0.17
Mean BIC ($\times 10^{9}$)	**3.02**	3.02	2.23	2.84	1.47	3.10
Individualised (G_{Kr}, G_{CaL}, G_{Na}) +		G_{K1}	G_{Ks}	G_{NaCa}	$\mathbf{G_{NaK}}$	G_{to}
$\mathcal{W}$ (ms)		150.4	173.2	192.3	**142.6**	173.7
$\mathcal{P}$		0.21	0.16	0.24	**0.23**	0.19
Mean BIC ($\times 10^{9}$)		2.56	2.24	2.39	**1.34**	2.89
Individualised (G_{Kr}, G_{CaL}, G_{Na}, G_{NaK}) +		G_{K1}	$\mathbf{G_{Ks}}$	G_{NaCa}		G_{to}
$\mathcal{W}$ (ms)		112.2	**106.9**	171.9		134.6
$\mathcal{P}$		0.32	**0.18**	0.38		0.22
Mean BIC ($\times 10^{9}$)		0.90	**0.99**	1.17		1.19
Individualised (G_{Kr}, G_{CaL}, G_{Na}, G_{NaK}, G_{Ks}) +		G_{K1}		G_{NaCa}		$\mathbf{G_{to}}$
$\mathcal{W}$ (ms)		121.3		187.4		**116.4**
$\mathcal{P}$		0.15		0.32		**0.34**
Mean BIC ($\times 10^{9}$)		0.76		0.76		**0.74**
Individualised (G_{Kr}, G_{CaL}, G_{Na}, G_{NaK}, G_{Ks}, G_{to}) +		$\mathbf{G_{K1}}$		G_{NaCa}		
$\mathcal{W}$ (ms)		**128.6**		152.4		
$\mathcal{P}$		**0.24**		0.32		
Mean BIC ($\times 10^{9}$)		**0.50**		0.39		
Individualised (G_{Kr}, G_{CaL}, G_{Na}, G_{NaK}, G_{Ks}, G_{to}, G_{K1}) +				$\mathbf{G_{NaCa}}$		
$\mathcal{W}$ (ms)				**168.7**		
$\mathcal{P}$				**0.40**		
Mean BIC ($\times 10^{9}$)				**0.29**		

Table 6.7: Evolution of $\mathcal{W}$ (Eq. 6.6), of $\mathcal{P}$ (Eq. 6.7), and of the BIC (Eq. 6.8) after individualising increasing sets of parameters in model calibration to the GPB data (Figure 6.10). Values in bold indicate the sets of individualised parameters which yielded the lowest $\mathcal{W}$ for a given number of individualised parameters.

When only 2 parameters (G_{Kr} and G_{CaL}) were individualised, the trained model was likely to overpredict ΔAPD_{90} (13% of predictions with $\epsilon \geq +100$ ms). After individualising 3 parameters (G_{Kr}, G_{CaL}, and G_{Na}), extreme errors in ΔAPD_{90} predictions are more rare. Yet, improvements in the central part of the CDF around $\epsilon = 0$ ms are not clearly visible. With 4 to 7 inferred parameters, CDFs of ϵ were very similar and exhibited a steep increase around $\epsilon = 0$ ms, in token of the increase in the precision of ΔAPD_{90} predictions (Table 6.7). When all the adjustable conductance parameters were individualised, the

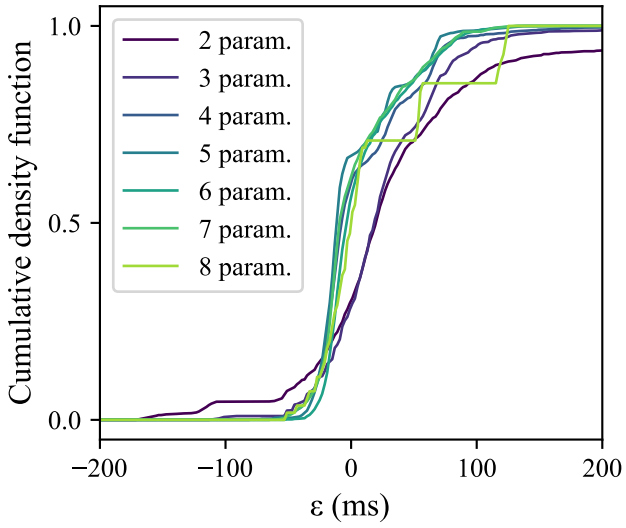

Figure 6.13: Cumulative density function of ϵ obtained in individual-specific versions of the TP model calibrated to the GPB data. For each number of individualised parameters, the set of individualised parameters yielding the lowest $\mathcal{W}$ (highlighted in bold font in Table 6.7) was used.

CDF of ϵ was shifted again towards higher ϵ.

6.4.3 Discussion

Model discrepancy made the identifiability of parameters more difficult to achieve than in Part II. Many repeats of model training were needed to ensure that the adjusted parameterisation of the model corresponds to the global optimum of $\mathcal{C}$ (Table 6.6 and Table D.3 in the Appendix). Therefore, the identifiability of parameters *in practice* was limited by model discrepancy, although the parameters were technically still practically identifiable (see (Raue *et al.*, 2009) and Section 2.5.3). We therefore suggest that the definition of practical identifiability should also include the practical reproducibility of the results of parameter optimisation. On a side note, our results outline the importance of the fine tuning of hyperparameters selected for the optimisation algorithm when model discrepancy is introduced into the model calibration process.

The results observed during the calibration of the TP model to the GPB data suggest that model discrepancy limits substantially the predictivity of individual-specific models. Without model discrepancy, no error in ΔAPD_{90} predictions were observed with 8 individualised parameters ($\mathcal{W}$ and $\mathcal{P}$ converged towards 0 ms and 1 respectively). With model

discrepancy, the maximum of $\mathcal{P}$ was reached with 8 individualised parameters ($\mathcal{P} = 0.40$), and the minimum of $\mathcal{W}$ was reached with 5 individualised parameters ($\mathcal{W} = 106.9\,\text{ms}$).

With the objective of minimising $\mathcal{W}$, the optimal set of parameters to individualise was G_{Kr}, G_{CaL}, G_{Na}, G_{NaK}, and G_{Ks}. The 8 adjustable conductance parameters (Table 6.1) were identifiable in the TP model and *could* be individualised, but the results of Part III point to the conclusion that these parameters *should not necessarily* be individualised when model discrepancy was introduced into the model calibration process.

Furthermore, the BIC was misleading in the selection of parameters to individualise. To minimise the BIC, all the adjustable conductance parameters should be individualised, whilst the optimal set of parameters to individualise included only 5 parameters (Table 6.7). These results suggest that careful use should be made of the BIC (and other methods based on the goodness-of-fit) for the selection of parameters to individualise, similarly to the observation of Liu (2000). Instead, methods based on the assessment of model predictions, such as the method introduced in the present work, are more reliable for the selection of parameters to individualise.

These results therefore suggest that model discrepancy exacerbates the loss of correlation between goodness-of-fit and model predictivity, previously observed in Part II (Figure 6.8), thus making model calibration more prone to overfitting (Section 2.5.3), i.e, pursuing improvements in goodness-of-fit by calibrating additional parameters without improving model predictivity. Model selection impacts model discrepancy, hence the occurrence of overfitting. Overfitting is also impacted by the metric used to assess the predictivity of the model over its context of use ($\mathcal{W}$ and $\mathcal{P}$ yield different results in Table 6.7). Attention should be paid to these two aspects of model development.

Given the differences between calibration to $\Phi_{\text{data},1}$ data and to $\Phi_{\text{data},2}$ data in Part II, the appearance of overfitting may also depend on each individual. As a consequence, the appearance of overfitting is very problem-dependent, and should be carefully assessed when model discrepancy is introduced into the calibration of individual-specific AP models.

As a conclusion, with model discrepancy, parameters that *can* and *should* be individualised should be carefully identified, in particular because they may be different sets of parameters.

6.5 General discussion

6.5.1 Finer uncertainty quantification for higher model credibility

In the present work, the synthetic validation data were excluded from model training, and was only used to select the parameters to individualise. Thorough uncertainty quantification, and independence of model training and validation are central parts of model credibility assessment (Musuamba *et al.*, 2021).

The set of parameters to individualise in models should be selected in the light of the desired context of use, and these choices should be reflected onto the uncertainty in model predictions (Galappaththige *et al.*, 2022). Results in Part III also suggest that the set of individualised parameters requires particular attention, given the ubiquity of model discrepancy in the calibration of biophysically-detailed models (Engl *et al.*, 2009). Furthermore, results in Part II suggest that the selection of individualised parameters may be individual-dependent: different levels of individualisation may be needed to recapitulate observations in different individuals.

Common methods for uncertainty quantification in systems biology rely on forwarding the uncertainty in parameter estimates, mainly due to experimental noise, onto model predictions (Villaverde *et al.*, 2019). The uncertainty in parameter estimates stemming from the uncertainty and/or variability in non-individualised parameters adds on top of the classic uncertainty in parameter estimates. Our methods stand out because the uncertainty and/or variability in non-individualised parameters *propagates to the model calibration process, not only to the forward simulations made with the calibrated model*. When this contribution to the uncertainty in parameter estimates is missing, parameter uncertainty may be underestimated.

By leveraging preliminary knowledge on the variability in fixed parameters during model training, our method can be used to estimate accurately the uncertainty in individualised parameters, and how it propagates to model predictions. In essence, this approach is similar to tests based on restricted maximum likelihood estimation, e.g., (Wald & Wolfowitz, 1940; Aitchison & Silvey, 1958).

Note that considerable correlations were observed between the 8 adjustable conductance parameters (Figure 6.3). By fixing the non-individualised parameters to values taken from

random digital twins, the correlation between the non-individualised parameters was kept, which contributed to a more realistic estimation of the uncertainty in parameter estimates.

6.5.2 Calibration of an action potential model exhibiting chaotic behaviour

The chaotic behaviour of a modified version of the TP model, with various bifurcation parameters, was previously studied by Erhardt & Solem (2022). Similarly, we observed in Section D.4 in the Appendix the occurrence of chaotic behaviour of the TP model induced by I_{Kr} and/or I_{CaL} inhibition (Figure D.2 in the Appendix), and its impact on model calibration. The chaotic behaviour of the model makes the surface of $\mathcal{C}$ (Eq. 6.4) non-smooth, hence making the parameter space much harder to explore for the CMA-ES algorithm during model training (Figure D.4 in the Appendix). Practical identifiability of conductance parameters of the TP model was therefore lost, even when no model discrepancy was introduced into model calibration. Therefore, we recommend ensuring that AP models do not exhibit chaotic behaviour during model calibration, e.g., by adding a constraint during model training.

6.5.3 Application of the methods introduced in this work to other modelling frameworks

The work presented in this study can be re-used to investigate the impact of three aspects on the calibration of mathematical models.

Impact of the inter-individual variability on model outputs

If (surrogate) information is available for the IIV in parameters that are individualised, this information can be used to simulate model outputs for digital twins, as in Section 6.2.1. Thus, the variability in model outputs between potential individual-specific models can be estimated, and the relevance of individual-specific models can be assessed.

Selection of the optimal set of parameters to individualise

The ideal case where both training and validation datasets can be obtained for each individual was investigated in this work. In such cases, our method is directly applicable to each individual data, provided sufficient computational power is available. As suggested

by our results reported in Part II, individual-specific models for different individuals might require different levels of individualisation, in particular when not all the adjustable parameters are identifiable. Therefore, an optimal set of parameters to individualise should be determined for each individual (Figure 6.14). The optimal set of parameters to individualise can be selected with the iterative process described in Algorithm 2.

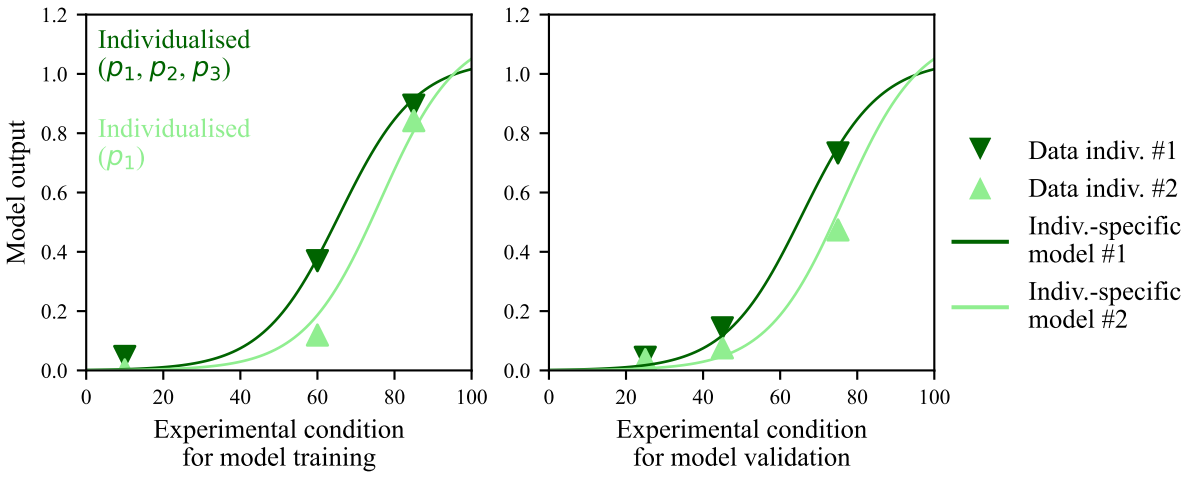

Figure 6.14: When the training data (**left**) and the validation (**right**) data are available in each individual, the optimal set of parameters to individualise can be selected independently for each individual. The two panels show sketches, for illustrative purposes only.

In less ideal cases, because of experimental limitations, the validation data may be generated with different individuals than the training data (see Figure 6.15). In such cases, a collection of individual-specific models can be trained by individualising the same set of parameters in all individuals. If the collection of individual-specific models is sufficiently large, the parametric variability is indirectly captured by the calibration of the collection of individual-specific models. The optimal set of parameters to individualise can then be selected with the iterative process described in Algorithm 2.

Testing the impact of model discrepancy and modelling assumptions on model calibration

In Part III, we showed that model discrepancy may arise from the modelling choices, such as model selection, and may limit the predictivity of the calibrated model. The strategy of Part III can be re-used in many other modelling exercises. Synthetic data for model training and validation can be generated with models that rely on different modelling

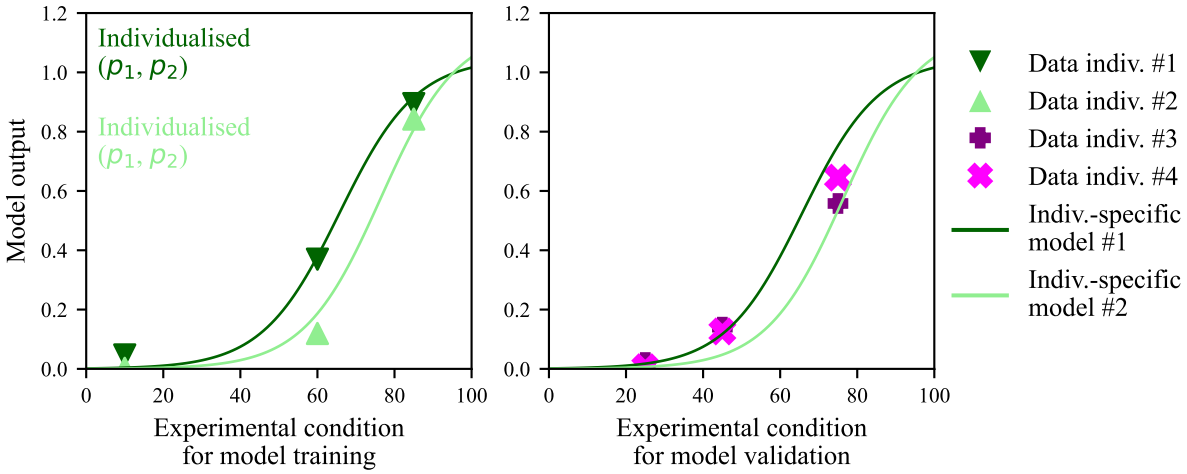

Figure 6.15: When the training data and the validation data are generated in different individuals, the same set of parameters is individualised for all individuals. A population of individual-specific models (#1 and #2) is prepared in model training (**left**), and the subsequent model predictions are assessed against the validation data generated in different individuals (#3 and #4) (**right**). The two panels show sketches, for illustrative purposes only.

assumptions, and the model of interest can be calibrated to such synthetic data. Doing so, the importance of the various modelling assumptions can be assessed.

As a concrete example, when calibrating a model to a noisy time series, the noise level at each time point may be assumed to be independent and identically distributed. To study the impact of this assumption, synthetic data can be generated with the model of interest and random noise described with another reasonable distribution, e.g., auto-correlated noise (Lambert *et al.*, 2023). The impact of an erroneous noise model — a form of model discrepancy — on model predictivity can thus also be estimated.

6.5.4 Limitations

Maximal conductance parameters of ionic currents were modelled as linearly dependent on the RNA level of expression in this work. Whilst a strong correlation ($r^2 = 0.89$) was observed in neurons between the amount of corresponding mRNA and the maximal current density through $K_V2.1$ channels (Veys *et al.*, 2012), *numerous* mechanisms are overlooked with this model, e.g., the regulation by miRNA of the expression of genes coding for repolarisation ion channels (Esfandyari *et al.*, 2022). Furthermore, the normalisation to housekeeping genes is an imperfect method (Tricarico *et al.*, 2002). Therefore, the approximation that we made is a very simplistic approximation of the IIV

to expect in ion channel conductances. Whilst it is acceptable to use this estimation for exploration in a synthetic exercise like this one, it should be used with much caution for predictions of inter-patient variability.

Ideally, the training and validation datasets should be generated in a single individual (Groenendaal *et al.*, 2015). However, experimental limitations make sometimes impossible the generation of such data. For example, recording steady-state APs under 56 different conditions of I_{Kr} and I_{CaL} inhibition in the same adult human ventricular tissue is not feasible. In such situations, the training dataset is generated in different individuals than the validation dataset. Still, the method developed in the present work remains applicable in this situation, as discussed in Section 6.5.3.

The method introduced in this work required to train the model with increasing levels of individualisation, which is a brute force approach to select the optimal set of parameters to individualise in the model. Model training can be computationally expensive and might limit the applicability of our method. In our case, the computational cost of the study was a considerable bottleneck. For each synthetic dataset, 21 sets of individualised parameters were tested. Each set of parameters was individualised with 30 values for the non-individualised parameters, repeating the model training process with 10 random initialisations. This amounts to a total of 25,200 inverse problems solved for this work. Furthermore, AP models are themselves computationally expensive to solve, because of their stiffness, numerous state variables, and numerous time steps to solve until steady-state is reached. This therefore amounted to an approximate CPU time of 50,000 days.

To achieve these computational requirements, the scripts were run in the high performance computer of F. Hoffmann-La Roche Ltd. (composed of processors Intel Xeon Platinum 9242 at 2.3 GHz and Intel Xeon Platinum 8358 at 2.6 GHz). There, CPU resources are dynamically allocated to various jobs, therefore making it hard to compute the exact cost of the study. Therefore, the evaluated computational cost of the study is a rough approximation.

6.6 Conclusion and future work

In the calibration of (individual-specific) models, uncertainty and/or variability in non-calibrated parameters propagates to parameter estimates and subsequent model predictions. Due to this source of uncertainty in parameter estimates, the goodness-of-fit and model predictivity may be weakly correlated, and the optimal set of parameters to optimise may be individual-specific (Part II). In such situations, particular care is required to select the set of parameters that should be calibrated.

Model discrepancy may exacerbate these effects, therefore limiting the predictivity of the calibrated model, and potentially the number of parameters that can be calibrated (Part III). It remains to be seen how correction terms to mitigate for model discrepancy (e.g., Brynjarsdóttir & O'Hagan (2014); Tuo & Wu (2015)) can affect these observations.

The synthetic studies carried out in this work are examples of studies that can be applied to many other modelling frameworks. For instance, we showed in Part I how to use a priori knowledge about parameter variability to investigate the relevance of individual-specific models. The iterative method introduced in Part II can be applied to the selection of the optimal set of parameters to calibrate, accounting for the uncertainty/variability in non-calibrated models, eventually after adaptation (Section 6.5.3). The approach of Part III can also be applied to investigate the importance of modelling assumptions. This is particularly applicable in fields where competing models exist for the same system, e.g., in quantitative systems pharmacology (QSP).

The methods introduced in the present Chapter can be applied to the calibration of new AP models. In Chapter 7, trabecula-specific models are calibrated to normalised AP data recorded *ex vivo* under various conditions with I_{Kr} and I_{CaL} inhibition (introduced in Chapter 4). To select the parameters to calibrate, the methods studied in this Chapter are applied.

Acknowledgements

The Genotype-Tissue Expression (GTEx) Project was supported by the Common Fund of the Office of the Director of the National Institutes of Health, and by NCI, NHGRI, NHLBI, NIDA, NIMH, and NINDS. The data used for the analyses described in this

manuscript were obtained from: the GTEx Portal on 12/05/2021. The ReCount2 protocol was applied to the GTEx data by colleagues in, F. Hoffmann-La Roche Ltd., Pharma Research and Early Development, Pharmaceutical Sciences.

7

Calibration of a human ventricular action potential model for prediction of changes in action potential duration induced by acute inhibition of two major ionic currents

Preamble

Drug-induced inhibition of the rapid delayed rectifier K^+ current (I_{Kr}) prolongs the action potential (AP) duration (APD), which is associated with prolongation of the QT interval, a risk factor for proarrhythmia. Pre-clinical guidelines for cardiac safety assessment focus on I_{Kr} inhibition measured in vitro as a safety marker. New AP data acquired ex vivo in adult human ventricular trabeculae (Chapter 4) and previous studies have shown that the inhibition of the L-type Ca^{2+} current (I_{CaL}) mitigates the APD prolongation induced by I_{Kr} inhibition, and the subsequent proarrhythmic risk. Drugs inhibiting concurrently I_{Kr} and I_{CaL} may therefore be incorrectly deemed proarrhythmic, and potentially beneficial compounds may be unnecessarily abandoned.

Biophysically-detailed AP models have emerged as tools to integrate in vitro measurements of drug-induced inhibition of ionic currents into predictions of proarrhythmic risk. However, none of the existing AP models accurately predict APD changes induced by I_{Kr} and I_{CaL} inhibition (Chapter 5). In this Chapter, we use methods developed

in Chapter 6 to calibrate a new AP model to the new ex vivo data, to predict APD changes induced by I_{Kr} and I_{CaL} inhibition.

7.1 Introduction

In Chapter 4, drugs that inhibit simultaneously the L-type Ca^{2+} current (I_{CaL}) and the rapid delayed rectifier K^+ current (I_{Kr}) were applied to adult human ventricular trabeculae. Inhibition of I_{CaL} mitigated prolongation of the AP duration at 90% repolarisation (APD_{90}) induced by I_{Kr} inhibition. AP models available in the literature showed limited accuracy in predicting the APD_{90} response to the inhibition of I_{Kr} and I_{CaL} (Chapter 5). So far, no AP model has been calibrated to AP data generated with concomitant inhibition of I_{Kr} and I_{CaL}, thus (partially) explaining why no current AP model captures the APD_{90} response to such perturbations accurately.

In the present Chapter, we attempt to calibrate a newly reformulated version of the Grandi *et al.* (2010) (GPB) model to AP data generated in adult human ventricular trabeculae under various conditions of drug-induced I_{Kr} and I_{CaL} inhibition, that we presented in Chapter 4.

Following the two-step process for model calibration described in Chapter 6, the AP data are split into a training dataset (five drugs, 57 trabeculae), and a validation dataset (four drugs, 37 trabeculae).

First, the training dataset is *naive-pooled* (Sheiner & Beal, 1980), that is, the AP data recorded in all trabeculae exposed to training drugs are used at the same time, as though they were generated from a single generic trabecula. With this approach, a version of the new AP model corresponding to a generic trabecula is created, denoted "Gen-NP", for "Generic model calibrated with a Naive-Pooled approach". Predictions by the Gen-NP model are then tested against the validation dataset, ΔAPD_{90} predictions are visually assessed in a 2-D map (as in Chapter 5), and we calculate the error measure for ΔAPD_{90} predictions (Eq. 5.2), which was previously used to compare model predictions in Chapter 4.

Trabecula-specific models are then trained on normalised AP data using each of the 57 trabeculae constituting the training dataset, and using the Gen-NP model as an

initial guess for parameter exploration. Thus, a collection of trabecula-specific models is created and denoted "Col-NP", for "Collection of trabecula-specific models using the Gen-NP model as initial guess".

Col-NP is similar in its aim to a population of models (Britton *et al.*, 2013). However, an important distinction must be made between the two approaches. Populations of AP models are typically calibrated by retaining parameterisations of AP models which match experimental ranges of AP markers such as RMP, peak voltage and APD_{90}. Here, each model constituting Col-NP has been individualised to data recorded in a specific trabecula.

As previously investigated in Chapter 6, the optimal set of parameters to individualise may not necessarily include all the identifiable parameters when the model is imperfect. Therefore, the collection of trabecula-specific models is calibrated with different sets of individualised parameters.

Drug-induced I_{Kr} and I_{CaL} inhibition, used as input for the simulations of this Chapter, are computed with a Hill equation (Hill, 1910), using the *in vitro* data presented in Chapter 4. To make a first assessment of our sensitivity to data variability, four *in vitro* datasets can be created by combining the two *in vitro* datasets (CiPA and Pharm, Table 4.2) for two channels. The calibration of the new AP model is repeated with each of these four datasets, labelled Dataset #1 through #4. Doing so, the most predictive model, coupled with the most predictive *in vitro* dataset, is identified, paving the way for improved integration of *in vitro* data into *in silico* predictions of the preclinical cardiac safety of small molecules.

7.2 Methods

In this section, we describe how the *ex vivo* tissue data and the *in vitro* screening data were used for model calibration. Then, we describe the methods for model training and validation, which were designed using the lessons learned from previous Chapters.

7.2.1 Action potential data

The AP data used in this work were presented in Chapter 4. Briefly summarised, AP data were recorded by the AnaBios Corporation at 37°C with the sharp electrode recording

technique, in isolated cardiac muscle fibers extracted from adult human ventricular trabeculae of the inner endocardial wall and exposed to increasing concentrations of various drugs. The AP data used for model training were recorded at steady-state after 25 min of 1 Hz steady pacing (Figure 4.5). For more information on the recording protocol, see Page *et al.* (2016) and Chapter 4.

Different trabeculae were exposed to nine drugs, used either for model training or for model validation. Each trabecula was exposed to increasing concentrations of one drug (Tables 4.3–4.4).

The AP data were generated in two phases (2014–2016 and 2019–2022). In Phase 2 experiments, an additional bioanalytical analysis of the bath solution was performed to measure whether the drug concentrations present in the bath solution, "measured concentrations", where the same as those intended, "nominal concentrations" (Section 4.11).

Note that the AP data for Dofetilide and Nifedipine were recorded with concomitant administration of both drugs in Phase 2 experiments. The AP data recorded under conditions with two concomitant drugs were excluded from the dataset and only AP data recorded under single drug treatment was used for model development (Section 4.10). Only the data for single drug treatment were used for model calibration.

The drugs used for the generation of the AP data for model training and validation, the number of tested trabeculae, and the number of trabeculae for which the bioanalysis of the bath solution was performed are summarised in Table 7.1.

Use	Drug	Number of trabeculae	Drug concentrations measured
Training	Chlorpromazine	6	6/6
	Dofetilide	21	6/21
	Nifedipine	11	7/11
	Thioridazine	4	4/4
Validation	Clozapine	11	6/11
	Fluoxetine	5	5/5
	Mesoridazine	6	6/6
	Quinidine	15	0/15

Table 7.1: Drugs used for model training and for model validation.

AP data post-processing was also described in Chapter 4. In brief, 895 ms of recording for each AP were used for model calibration to exclude stimulation artefacts, 60 Hz harmonics were filtered out, and APs were normalised using the resting membrane potential (RMP) and the peak voltage (V_{95}) as reference points (Eq. 4.3).

7.2.2 Data for in vitro ion channel inhibition

As in the previous Chapters, drug effects were modelled as simple pore block, with the reduction of the affected current computed with the Hill equation (Hill, 1910):

$$I(D) = \frac{1}{1 + \left(\frac{D}{\text{IC50}}\right)^h} \times I(0), \tag{7.1}$$

with $I(D)$ the current with drug effect, D the drug concentration, h the Hill coefficient, IC_{50} the half-maximal inhibitory drug concentration, and $I(0)$ the ionic current without drug effect.

Similarly to Chapter 5, I_{Kr} and I_{CaL} inhibition were computed using the measured drug concentration, if available (Phase 2 data). Otherwise, the nominal drug concentration was used.

Values for IC_{50} and h are reported in Table 4.2. As detailed previously in Section 4.3, IC_{50} and h were measured with voltage-step patch-clamp experiments, using two different voltage-step protocols for the inhibition of each ionic current (I_{Kr} CiPA, I_{Kr} Pharm, I_{CaL} CiPA, and I_{CaL} Pharm). Their combinations create four datasets of IC_{50} and h, reported in Table 7.2. Note that IC_{50} Datasets #1 and #2 correspond to the datasets called "CiPA" and "Pharm" in Chapter 4.

7.2.3 Simulations with *in silico* AP models

The Grandi *et al.* (2010) (GPB) model reformulated by Mann *et al.* (2016) (GPB-M) was qualitatively and quantitatively among the most predictive existing AP models in Chapter 5. We applied some changes to it in this work, by:

- Unclamping the intracellular concentrations of K^+ and Cl^- ions, thus allowing for rewriting the voltage equation in its algebraic form, as recommended in Chapter 3 (details in Section E.1 in the Appendix);
- Adjusting the I_{Kr} component to 37°C by using the model developed by Lei *et al.* (2019), thus matching the temperature at which the AP data were recorded.

Dataset for model inputs	Voltage-step protocol for measuring I_{Kr} inhibition	Voltage-step protocol for measuring I_{CaL} inhibition
Dataset #1	I_{Kr} CiPA (Kramer *et al.*, 2020)	I_{CaL} CiPA (Li *et al.*, 2019)
Dataset #2	I_{Kr} Pharm (Chapter 4)	I_{CaL} Pharm (Chapter 4)
Dataset #3	I_{Kr} CiPA (Kramer *et al.*, 2020)	I_{CaL} Pharm (Chapter 4)
Dataset #4	I_{Kr} Pharm (Chapter 4)	I_{CaL} CiPA (Li *et al.*, 2019)

Table 7.2: Four datasets for IC_{50} and h were created from the four combinations of voltage-step protocols used to measure the drug-induced inhibition of I_{Kr} and I_{CaL}.

These changes were made so that the new AP model predicts higher APD_{90} change from baseline (ΔAPD_{90}) with selective I_{Kr} inhibition than the GPB model, while preserving the mitigation by I_{CaL} inhibition of APD_{90} prolongation induced by the I_{Kr} inhibition (Chapter 5).

The GPB-M model used in Chapter 5 was reused to construct the new AP model. Simulations with the new AP model were performed with Myokit 1.33.9 (Clerx *et al.*, 2016) and CVODE 5.7.0 (Hindmarsh *et al.*, 2005). The absolute and relative solver tolerance were both set to 10^{-9} to ensure numerical accuracy of simulations.

The model was paced at 1 Hz for 750 s to bring it close to steady-state (Section E.2 in the Appendix). The simulated AP was read out with a 0.05 ms resolution, matching that of the experimental data.

The external ionic concentrations were set to values matching with the ionic concentrations in the bath solution, reported in Table 7.3. Unless stated otherwise, initial values for internal concentrations were left at their original CellML values.

Species	K^+	Ca^{2+}	Na^+	Cl^-
External concentration	4 mM	1.8 mM	148.35 mM	143.6 mM

Table 7.3: Values for external ionic concentrations used in simulations, matching with ionic bath concentrations used during ex vivo recordings.

Similarly to previous Chapters, the conductance parameters were not directly changed during calibration, but a log-transformed scaling factor was applied instead, which enables

better exploration of the search space by optimisers (Whittaker *et al.*, 2020). Therefore, the values of the conductance (and permeability) parameters G used for simulations in the present Chapter were computed as:

$$G = \bar{G} \times e^{\hat{g}}, \tag{7.2}$$

with $\bar{G}$ the parameter value in the GPB-M model, and $\hat{g}$ the associated log-transformed scaling factor.

It was previously observed in Chapter 6 with the Ten Tusscher & Panfilov (2006) (TP) model that a chaotic "multi-AP alternans" phenomenon may occur, which limits the identifiability of model parameters (Section D.4 in the Appendix). To avoid a similar phenomenon with the new AP model during fitting, 25 consecutive APs were simulated after pre-pacing, and they were checked for multi-AP alternans. Whenever multi-AP alternans was observed, a negative infinite likelihood was returned.

The methods for simulations are summarised in Figure 7.1.

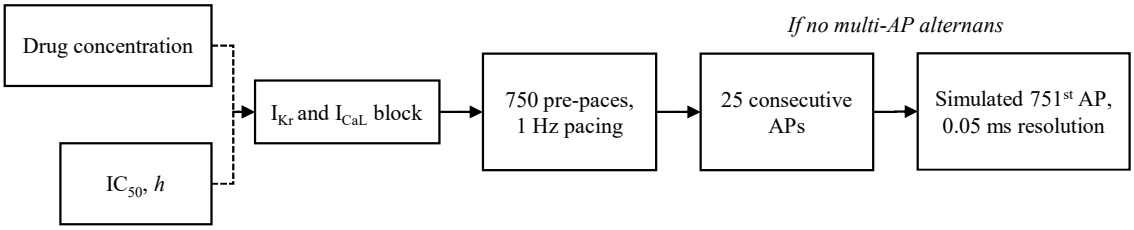

Figure 7.1: Summary of methods used to run simulations to calibrate the new AP model in this study. If the effect of a drug was taken into account for the simulation, the I_{Kr} and I_{CaL} inhibition were computed with Eq. 7.1.

7.2.4 Model training

Action potential model for a generic trabecula (Gen-NP)

The AP data obtained in all 57 trabeculae exposed to training drugs (Table 7.1) were naive-pooled (Sheiner & Beal, 1980). The log-likelihood of the vector of parameters θ_{NP} was computed assuming that the noise followed a independent identically distributed Gaussian distribution at each time point (Section 2.5.1):

$$\ell_{NP}(\theta_{NP}) = -\frac{N_{NP}}{2}\ln 2\pi - N_{NP}\ln\sigma_y - \frac{1}{2\sigma_y^2}\sum_{trab}\sum_{c}\sum_{t}\left(y^*_{c,trab}(t) - y_c(\theta_{NP}, t)\right)^2, \tag{7.3}$$

with N_{NP} the total number of time points in the training dataset, σ_y the standard deviation of the noise, $y^*_{c,trab}$ the normalised AP data recorded under the experimental condition with drug c to which the trabecula $trab$ was exposed, and $y_c(\theta_{NP})$ the normalised AP under c simulated with the new AP model parameterised with θ_{NP}. $\sigma_y = 0.001$ was estimated from variations of the normalised AP data during the resting phase. Note that the same weight was attributed to the AP data from all trabeculae.

The identifiability test of model parameters and the selection of parameters included in θ_{NP} (G_{Kr}, G_{CaL}, G_{K1}, G_{NaCa}, G_{NaK}, G_{Ks}, and G_{ClCa}) are detailed in Section E.2 in the Appendix. The vector of parameter estimates (θ^*_{NP}) was found by maximising ℓ_{NP}.

The generic AP model trained using Dataset #X is labelled "Gen-NP#X" in the following.

Trabecula-specific models

The Gen-NP model was used to define the search space for trabecula-specific parameters: $\bar{G}$ (Eq. 7.2) was replaced by the value of the conductance parameters in the Gen-NP model. Then, a trabecula-specific model was trained on the AP data in each of the 57 trabeculae exposed to training drugs.

The trabecula-specific parameter estimates, θ^*_{trab}, for the trabecula $trab$ were found by maximising the log-likelihood ℓ_{trab} computed with the same assumptions as ℓ_{NP} (Eq. 7.3):

$$\ell_{trab}(\theta_{trab}) = -\frac{N_{trab}}{2}\ln 2\pi - N_{trab}\ln\sigma_y - \frac{1}{2\sigma_y^2}\sum_c\sum_t\left(y^*_{c,trab}(t) - y_c(\theta_{trab},t)\right)^2, \quad (7.4)$$

with N_{trab} the total number of time points in the AP data for trabecula $trab$.

Parameters included in θ_{trab} were selected among the three identifiable parameters (G_{Kr}, G_{CaL}, G_{NaK}) (Section E.4 in the Appendix). Applying the same logic as in Chapter 6, two collections of trabecula-specific models were created by individualising (G_{Kr}, G_{CaL}) and (G_{Kr}, G_{CaL}, G_{NaK}), denoted "Col-NP$_2$" and "Col-NP$_3$" in the following, respectively. Note that parameters that were not individualised were left to values corresponding to θ^*_{NP}.

Finding parameter estimates that maximise ℓ_{trab} defines an optimisation problem. To be confident that the vector of found estimates θ^*_{trab} correspond to the global maximum of ℓ_{trab}, 10 repeats of the same optimisation problem were necessary (Section E.4). Training 57 trabecula-specific models therefore required solving $57\times10 = 570$ optimisation problems.

Individualising two different sets of parameters totals 1140 optimisation problems, which comes at a large computational cost. Therefore, the computational cost of this study was kept as low as possible by calibrating only two collections of trabecula-specific models (Col-NP$_2$ and Col-NP$_3$), using the most predictive Gen-NP model as a starting point. The dataset for IC$_{50}$ and h enabling the most predictive Gen-NP model was reused for the calibration of Col-NP$_2$ and Col-NP$_3$.

Methods for finding parameter estimates

The optimisation problems encountered in this Chapter were solved with the Covariance Matrix Adaptation Evolution Strategy (CMA-ES) algorithm (Hansen, 2016) implemented in the `PINTS` Python package (Clerx *et al.*, 2019). Different settings for the CMA-ES algorithm were used for training the Gen-NP models and the trabecula-specific models constituting Col-NP$_2$ and Col-NP$_3$. Settings used for solving the three optimisation problems of this Chapter are summarised in Table 7.4. Values indicated for Σ_0, the initial proposal covariance matrix for new parameter samples, correspond to the value of diagonal elements; non-diagonal elements were set to 0. The justification of these settings is provided in Sections E.3–E.4 in the Appendix.

Optimisation problem	Setting	Value
Gen-NP training	Training data	Naive-pooled normalised APs from 57 trabeculae
	Objective function	ℓ_{NP} (Eq. 7.3)
	Estimated parameters	G_{Kr}, G_{CaL}, G_{K1}, G_{NaCa}, G_{NaK}, G_{Ks}, G_{ClB}
	Search space	$-5 < \hat{\mathrm{g}} < +5$
	$\mathcal{N}$	12
	Σ_0	4
	Random starting points	50
Col-NP training	Training data	Normalised APs recorded in a single trabecula
	Objective function	ℓ_{trab} (Eq. 7.4)
	Estimated parameters	(G_{Kr}, G_{CaL}) or (G_{Kr}, G_{CaL}, G_{NaK})
	Search space	$-2.5 < \hat{\mathrm{g}} < +2.5$
	$\mathcal{N}$	6
	Σ_0	0.5
	Random starting points	10

Table 7.4: Summary of methods used for model training with the different approaches.

In trabecula-specific models, $\bar{G}$ was replaced by parameter values in the Gen-NP model, and the search space was constrained to a width similar to the inter-individual

variability in conductance parameters estimated from RNA sequencing data in Section 6.2.

7.2.5 Uncertainty in parameter estimates

The surface of the log-likelihood over the parameter space was visualised using the "ensemble modelling approach" by Villaverde *et al.* (2015), introduced in Section 2.5.1. The ensemble modelling approach reuses the evaluation of the log-likelihood (Eq. 7.3 or Eq. 7.4) for all the points of the parameter space sampled by the optimisation algorithm (CMA-ES in the present case). This method therefore produces a rough but readily-available approximation of the uncertainty in parameter estimates.

The parameter estimate found after model training, ℓ^*, corresponds to the parameter value yielding the maximum of ℓ. The 95% confidence interval in parameter estimates was calculated as the range of parameter values that yield a log-likelihood within a 1.92 tolerance range in ℓ around ℓ^*. For more details, please refer to Section 2.5.1 or Villaverde *et al.* (2019).

7.2.6 Evaluation of ΔAPD_{90} predictions by the trained model

The AP response to the four validation drugs (Table 7.1) was simulated with the Gen-NP#1 through Gen-NP#4 models and with all trabecula-specific models in Col-NP_2 and Col-NP_3. ΔAPD_{90} predictions were then compared with ΔAPD_{90} measured *ex vivo*: for a given condition with drug, ΔAPD_{90} predictions within the mean experimental ΔAPD_{90} $\pm$ two times the standard error in the mean (σ_M) were considered acceptable.

The error metric, E (Eq. 5.2), was calculated to compare predictions by the various models created in the present Chapter with predictions by models from the literature, as in Chapter 5. ΔAPD_{90} predictions by the GPB-M were generated with exactly the same methods as the new AP model, and used as a benchmark.

Model predictions were also assessed qualitatively by plotting the 2-D map of ΔAPD_{90} as a function of I_{Kr} and I_{CaL} inhibition, with the same methods as described previously in Chapter 5 (Figure 5.2).

7.3 Results

7.3.1 Action potential model for a generic individual, calibrated to the naive-pooled data

Model training

Parameter estimates θ^*_{NP} obtained after model training using the four *in vitro* screening datasets are reported in Table 7.5.

Model	$\ell_{NP}(\theta^*_{NP})$	$\hat{g}_{Kr}$	$\hat{g}_{CaL}$	$\hat{g}_{K1}$	$\hat{g}_{NaCa}$	$\hat{g}_{NaK}$	$\hat{g}_{Ks}$	$\hat{g}_{ClB}$
Gen-NP#1	-1.310×10^{10}	−4.16	0.55	0.32	−0.41	−1.41	−1.22	0.24
Gen-NP#2	-1.241×10^{10}	−4.11	0.62	0.33	−0.37	−0.93	−2.19	0.48
Gen-NP#3	-1.258×10^{10}	−4.12	0.59	0.32	−0.33	−0.91	−2.38	0.46
Gen-NP#4	-1.285×10^{10}	−4.12	0.58	0.34	−0.40	−1.40	−1.17	0.26

Model	$\ell_{NP}(\theta^*_{NP})$	G_{Kr} (mS/μF)	G_{CaL} (cm/s)	G_{K1} (mS/μF)	G_{NaCa} (A/F)	G_{NaK} (A/F)	G_{Ks} (mS/μF)	G_{ClB} (mS/μF)
Gen-NP#1	-1.310×10^{10}	0.015	4.97×10^{-4}	0.177	11.1	0.442	0.026	0.017
Gen-NP#2	-1.241×10^{10}	0.015	5.33×10^{-4}	0.179	11.5	0.718	0.010	0.022
Gen-NP#3	-1.258×10^{10}	0.015	5.15×10^{-4}	0.177	11.9	0.727	0.008	0.021
Gen-NP#4	-1.285×10^{10}	0.015	5.14×10^{-4}	0.180	11.2	0.446	0.027	0.017

Table 7.5: Scaling factors, $\hat{g}$ (Eq. 7.2), and corresponding parameter estimates in the four Gen-NP models. The log-likelihood ℓ_{NP} was computed with Eq. 7.3.

Similar maxima of ℓ_{NP} were obtained in model training with the four IC_{50} datasets. The highest ℓ_{NP}, i.e., the best fit, was achieved with the model Gen-NP#2 ($\ell_{NP} = -1.241 \times 10^{10}$).

The distance between the parameter estimates corresponding to the Gen-NP models was small, in comparison with the size of the search space ($-5 < \hat{g} < +5$ for all parameters). The biggest variations in the scaling factors are for G_{Ks}, with $-2.38 < \hat{g}_{Ks} < -1.17$. An even smaller distance was observed between the parameter estimates corresponding to the Gen-NP#1 and the Gen-NP#4 models, and between the parameter estimates corresponding to the Gen-NP#2 and the Gen-NP#3 models.

The APs under baseline conditions simulated with the four Gen-NP models are shown in Figure 7.2.

To qualitatively assess the goodness-of-fit of the Gen-NP models, ΔAPD_{90} predictions by the Gen-NP models were computed for all the drug conditions used for model training, and compared with ΔAPD_{90} observed experimentally in the corresponding trabeculae (Figure 7.3).

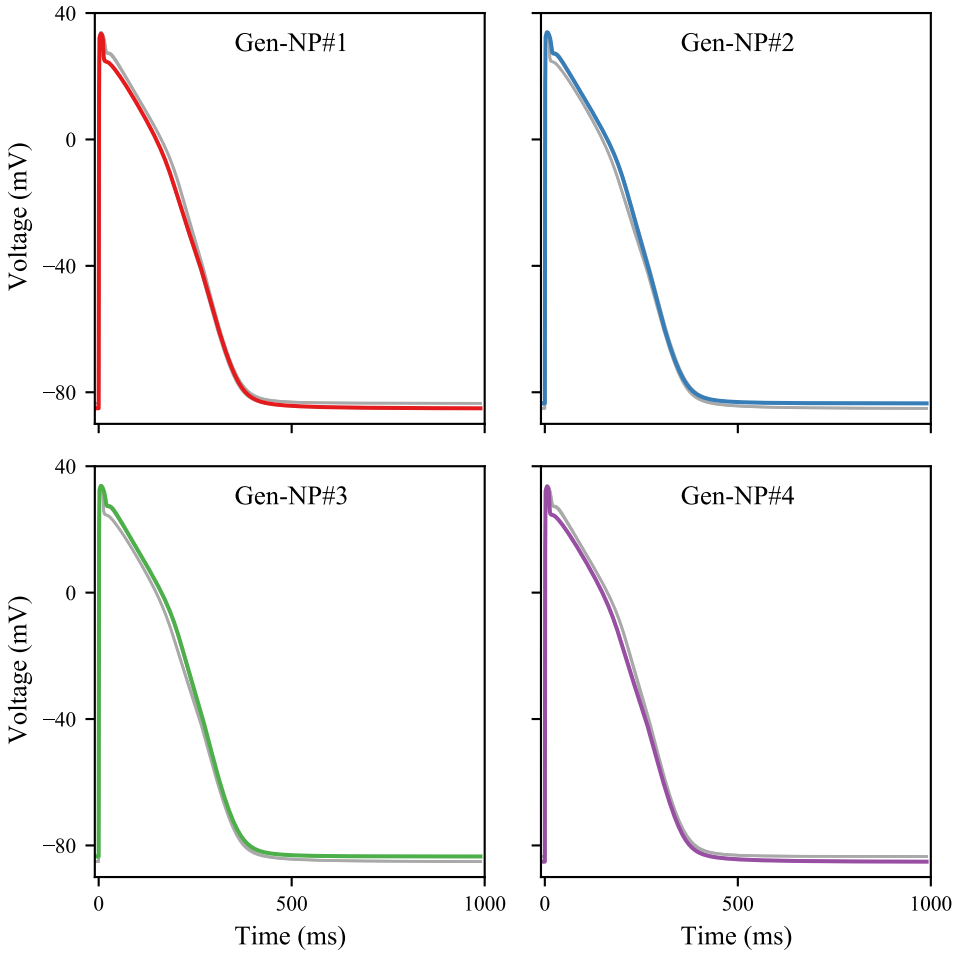

Figure 7.2: AP simulated under baseline condition with the four Gen-NP models. In each panel, the three other baseline APs are plotted in grey for comparison.

Overall, the similarities in θ^*_{NP} led to similar ΔAPD_{90} predictions. The mitigation of I_{Kr} inhibition by I_{CaL} inhibition (Chlorpromazine, Thioridazine, Verapamil) could be reproduced by the model, at the same time as the marked APD_{90} prolongation induced by selective I_{Kr} inhibition (Dofetilide). The predicted ΔAPD_{90} were within the experimental range for Chlorpromazine, Dofetilide, Thioridazine and Verapamil, except for 10 nM Dofetilide where the predicted ΔAPD_{90} ($+25\,\text{ms} < \Delta APD_{90} < +26\,\text{ms}$) was lower than ΔAPD_{90} observed experimentally ($+41\,\text{ms} < \Delta APD_{90} < +160\,\text{ms}$).

The shortening of APD_{90} induced by the selective inhibition of I_{CaL} by Nifedipine was less accurately reproduced, with ΔAPD_{90} predictions visibly lower than ΔAPD_{90} observed experimentally. The worst predictions of Nifedipine-induced ΔAPD_{90} were made with the Gen-NP#2 and Gen-NP#3 models, even though ℓ_{NP} was higher with these two models.

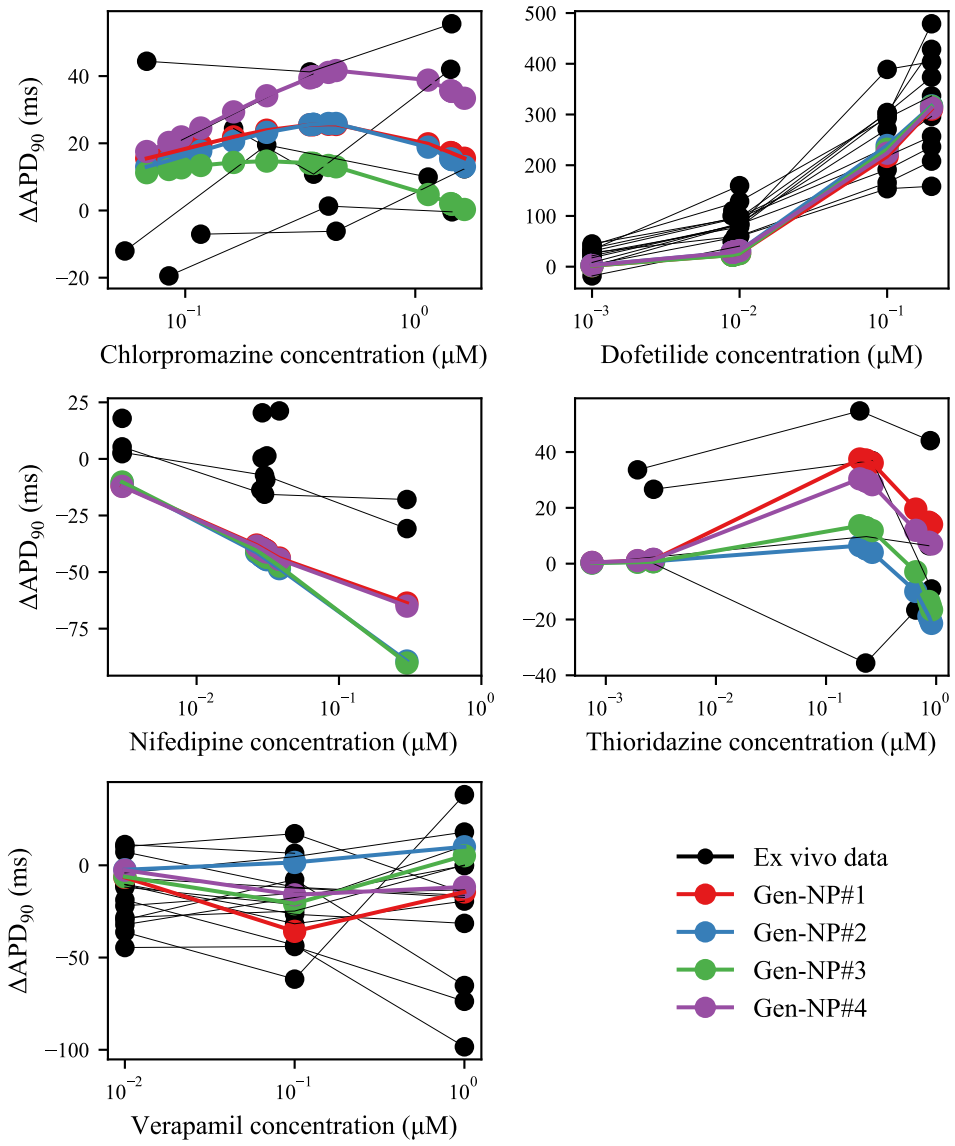

Figure 7.3: Predicted ΔAPD_{90} for the training drugs (Table 7.1), by the new AP model trained with the naive-pooled data strategy. The *ex vivo* data are shown in **black**, each line corresponding to one trabecula.

Uncertainty in parameter estimates

In Figure 7.4, ℓ_{NP} (Eq. 7.3) is plotted as function of the parameter value for all the points of the parameter space explored by the CMA-ES algorithm.

For most parameters, the region corresponding to high ℓ was narrow, meaning that the uncertainty in parameter estimates is low. In contrast, the flat surface of ℓ as a function of $\hat{g}_{Ks}$ suggests that the uncertainty is higher in the estimate of G_{Ks} than other parameters. With the likelihood ratio method and the threshold in ℓ of 1.92 for the 95%

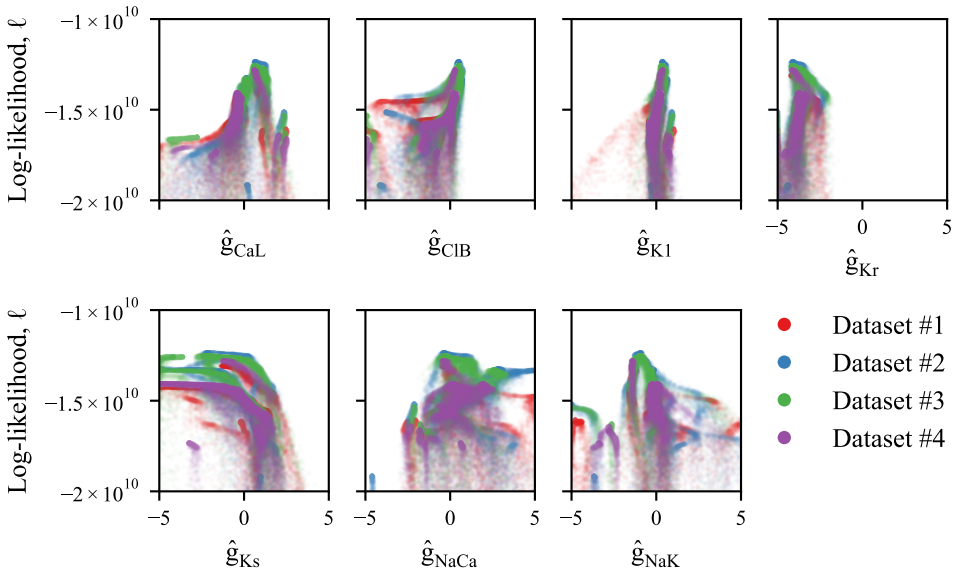

Figure 7.4: Log-likelihood ℓ_{NP} (Eq. 7.3) as a function of parameter values sampled during model training. Each point corresponds to one sample in the parameter space explored by the CMA-ES algorithm during model training with the four IC_{50} datasets listed in Table 7.2.

confidence interval, the uncertainty in the scaling factors was lower than 10^{-5}, for all parameters including G_{Ks}. Such a low uncertainty in parameter estimates does not make any noticeable difference in model predictions (e.g., Figure 4.14). As a conclusion, the estimated uncertainty was negligible in all parameter estimates obtained during model training with the naive-pooled data strategy[1].

Validation of ΔAPD_{90} predictions by the Gen-NP models

ΔAPD_{90} predictions for the validation drugs by the Gen-NP models are shown in Figure 7.5.

Predictions of ΔAPD_{90} by the four Gen-NP models were similar, except for high drug concentrations. Predictions of ΔAPD_{90} by the Gen-NP models were acceptable for low Clozapine concentrations (only Gen-NP#1 and Gen-NP#4), Mesoridazine 40 nM, Quinidine 100 nM, and Quinidine 10 μM (only Gen-NP#1 and Gen-NP#2). The Gen-NP#4 model was the only Gen-NP model producing acceptable predictions of ΔAPD_{90} induced by 3 μM Fluoxetine and 10 μM Mesoridazine.

[1]The calculation of ℓ_{NP} (Eq. 7.3–7.4) relies on the assumption that the model was trained without model discrepancy and that the noise model is correct. Although making these assumptions presents practical advantages, this leads to overconfidence in parameter estimates (Lei *et al.*, 2020).

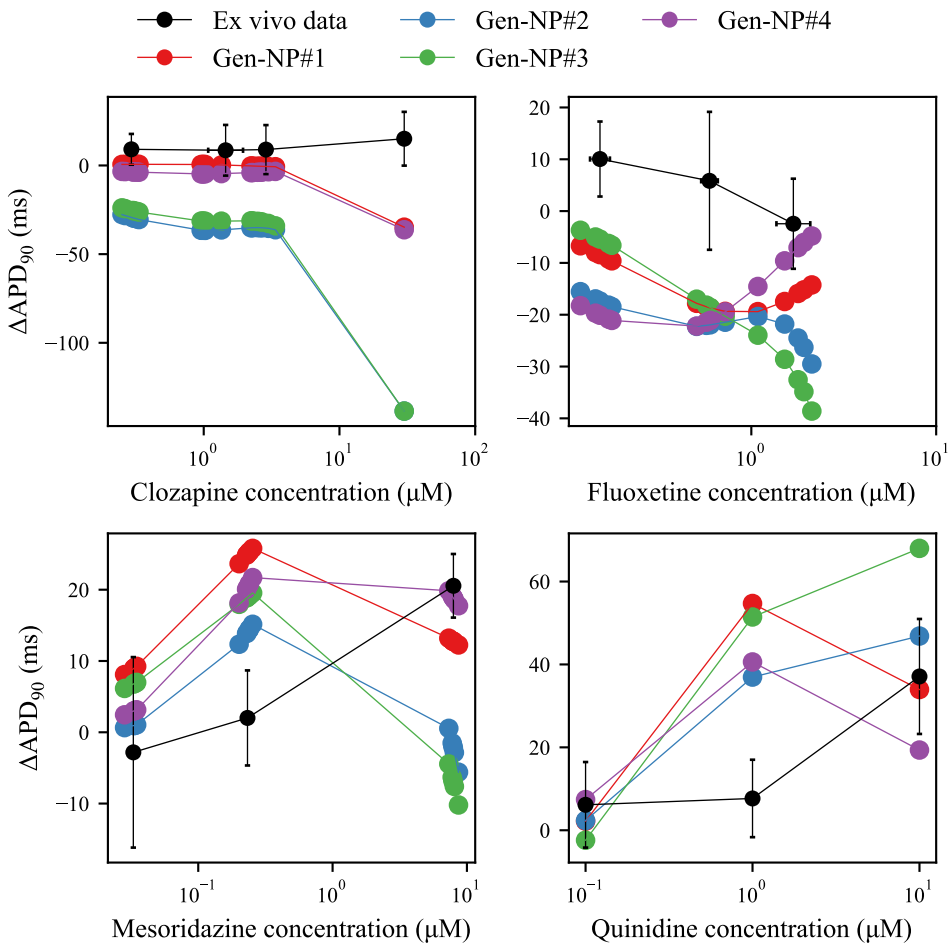

Figure 7.5: ΔAPD_{90} predicted by the Gen-NP models for the four validation drugs (Table 7.1). Here, the *ex vivo* data (**black**) are grouped by nominal drug concentration. Error bars indicate two σ_M.

ΔAPD_{90} induced by 30 μM Clozapine ($+15 \pm 9$ ms) was underpredicted by the four Gen-NP models, in particular with the Gen-NP#2 and the Gen-NP#3 models ($\Delta APD_{90}=-139$ ms). Also, ΔAPD_{90} induced by 1 μM Quinidine ($+8\pm5$ ms) and 250 nM Mesoridazine ($+2 \pm 4$ ms) was overpredicted by all Gen-NP models ($+55$ ms and $+25$ ms predicted by the Gen-NP#1 model for Quinidine and Mesoridazine, respectively).

Predictions of ΔAPD_{90} induced by increasing concentrations of Mesoridazine and Quinidine were non-monotonic with the Gen-NP models, which was not observed experimentally. A similar (although less marked) pattern was observed for predictions of ΔAPD_{90} induced by Fluoxetine by the Gen-NP#1 and Gen-NP#4 models.

The lowest error measure $E = 81.5$ (Eq. 5.2) was achieved with the Gen-NP#4 model.

E was lower with the Gen-NP#4 model than with the GPB model reformulated by Mann *et al.* (2016) (GPB-M), used to construct the new AP model ($E \geq 102.0$). Nevertheless, the Ten Tusscher & Panfilov (2006) (TP) model remains the model with the lowest error measure ($E = 79.0$ with Dataset #1, Figure 5.5). The other 10 AP models for which E was computed in Chapter 5 yielded a higher error measure than the Gen-NP#4 model ($E \geq 86.3$). Details of the error measure calculated from ΔAPD_{90} predictions by the four Gen-NP models are provided in Section E.5 in the Appendix.

Visual assessment of ΔAPD_{90} predictions by the generic AP models

As previously discussed in Section 5.4, E is biased by the selection of a majority of drugs that induce small changes in ΔAPD_{90}. The comparison of the predictivity of AP models can therefore be complemented by qualitatively comparing the 2-D map of ΔAPD_{90} predictions by the Gen-NP models with predictions by existing AP models (Figure 5.3) and with the experimental ΔAPD_{90} (Figure 4.20).

The 2-D maps of ΔAPD_{90} predicted by the Gen-NP models as a function of I_{Kr} and I_{CaL} inhibition are shown in Figure 7.6, together with the mean experimental ΔAPD_{90} across all trabeculae exposed to the same nominal drug concentration (Table 4.7). Model predictions were in qualitative agreement with the experimental data, with little or no prolongation of APD_{90} induced by mixed I_{Kr} and I_{CaL} inhibition, and marked prolongation of APD_{90} induced by selective inhibition of I_{Kr}.

The similarities observed in θ^*_{NP} corresponding to the four Gen-NP models (Table 7.5) transferred as well to the 2-D maps of ΔAPD_{90} prediction. The 2-D maps were overall similar for the four Gen-NP models but the upper right quarter of the maps differed. The points of ΔAPD_{90} measured experimentally with Verapamil (blue-grey points in the middle of the 2-D maps) were the most variable between the IC_{50} datasets used to compute I_{Kr} and I_{CaL} block. These points correspond to data used in model training, hence the differences in the 2-D maps. The ΔAPD_{90} surfaces predicted by the Gen-NP#1 and the Gen-NP#4 models exhibited qualitatively good agreement with the experimental ΔAPD_{90}, with no outliers from the surface.

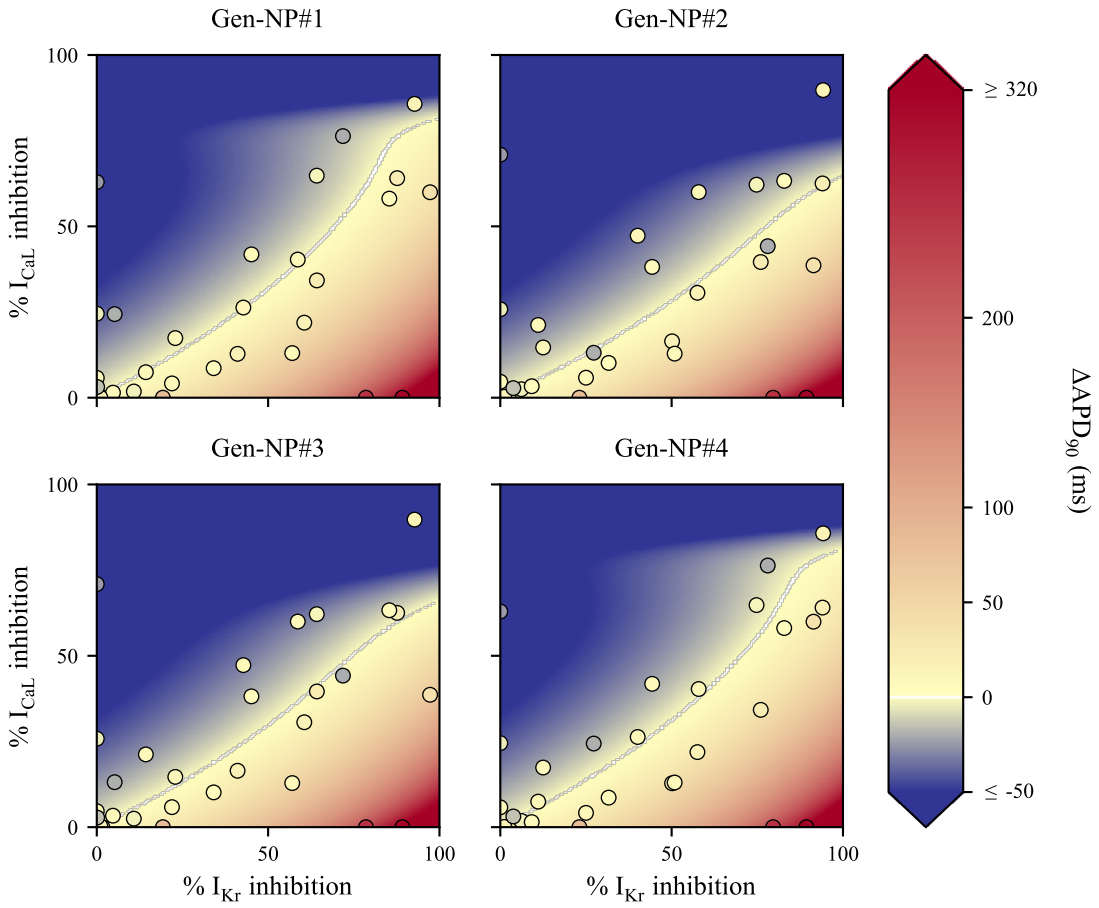

Figure 7.6: 2-D maps of ΔAPD_{90} predicted by the four Gen-NP models, as a function of I_{Kr} and I_{CaL} inhibition. **Circles**: *ex vivo* data points, reported from Figure 4.20.

For comparison, the 2-D map of ΔAPD_{90} predictions by the TP model, yielding a lower value of E than the Gen-NP#4 model, was visibly less in agreement with the experimental ΔAPD_{90} observations (Figure 5.3). The Gen-NP#4 model yielded more accurate predictions of ΔAPD_{90} response to selective I_{Kr} and selective I_{CaL} inhibition than the models based on the TP and the GPB models. Furthermore, predictions of ΔAPD_{90} induced by mixed I_{Kr} and I_{CaL} inhibition by the Gen-NP#4 model were visibly more accurate than predictions by the models similar to the ORd model.

As a conclusion, predictions of ΔAPD_{90} response to I_{Kr} and I_{CaL} inhibition were improved with the Gen-NP#4 model in comparison with AP models available in the literature. Qualitative agreement with the experimental ΔAPD_{90} was achieved, but quantitative interpretation of model predictions remains subject to caution.

7.3.2 Trabecula-specific models

Col-NP$_2$ and Col-NP$_3$ were calibrated using the Gen-NP#4 model as a starting point, and using Dataset #4 for IC_{50} and h.

Parameter estimates

The scaling factors corresponding to the trabecula-specific parameter estimates in Col-NP$_2$ and Col-NP$_3$ are shown in Figure 7.7, and the mean of the scaling factors corresponding to trabecula-specific parameter estimates is reported in Table 7.6.

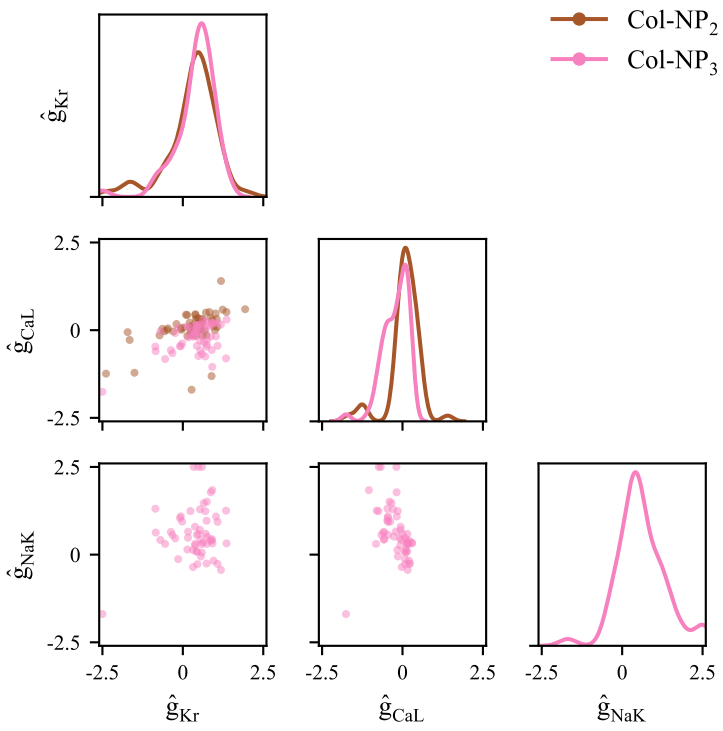

Figure 7.7: Scaling factors corresponding to the trabecula-specific parameter estimates found for the 57 trabeculae used for model training. $\hat{g} = 0$ (Eq. 7.2) corresponds to the parameter value in the Gen-NP#4 model, which was used as a starting point.

Collection of models	Sum of ℓ_{trab}	Mean $\hat{g}_{Kr}$	Mean $\hat{g}_{CaL}$	Mean $\hat{g}_{NaK}$
Col-NP$_2$	-3.321×10^9	0.28	0.07	
Col-NP$_3$	-2.254×10^9	0.40	-0.22	0.62

Table 7.6: Mean of the scaling factors corresponding to the trabecula-specific parameter estimates in Col-NP$_2$ and Col-NP$_3$. The cost function ℓ_{trab} was computed with Eq. 7.4 with each trabecula-specific model and summed over the collection of models.

The distributions of $\hat{g}_{Kr}$ and $\hat{g}_{CaL}$ in Col-NP$_2$ and Col-NP$_3$ are similar. Most trabecula-

specific parameter estimates (110/114) were within the search space ($-2.5 < \hat{g} < +2.5$), which was estimated from the RNA-Seq data (Figure 6.3). A weak correlation was observed between trabecula-specific estimates of $\hat{g}_{Kr}$ and $\hat{g}_{CaL}$ in Col-NP$_2$ (Pearson $r = 0.51$) and Col-NP$_3$ (Pearson $r = 0.48$). Note that the distributions of parameter estimates in Col-NP$_2$ and Col-NP$_3$ were not centered on $\hat{g} = 0$, although this value corresponds to the parameter value in the Gen-NP#4 model, which represents a generic individual.

The sum of ℓ_{trab} over the 57 trabeculae used for model training is equivalent to ℓ_{NP}, replacing $y(\theta_{NP})$ by $y(\theta_{trab})$ in Eq. 7.3. The sum of ℓ_{trab} was lower for Col-NP$_2$ and Col-NP$_3$ than ℓ_{NP} for the Gen-NP#4 model: the goodness-of-fit in each trabecula was improved with trabecula-specific models.

ΔAPD$_{90}$ predictions for training drugs

The ΔAPD$_{90}$ response to the training drugs predicted by Col-NP$_2$ is shown in Figure 7.8. The figure consists of five panels, each corresponding to a different training drug. In each panel, the predictions of all 57 trabecula-specific models are compared with the *ex vivo* data. For some of the models, this comparison represents a test of their ability to generalize to unseen data, while for other models it represents a check on the goodness-of-fit of their predictions to the data used for training.

Overall, there was poor agreement between the ΔAPD$_{90}$ predictions by Col-NP$_2$ and the experimental data. For low concentrations of Dofetilide, Thioridazine and Verapamil, the variability in predictions of ΔAPD$_{90}$ was underestimated. For high drug concentrations, ΔAPD$_{90}$ predictions varied vastly between the models constituting Col-NP$_2$, with more than 800 ms variation between trabecula-specific predictions in the extreme case of 200 nM Dofetilide. Some models (mostly for trabeculae exposed to Verapamil, see the light green points) even predict that Dofetilide treatment shortens the APD$_{90}$ (ΔAPD$_{90}$< 0 ms). The median of ΔAPD$_{90}$ predictions by Col-NP$_2$ for 200 nM Dofetilide (+153 ms) is out of the experimental range.

Although Verapamil was not an outlier in the experimental ΔAPD$_{90}$ surface with IC$_{50}$ Dataset #4 (Figure 7.6), predictions by models for trabeculae exposed to Verapamil were visibly different from the other models in Col-NP$_2$. Selection criteria for trabeculae

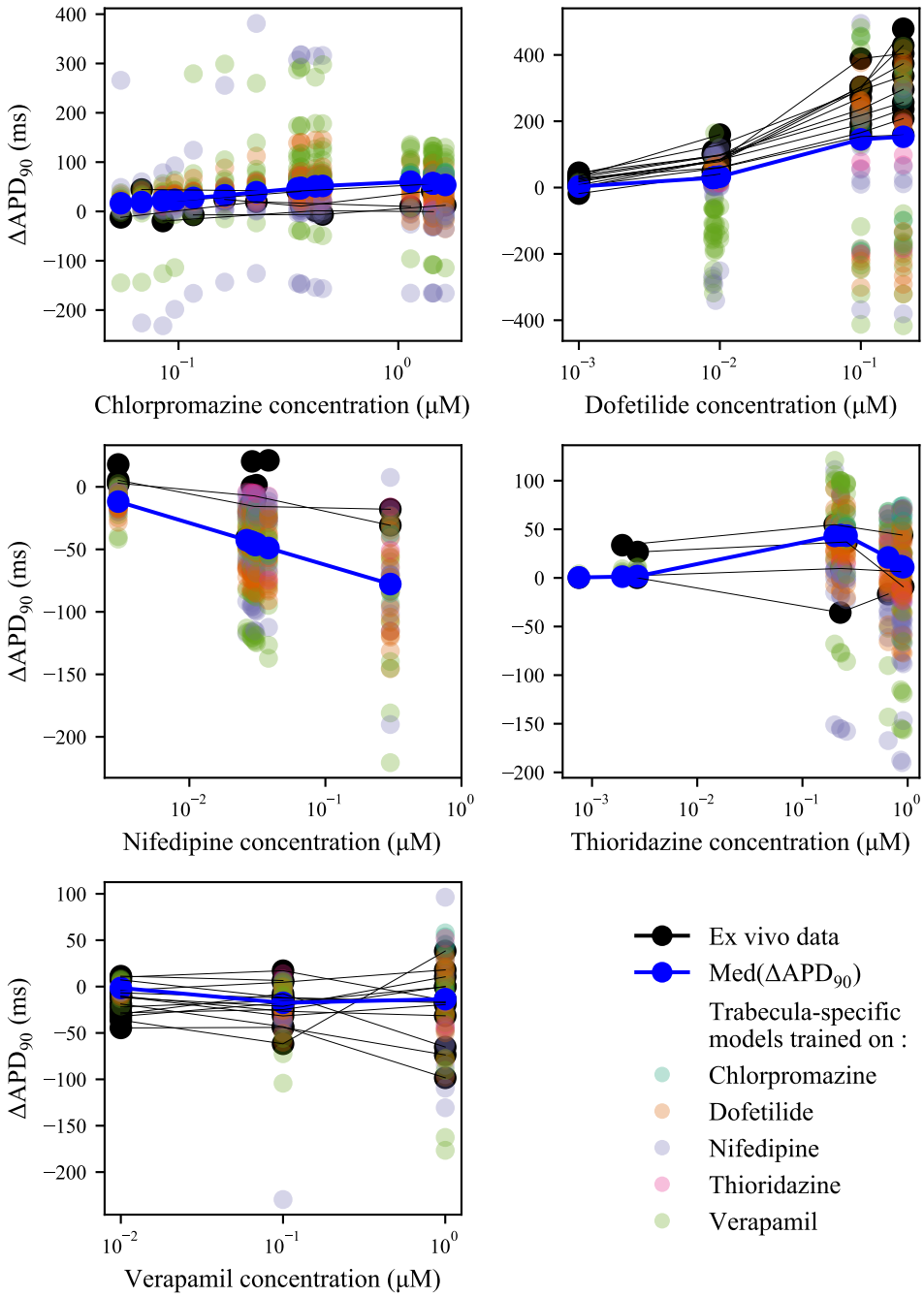

Figure 7.8: Predicted ΔAPD_{90} by Col-NP_2 for training drugs. ΔAPD_{90} observed in the 57 trabeculae used for model training are shown in **black**. The median of ΔAPD_{90} predicted by Col-NP_2 (Med(ΔAPD_{90})) is shown in **blue**.

exposed to Verapamil were not different from other trabeculae, so there was no obvious physiological reason to explain the differences in ΔAPD_{90} predictions.

Therefore, the trabecula-specific models could not be used individually to predict the drug response of specific trabeculae. The same conclusions was made for ΔAPD_{90} predictions by Col-NP_3 for training drugs (Figure E.7 in the Appendix).

However, we explored the median of ΔAPD_{90} predicted by the 57 trabecula-specific models constituting Col-NP_2, denoted "Med(ΔAPD_{90})", to see whether the errors at individual level compensate when using the collection of models. In the following, all predictions by Col-NP_2 and Col-NP_3 are reported as Med(ΔAPD_{90}). Med(ΔAPD_{90}) predicted by Col-NP_2 and Col-NP_3 are compared with predictions of ΔAPD_{90} by the Gen-NP#4 and the GPB-M models for training drugs in Figure 7.9.

Predictions by the Gen-NP#4 model, Col-NP_2 and Col-NP_3 of ΔAPD_{90} induced by Nifedipine were similar: in all cases, ΔAPD_{90} induced by Nifedipine was incorrectly predicted.

ΔAPD_{90} induced by Verapamil was best predicted by the Gen-NP#4 model and Col-NP_3: their predictions were acceptable for medium and high Verapamil concentrations, and close to acceptable for the lowest Verapamil concentration. Predictions by the GPB-M model were also acceptable, but less accurate.

The GPB-M model made the most accurate predictions of ΔAPD_{90} induced by Chlorpromazine, but predictions by the Gen-NP#4 model were similarly accurate.

ΔAPD_{90} induced by Dofetilide and Thioridazine was best predicted by the Gen-NP#4 model. Predictions of ΔAPD_{90} by Col-NP_2 and Col-NP_3 for low Thioridazine concentrations were also acceptable. Predictions of ΔAPD_{90} induced by Chlorpromazine, Dofetilide and Thioridazine were similar for the Gen-NP#4 model, Col-NP_2, and Col-NP_3 at low drug concentrations. At high drug concentrations, predictions by Col-NP_2 and Col-NP_3 were less accurate than predictions by the Gen-NP#4 model.

For all training drugs, predictions of ΔAPD_{90} by the Gen-NP#4 model were equally or more accurate than predictions by the GPB-M model. In particular, the GPB-M model underpredicted visibly the prolongation of APD_{90} induced by 200 nM Dofetilide

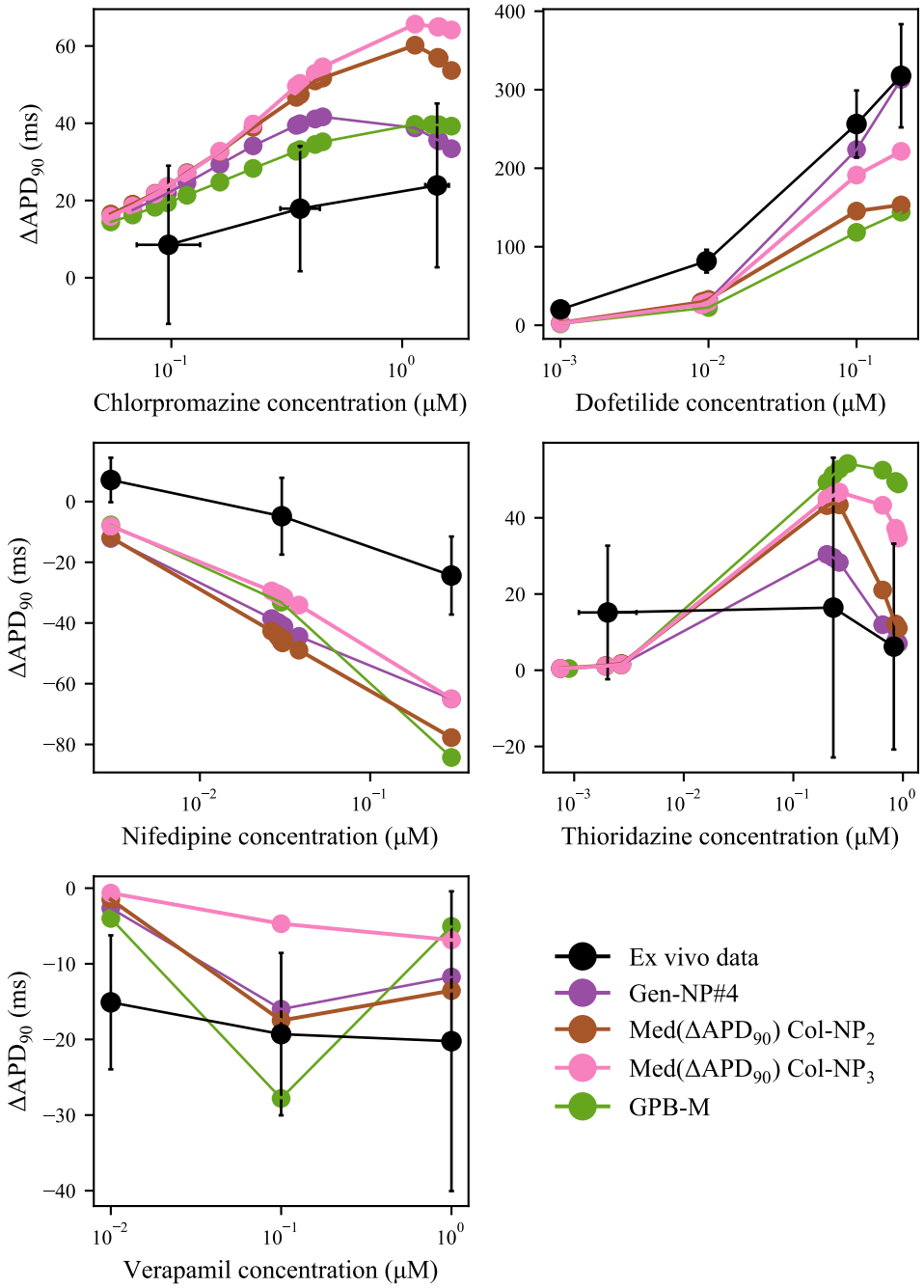

Figure 7.9: Med(ΔAPD_{90}) predicted by Col-NP_2 and Col-NP_3, and ΔAPD_{90} predicted by the Gen-NP#4 and the GPB-M models, for training drugs. The mean experimental ΔAPD_{90} is shown in **black**, with error bars representing two σ_M.

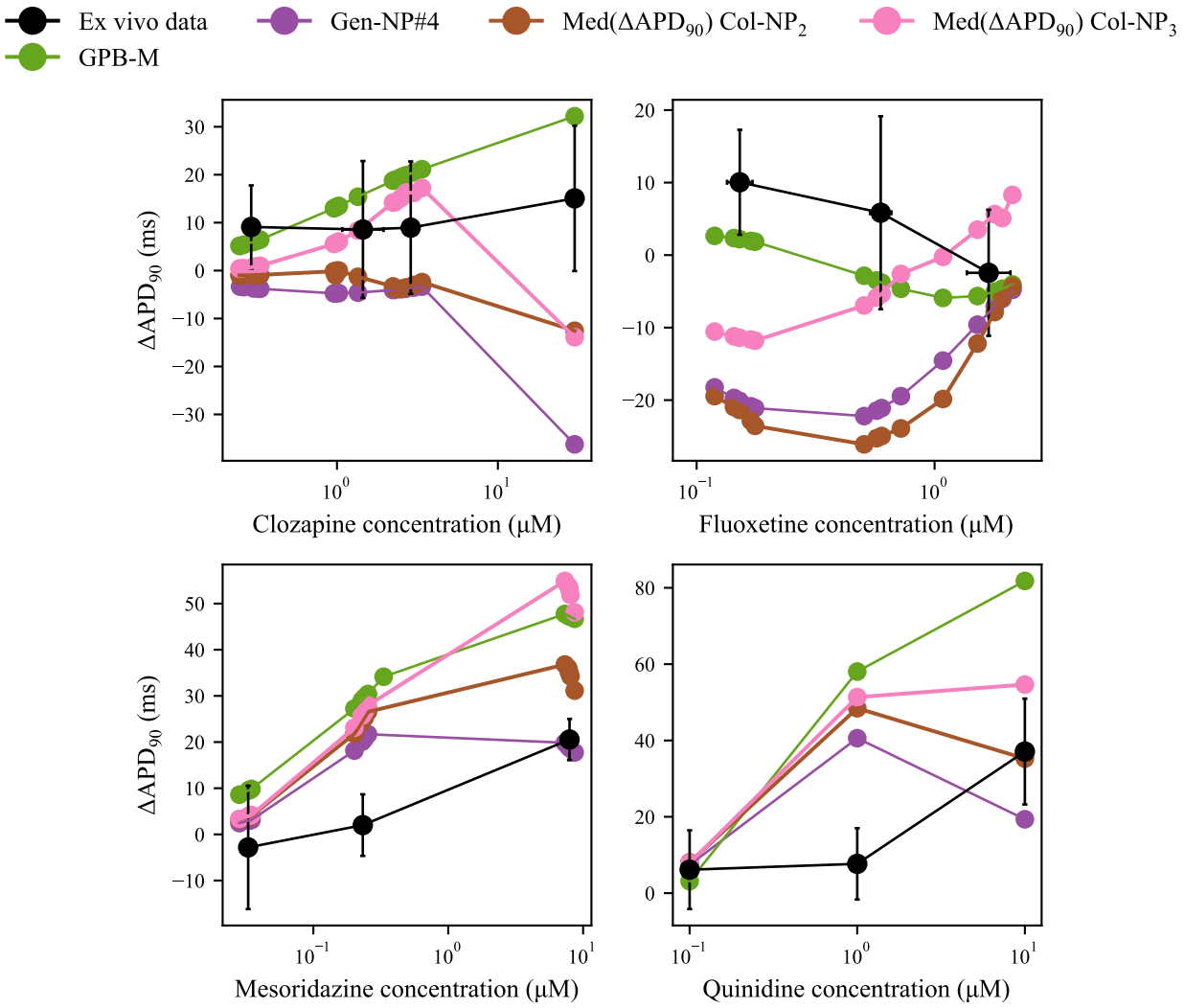

Figure 7.10: Med(ΔAPD$_{90}$) predicted by Col-NP$_2$ and Col-NP$_3$, and ΔAPD$_{90}$ predicted by the Gen-NP#4 and the GPB-M models, for validation drugs. The mean experimental ΔAPD$_{90}$ is shown in **black** with error bars representing two σ_{M}.

(ΔAPD$_{90}$= +144 ms), and it overpredicted ΔAPD$_{90}$ induced by 2 μM Thioridazine (ΔAPD$_{90}$= +49 ms).

ΔAPD$_{90}$ predictions for validation drugs

Med(ΔAPD$_{90}$) predicted by Col-NP$_2$ and Col-NP$_3$ is compared with predictions by the Gen-NP#4 and the GPB-M models for validation drugs in Figure 7.10.

With Col-NP$_3$, the predictions of Fluoxetine effect were noticeably improved: the predictions were acceptable (or close to acceptable) for intermediate and high Fluoxetine concentrations. Predictions of ΔAPD$_{90}$ induced by high Clozapine concentrations were

also improved with Col-NP$_3$ in comparison with the Gen-NP#4 model. Yet these predictions remained incorrect for 30 μM Clozapine (-14 ms predicted vs $+15 \pm 9$ ms experimentally), while the GPB-M predicted it acceptably. Furthermore, predictions of Mesoridazine and Quinidine effects were less accurate with Col-NP$_3$ and the GPB-M model than with the Gen-NP#4 model, in particular 1 μM Quinidine.

Predictions of Clozapine effect by Col-NP$_2$ were also more accurate than predictions by the Gen-NP#4 model. Predictions of Fluoxetine effects by Col-NP$_2$ and by the Gen-NP#4 model were similarly accurate. Predictions of Quinidine effect by Col-NP$_2$ are non-monotonic, like with the Gen-NP#4 model. They were correct for 0.1 μM and 10 μM Quinidine, but the effect of 1 μM Quinidine was overpredicted. ΔAPD$_{90}$ induced by low Mesoridazine concentrations was less accurately predicted by Col-NP$_2$ than by the Gen-NP#4 model.

Using the collections of models instead of the Gen-NP#4 model improved the predictions of ΔAPD$_{90}$ induced by Fluoxetine or Clozapine, but predictions of ΔAPD$_{90}$ induced by the training drugs, Mesoridazine, and Quinidine were less accurate than with the Gen-NP#4 model.

The error measure E (Eq. 5.2) was also computed for Col-NP$_2$ and Col-NP$_3$, by comparing Med(ΔAPD$_{90}$) with the *ex vivo* data: $E = 97.6$ and $E = 104.3$, respectively. E was therefore higher with collections of models than with the Gen-NP#4 model ($E = 81.5$), and similar to E obtained with the GPB-M model (Figure 5.5).

Visual assessment of ΔAPD$_{90}$ predictions by the collections of trabecula-specific models

The 2-D map of Med(ΔAPD$_{90}$) predicted by Col-NP$_2$ and Col-NP$_3$ as a function of I_{Kr} and I_{CaL} inhibition is shown in Figure 7.11.

Med(ΔAPD$_{90}$) predicted by Col-NP$_2$ and Col-NP$_3$ exhibited qualitatively lower agreement with the experimental ΔAPD$_{90}$ than the 2-D map of ΔAPD$_{90}$ predicted by the Gen-NP#4 model (Figure 7.6). The "0-ms line", corresponding to combinations of I_{Kr} and I_{CaL} inhibitions for which $|\Delta\text{APD}_{90}| < 1$ ms, matches experimental observations qualitatively. Yet, the prolongation of APD$_{90}$ induced by 100 nM and 200 nM Dofetilide

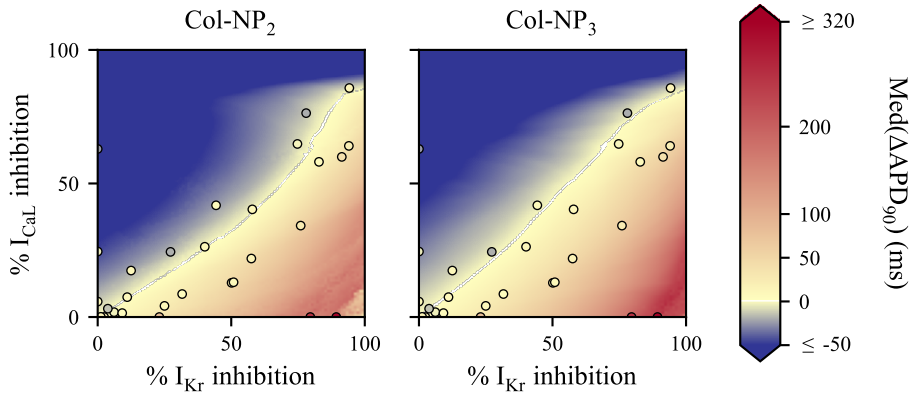

Figure 7.11: 2-D map of Med(ΔAPD$_{90}$) predicted by Col-NP$_2$ (**left**) and Col-NP$_3$ (**right**), as a function of I_{Kr} and I_{CaL} inhibition. **Circles**: *ex vivo* data points, reported from Figure 4.20.

was less accurately predicted than by the Gen-NP#4 model. In particular, many trabecula-specific models in Col-NP$_2$ predicted failing APs with 100 nM and 200 nM Dofetilide, which were not observed experimentally.

Qualitatively and quantitatively, the Gen-NP#4 model is the most predictive. Moreover, trabecula-specific models in Col-NP$_2$ and Col-NP$_3$ cannot be used individually. ΔAPD$_{90}$ predictions by the Gen-NP#4 model were therefore preferable to predictions of Med(ΔAPD$_{90}$) by the collections of models.

7.4 Discussion

7.4.1 Main findings

In the present Chapter, a new AP model was constructed, and it was calibrated to the *ex vivo* data previously introduced in Chapter 4. Firstly, an AP model for a generic individual (Gen-NP) was created by training on naive-pooled normalised AP data recorded in 57 trabeculae exposed to five different training drugs. Using four different IC$_{50}$ datasets to compute drug-induced I_{Kr} and I_{CaL} inhibition (Table 7.2), four Gen-NP models were created, labelled Gen-NP#1 through Gen-NP#4. Gen-NP#1 and Gen-NP#4 were the most predictive, with little difference between the two models: their ΔAPD$_{90}$ predictions are qualitatively correct, but limited quantitative use of the predictions can be made with both models. Still, the error measure E (Eq. 5.2), previously used to compare predictions of existing AP models in Chapter 5, was lower for the Gen-NP#4 model

than for most AP models. Only the TP model yielded a lower E. Nevertheless, the 2-D map of predicted ΔAPD_{90} as a function of I_{Kr} and I_{CaL} inhibition was visibly improved with the Gen-NP#4 model (Figure 7.6).

The Gen-NP#4 model was used as an initial point for the training of collections of trabecula-specific models. The training was performed using the same dataset for IC_{50} and h as for the training of the Gen-NP#4 model. Following the recommendations of Chapter 6, two sets of parameters were individualised (G_{Kr}, G_{CaL}) and (G_{Kr}, G_{CaL}, G_{NaK}), thus creating two collections of trabecula-specific models, respectively denoted "Col-NP_2" and "Col-NP_3".

The variability in predictions of both collections of models is noticeably larger than observed experimentally, and limited agreement is observed between the trabecula-specific models and the corresponding trabeculae. Therefore, the trabecula-specific models cannot be used as accurate representations of individual trabeculae. The median of ΔAPD_{90} predicted by Col-NP_2 and Col-NP_3 was nevertheless investigated, still without improvement on predictions by the Gen-NP#4 model.

As a conclusion, the Gen-NP#4 model is the model for the human ventricular AP which is the most predictive of ΔAPD_{90} induced by joint I_{Kr} and I_{CaL} inhibition. The Gen-NP#4 model addresses the need identified in Chapter 5 for an AP model which is sensitive to selective inhibition of I_{Kr}, and which correctly predicts the mitigation of I_{Kr} inhibition by I_{CaL} inhibition.

Nevertheless, predictions by the Gen-NP#4 model were not always within two times the standard deviation from the experimental mean drug effect. Before quantitative use can be made with our new AP model, e.g., to replace *ex vivo* experiments in human ventricular trabeculae or animal testing, further improvements would be required.

7.4.2 Context of use of the Gen-NP#4 model

The Gen-NP#4 model was trained and validated on AP data generated in adult human ventricular trabeculae exposed to *acute* I_{Kr} and I_{CaL} inhibition. This therefore defines the context of use of the Gen-NP#4 model. The novel AP model opens the way to various

follow-up studies to use of it for further predictions, but its predictions would require additional validation for any extension of its context of use.

For example, drug-induced prolongation of APD_{90} in ventricular tissues is linked with drug-induced prolongation of the ventricular repolarisation time (Vicente *et al.*, 2018), itself associated with increased proarrhythmic risk. Our new AP model could be implemented in tissue simulations to predict pseudo-ECGs, and predictions of drug effect could be validated against clinical effect of drugs on JT_{peak} or on QT.

Jeong *et al.* (2022) simulated the AP response to the 28 CiPA reference compounds, with the Tomek *et al.* (2019) model, and compared the predictivity of various AP markers. Limited predictivity was observed when classifying drugs into low and intermediate TdP risk categories (AUCs of 0.50 to 0.77) based on APD_{90} predictions. This is (partially) explained by the fact that the Tomek *et al.* (2019) model was not trained or validated to recapitulate APD_{90} response to concomitant inhibition of I_{Kr} and I_{CaL}. The study of Jeong *et al.* could be repeated with our new AP model, to observe the predictivity of the various AP markers for TdP risk, in particular ΔAPD_{90}.

7.4.3 A collection of trabecula-specific models to capture the inter-individual variability of response to current inhibition

The population of models approach was established to incorporate the inter-individual variability into AP models (Britton *et al.*, 2013), and to integrate this knowledge into *in silico* predictions of proarrhythmic risk (Zhou *et al.*, 2020; Britton *et al.*, 2017; Passini *et al.*, 2017). Populations of AP models are typically calibrated by identifying ranges of parameters that produce baseline APs characterised by AP markers, e.g., RMP or APD_{90}, within experimental bounds (Britton *et al.*, 2017).

The approach of the present work differs from that approach, because the trabecula-specific models calibrated in this work were trained on experimental AP data obtained in 57 different trabeculae exposed to different perturbations.

The trabecula-specific models developed in this work could not be validated in the trabecula used for training, which limits the reliability and accuracy of their predictions (Tomaiuolo *et al.*, 2012). Simulations with trabecula-specific models exhibited limited agreement with the training data, so it would be unlikely that predictions would be

improved for validation, even if the validation data were generated in the same trabecula. This effect was certainly exacerbated by model discrepancy, therefore limiting the usability of ΔAPD_{90} predictions by trabecula-specific models (Whittaker *et al.*, 2020). As a conclusion, the data quality and quantity currently producible in adult human ventricular tissue, combined with the unavoidable model discrepancy, does not enable the calibration of trabecula-specific AP models that predict accurately and reliably the ΔAPD_{90} response to inhibition of I_{Kr} and I_{CaL} in the modelled trabecula.

In Chapter 6, individual-specific parameters were estimated from RNA sequencing (RNA-Seq) data. A correlation was observed between individual-specific scaling factors for G_{Kr}, G_{CaL}, and G_{NaK}. Such a correlation was not observed in trabecula-specific parameter estimates found in this study (Figure 7.7). This raises further questions about whether the trabecula-specific parameter estimates are representative of the contribution of the respective ionic current to the AP in the different trabeculae, and how well the variability in trabecula-specific parameter estimates approximates the variability between individuals.

To answer these questions, RNA sequencing of the trabeculae used in this work could be performed to measure the level of expression of genes encoding the α-subunits of major ion channels (Table 6.1). Such data could be used to calculate trabecula-specific conductance parameters, similarly to the GTEx data used in Section 6.2. The trabeculae-specific parameters calculated from the RNA sequencing data would then be compared with the trabecula-specific estimates found in the present Chapter (Figure 7.7).

Note that this estimation would face the same limitations as the work in Chapter 6. Namely the linearity of the relationship between the number of mRNA transcripts and the number of functional ion channels (or pumps or exchangers) on the cell surface is a rough approximation.

7.4.4 Extreme computational cost of model training

The new AP model features 46 state variables, it is stiff, and many pre-paces were required to bring it (close) to steady-state (Figure E.1 in the Appendix), which leads to a very high computational cost of model simulation and calibration.

To test the identifiability of 15 parameters (50 optimisation problems) calibrated to create the Gen-NP models, the used CPU time was of approximately 4,000 days. The calibration of the Gen-NP models (50 optimisation problems each) then represents an approximate CPU time of 2,500 days per model.

The tests for the identifiability of trabecula-specific parameters (450 optimisation problems, Section E.4 in the Appendix) cost approximately 4,000 CPU days. Training one collection of trabecula-specific models (570 optimisation problems) requires an approximate CPU time of 6,000 days.

In total, the computational cost of the study presented in this Chapter was estimated at 30,000 CPU days, which is lower than the computational cost of the study presented in Chapter 6 (a monstrous total of 50,000 CPU days), but still very high.

Training the collection of trabecula-specific models using the Gen-NP#1, the Gen-NP#2 and the Gen-NP#3 models as starting points would increase the cost of the study by approximately 36,000 CPU days. Because Col-NP_2 and Col-NP_3 did not yield better predictions than the Gen-NP#4 model, it is unlikely that collections of trabecula-specific models based on the other Gen-NP models would be worth spending such a high amount of resources on.

The scripts were run on the high performance computer of Hoffmann-LaRoche Ltd., where resources were dynamically allocated to different tasks, and jobs were paused and restarted multiple times. Therefore, it was difficult to compute the exact cost of the study, and the cost reported here are only rough approximations.

7.4.5 Study limitations

In this work, four different datasets for drug-induced inhibition of I_{Kr} and I_{CaL} were used to compute the inputs for simulations (Table 7.2). Parameter estimates and model predictivity depended on the IC_{50} dataset used for model calibration. Given the considerable variability of measurements of drug-induced current inhibition with patch-clamp experiment between experimenters and protocols (Ridder *et al.*, 2020), the new AP model may need to be re-calibrated before using it with input data generated in a different experimental setup (e.g., with a different patch-clamp setup).

Furthermore, some drugs studied in this work affect ionic currents beyond I_{Kr} and I_{CaL}, and the integration of such effects may improve the predictivity of the models, as discussed in Section 5.4.

Recording artefacts impacting APD_{90} were estimated in Section 4.10 using AP data recorded with DMSO (the vehicle compound). Model predictions could be corrected for these recording artefacts. However, this was not done to avoid introducing an inconsistency between the training data (whole trace of the normalised AP which cannot be corrected for APD_{90} artefacts) and the validation data (ΔAPD_{90} only, which could be corrected for APD_{90} artefacts). Note that this correction was also not applicable to the 2-D maps of ΔAPD_{90} as a function of I_{Kr} and I_{CaL} inhibition.

The experimental AP data were variable under the sole action of DMSO (Figure 4.17). This variability was then exacerbated in the presence of other compounds (e.g., Figure 7.3), and predictions by trabecula-specific models were even more variable (Figure 7.8). Therefore, with the current limitations on AP data recorded with sharp electrodes in adult human ventricular trabeculae, the data cannot be used individually, and multiple repeats are required to gain understanding of the mean effect of a studied drug. Hence, only the median of the ΔAPD_{90} predictions of the collection of trabecula-specific models could be used for comparison with the mean ΔAPD_{90} measured *ex vivo*.

With the naive-pooled data approach, the data were treated as if generated in a single generic trabecula, and the variations were considered as random noise. The distributions of trabecula-specific parameter estimates were not centered on the parameter values in the model for this generic trabecula (Table 7.6 and Figure 7.7). This observation suggests that the generic model is not representative of any individual trabecula, a limitation often observed with the naive-pooled data approach (Sheiner & Beal, 1980). To try and address this limitation in future work, a nonlinear mixed effects model could be employed (Sheiner & Beal, 1980).

The new AP model most likely suffers from model discrepancy (Whittaker *et al.*, 2020). As observed previously in Chapter 6, increasing the goodness-of-fit did not always improve model predictions. For instance, a better goodness-of-fit was obtained with the Gen-NP#2 model than with the Gen-NP#4 model (Table 7.5), but its predictions were

less accurate (Figures 7.3–7.6). Furthermore, the most predictive model was obtained when none of the parameters were individualised.

The estimation of parameter uncertainty relied on the ensemble modelling approach (Villaverde *et al.*, 2022). This method allows for an estimation of the parameter uncertainty without additional computational cost. However, it relies on the log-likelihood (Eq. 7.4–7.4) computed under the assumption that the model was calibrated without model discrepancy, and that the noise model (Gaussian i.i.d.) is correct. In the most likely case that these assumptions are not verified, the confidence in parameter estimates is overly optimistic (Lei *et al.*, 2020; Lambert *et al.*, 2023). This can be partially addressed with approximate Bayesian computation (Csilléry *et al.*, 2010), but the computational cost of such a study is expected to be considerable. Furthermore, the likelihood ratio threshold of 1.92 relies on the assumption that scaling factors corresponding to conductance parameters, $\hat{g}$, are normally distributed. This is a reasonable first approximation, but it may need further refinement (Figure 6.3).

To improve the accuracy and precision of the Gen-NP#4 model, it may be necessary to revise the new AP model to better reflect the biological mechanisms and processes underlying the adult human ventricular AP. Generating additional training data and/or splitting differently the *ex vivo* data into a training dataset and a validation dataset may also enable the calibration of a more predictive model.

7.5 Conclusion

A new *in silico* model of the adult human ventricular AP was created to address the lack of an AP model accurately predicting the ΔAPD_{90} response to all combinations of I_{Kr} and I_{CaL} inhibition. Different attempts were made to calibrate the new AP model to AP data recorded *ex vivo* under various conditions of I_{Kr} and I_{CaL} inhibition, using different *in vitro* data to compute inputs for the simulations, and individualising different model parameters. Ultimately, the most predictive model was obtained by calibrating the new AP model to naive-pooled training data, individualising none of the parameters. The new AP model exhibited more accurate predictions of ΔAPD_{90} than pervious AP

models, and it constitutes a promising step towards specific and accurate assessment of the cardiac safety of small molecules based on *in vitro* measurements.

8

Discussion and future research

8.1 Summary of findings and conclusions

In this thesis, we have developed a novel model of the adult human ventricular action potential (AP) with improved predictions of drug-induced changes in the AP duration (APD). Combining novel *in vitro* and *ex vivo* data, understanding was gained on the relationship between APD, the inhibition of the rapid delayed rectifier K^+ current (I_{Kr}), and the inhibition of the L-type Ca^{2+} current (I_{CaL}). Predictions by existing AP models were compared with this data, showing that they either exhibit insufficient sensitivity to I_{Kr} inhibition or predict insufficient mitigation of I_{Kr} inhibition by I_{CaL} inhibition. A synthetic study was carried out to develop methods for the calibration of an AP model to the *ex vivo* data, with particular consideration for model discrepancy. These methods were then applied to the calibration of a novel AP model. Predictions of drug-induced changes in APD were improved with the calibrated AP model in comparison with existing AP models. Although this work contributes to a greater integration of *in vitro* experiments and *in silico* tools into predictions of cardiac safety, further improvements of our AP model remain necessary before *ex vivo* or *in vivo* experiments can be replaced.

In Chapter 1, cardiac safety assessment of novel small molecule drug candidates was briefly introduced. The difference in endpoints between pre-clinical and clinical guidelines was highlighted, because it may lead to false positives for proarrhythmic risk for some drugs inhibiting both I_{Kr} and I_{CaL}.

In Chapter 2, heart physiology was linked with the ventricular AP (Section 2.2), and the interplay of ionic currents underlying the AP was introduced (Section 2.3). Then, the existing AP models were briefly reviewed, as well as their use for predicting the cardiac safety of drugs (Section 2.4). Finally, various aspects of model development were introduced and discussed: model training, model validation, and model selection (Section 2.5). These aspects were illustrated with a particular focus on the techniques used in this thesis.

In the following Chapters, a framework to develop a new AP model predicting the change in APD at 90% repolarisation (APD_{90}) induced by I_{Kr} and I_{CaL} inhibition was established.

In Chapter 3, the derivative (Eq. 3.1) and algebraic forms (Eq. 3.6) of the equation for the transmembrane voltage (V) in AP models were compared. The algebraic-V form makes explicit the algebraic constraint on AP models that conserve charge. This improves the numerical accuracy of solutions without significantly altering the computation time (Section 3.2). Therefore, in the following Chapters, the algebraic-V form of AP models was used by default. Using the algebraic-V form, an integration constant appears (Γ_0, Eq. 3.7), which characterises the net intracellular concentration of un-modelled charges. Extreme variations of Γ_0 substantially impacted simulation outputs. In a synthetic exercise, we showed that calibrating an AP model using an incorrect value for Γ_0 led to incorrect parameter estimates. However, these could be corrected by inferring Γ_0 at the same time (Section 3.4). We showed that due to the conservation law, it is sufficient to fit the value of Γ_0 to capture the input of intracellular concentrations on steady state outputs (Section 3.3.2), unless bifurcations are present. We therefore recommend writing AP models in the algebraic-V form, and inferring Γ_0 from the training data during model calibration when possible.

In Chapter 4, the experimental data used to calibrate the new AP model were introduced. We analysed new data for inhibitor potency for I_{Kr} and I_{CaL} of nine drugs, measured *in vitro* in patch-clamp experiments (Section 4.3). Two patch-clamp protocols were used, thus creating two *in vitro* datasets: the CiPA and Pharm datasets (Table 4.2). With the nine drugs at different concentrations, various combinations of I_{Kr} and I_{CaL} inhibition were applied *ex vivo* to adult human ventricular trabeculae extracted from

the inner endocardial wall of donor hearts (Section 4.4). Under each baseline and drug-perturbed condition, the AP data were recorded with the sharp electrode technique. AP data post-processing was described in Section 4.5, and the data quality was reviewed thoroughly in Sections 4.6–4.9 to exclude data not usable for model calibration. In particular, movements of the sharp electrode during the experiments induced recording artefacts that reduced data usability. Normalisation of AP data (Eq. 4.3) was used to mitigate the effects of these artefacts (Section 4.8.2), with little impact on model calibration (Section 4.8.3). Finally, a consistent dataset usable for model calibration was obtained by excluding the data with two concomitant drugs (Figure 4.20).

In Chapter 5, predictions of ΔAPD_{90} by 11 models of the human ventricular AP were compared with the *ex vivo* data prepared in Chapter 4. The models were also used to predict ΔAPD_{90} induced by 0% to 100% inhibition of I_{Kr} and/or I_{CaL}. The results were then reported in 2-D maps with the I_{Kr} and I_{CaL} inhibition as X- and Y-axis coordinates, respectively. In this way, *in silico* predictions were qualitatively compared with the *ex vivo* data (Figure 5.3). For quantitative comparison, the drug-induced ΔAPD_{90} was predicted using drug-induced inhibition of I_{Kr} and I_{CaL} as input, computed from the *in vitro* data (Eq. 5.1). Models based on the Ten Tusscher & Panfilov (2006) (TP) model and on the Grandi *et al.* (2010) (GPB) model reproduced the mitigation of I_{Kr} inhibition by I_{CaL} inhibition, but failed to reproduce the strong APD_{90} prolongation induced by selective inhibition of I_{Kr}. Models based on the O'Hara *et al.* (2011) (ORd) model exhibited a strong sensitivity to I_{Kr} inhibition, but the mitigation of the I_{Kr} effect by I_{CaL} inhibition was insufficient to reproduce the experimental ΔAPD_{90}. Model predictivity was quantified with an error measure, E (Eq. 5.2). 7 out of the 9 selected drugs had mixed inhibitory effects on I_{Kr} and I_{CaL}, therefore E favoured the models based on the TP and on the GPB model (Figure 5.5). The lowest E was found with the TP model. Finally, by combining qualitative and quantitative comparisons between model predictions and the *ex vivo* data, the TP model and the GPB model reformulated by Mann *et al.* (2016) (GPB-M) were selected as the most promising base models for the calibration of the new AP model.

In Chapter 6, the importance of model discrepancy was investigated in the case of the calibration of individual-specific models, and methods to select the optimal parameters to

individualise were introduced. The inter-individual variability in conductance parameters was estimated from RNA sequencing data (Figure 6.3). The resulting substantial variability in AP model outputs supported the need for individual-specific models (Figure 6.4). The best set of parameters to individualise was identified in a synthetic data experiment, accounting for parametric variability estimated from the RNA sequencing data. At first, without model discrepancy, the correlation between model predictivity and goodness-of-fit to the training data was found to be weak because of parametric variability (Figure 6.8). Still, individualising all identifiable parameters maximised the goodness-of-fit and the predictivity of the individual-specific model. Eventually, individual-specific parameter estimates matched the parameter values used to generate the synthetic data, and there was no error in model predictions (Table 6.3). Our results however suggest that the best order in which to individualise parameters may depend on each individual (Table 6.5). When model discrepancy was introduced into the model calibration process, the reproducibility of model calibration decreased, and a higher number of repeats of model training was needed to ensure that parameter estimates corresponded to the global maximum of likelihood (Figure 6.11). Furthermore, predictivity did not correlate with goodness-of-fit, and overall poor predictivity could result. For example, when calibrating the TP model to synthetic data generated with the GPB model, 8 parameters were practically identifiable but the highest predictivity was achieved with 5 calibrated parameters (Table 6.7). Therefore, parameters that *can* be individualised *should not necessarily* be individualised in AP models. The methods developed in Chapter 6 help selecting the set of parameters that should be individualised.

The framework for the development of a new AP model, investigated and designed in previous Chapters, was applied in Chapter 7. The model was constructed based on the GPB-M model, by unclamping the intracellular concentrations of K^+ and Cl^-, and by changing the I_{Kr} component to the 37°C model by Lei *et al.* (2019). The normalised AP data were split into training (5 drugs) and validation (4 drugs) datasets. At first, the new AP model was trained on the data treated as if they were generated in the same generic trabecula. Using four *in vitro* datasets obtained by combining the CiPA and Pharm datasets (Table 7.2), four trained models were obtained, denoted Gen-NP#1

to Gen-NP#4 (Table 7.5). The predictions of the Gen-NP models were assessed by comparing simulated ΔAPD_{90} with the validation data (Table 7.5). Despite yielding higher E than the TP model, the Gen-NP models captured the APD_{90} response to I_{Kr} and I_{CaL} inhibition qualitatively better (Figure 7.6). Then, a trabecula-specific model was calibrated for each of the trabeculae exposed to the training drugs (Section 7.3.2), using the most predictive model (Gen-NP#4, $E = 81.5$) as an initial guess. Two collections of trabecula-specific models were obtained by individualising 2 or 3 parameters (Figure 7.7), denoted Col-NP_2 and Col-NP_3, respectively. Trabecula-specific models exhibited poor predictivity for the corresponding trabeculae. Col-NP_2 and Col-NP_3 therefore yielded less accurate predictions than the Gen-NP#4 model (Figures 7.9–7.10). The Gen-NP#4 model is therefore the model with the qualitatively best predictive power for ΔAPD_{90} induced by I_{Kr} and I_{CaL} inhibition. However, further improvements remain needed before quantitative predictions by the Gen-NP#4 model can replace *in vivo* or *ex vivo* experiments.

8.2 Future research

The largest contribution of this DPhil project may be the framework developed to calibrate an AP model to new experimental data, where many aspects were covered: experiment design and analysis, model selection, parameter selection, estimation of (the uncertainty in) parameters, and assessment of model predictivity. This framework can be reused for the calibration of AP models to other datasets.

Different directions for future research have been suggested throughout the chapters of this thesis. Four further topics are discussed here as potential continuation of the research undertaken in this DPhil thesis.

A first possible extension of the present work would be to recalibrate the model to additional data for response of the (normalised) AP to other drug perturbations. For instance, Romero *et al.* (2018) showed that proarrhythmic risk assessment can be improved by predicting the AP response to inhibition of inhibition of I_{Kr}, I_{CaL}, and the slow rectifier K^+ current (I_{Ks}). I_{Ks} does not contribute substantially to the adult human ventricular AP under baseline conditions (Figure 2.4), but it plays a key role in the repolarisation phase of the AP under conditions with I_{Kr} inhibition (Roden, 1998). Understanding the

effect of I_{Ks} inhibition on APD_{90} would therefore help refining the proarrhythmic risk of compounds, and also expanding the context of use of our new AP model.

Calibrating the model to additional conditions with drug treatment may also improve the identifiability of parameters and therefore model predictivity (Syed *et al.*, 2005). However, calibration to additional experimental data may be hindered by model discrepancy (Lei *et al.*, 2020). In such cases, refining the AP model selected in this work may help.

The refinement of our new AP model is another possible direction for future research. Given the importance of I_{CaL} inhibition to drug-induced ΔAPD_{90}, using up-to-date knowledge about I_{CaL} may improve the performance of our new AP model. Agrawal *et al.* (2023) reviewed models of I_{CaL}. The I_{CaL} component of the GPB model was based on the rabbit AP model by Shannon *et al.* (2004) and was recalibrated to human cardiomyocyte data at 37°C (Pelzmann *et al.*, 1998; Li *et al.*, 1999; Magyar *et al.*, 2002). Reformulating the component for I_{CaL} for a more recent model, e.g., (Bartolucci *et al.*, 2020), may improve model predictions of drug-induced ΔAPD_{90}. Other improvements to the model could be made, e.g., to capture the dynamics of drug binding to the hERG channel (Milnes *et al.*, 2010) and also to $Ca_V1.2$.

ΔAPD_{90} is a marker characterising the response to drug treatment at cellular level. However, clinically-relevant markers are observed at organ level (ICH, 2006). Building on our new AP model, one could try and link drug-induced ΔAPD_{90} with drug-induced changes in ECG features.

To do so, our new AP model could be used in 1-D, 2-D tissue or 3-D whole heart simulations, to predict drug effect on (pseudo-)ECGs. Predictions could be validated by comparison with clinical QT data corrected for heart rate (QT_c) and/or with clinical data for JT_{peak} (Vicente *et al.*, 2018).

Making reliable predictions of clinically-relevant markers is the ultimate goal, as this would enable replacing real world experiments on patients with *in silico* simulations. This would improve the specificity of pre-clinical safety assessment, and accelerate, therefore reduce the cost of, drug development. However, reliable predictions at organ level require robust, accurate predictions of drug-induced changes at cellular level.

Extending predictions of the AP model to (pseudo-)ECG predictions, the drug effect on the fast Na^+ current (I_{Na}) would have to be carefully evaluated. Indeed, I_{Na} inhibition has been shown to impact the conduction speed of the AP over the heart tissue and therefore the width of the QRS complex on the ECG (Erdemli *et al.*, 2012).

In this work, simulations were performed with steady periodic pacing of the AP models. In the patient, the heart rate is not perfectly periodic, and various factors influence the heart rate, e.g., breathing, nervous system control, and blood pressure regulation (Eckberg, 1983). These factors may induce short-term variability (STV) in APD_{90}, an increase in which has been identified as a pro-arrhythmia risk marker (Thomsen *et al.*, 2004; Sampedro-Puente *et al.*, 2019). Furthermore, Hondeghem *et al.* (2001) have shown that STV in APD_{90} and AP triangulation (difference between APD at different repolarisation levels) are central to arrhythmogenesis.

As a third direction for further research, variations in the pacing rate could be approximated with a random auto-correlated distribution for pacing cycle length. Pacing the Gen-NP#4 model with a random pacing frequency simulating, a relationship between APD_{90} and the pacing frequency could be established and linked with STV in APD_{90}. Doing so under baseline conditions and with drug-induced current inhibition, drug-induced ΔAPD_{90} and STV in APD_{90} could be simulated. Further investigations could potentially lead to a proarrhythmic risk marker combining drug-induced ΔAPD_{90} and drug-induced STV in APD_{90}.

Although it was not investigated in this DPhil, pace-to-pace variability was also observed in the *ex vivo* data where trabeculae were stimulated with a steady 1 Hz frequency. Investigating this variability and disentangling it from recording artefacts would likely help further improving predictions of STV in APD_{90}.

Finally, other proarrhythmic risk metrics, described in the literature, could be computed with the Gen-NP#4 model, e.g., Li *et al.* (2019); Gaur *et al.* (2020); Parikh *et al.* (2017); Passini *et al.* (2017); Yoo *et al.* (2021). As the Gen-NP#4 model was calibrated specifically to capture changes in the AP induced by drug perturbations, the predictivity of other proarrhythmic risk metrics simulated with it may be an improvement on existing models.

8.3 Closing remarks

Developing biophysically-detailed models is a complicated task. Following a stepwise approach as presented in this DPhil thesis makes it achievable. Here, we established a framework to develop biophysically-detailed models, from experiment design and data generation to predictivity assessment. Although it was applied to AP models, the process can be widely applied to other models. In particular, this work emphasises important aspects of model development:

- Algebraic constraints on the model, such as conservation laws, should be made explicit. Doing so, key hidden parameters may appear explicitly;
- Fine understanding of the dataset's limitations makes mitigation strategies possible. However, the benefits of mitigation strategies, e.g., increase of the size of the usable dataset, should not be overshadowed by the loss of information they may induce;
- Previously developed models can be benchmarked against the available data and be used to identify the most promising model to use as a starting point for model refinement;
- The impact of model discrepancy and modelling assumptions on model calibration can be investigated in synthetic studies. This is crucial to select the model and parameters to calibrate, and should be performed whenever possible;
- Parameters that cannot be reproducibly calibrated should be excluded from model training;
- Parameters that *can* be reproducibly calibrated *should not necessarily* be calibrated.

Appendices

A

A parameter representing missing charge should be considered when calibrating action potential models

A.1 Units correction in Ten Tusscher-Panfilov 2006 (TP) CellML File

Inconsistencies in units were observed between the TP CellML file taken from the CellML repository[1] and the Ten Tusscher & Panfilov (2006) paper where the model was described. However, the CellML model is consistent with the original C code published by Ten Tusscher on her website[2]. The units and values corrected for the present study are summarised in Table A.1 below.

Table A.1: Correction of the units of Ten Tusscher-Panfilov 2006 model from the CellML repository

Parameter	Published model value	Corrected value
F	96485 $C.mmol^{-1}$	96.485 $C.mmol^{-1}$
R	8314.472 $J.mol^{-1}.K^{-1}$	8.314472 $J.mol^{-1}.K^{-1}$
C_{m}	0.185 μF	1.85 $\times 10^{-4} \mu F$
$\mathcal{V}_c$	0.016404 μm^3	0.016404 nL
$\mathcal{V}_{SR}$	1.094 $\times 10^{-3} \mu m^3$	1.094 $\times 10^{-3} nL$
$\mathcal{V}_{SS}$	5.468 $\times 10^{-5} \mu m^3$	5.468 $\times 10^{-5} nL$
G_{CaL}	3.98 $\times 10^{-5} L.F^{-1}.s^{-1}$	3.98 $\times 10^{-2} L.F^{-1}.s^{-1}$

[1] https://models.physiomeproject.org/cellml
[2] http://www-binf.bio.uu.nl/khwjtuss/SourceCodes/

In most of the equations involving F or R, these parameters are used in the ratio $\frac{RT}{F}$, so the rescaling of both by a factor 1/1000 did not change anything in the model solving. The only exception is the computation of the L-type calcium current (I_{CaL}) where the ratio $\frac{RT}{F^2}$ is used. This is compensated by the rescaling of the conductance G_{CaL} by a factor 1000.

The total membrane capacitance of TP was modelled initially with the value $C_m = 0.185\mu F$. The experimental $\mathcal{O}(100pF)$ is orders of magnitude away from it, but is consistent with the corrected value.

The volumes of the cell compartments were not physiological when of $\mathcal{O}(\mu m^3)$ and match much better with experimental knowledge when corrected to $\mathcal{O}(nL)$.

These changes have been made to the CellML file in the Physiome Model Repository (Yu *et al.*, 2011).

A.2 Comparison of algebraic voltage equations

Studies from the literature proposed integration constants in algebraic expressions for V_m that take into account the charge of omitted species in various ways. The integration constant binding the ionic concentrations and the membrane voltage takes various forms in the literature and represents slightly different concepts: V_0 (Varghese & Sell, 1997; Endresen *et al.*, 2000), C_0 (Hund *et al.*, 2001), Q_{ns} (Jacquemet, 2007; Livshitz & Rudy, 2009). These constants have essentially the same modelling properties, as they involve writing the model using the algebraic voltage expression to satisfy a conservation law. The integration constants in various formulations for algebraic voltage equations are compared in Table A.2.

The transmembrane voltage is generated by a difference of electrical potential between the intra- and extracellular spaces. As such, the integration constants in the algebraic expression of V account for all the electrically-charged species, and their expression and value depend on the species that are included in the model. The complexity of the interpretation of these constants is therefore due to the fact that the extracellular space does not have a null electrical charge, contrary to Jacquemet's assumption when computing Q_{ns} (Jacquemet, 2007).

To compute the "non-specific charge Q_{ns}" as defined by Jacquemet (2007) (same as Q_0 from Livshitz & Rudy (2009)), the external concentrations are omitted:

$$C_{\mathrm{m}}V = \mathcal{V}_{\mathrm{i}}F\sum_{X}\sum_{k}\frac{\mathcal{V}_k}{\mathcal{V}_{\mathrm{i}}}z_X[X]_{\mathrm{tot,\,k}} + Q_{ns}. \tag{A.1}$$

Varghese & Sell, as well as Jacquemet (Jacquemet, 2007), noted that the "principle of Faraday: $Q = CV$, rewritten in terms of ionic concentrations rather than the charge" applies (Varghese & Sell, 1997). Eq. A.1 is the direct application of the Faraday equation to models where extracellular concentrations are constant.

$C_{\mathrm{m}}V$ corresponds physiologically to the difference in total charge across the cell membrane or the *net charge* of the cell. The double sum of Eq. A.1 corresponds to the total charge of modelled species across all intracellular compartments, and Q_{ns} is therefore the sum of the remaining charges: non-modelled intracellular charges and total extracellular charges.

Similarly to Q_{ns}, the constant C_0, as defined by Hund *et al.* (2001), includes the total concentration of non-modelled charges and the concentration of extracellular charges for modelled species. C_0 can be understood as the concentration of charge leading to Q_{ns}, so it suffers from the same limited physiological meaning.

Table A.2 compares the various expressions used in the literature to express the integration constant arising from the conservation principle. Note that in the expressions by Varghese & Sell (1997), the constant is labeled C_0 but is consistent with a voltage. Also, in their expressions, the volumes of the compartments of the junctional and network sarcoplasmic reticula were omitted. We corrected these omissions in Chapter 3, in particular when writing Eq. 3.2.

Reference	Label	Expression	Note
Varghese & Sell (1997)	C_0	No expression	Did not explore it further, focused on consequences of the implicit conservation law.
Endresen *et al.* (2000)	V_0	$v_0 = -\frac{F\mathcal{V}_\mathrm{i}}{C_\mathrm{m}}([\mathrm{K}^+]_\mathrm{ext} + [\mathrm{Na}^+]_\mathrm{ext} + 2[\mathrm{Ca}^{2+}]_\mathrm{ext})$	v_0 expressed as voltage offset.
Hund *et al.* (2001)	C_0	No expression	C_0 computed so that initial conditions for intracellular concentrations match with initial voltage in the model.
Jacquemet (2007)	Q_{ns}	$Q_{ns} = \mathcal{V}_\mathrm{i} F [NS]_\mathrm{i}$	$[NS]_\mathrm{i}$ corresponds to the non-specific charge concentration. Can be computed following Endresen or Hund approach.
Livshitz & Rudy (2009)	Q_0	$C_\mathrm{m} V = -Q_0 + Q_\mathrm{stim} + F\sum_X \sum_y \mathcal{V}_k z_X [X]_y$	"Q_0 accounts for charge contributed by nonspecific, mainly anionic, charged intracellular molecules (e.g. impermeable proteins)".

Table A.2: Table comparing the different expressions of the integration constant in the algebraic voltage equations from literature.

A.3 Changing the voltage expression of a model to the algebraic expression

Changing to the algebraic expression for voltage in the model requires that we account exactly for all the charged species included in the model. This ensures that the model satisfies the conservation of charge principle, but requires extra caution when building and using AP models. Therefore, we aim here at providing the reader with help on how to proceed.

A.3.1 Computation of total Ca^{2+} concentration

To compute Γ_0 in a model, it is necessary to compute the total concentrations of all ions, including the buffered ones. This section provides an example of how to compute total intracellular calcium concentrations, with buffer equations as in the TP and ORd-CiPA models. Usually, the models include buffers for Ca^{2+}, but any total ionic concentration can be computed following the example below. Total intracellular concentrations can be

added as variables of the corresponding compartment. It is recommended to include them in the same compartment as the buffered concentrations, to make eventual reading by other modellers easier.

Ten Tusscher 2006 model

In the TP model, the free calcium concentration in the cytosolic space is updated taking into account a buffer:

$$\frac{\mathrm{d}Ca_{i,free}}{\mathrm{d}t} = BCa_i \left(\sum_{currents} I \times \frac{C_\mathrm{m}}{\mathcal{V}_c F} + \sum_{transporters} T_{yy'} \frac{\mathcal{V}'_y}{\mathcal{V}_y} \right),$$

with:

$$BCa_i = \frac{1}{1 + Buf_c \frac{K_{buf_c}}{(Ca_i + K_{buf_c})^2}}.$$

BCa_i is the fraction of free Ca^{2+}, K_{buf_c} is the equilibrium constant between the buffered Ca^{2+} and the free Ca^{2+}, and Buf_c is the concentration of buffer.

The expression of the buffer could be integrated so that:

$$Ca_{i,total} = Ca_i + Ca_i \frac{Buf_c}{Ca_i + K_{bufc}},$$

and

$$\frac{\mathrm{d}Ca_{i,total}}{\mathrm{d}t} = \sum_{currents} I \times \frac{C_\mathrm{m}}{\mathcal{V}_c F} + \sum_{transporters} T_{yy'} \frac{\mathcal{V}'_y}{\mathcal{V}_y}.$$

The total concentration of calcium in the subspace and the SR are computed similarly for TP:

$$Ca_{ss,total} = Ca_{ss} + Ca_{ss} \frac{Buf_{ss}}{Ca_{ss} + K_{bufss}},$$
$$Ca_{sr,total} = Ca_{sr} + Ca_{sr} \frac{Buf_{sr}}{Ca_{sr} + K_{bufsr}}.$$

O'Hara CiPA 2017 model

In the ORd-CiPA model, the free calcium concentration is computed similarly to TP model, however, there are two buffers this time:

$$BCa_i = \frac{1}{1 + \frac{cm_{max} k_{cm}}{(Ca_i + k_{cm})^2} + \frac{tr_{max} k_{tr}}{(Ca_i + k_{tr})^2}}$$

Like previously, the total concentrations of calcium in the different compartments are computed as follows:

$$Ca_{i,total} = Ca_{i,free} \times \left(1 + \frac{cm_{max}}{Ca_{i,free} + k_{cm}} + \frac{tr_{max}}{Ca_{i,free} + k_{tr}}\right),$$
$$Ca_{ss,total} = Ca_{ss,free} \times \left(1 + \frac{BSR_{max}}{Ca_{ss,free} + Km_{BSR}} + \frac{BSL_{max}}{Ca_{ss,free} + Km_{BSL}}\right),$$
$$Ca_{jsr,total} = Ca_{jsr,free} \times \left(1 + \frac{csqn_{max}}{Ca_{jsr,free} + k_{csqn}}\right).$$

A.3.2 Computing Γ_0 from the initial conditions

Γ_0 is computed after integrating Eq. 3.1, meaning that the integration constant must be computed to use the algebraic voltage expression. This can be done at initial state by re-arranging Eq. 3.6. For the TP model, using the previous notation:

$$\Gamma_0 = [\mathrm{K}^+]_\mathrm{i} + [\mathrm{Na}^+]_\mathrm{i} + 2[\mathrm{Ca}^{2+}]_{\mathrm{i,\ total}} + 2[\mathrm{Ca}^{2+}]_{\mathrm{SR,\ total}}\frac{\mathcal{V}_{SR}}{\mathcal{V}_c} + 2[\mathrm{Ca}^{2+}]_{\mathrm{SS,\ total}}\frac{\mathcal{V}_{SS}}{\mathcal{V}_c} - [\mathrm{Na}^+]_\mathrm{o} - [\mathrm{K}^+]_\mathrm{o} - [\mathrm{Ca}^{2+}]_\mathrm{o} - \frac{VC_\mathrm{m}}{F\mathcal{V}_c}.$$

For the ORd-CiPA model:

$$\Gamma_0 = [\mathrm{K}^+]_\mathrm{i} + [\mathrm{Na}^+]_\mathrm{i} + 2[\mathrm{Ca}^{2+}]_{\mathrm{i,\ total}} + \left([\mathrm{K}^+]_{SS} + [\mathrm{Na}^+]_{SS} + 2[\mathrm{Ca}^{2+}]_{\mathrm{SS,\ total}}\right)\frac{\mathcal{V}_{SS}}{\mathcal{V}_c} + 2[\mathrm{Ca}^{2+}]_{\mathrm{SR,\ total}}\frac{\mathcal{V}_{SR}}{\mathcal{V}_c} - [\mathrm{Na}^+]_\mathrm{o} - [\mathrm{K}^+]_\mathrm{o} - [\mathrm{Ca}^{2+}]_\mathrm{o} - \frac{VC_\mathrm{m}}{F\mathcal{V}_c}.$$

A.3.3 Swapping the voltage expression in your model

Before updating the expression for voltage in your model, it is advised to check that the difference between intra- and extracellular concentrations follows the voltage. It is recommended to run the model with the derivative voltage expression, and plot the voltage and the difference between intra- and extracellular concentrations, namely the part of Eq. 3.6 in brackets. The two curves should overlay, with a rescaling factor and offset. If not, this gives a hint about which concentration was omitted in the computation of total ionic intracellular concentrations.

To illustrate with the TP model, the voltage expression becomes:

$$V = \frac{F\mathcal{V}_c}{C_\mathrm{m}}([\mathrm{K}^+]_\mathrm{i} + [\mathrm{Na}^+]_\mathrm{i} + 2[\mathrm{Ca}^{2+}]_{\mathrm{i,\ total}} + 2[\mathrm{Ca}^{2+}]_{\mathrm{SR,\ total}}\frac{\mathcal{V}_{SR}}{\mathcal{V}_c} + 2[\mathrm{Ca}^{2+}]_{\mathrm{SS,\ total}}\frac{\mathcal{V}_{SS}}{\mathcal{V}_c} - [\mathrm{Na}^+]_\mathrm{o} - [\mathrm{K}^+]_\mathrm{o} - 2[\mathrm{Ca}^{2+}]_\mathrm{o} - \Gamma_0).$$

And the equation of voltage for the ORd-CiPA model becomes:

$$V = \frac{F\mathcal{V}_c}{C_\mathrm{m}}([\mathrm{K}^+]_\mathrm{i} + [\mathrm{Na}]_i + 2[\mathrm{Ca}^{2+}]_{\mathrm{i,\ total}} + ([\mathrm{K}^+]_{SS} + [\mathrm{Na}]_{SS} + 2[\mathrm{Ca}^{2+}]_{\mathrm{SS,\ total}})\frac{\mathcal{V}_{SS}}{\mathcal{V}_c} + 2[\mathrm{Ca}^{2+}]_{\mathrm{SR,\ total}}\frac{\mathcal{V}_{SR}}{\mathcal{V}_c} - [\mathrm{Na}]_\mathrm{o} - [\mathrm{K}^+]_\mathrm{o} - 2[\mathrm{Ca}^{2+}]_\mathrm{o} - \Gamma_0).$$

A.3.4 Troubleshooting

When trying to use the algebraic expression for voltage in a model provided with its derivative expression, several problems can arise. The list below points out eventual sources of "bugs" that were encountered during the present work and that could lead to a mismatch between the two voltage expressions:

- When using an user-defined value of Γ_0 for simulations, the voltage will be computed according to Eq. 3.6. However, due to the prefactors, small changes in Γ_0 lead to big differences in voltage, with approximately 0.01 mM changes in Γ_0 leading to 100 mV variations. Therefore, when changing the value of Γ_0, we recommend to adjust the initial concentration of potassium ($[\mathrm{K}^+]_\mathrm{i}$) to maintain the initial voltage at physiological values. Otherwise, voltage can be pushed to values of several kV in extreme cases. The advantage of adjusting $[\mathrm{K}^+]_\mathrm{i}$ is that its range is high enough to enable a wide scan of Γ_0 values, while remaining positive.

- Note that the total membrane capacitance is computed differently from one model to another. It is usually introduced either as a model parameter, or as a product of capacitance per area unit and cell surface, or sometimes as a combination of capacitance per area unit, surface to volume ratio, and volume of the cell.

- The model must satisfy the conservation of charge principle. All the currents (including the stimulus current) carry charges; all fluxes result in changes in ionic concentrations that should be included.

- If adjustment is needed for the model to satisfy the conservation of charge principle, check that the right currents are used to update the right concentrations. For example, Grandi 2010 model includes only the intracellular potassium concentration

in the bulk cytosol, clamped to its initial value. The Na^+-K^+ exchanger currents, however, are computed in the sarcolemma and junctional domains. This means that in sarcolemma and junctional domains, 3 Na^+ ions are exchanged for 2 K^+ ions, which should be accounted for in these compartments. Thus, when considering dynamic potassium concentrations in the Grandi *et al.* (2010) model, one needs to add variables for the K^+ concentrations into the different compartments of the model.

- Verify that **all of the charge-carrying species** were included in the voltage equation. One can check this by differentiating over time the algebraic expression of voltage and comparing it with the sum of the ionic currents through the membrane (derivative of the voltage expression). When differentiating, do not forget that intracellular concentrations are not constant (important for buffered species).

- Verify that **all of the buffered forms** of the ions are taken into account for total ionic concentrations computation.

- The value for Γ_0 must be computed using the initial conditions for **total** ionic concentrations. This is particularly relevant for Ca^{2+} ions which are often buffered.

- The variable for voltage must be demoted from "state variable" to "computed variable". Depending on the software/language used, this might require special treatment.

A.4 Convergence towards paced limit cycle

For this section, the absolute and the relative solver tolerances are set to the same value, ranging from 10^{-9} to 10^{-5}. The TP and ORd-CiPA models are each used to simulate 3000 paces. The intracellular potassium concentration at the end of the AP (at time $t = 0\,\text{ms}$) is recorded and plotted for the extreme solver tolerances in Figures A.1 to A.4. Overall, the potassium concentrations converge towards the same value, no matter the solver tolerance used. The zooms on the phase of the simulation after the 2000^{th} beat show however that the models do not always converge as the higher level view might suggest.

For coarse solver tolerances, the derivative voltage model is not even converging towards a paced limit cycle. Indeed, because of numerical error, conservation of charge is not preserved anymore and there is divergence of the intracellular concentrations. On the other hand, the algebraic voltage model does converge, even though the reached value is visibly noisy around the limit cycle value. Note that the two models are mathematically identical, meaning that the differences in observed behaviours are due only to the numerical solving.

For fine solver tolerances, both models seem to converge nicely to the same limit cycle value. But a zoom into the "converged" phase shows that the derivative voltage model actually still drifts away, even with solver tolerances set to 10^{-9}. The slope of the drift is much reduced with the fine solver tolerance though. In practice, this deviation would not induce any visible variations of the outputs that are usually studied.

To grade the stability of the model, a score taking into account the noisy variations around limit cycle values and the drifting away of $[K^+]_i$ was needed. From the higher scale view, it seemed that 2000 beats was a good cutoff to observe deviation from the limit cycle. Therefore, the 2000^{th} beat was selected as reference, and the stability compared to that value. To quantify the deviation, the averaged distance to the reference value seemed to be sufficient. To have a more visual map representing all together the various scales of deviation, a log-rescale was applied on the score.

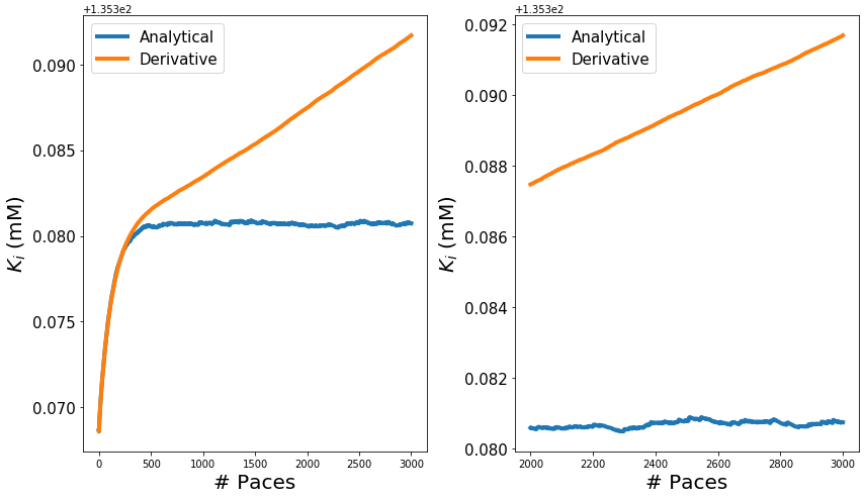

Figure A.1: Convergence of intracellular potassium to its limit cycle value, for the TP model, for solver tolerances set to 10^{-5} . The **left** panel shows the convergence towards the paced limit cycle from the initial conditions. The **right** panel shows a zoom on the evolution of the intracellular potassium after the 2000^{th} beat where the model is supposed to have already reached the paced limit cycle.

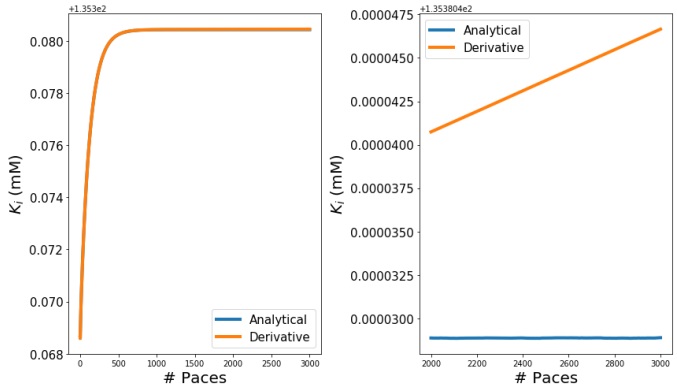

Figure A.2: Convergence of intracellular potassium to its limit cycle value, for the TP model, for solver tolerances set to 10^{-9} . The **left** panel shows the convergence towards the paced limit cycle from the initial conditions. The **right** panel shows the evolution of the intracellular potassium after the 2000^{th} beat where the model is supposed to have already reached the paced limit cycle.

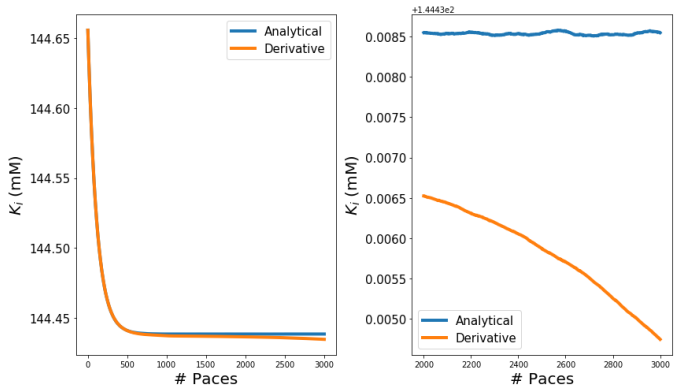

Figure A.3: Convergence of intracellular potassium to its limit cycle value, for the ORd-CiPA model, for solver tolerances set to 10^{-5}. The **left** panel shows the convergence towards the paced limit cycle from the initial conditions. The **right** panel shows a zoom on the evolution of the intracellular potassium after the 2000^{th} beat where the model is supposed to have already reached the paced limit cycle.

A.4.1 Comparison of solving speed between derivative and algebraic voltage expressions

The relative simulation time of solving the underlying sytem equations with the different voltage expressions were also compared, and similar maps are plotted in Figure A.5 for the TP and ORd-CiPA models. These maps are mostly smooth, with the possible exception of the ORd-CiPA written with the algebraic voltage. As expected, increasing the solver tolerance increases the time-steps hence the speed of solving of the model.

Actually, as the same system can be described with the two expressions for voltage, this means that the system is overdetermined when written with the voltage as state variable.

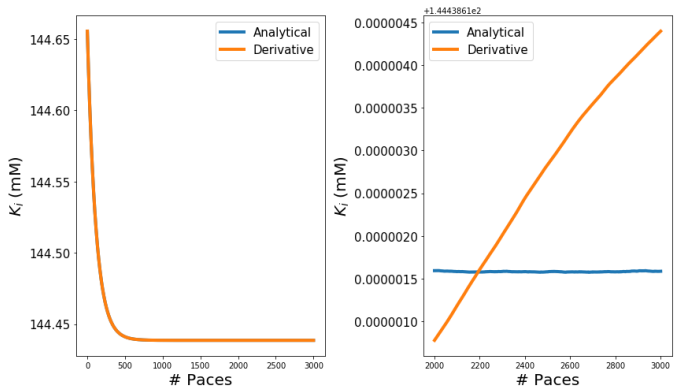

Figure A.4: Convergence of intracellular potassium to its limit cycle value, for the ORd-CiPA model, for solver tolerances set to 10^{-9} . The **left** panel shows the convergence towards the paced limit cycle from the initial conditions. The **right** panel shows the evolution of the intracellular potassium after the 2000^{th} beat where the model is supposed to have already reached the paced limit cycle.

Therefore, writing the voltage as a computed variable breaks the overdetermination of the system, and the number of state variables in the model is reduced.

Having fewer state variables to compute was expected to accelerate the solving by CVODE. However, the maps of speed of solving do not agree with these expectations. The time-step needed to meet with the solver tolerance does not change, and neither does the speed of solving. The break of the overdetermination of the system of equations describing the model could explain the improvement in simulation stability observed in Chapter 3 though.

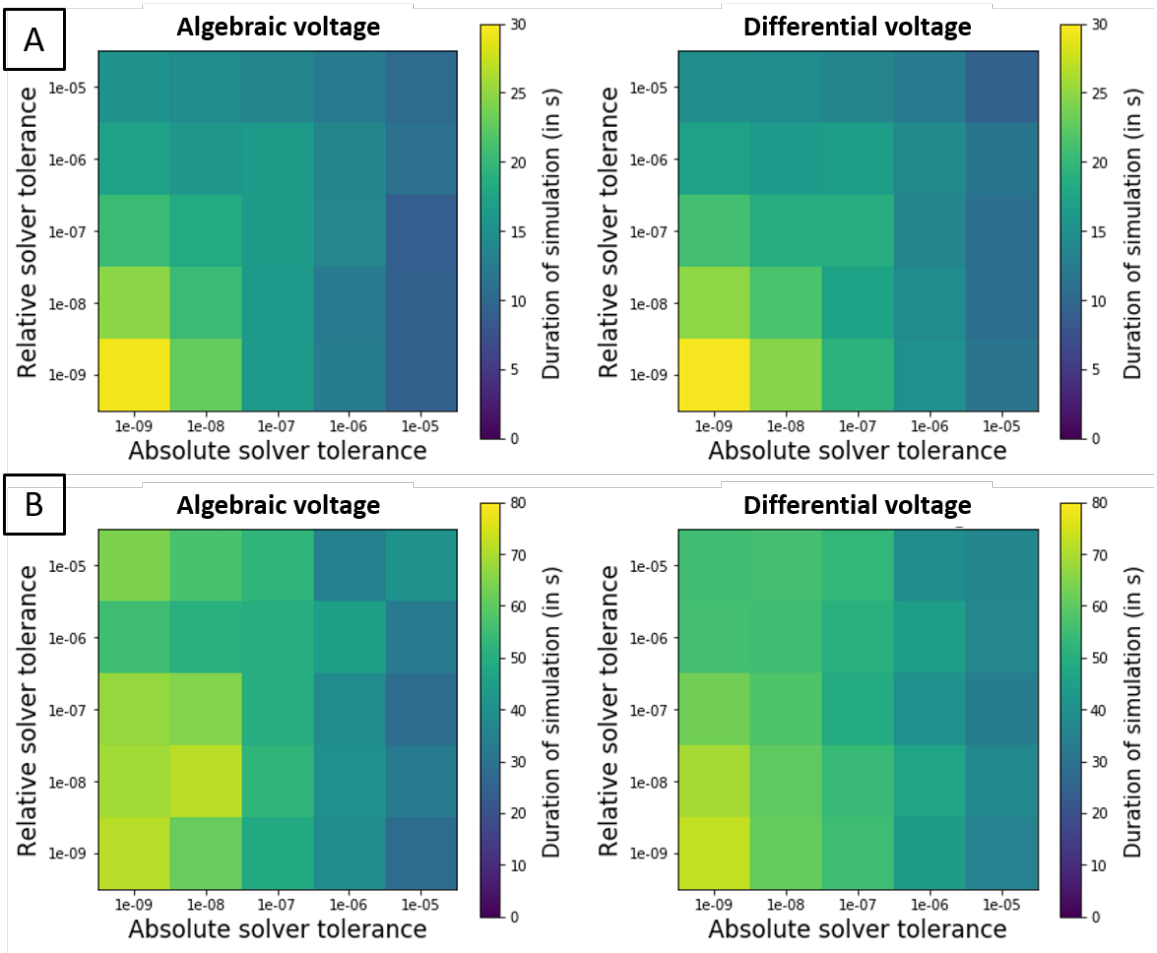

Figure A.5: Map of speed for **A:** the TP model and **B:** the ORd-CiPA model, **Left:** using the algebraic voltage expression, and **Right:** using the derivative voltage expression. The colorcode corresponds to the speed of solving of the model. The darker the map, the lower the simulation duration, hence the faster the simulation the simulation.

B

Analysis and curation of adult human ventricular action potential data recorded under drug treatment

B.1 In vitro measurements of I_{Kr} and I_{CaL} inhibition by drugs

Cell culture

The CHO Cre-Lox hERG cell line was generated and validated at Roche (Guthrie *et al.*, 2005). The CHO-hCa$_V$1.2/β2/α2δ cell line was purchased from ChanTest (USA, Catalog #CT6004). Vials with cryopreserved cells were thawed at 37°C, washed with the pre-warmed IMDM cell culture medium (Gibco Life Technologies, USA) and re-suspended in the extracellular solution.

For the hERG assay, the extracellular solution contained (in mM): NaCl, 80; KCl, 4; $CaCl_2$, 1; $MgCl_2$, 1; NMDG, 40; HEPES, 10; sorbitol, 40; glucose, 5; pH 7.2–7.4 with NaOH, osmolarity 290–330 mOsm and the internal solution contained (in mM): KCl, 10; KF, 100; NaCl, 10; HEPES, 10; EGTA, 20; pH = 7.0–7.4 with KOH, osmolarity 260–300 mOsm. For the L-type Ca$_V$1.2 assay the extracellular solution contained (in mM): NaCl, 80; KCl, 4; $CaCl_2$, 1.8; $MgCl_2$, 1; NMDG, 40; HEPES, 10; sorbitol, 40; glucose, 5; pH 7.2–7.4 with NaOH, osmolarity 290–330 mOsm and the internal solution contained (in mM): KCl, 10; KF, 100; NaCl, 5; HEPES, 10; EGTA, 10; Na-ATP 4; Na-GTP 0.1; pH = 7.0–7.4 with KOH, osmolarity 260–300 mOsm.

Electrophysiology recordings

Current recordings were performed using automated patch clamp system SynchroPatch 384 (Nanion Technologies GmbH, Germany) at 35–37°C following the experimental procedure described below. On the day of the experiment, an aliquot of the cell suspension in a 2:1 mixture of the HBSS and external solution was placed in the Cellhotel. The cells were subsequently added into the 384-well sealchip where the currents were recorded in single cells with the patch-voltage-clamp technique in the whole-cell configuration at 35–37°C using the built-in 384 channel amplifier and associated software (PatchControl 384). Currents were low-pass filtered using an analog 3 kHz Bessel filter and a digital 3 kHz Lanczos filter and were digitized at 5 kHz. Series resistance was typically 2–9 MΩ and was compensated by 80%. The reported current amplitudes represent the maximal amplitude of a peak current.

B.2 Filtering frequencies above 4 kHz in the Fourier spectrum of action potentials

The importance of the various Fourier frequencies and their contributions to the AP were investigated further. The Fourier spectrum was computed for the last AP recorded under control conditions after sustained steady 1 Hz pacing of trabecula #2021030402. The 60 Hz harmonics were eliminated as described in Section 4.5 to obtain the cleaned spectrum. For various thresholds ranging from 100 Hz to 10 kHz, the frequencies above the threshold were put to zero and the AP corresponding to the truncated spectrum was computed. Figure B.1A shows the parts of the spectrum that were truncated at the different thresholds.

For each threshold frequency, the AP corresponding to the truncated spectrum was compared to the filtered AP without spectrum truncation. The distance between the two APs was computed as the sum of square errors (SSE) and plotted as a function of the cut-off frequency, in Figure B.1B.

The APs obtained from the various truncated spectra are plotted in Figure B.1C, with zooms on the upstroke and on the end of the AP.

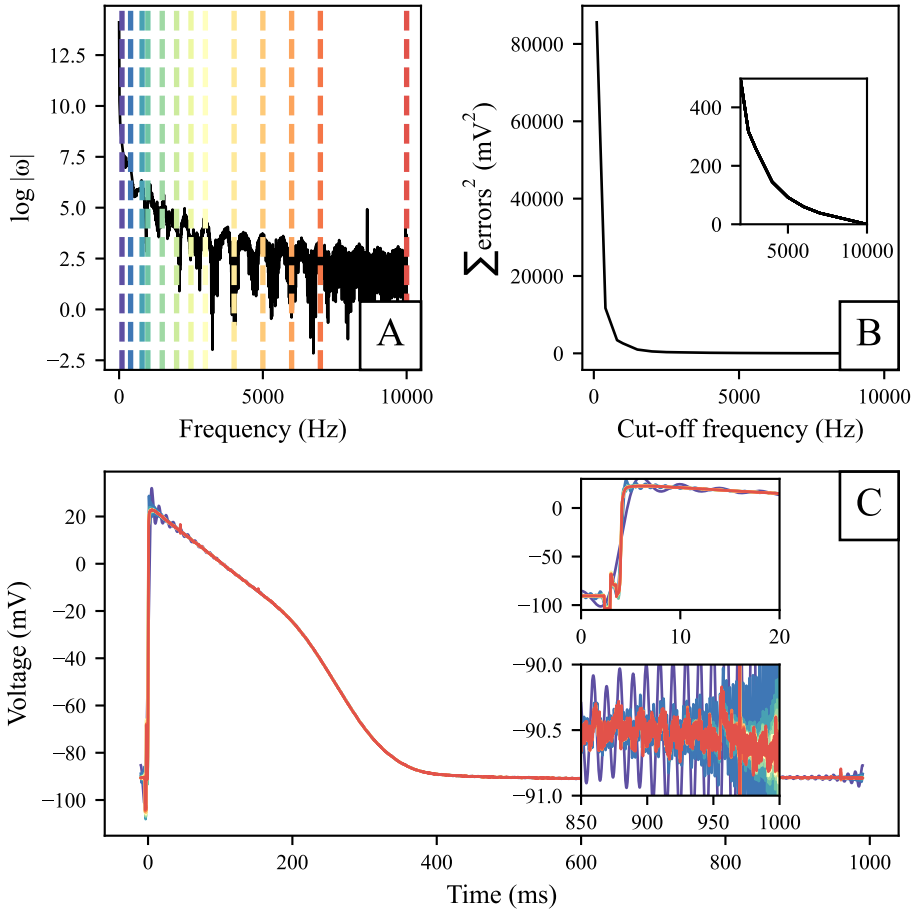

Figure B.1: Effect of truncating the Fourier spectrum of an action potential (AP) above a cut-off frequency. **A:** Log-modulus of the Fourier spectrum of an AP at steady-state after sustained 1 Hz pacing. The cut-off frequencies are indicated with the dashed vertical lines. **B:** Distance between the AP with the full spectrum (up to 10 kHz) and APs with their spectrum truncated above various frequencies. **C:** APs corresponding to the truncated Fourier spectra. The colours of the APs match with the colours of the dashed lines visualising the truncation cut-off frequency in the panel A.

In Figure B.1B, there is a steep increase in the SSE when the low frequencies are discarded from the spectrum. Therefore, low frequencies provide most information on the AP. For a cut-off frequency of 4 kHz, the SSE is lower than 200 mV^2, which corresponds to the SSE of noise with a 0.1 mV average amplitude. Moreover, APs with their spectrum truncated above 4 kHz cannot be distinguished from the AP with the full spectrum — Figure B.1C. Therefore, the frequencies above 4 kHz can be attributed to the noise and were discarded for the rest for the following.

Interestingly, the whole AP spectrum exhibits periodicity in both modulus — Figure B.1A — and argument — Figure 4.7C. The implications of these features were not

investigated for the work presented in this thesis. Nevertheless, there is probably work to carry out further in this direction. No literature study could be found concerning Fourier spectrum studies of the cardiac AP.

B.3 Stability of the sharp electrode: 1 Hz vs 2 Hz

To investigate whether the loss of electrode impalement depended on pacing rate, a statistical analysis of the data was carried out, in which the frequency of loss of impalement was compared when pacing the tissue at 1 Hz and at 2 Hz.

Loss of impalement was defined as RMP> -50 mV or RMP< -120 mV. The loss could be sudden or progressive, i.e., a steady or a steep increase of the RMP. In the progressive case, the loss was attributed to the pacing frequency where RMP started to rise up. When there was loss of electrode impalement for only one pace before the electrode returned to its previous position, the event was disregarded for this analysis. The counts of loss of electrode impalement are reported in Table B.1. No significant difference between the stability of impalement with 1 Hz and 2 Hz pacing was found ($p = 0.6$, Fisher's exact test). Therefore, we concluded that the frequency of tissue stimulation (and contraction) did not impact the likelihood of loss of electrode impalement.

Pacing frequency	**Duration of the experiment**	**Number of impalement losses**
1 Hz	25 min	40
1 Hz	3 min	6
2 Hz	3 min	6

Table B.1: The number of times impalement was lost does not depend on pacing frequency.

B.4 Fitting of a quadratic surface through the experimental ΔAPD_{90} data

Based on preliminary simulations with different AP models, performed in the cardiac electrophysiology Web Lab (Cooper *et al.*, 2016), ΔAPD_{90} induced by I_{Kr} inhibition seems reasonably approximated with a quadratic polynomial function (see results at the address: https://scrambler.cs.ox.ac.uk/experiments/compare/33996/50

00/5293/5427/5770/35490/26963/27674/28504/show/outputs_APD90_gnuplot_data.csv/displayPlotFlot). For a visualisation of the experimental relationship between ΔAPD_{90} and I_{Kr} and I_{CaL} inhibition with a small number of parameters, a quadratic surface was therefore fitted through the *ex vivo* data points. The quadratic surface was computed following the equation:

$$z = \text{surf}(x, y, \boldsymbol{\theta}) = \theta_1 x^2 + \theta_2 x + \theta_3 xy + \theta_4 y + \theta_5 y^2 + \theta_6, \tag{B.1}$$

with z the approximated ΔAPD_{90}, x and y the percentage of inhibition of I_{Kr} and I_{CaL}, respectively, and $\boldsymbol{\theta}$ the parameters describing the quadratic surface. The location of each data point for each tested trabecula (x and y coordinates) was computed using the IC_{50} data (Table 4.2) and the actual drug concentration in the bath solution if available. The nominal drug concentration was used otherwise.

The quadratic surface was fitted through the experimental ΔAPD_{90} data points, by minimising the cost function:

$$\mathcal{S}(\boldsymbol{\theta}) = \sum_{\text{trab}} \sum_{k} \left(\text{surf}(x_k, y_k, \boldsymbol{\theta}) - \Delta APD_{90,\text{exp,k, trab}}\right)^2, \tag{B.2}$$

with $\Delta APD_{90,\text{ exp, k, trab}}$ the experimental ΔAPD_{90} for the drug perturbation k averaged over 30 consecutive APs in the trabecula *trab*. For each k, the associated inhibition of I_{Kr} and I_{CaL} was computed using Eq. 4.1 and the IC50 data reported in Table 4.2. The minimisation of the cost function was performed using the `scipy` Python package. Based on *a priori* observations, the following constraints were put on the quadratic surface during its fitting:

- ΔAPD_{90}= 0 ms at baseline, i.e., $\theta_6 = 0$;
- $\Delta APD_{90} \leq -50$ ms for 100% I_{CaL} block ;
- $\Delta APD_{90} \geq +320$ ms for 100% I_{Kr} block ;
- $\frac{dz}{dx} > 0$, translating that an increase in I_{Kr} inhibition prolongs the APD_{90};
- $\frac{dz}{dy} < 0$, translating that an increase in I_{CaL} inhibition shortens the APD_{90}.

When the constraints were not satisfied, the cost (Eq. B.2) was multiplied by 100.

B.5 Comparison of 2D maps using nominal concentrations and using measured drug concentrations in the bath solution (when available)

In Section 4.11, drug concentrations in the bath solution were measured for some compounds, while they were not measured for other compounds. Furthermore, substantial differences between measured and nominal concentrations were observed for some compounds (Table 4.8). Note that for Clozapine, the actual drug concentration was measured in 7 trabeculae exposed to 0.3–3 μM but not in the 4 trabeculae exposed to 0.3–30 μM.

The fitting of the quadratic surface was repeated with three approaches. In each approach, the drug concentrations used to compute the current inhibition were used differently, therefore the experimental data points were located differently on the 2-D map, and the fitted surfaces were different (Eq. B.1):

1. using the measured drug concentration in the bath solution for each trabecula under each tested drug condition, when the drug concentration was measured. Otherwise, the nominal concentration was used. In this case, ΔAPD_{90} is reported separately for each trabecula for each drug condition ;

2. averaging the measured drug concentration for all trabeculae tested with the same nominal drug concentration, when available. Otherwise, the nominal drug concentration was used. The drug-induced ΔAPD_{90} effect was averaged over the trabeculae tested with the same nominal concentration ;

3. using only the nominal drug concentrations. The drug-induced ΔAPD_{90} effect was averaged over the trabeculae tested with the same nominal concentration.

The experimental data points were placed on the 2-D map following the three methods, and the corresponding quadratic surfaces were fitted through these data points. The fitting of the quadratic surface was repeated with the CiPA and Pharm protocols, and the results are visualised in Figure B.2.

The exact location of points was changed due to the measured concentrations in the bath solution not matching exactly with the nominal concentrations. Yet, the quadratic surfaces fitted to the experimental points with the three methods described above were very similar.

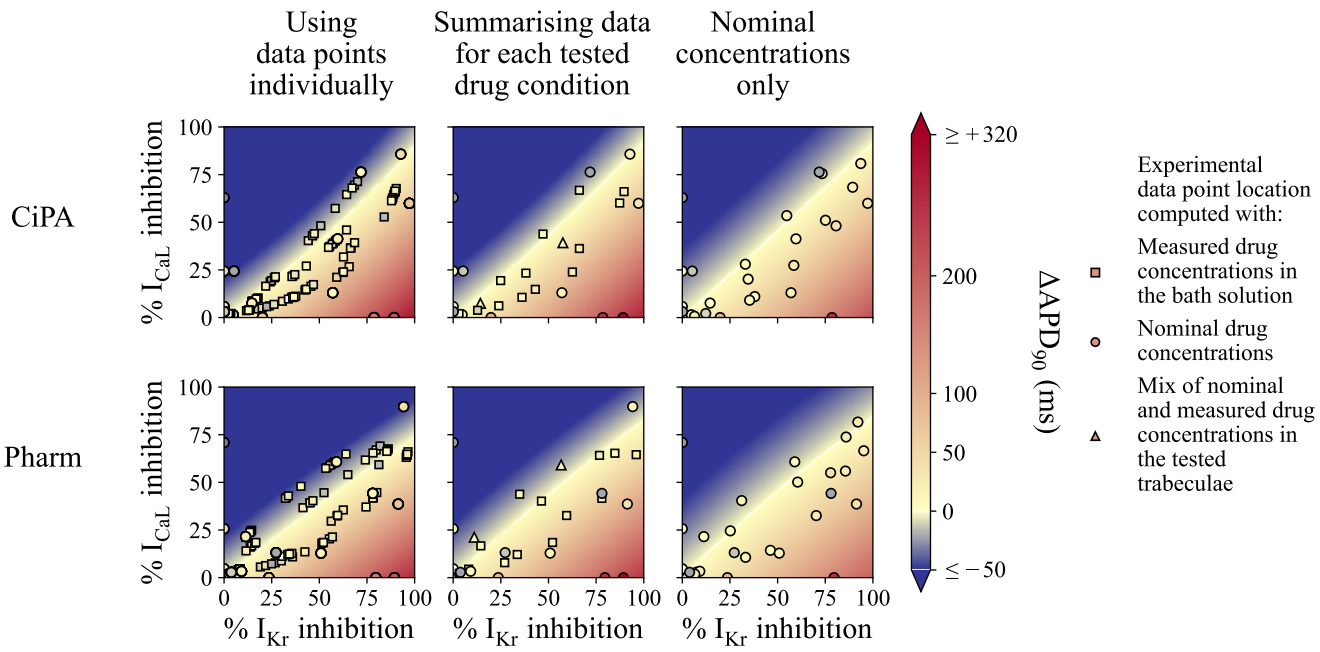

Figure B.2: Impact of reporting drug concentrations measured in the bath solution or nominal concentrations on the quadratic surface and on the interpretation of the results in Chapter 4. Experimental ΔAPD_{90} measured *ex vivo* under various drug conditions in human ventricular trabeculae, as a function of I_{Kr} and I_{CaL} inhibition. A quadratic surface approximating the experimental data points is plotted in the background. Each data point was placed with the current inhibition computed with Eq. 4.1 from drug concentrations and the drug IC50 for I_{Kr} and I_{CaL} (Table 4.2). **Left:** ΔAPD_{90} is reported with one point per tested drug condition per trabecula. The quadratic surface was fitted to all the data points for all the trabeculae. **Middle:** A single point is plotted per tested drug condition. The data for drug concentration and drug-induced ΔAPD_{90} was averaged across trabeculae tested with the same nominal concentration. **Right:** A single point is plotted per tested drug condition, using the nominal drug concentrations only. ΔAPD_{90} was averaged similarly to the middle panels.

B.6 Comparison of drug-induced ΔAPD_{90} with relative APD_{90} change from baseline as a percentage

To investigate whether drug-induced changes in APD_{90} should be reported in absolute or relative values, the correlation between baseline APD_{90} and response to drug perturbation was observed. For 15 trabeculae exposed to 1 μM Verapamil, the absolute change in APD_{90} (ΔAPD_{90}) was computed. From there, the relative change in APD_{90} was computed with the following equation:

$$\%\Delta APD_{90} = \Delta APD_{90}/APD_{90,\text{baseline}}, \tag{B.3}$$

$APD_{90,\text{ baseline}}$ referring to the baseline APD_{90}.

The scatter plot of ΔAPD_{90} and $\%\Delta APD_{90}$ against baseline APD_{90} is plotted in Figure B.3. The ΔAPD_{90} and $\%\Delta APD_{90}$ showed no correlation with baseline APD_{90}. Consistent results were obtained for all drugs and all drug concentrations.

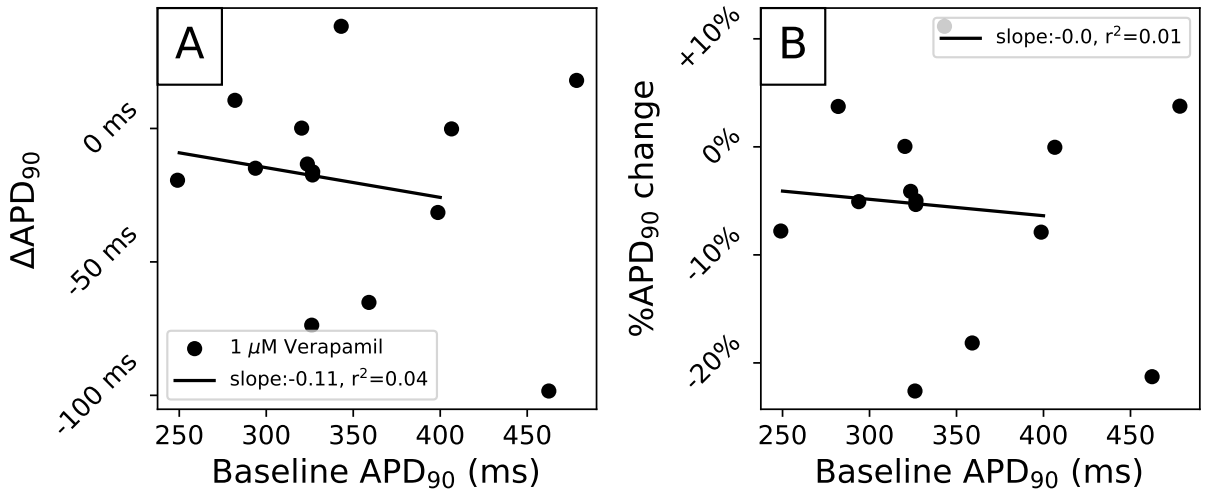

Figure B.3: Correlation between baseline APD_{90} and Verapamil-induced perturbations, measured as absolute change in APD_{90} (**A**) and as relative change in APD_{90} (**B**). No correlation was found.

Therefore, normalising ΔAPD_{90} to the baseline APD_{90} would not improve the understanding of drug effect. Furthermore, in the clinic, changes in QT are measured in absolute, average prolongation of the QT interval corrected for heart rate (QT_c). QT_c prolongation by more than +5 ms is the limit of tolerance (ICH, 2006). At the cellular level, ΔAPD_{90} is more directly linked with the safety marker than $\%\Delta APD_{90}$. As a conclusion, the ΔAPD_{90} was used for the remainder of this thesis.

To investigate further the importance of using ΔAPD_{90} over $\%\Delta APD_{90}$ in this Section, the results of the main text were repeated using the relative APD_{90} change expressed as a percentage of the baseline APD_{90} ($\%\Delta APD_{90}$), instead of ΔAPD_{90}. The relative APD_{90} change was computed in each trabecula as:

$$\Delta_{\%}APD_{90} = 100 \times \Delta APD_{90}/APD_{90,\,\text{baseline}}. \tag{B.4}$$

The experimental $\%\Delta APD_{90}$is shown in Figure B.4. The fitted quadratic surface is very similar to the quadratic surface observed in Figure 4.20, granted the scalings differed between the two figures.

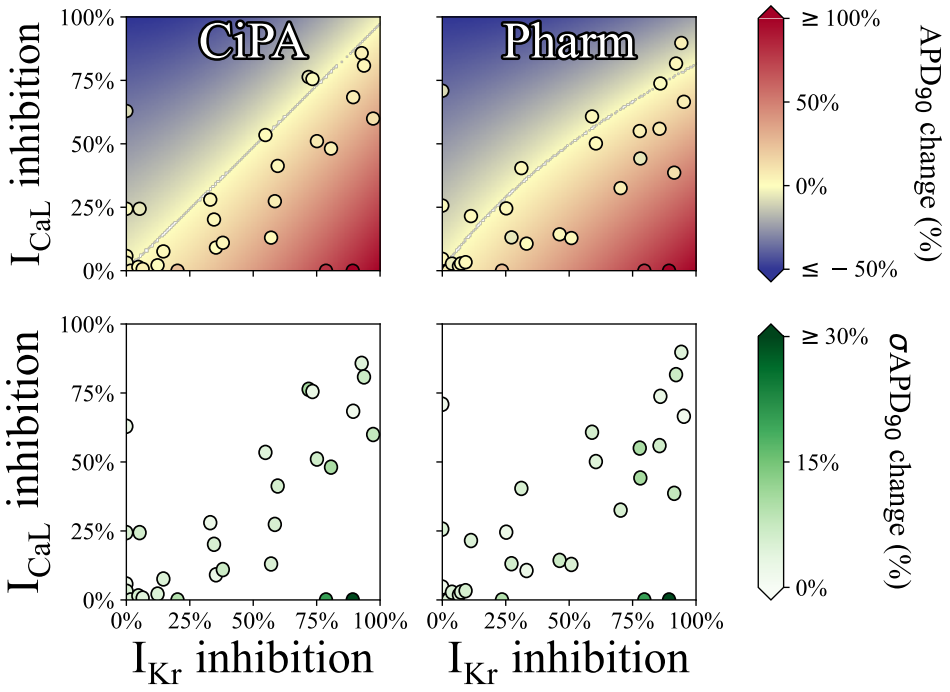

Figure B.4: Experimental %ΔAPD$_{90}$ measured *ex vivo* under various drug conditions in human ventricular trabeculae, as a function of I_{Kr} and I_{CaL} inhibition and quadratic surface approximating the experimental data points in the background. I_{Kr} and I_{CaL} inhibition were computed using the Hill equation (Eq. 4.1), with the CiPA (left) and Pharm (right) datasets (Table 4.2) and nominal drug concentrations (Tables 4.3–4.4).

B.7 Correction for DMSO effect of experimental change in APD$_{90}$ from baseline with drug exposure

The mean drug-induced ΔAPD$_{90}$, $\mu_{\Delta APD90}$, and the SEM, σ_M, can be corrected for DMSO effect:

$$\begin{aligned} \mu_{\Delta APD90} &= \overline{\Delta} APD_{90} - \overline{\Delta} APD_{90,\text{ DMSO rep}}, \\ \sigma_{\text{M},\,\Delta APD90} &= \sqrt{\sigma_{\text{M}}(\Delta APD_{90})^2 + \sigma_{\text{M}}(\Delta APD_{90,\text{ DMSO rep}})^2}, \end{aligned} \tag{B.5}$$

with $\overline{\Delta} APD_{90}$ the mean ΔAPD$_{90}$ measured in trabeculae exposed to the same nominal drug concentration, $\sigma_{\text{M}}(\Delta APD_{90})$ the corresponding SEM, $\overline{\Delta} APD_{90,\text{ DMSO rep}}$ the mean DMSO-induced ΔAPD$_{90}$ at the corresponding repeat, and $\sigma_{\text{M}}(\Delta APD_{90,\text{ DMSO rep}})$ the corresponding SEM.

The ΔAPD$_{90}$ data (Table 4.7) corrected for DMSO effect with Eq. B.5 is reported in Table B.2.

Overall, the correction for DMSO effect does not introduce any major difference in ΔAPD$_{90}$ (Table 4.7). However, it is worth noting that after correction for DMSO effect,

Drug	Mean baseline APD_{90} (STD) in ms	Nominal drug conc (μM)	Mean ΔAPD_{90} (SEM), in ms
Chlorpromazine	299 (36)	0.3	+1 (11)
		1	+23 (9)
		3	+23 (11)
		3 + 0.1 μM Dof	+135 (32)
Clozapine	324 (51)	0.3	+0 (6)
		1	+13 (11)
		3	+8 (6)
		30	+15 (9)
		3 + 0.1 μM Dof	+148 (30)
		30 + 0.1 μM Dof	+129 (28)
Dofetilide	317 (51)	0.001	+13 (5)
		0.01	+94 (10)
		0.1	+255 (21)
		0.2	+318 (33)
Dofetilide + Nifedipine	342 (25)	0.01 + 0.03	+80 (20)
		0.03 + 0.05	+152 (41)
		0.05 + 0.15	+169 (46)
Fluoxetine	271 (36)	0.3	+3 (5)
		1	+11 (9)
		3	−4 (5)
		3 + 0.1 μM Dof	+174 (25)
Mesoridazine	334 (60)	0.04	−10 (8)
		0.25	+7 (6)
		10	+19 (3)
		10 + 0.1 μM Dof	+70 (7)
Nifedipine	336 (55)	0.003	+0 (4)
		0.03	−4 (14)
		0.3	−25 (7)
		0.3 + 0.1 μM Dof	+172 (26)
Nifedipine + Dofetilide	372 (33)	0.03 + 0.003	+7 (7)
		0.03 + 0.01	+85 (11)
		0.03 + 0.1	+232 (51)
Quinidine	302 (53)	0.1	−1 (6)
		1	+13 (7)
		10	+36 (7)
		10 + 0.1 μM Dof	+174 (18)
Thioridazine	307 (48)	0.012	+8 (9)
		0.6	+22 (20)
		2	+5 (14)
		2 + 0.1 μM Dof	+83 (59)
Verapamil	349 (61)	0.01	−22 (5)
		0.1	−14 (7)
		1	−22 (10)
		1 + 0.1 μM Dof	+180 (14)

Table B.2: Experimental data for average APD_{90} baseline and APD_{90} change with drug exposure, corrected for DMSO effect. SEM: standard error of the mean. STD: standard deviation.

ΔAPD_{90} induced by 3 nM Nifedipine is not positive anymore, which is the expected effect of Nifedipine ($\Delta APD_{90} \leq 0$ ms with selective I_{CaL} inhibitors).

B.8 Experimental sex-related differences in APD_{90} under baseline conditions

The sex of an individual is commonly known to influence their physiology. With respect to cardiac physiology, structural and functional differences exist between male and female cardiomyocytes (Ramaekers *et al.*, 1998; Gaborit *et al.*, 2010), which translate into differences at the heart level (Ramaekers *et al.*, 1998; James *et al.*, 2007).

The hypothesis that there are differences in APD_{90} at baseline between sexes was tested on the new *ex vivo* data. The baseline APD_{90} was measured in all available trabeculae, and the distributions for trabeculae from the left ventricle were compared for males versus females. The distributions are plotted in Figure B.5A.

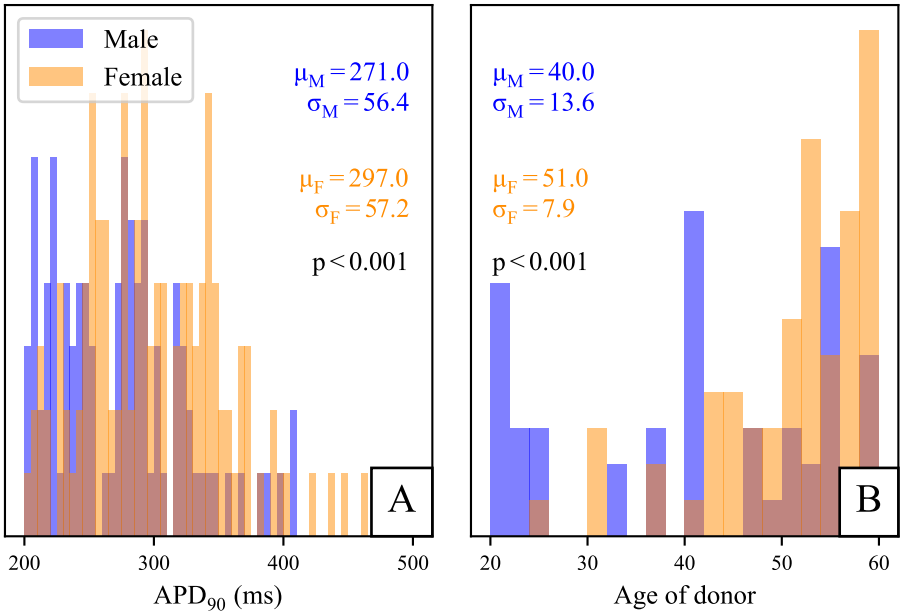

Figure B.5: Sex-related differences in APD_{90} under baseline conditions measured from human *ex vivo* ventricular trabeculae. **A:** Distribution of APD_{90} observed in the *ex vivo* data, filtered on the sex of the donor. **B:** Distribution of the age of male and female donors which hearts were used to obtain the trabeculae. *p*-values were computed with the Mann-Whitney U-test.

APD_{90} in trabeculae extracted from female donor hearts was observed to be significantly longer than from male donor hearts under baseline conditions, in accordance with the literature (James *et al.*, 2007; Peirlinck *et al.*, 2021). The experimental results

from this *ex vivo* study are nevertheless mitigated by the significant age difference between male and female donors. Reardon & Malik (1996) have observed that the QT interval was prolonged by ageing, and they interestingly did not find any significant effect of gender on the QT interval.

Ultimately, it can only be concluded from the *ex vivo* data presented in Chapter 4 that older female patients have longer APD_{90} under baseline conditions than younger male patients.

C

Comparison of in silico predictions of action potential duration in response to inhibition of I_{Kr} and I_{CaL} with new human experimental data

C.1 Comparison of error measures using only nominal drug concentrations even when measured drug concentrations in the bath solution are available

As reported in Table 5.1, drug concentrations in the bath solution were measured for some compounds, while they were not measured for other compounds. In this section we compare whether simulating the drug-induced ΔAPD_{90} with nominal concentrations impacts the (mis)match between predictions by *in silico* AP models and *ex vivo* measurements of ΔAPD_{90}.

Measured drug concentrations in the bath solution did not match exactly with nominal drug concentrations (Table 4.8). Therefore, the exact location of experimental points on the 2-D maps changes when using nominal or measured drug concentrations. Yet, the quadratic surfaces fitted to the experimental points with nominal and measured drug concentrations were very similar (Section B.5). Therefore, the qualitative comparison of model predictions with the experimental data yields the same results when the nominal drug concentrations are used to compute the drug-induced inhibition of I_{Kr} and I_{CaL}.

To further support that the interpretation of our results were not sensitive to the discrepancy between measured drug concentrations in the bath solution and nominal

drug concentrations, the error measure, E (Eq. 5.2), was recomputed using nominal concentrations for all tested drugs, similarly to Figure 5.5.

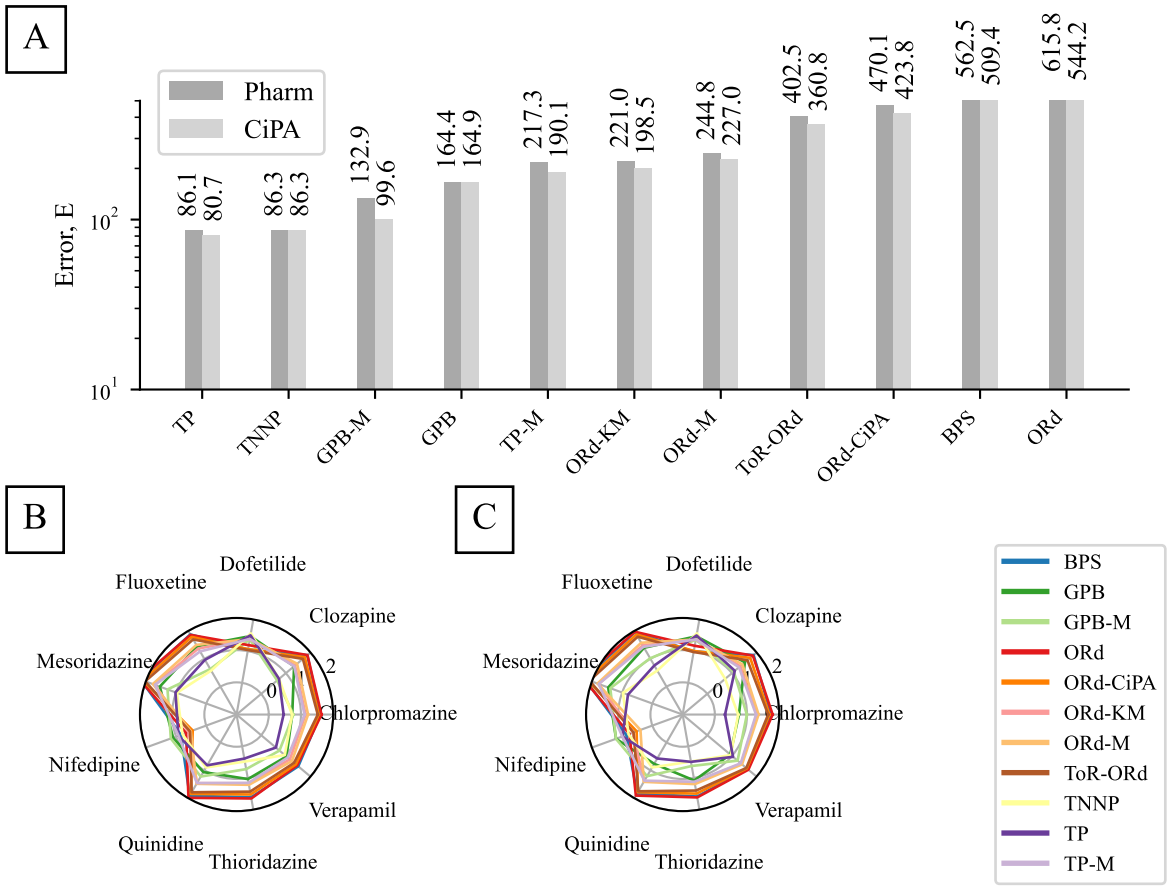

Figure C.1: Comparison of the abilities of human ventricular AP models to reproduce the APD_{90} response to I_{Kr} and I_{CaL} inhibition observed *ex vivo*, using only nominal drug concentrations as inputs for simulations. The error metric was computed from Eq. 5.2. **A:** The error measure was summed over all the drugs used in this study, when using the Pharm and CiPA protocols to compute the reduction of ionic currents by drugs. For each model, two bar plots were plotted, to compare the predictive power of models with the Pharm (left bar) and the CiPA (right bar) datasets. **B and C:** Detail of the error measures associated to each of the drugs with the CiPA and Pharm datasets, respectively, for each model. The $\log_{10}$ of the error measure is plotted along the radial-axis.

The results (Figure C.1) are similar to the results obtained with measured drug concentrations in the bath solution (when available), and the interpretation of our results therefore did not depend on the discrepancy between the measured and nominal drug concentrations.

D

Goodness-of-fit versus model predictivity, or parameters that could versus should be calibrated

D.1 Duration of pre-pacing to approach steady-state

To determine when the TP model converged to its limit cycle with various parameter values tested during optimisation, the TP model was paced for 2000 s with different values for the conductance parameters that cover the search space described in Section 6.3.3. 30 digital twins were created with the TP model by sampling values for the scaling factors for 8 conductance parameters of the TP model (Table 6.1) within $-4 < \hat{g} < +4$, with the Latin hypercube sampling method (Loh, 1996). Conductance parameters used in simulations were computed with Eq. 6.1. APs were read out after different numbers of pre-paces (50, 100, 200, 500, 1000, 1500, 2000 paces) and the distance to the AP obtained after 2000 pre-paces was computed for each synthetic individual as:

$$\text{distance}(\tau) = \sum_{t=0\ ms}^{t=1000\ ms} |V_\tau(t) - V_{2000}(t)|, \tag{D.1}$$

with τ the number of pre-paces, and V_τ the simulated voltage after τ pre-paces. This was repeated for the different combinations of I_{Kr} and I_{CaL} inhibition used for model training (0%/0%, 25%/20%, 50%/40%, 75%/60%, respectively). The mean deviation is plotted in Figure D.1.

After 500 pre-paces, the deviation from the limit cycle AP was acceptable (< 0.5 mV) for 26 out of 30 model parameterisations. The parameterisations of the TP model for

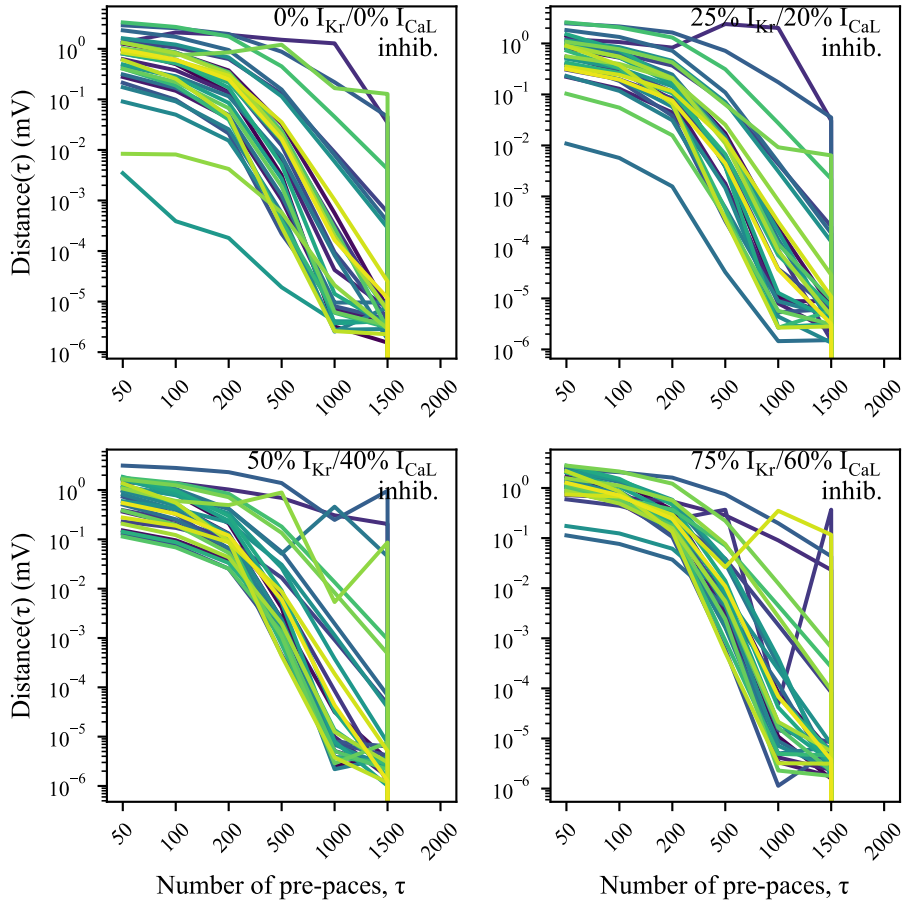

Figure D.1: Distance from the limit cycle AP after different numbers of pre-paces τ (Eq. D.1), computed for four combinations of I_{Kr} and I_{CaL} inhibition, for 30 parameterisations of the TP model.

which the AP was far from its limit cycle after the 500th pace (in blue and indigo) generated pathological APs under baseline conditions, so they are disregarded. 500 pre-paces was therefore selected as a trade-off between reducing computational cost of simulations while preserving accurate simulation outputs. Unless stated otherwise, simulations in this study were performed with 1 Hz steady pacing for 500 pre-paces to bring the TP model to steady-state.

D.2 Boundaries for the search space compared with the variability in maximal conductance parameters between the published models for human ventricular action potential

The parameters considered in this study were the maximal conductance parameters of the TP model. To define reasonable boundaries for the search space during model training, the variability of the maximal conductance parameters in the literature was investigated.

The values of maximal conductance parameters published in 12 models for the adult human ventricular AP were reported in the Table D.1 below (Bartolucci *et al.*, 2020; O'Hara *et al.*, 2011; Grandi *et al.*, 2010; Tomek *et al.*, 2020; Ten Tusscher *et al.*, 2004; Ten Tusscher & Panfilov, 2006; Dutta *et al.*, 2017; Fink *et al.*, 2008; Asakura *et al.*, 2014; Himeno *et al.*, 2015; Bernus *et al.*, 2002; Mann *et al.*, 2016). The models are labelled consistently with previous Chapters, namely BPS, ORd, GPB, ToR-ORd, TNNP, TP, ORd-CiPA, Fink 2008, Asakura 2014, Himeno 2015, Bernus 2002, and ORd-M and TP-M, respectively. Note that the units of the TP model needed to be corrected by adding a factor 1000 to p_{CaL} (Barral *et al.*, 2022b). Also, in the ORd and ORd-CiPA models, the conductance parameters for Na^{+}-Ca^{2+} and Na^{+}-K^{+} exchangers are consistent with $C{\cdot}F^{-1}$ units, while other models use $A{\cdot}F^{-1}$ units.

Model	G_{CaL}	G_{NaK}	G_{NaCa}	G_{pCa}	G_{Kr}	G_{Ks}	G_{K1}	G_{to}	G_{pK}	G_{KB}	G_{CaB}
BPS (cell type 1)	1.26e-01	2.30e-03	5.40e01	5.00e-04	6.07e-02	9.52e-03	1.63e-01	8.00e-02		1.80e-03	2.50e-08
GPB Endo	2.70e-01	4.50e00	1.80e00*	6.73e-02	3.50e-02	3.50e-03	3.50e-01	1.40e-03	2.00e-03		5.51e-04
ORd (cell type 1)	1.20e-01	8.80e-04	2.70e01	5.00e-04	5.98e-02	4.76e-03	2.29e-01	8.00e-02		1.80e-03	2.50e-08
ORd-M (cell type 3)	2.01e-01	2.36e-03	2.74e02	5.00e-04	4.60e-02	1.96e-02	1.91e-01	2.00e-02		3.00e-03	2.50e-08
ORd-CiPA (cell type 1)	1.21e-01	8.80e-04	2.70e01	5.00e-04	6.06e-02	6.36e-03	3.89e-01	8.00e-02		1.80e-03	2.50e-08
ToR-ORd (cell type 2)	1.68e-01	4.76e-03	1.08e01	5.00e-03	2.57e-02	1.10e-03	9.09e-01	3.20e-01	4.32e00	1.89e-02	5.92e-08
TP Epi	3.98e-02	1.00e03	2.72e00*	1.24e-01	1.53e-01	3.92e-01	5.41e00	7.30e-02	1.46e-02		5.92e-04
TP-M	3.12e-02	2.67e03	5.67e00*	1.24e-01	4.06e-01	1.61e-01	5.41e00	7.30e-02	1.46e-02		5.92e-04
Fink 2008	1.97e-02	2.00e+02	1.297*	6.19e-02	2.40e-02	3.92e-02	6.82e-01	2.00e-01	9.73e-03		4.74e-04
Asakura 2014 Epi	1.42e+01	6.11e+01	2.44e+01		1.00e-02	0.6955^{+}	1.35e+00	0.08553^{+}	1.77e+01		6.822e-04^{+}
Himeno 2015	1.42e+01	3.05e+01	2.52e+01	1.90e-01	1.66e-02	2.782e-03^{+}	3.18e-02	3.12e-02		1.4e-04^{+}	6.822e-05^{+}
Bernus 2002	0.064 mS.μF^{-1}	1.00e+03	1.3*			1.90e-02	3.90e+00	4.00e-01			8.50e-04
Parameter amplitude (max/min)	**721.32**	**1.14e+06**	**25**	**380**	**41**	**356**	**170**	**286**	**8837**	**11**	**34000**

Model	G_{Na}	G_{NaL}	G_{NaB}	G_{ClCa}	G_{ClB}
BPS (cell type 1)	2.03e01	1.47e-02	3.75e-10		
GPB Endo	2.30e01		5.97e-04	5.48e-02	9.00e-03
ORd (cell type 1)	7.50e01	4.50e-03	3.75e-10		
ORd-M (cell type 3)	7.50e01	7.50e-03	3.75e-10		
ORd-CiPA (cell type 1)	7.50e01	1.20e-02	3.75e-10		
ToR-ORd (cell type 2)	1.18e01	2.79e-02	1.92e-09	2.84e-01	1.98e-03
TP Epi	1.48e01		2.90e-04		
TP-M	1.48e01	1.43e-02	2.90e-04		
Fink 2008	1.10e+01		2.90e-04		
Asakura 2014 Epi	6.756 pA.mM^{-1}	1.06 pA.mM^{-1}			
Himeno 2015	8.1072^{+}		3.5e-04^{+}		
Bernus 2002	1.60e+01		1.00e-03		
Parameter amplitude (max/min)	**7**	**6**	**2.7e+06**	**5**	**5**

Table D.1: Maximal conductance parameters in published AP models. G_{CaL} is expressed in L·F^{-1}·s^{-1}, G_{NaCa} and G_{pCa} are expressed in A·F^{-1}, G_{NaK} is expressed in C·F^{-1}, and the remaining conductances, noted with a g, are expressed in mS·μF^{-1}. Values indicated with a * are expressed in A·F^{-1}, $^{+}$ are expressed in L·F^{-1}·s^{-1}.

The various models did not include all the same currents. For example, the Bernus *et al.* (2002) model features only 9 ionic currents, while the Tomek *et al.* (2020) model features 16 different ionic currents. This suggests high model discrepancy between the various AP models, for which the conductance parameters must compensate. As a consequence, most parameters vary by a factor > 100 in the different models: G_{CaL}, G_{NaK}, G_{pCa}, G_{Ks}, G_{K1}, G_{to}, G_{pK}, G_{CaB}, G_{NaB}. G_{CaL} varies by a factor 721 between the Asakura *et al.* (2014); Himeno *et al.* (2015) models and the Fink *et al.* (2008) model. G_{Kr} varies by a factor 41 "only", between the Tomek *et al.* (2020) model (cell type 2 version) and the TP model (epicardial version). In the extreme case, the conductance parameters of the Ca^{2+} and Na^{+} background currents (G_{CaB} and G_{NaB}, respectively) vary by factors 34,000 and 2.7×10^6 between the different models, respectively.

For the Cl^{-}-activated Ca^{2+} current ($\mathrm{I_{ClCa}}$) and the Cl^{-} background current ($\mathrm{I_{ClB}}$), the low variability can be explained by the fact that they are featured only in two models that included these currents based on the same experimental dataset.

Compared with other currents, relatively minor changes where applied to the formulation of $\mathrm{I_{Na}}$ since the work of Hodgkin & Huxley. This partially explains the small variability in G_{Na} between models ("only" a factor 7 between the different models which express it in $\mathrm{mS{\cdot}\mu F^{-1}}$).

When ionic currents are combined together in an AP model, conductance parameters of major, well understood currents, such as $\mathrm{I_{Na}}$ and $\mathrm{I_{Kr}}$, are often set to values measured experimentally. Note how the major currents tend to vary less between the models. However, the remaining parameters have often been tuned to achieve physiological features. For example in the TP model, G_{Na} has been set to values matching experimental measurements of conduction velocity, whilst G_{Kr}, G_{Ks}, $\mathrm{G_{pCa}}$, and $\mathrm{G_{pK}}$ were scaled to achieve a physiological APD (Ten Tusscher & Panfilov, 2006).

From such substantial variations in the conductance parameters used in the various published AP models, a wide search space was defined. When model discrepancy was introduced between the calibrated and the true model (GPB and ORd-CiPA models as true models), the search space for the conductance parameters was set to $-8 < \hat{g} < +5$ (Eq. 6.1), corresponding to scaling factors between 3.4×10^{-4} and 148. Without model

discrepancy (TP#1 and TP#2 models as true models), the boundaries of the search space were set to $-4 < \hat{g} < +4$, corresponding to scaling factors between 1.8×10^{-2} and 55. Thus, the search space is approximately 1.5 times wider than the range of variations observed in the RNA-Seq data (Section 6.2.1).

D.3 Tuning of hyperparameters of the CMA-ES algorithm for model training

D.3.1 TP#1 and TP#2 data: without model discrepancy

The number of particles used in each iteration of the CMA-ES algorithm and the number of repeats needed to achieve identifiability of the parameters of the TP model were investigated. Synthetic training data were generated with the original TP model exposed to four combinations of I_{Kr} and I_{CaL} inhibition (Figure 6.5A). The eight adjustable conductance parameters of the TP model (Table 6.1) were then inferred from the training synthetic data using the CMA-ES algorithm and various hyperparameter settings.

Different numbers of particles exploring the parameter space, $\mathcal{N}$, and different values of the diagonal elements of the initial proposal covariance for new parameter samples, Σ_0, were used. With the computational facility available, the goodness-of-fit for up to 24 particles could be evaluated in parallel, which was selected as maximal number of particles considered in this section. The number of optimisation repeats yielding correct parameter estimates are reported in the Table D.2.

$\mathcal{N}$	**7**	**10**	**14**	**24**
$\Sigma_0 = 0.3$	6/10	6/10	8/10	9/10
$\Sigma_0 = 0.6$	7/10	6/10	7/10	9/10
$\Sigma_0 = 1$	7/10	6/10	8/10	10/10
$\Sigma_0 = 1.5$	**8/10**	7/10	8/10	10/10

Table D.2: Number of optimisation repeats needed to find correct parameter values, when inferring values of eight conductance parameters of the TP model from synthetic data generated using the same TP model. Numbers in the table are reported as number of optimisation repeats yielding the correct parameter values/total repeats performed. In bold, $\mathcal{N}$ and Σ_0 achieving the best trade-off between computational cost and accuracy of results.

With $\mathcal{N} = 7$ and $\Sigma_0 = 0.3$, incorrect parameters were inferred 4 times out of 10 times, as the optimisation algorithm converged to a suboptimal solution different from the true parameters, i.e., a local optimum. Increasing the number of particles increased

the number of inference repeats that converged to the the true parameter values, i.e., the global optimum. For instance, with 24 particles and $\Sigma_0 > 0.6$, all 10 optimisation repeats yielded the global optimum. Increasing the spread of the initial particles Σ_0 also improved the outcome of parameter inference. With $\Sigma_0 = 1.5$, the initial particles were spread over the whole search space, thus enabling a more complete exploration of the search space. These improvements thus reduce the need for inference repeats.

The best trade-off ensuring reliably that the global optimum was found with minimal computational cost was selected as 7 particles with an initial spread of particles $\Sigma_0 = 1.5$. These hyperparameters were therefore used in the CMA-ES algorithm when the true model was the TP#1 or the TP#2 model.

D.3.2 GPB data: with model discrepancy

The same process as above was repeated, training the TP model on the GPB data (Figure 6.10).

The synthetic training data were generated with the GPB model, under the same four conditions of I_{Kr} and I_{CaL} inhibition (Figure 6.5A). The values for adjustable conductance parameters of the TP model (Table D.3) were inferred from the synthetic data using the CMA-ES algorithm with 7 to 48 particles. Diagonal elements of Σ_0 were set to 1.5, and the off-diagonals to 0. 100 inference repeats were performed.

The number of inference repeats that found the global optimum of $\mathcal{C}$ are reported in Table D.3. Note that in this case, the true values are not known because of the discrepancy between the GPB model and the TP model. The global optimum was therefore defined as parameter values for which the minimal value of $\mathcal{C}$ was found.

Number of particles	**7**	**10**	**14**	**24**	**48**
True model: GPB	2/100	8/100	19/100	**26/100**	43/100

Table D.3: Results of model training, when individualising all the variable conductance parameters (Table 6.1) of the TP model to the GPB data.

With the GPB model as the "true model", results concur with previous observations without model discrepancy: increasing the number of particles used to explore the search space improved the proportion of optimisation repeats converging to the global optimum.

A considerably lower proportion of inference repeats found the global optimum (43/100 with $\mathcal{N} = 48$ vs up to 10/10 without model discrepancy). Therefore, $\mathcal{N} = 24$ and 10 repeats were used to train the TP model on synthetic data generated with the GPB model, while $\mathcal{N} = 7$ was sufficient when there was no model discrepancy.

D.4 Chaotic behaviour of the TP model induced by particular changes in I_{Kr} and I_{CaL}

The chaotic behaviour of the TP model, previously mentioned in the literature for afterdepolarisations (Kügler *et al.*, 2017; Sato *et al.*, 2009), was investigated under conditions of reduced I_{Kr} and I_{CaL}, consistent with the perturbations of interest for this study.

Periodic outputs were observed over 25 APs after steady 1 Hz pacing for 1500 pre-paces, with periods sometimes longer than 2 APs — see illustrative example in Figure D.2A. The mean changes in APD_{90} from baseline (no I_{Kr} or I_{CaL} inhibition) were computed for all perturbations, and plotted as a 2-D map in Figure D.2B. APD_{90} was measured for 25 consecutive APs and the APD_{90} alternans was deduced, then plotted in Figure D.2C for all I_{Kr} and I_{CaL} perturbations. The period of the limit cycle was plotted in Figure D.2D for all the I_{Kr} and I_{CaL} perturbations. Limit cycles with periods longer than 2 APs are denoted as exhibiting "multi-AP alternans" in the following text.

The 2-D map of mean changes in APD_{90} induced by inhibition of I_{Kr} and I_{CaL} is smooth (Figure D.2B), so no chaotic behaviour could be observed at this level. Still, 3 regimes were observed (Figures D.2C and D) over the variety of perturbations. For more than 50% or less than 40% I_{CaL} inhibition, no alternans was observed. In between, APD_{90} alternans varied between 0.2 ms (0% I_{Kr}/50% I_{CaL} inhibition) and 5 ms (100% I_{Kr}/47% I_{CaL} inhibition).

A synthetic individual — denoted $\Phi_{data,3}$ — was created by rescaling the conductance parameters of the TP model based on RNA-Seq data for one of the 303 samples, reported in Table D.4 below. The limit cycle of the $\Phi_{data,3}$ model exhibited multi-AP alternans with a period of 6 APs with 75% I_{Kr}/60% I_{CaL} inhibition (Figure D.3).

Note that the chaotic behaviour — characterised by what we denote "multi-AP alternans", see Section D.2 — of the TP model was not observed in adult human ventricular tissue exposed to similar I_{Kr} and I_{CaL} perturbations in Chapter 4. Yet,

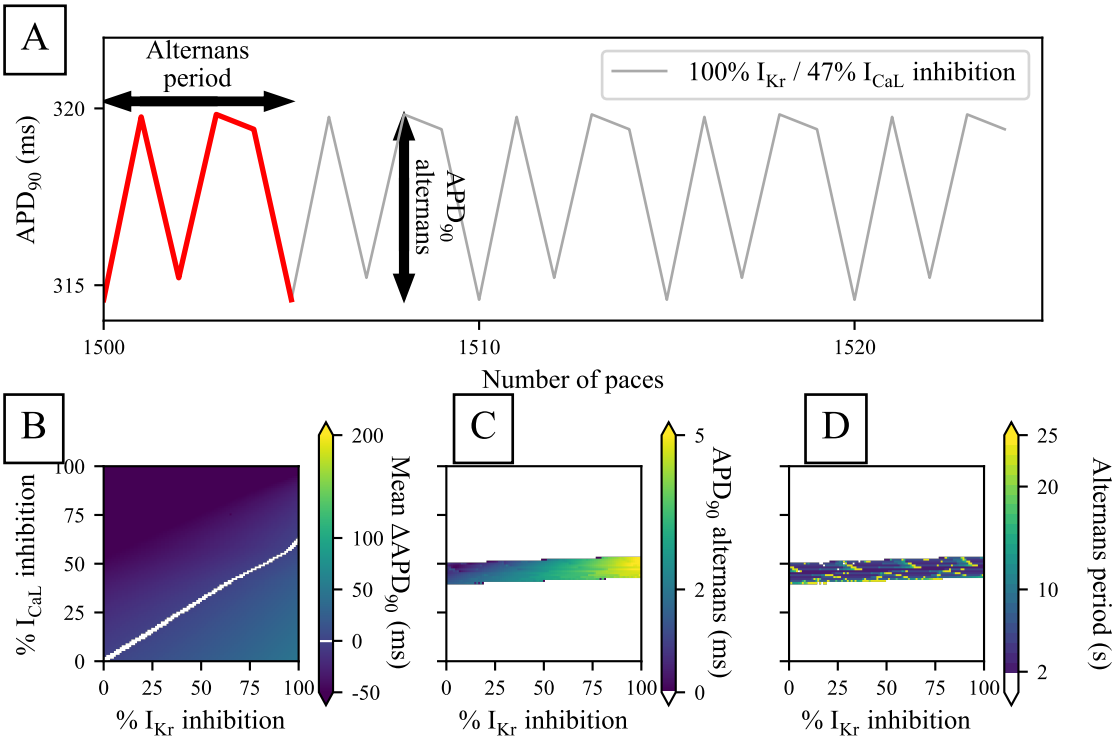

Figure D.2: TP chaotic behaviour with multi-AP alternans appearing after inhibition of I_{Kr} and I_{CaL}. **A:** Illustrative alternans of APD_{90} after 100% I_{Kr} and 47% I_{CaL} inhibition, with 5 s period of alternans. **B:** APD_{90} change from baseline, averaged over the 25 output APs. **C:** APD_{90} variations during the limit cycle. **D:** Period of the limit cycle.

whether the chaotic behaviour is a desirable feature that should be reproduced in AP models is beyond the scope of the present thesis.

Parameter	$\hat{g}_{Kr}$	$\hat{g}_{CaL}$	$\hat{g}_{Ks}$	$\hat{g}_{K1}$	$\hat{g}_{Na}$	$\hat{g}_{NaCa}$	$\hat{g}_{NaK}$	$\hat{g}_{to}$
Value	-0.68	-0.80	-0.71	-0.71	-0.78	-0.70	-0.87	-0.78

Table D.4: Log-transformed scaling factors, $\hat{g}$ (Eq. 6.1), applied to maximal conductance parameters of the TP model to create the synthetic data for $\Phi_{data,3}$.

The multi-AP alternans period of the limit cycle was chaotic (Figure D.2D). A slight change in I_{Kr} or I_{CaL} inhibition (or similarly a slight change in conductance parameters) can lead to important variations in the period of the limit cycle. Sudden changes in the period of multi-AP alternans lead to sudden changes in the fitness of parameters consituting a multitude of local optima (Figure D.4). We hypothesised that such discontinuities in the cost function during parameter inference make the parameter space harder to explore for the optimisation algorithm which is more likely to be "trapped" in local optima. This hypothesis was tested with the $\Phi_{data,3}$ model as the true model.

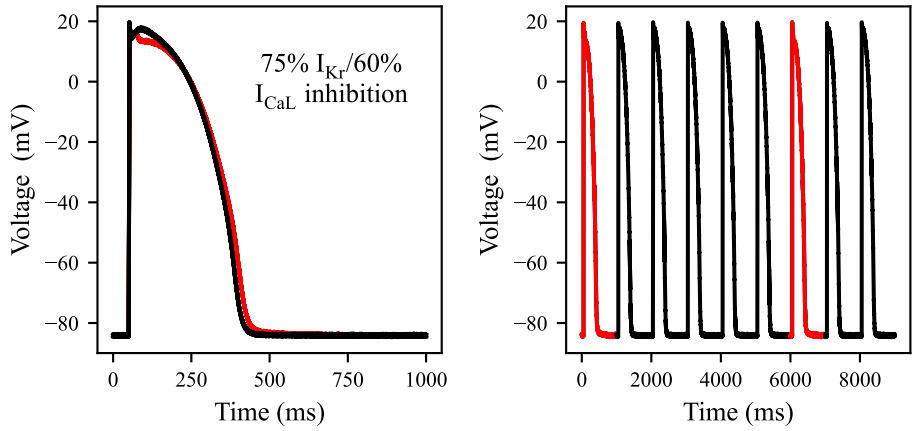

Figure D.3: Multi-AP alternans in the training synthetic dataset generated with the TP model parameterisation corresponding to individual #3 (Table D.4). The 1st and 7th APs are plotted in red, while the remaining ones are plotted in black.

Synthetic AP data were generated with the $\Phi_{\text{data,3}}$ model, and used to develop individual-specific TP models, similarly to Part II (Algorithm 1). The evolution of the metrics $\mathcal{W}$ (Eq. 6.6) and $\mathcal{P}$ (Eq. 6.7) with the increase of the number of inferred parameters is reported in Table D.5.

	Number of fitted parameters	2	3	4	5	6	7	8
$\Phi_{\text{data,3}}$	Added parameter	($\hat{g}_{\text{Kr}}$, $\hat{g}_{\text{CaL}}$)	$\hat{g}_{\text{Na}}$	$\hat{g}_{\text{Ks}}$	$\hat{g}_{\text{K1}}$	$\hat{g}_{\text{NaK}}$	$\hat{g}_{\text{NaCa}}$	$\hat{g}_{\text{to}}$
	$\mathcal{W}$ (ms)	212.9	130.4	59.7	40.6	27.1	25.4	23.0
	$\mathcal{P}$ (ms)	0.16	0.16	0.50	0.62	0.86	0.91	0.94
	Average BIC	10^{10}	10^{10}	3×10^{9}	6×10^{8}	4×10^{8}	3×10^{8}	5×10^{7}

Table D.5: Evolution of the width of the 95% CI of error in ΔAPD_{90} prediction ($\mathcal{W}$) and proportion of ΔAPD_{90} predictions within 10 ms from the validation data ($\mathcal{P}$), with increasing numbers of parameters inferred. The true model corresponded to the $\Phi_{\text{data,3}}$ model, as described in Table D.4. The Bayesian Information Criterion (BIC) was computed with Eq. 6.8 and averaged over the 30 individual-specific parameterisations of the model found for each set of inferred parameters.

$\mathcal{W}$ and $\mathcal{P}$ were improved with increasing numbers of inferred parameters. Yet, $\mathcal{W}$ reached 23 ms and $\mathcal{P}$ reached 0.94 when all conductance parameters were inferred, while they converged respectively towards 0 ms and 1, with both $\Phi_{\text{data,1}}$ and $\Phi_{\text{data,2}}$ (Table D.5). This supports that the identifiability of the conductance parameters was lost when the $\Phi_{\text{data,3}}$ model was used as true model.

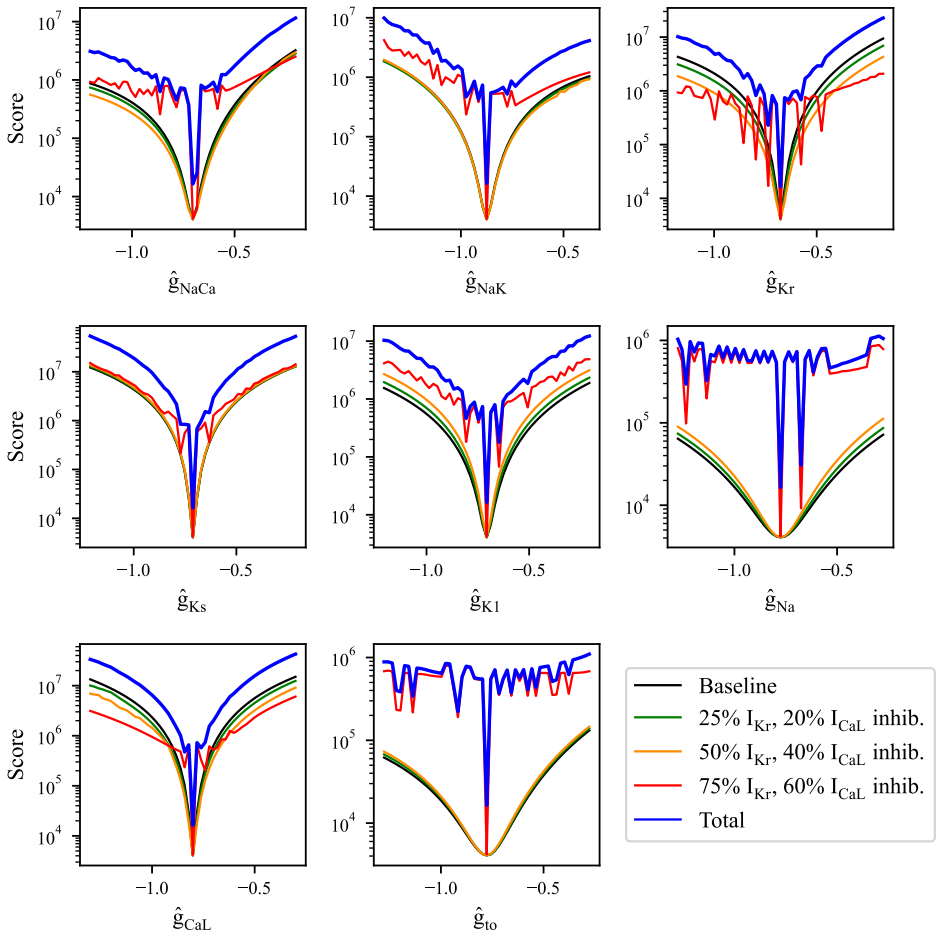

Figure D.4: One-at-a-time sensitivity analysis of the cost function (Eq. 6.4) surface around parameter values corresponding to $\Phi_{\text{data},3}$ (Table D.4).

D.5 Choice of the number of samples for the propagation of uncertainty in fixed parameters

In this study, the effect of uncertainty in fixed parameters was recapitulated by setting them to different values covering their uncertainty range found from experimental data (Figure 6.3). In this subsection, we justify the number of samples for fixed parameters used to estimate correctly the uncertainty in fixed parameters. The number of samples for fixed parameters needed to achieve a trade-off between computational cost and accurate estimation of the error in predictions. To select the number of samples, $\mathcal{P}$ (Eq. 6.7) was observed as a function of the number of samples for fixed parameters.

The models for 100 digital twins returning non-pathological APs were taken from the RNA-Seq data introduced in Section 6.2.1. Values for G_{Kr}, G_{CaL}, and G_{Ks} were inferred

from the $\Phi_{\text{data},1}$ data (Figure 6.5) with values for G_{K1}, G_{to}, G_{Na}, G_{NaK}, and G_{NaK} taken from 100 random digital twins. 100 trained versions of the TP models were thus obtained.

Predictions of ΔAPD_{90} response to 55 I_{Kr} and I_{CaL} inhibition conditions (Figure 6.5B) were simulated for each of the 100 trained models. The predictivity metric $\mathcal{P}$ was computed following Eq. 6.7 from predictions taken randomly from 1 to 100 samples. The process was repeated inferring (G_{Kr}, G_{CaL}, G_{Ks}) and fixing values of (G_{K1}, G_{to}, G_{Na}, G_{Ks}, G_{NaCa}). The evolution of $\mathcal{P}$ as a function of the number of samples for fixed parameters is plotted in Figure D.5.

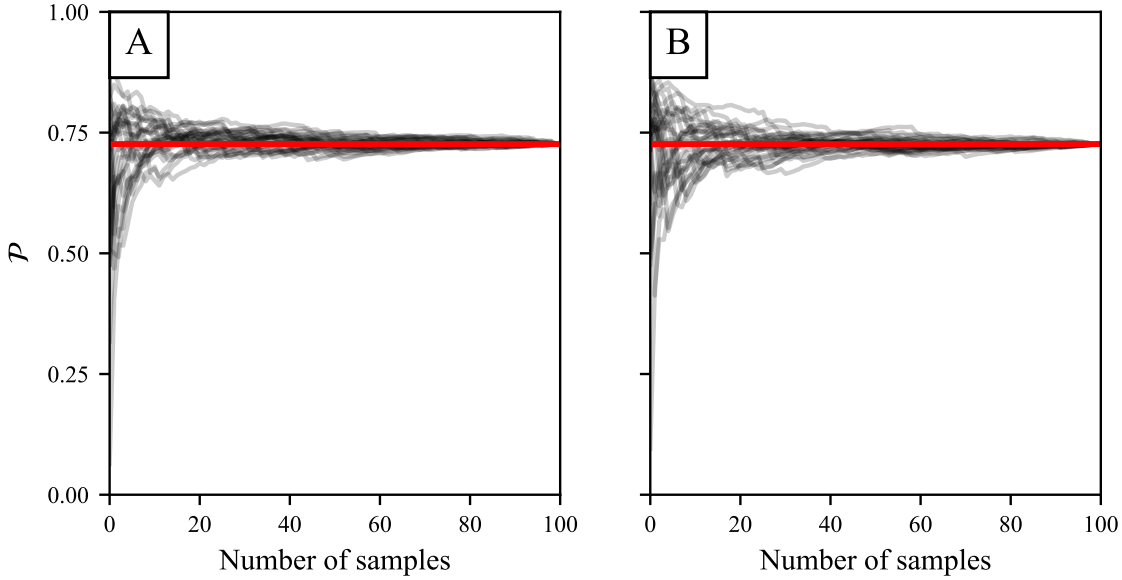

Figure D.5: Evolution of the predictivity metric $\mathcal{P}$ with the number of samples for fixed parameters used to estimate it. **A:** Individual-specific values for (G_{Kr}, G_{CaL}, G_{Ks}) were inferred. **B:** Individual-specific values for (G_{Kr}, G_{CaL}, G_{NaK}) were inferred.

The metric $\mathcal{P}$ was very variable when the number of samples was low, as each ϕ sample had a higher individual contribution to $\mathcal{P}$. Then, from 30 to 80 samples, low variations of $\mathcal{P}$ were observed. Therefore, 30 samples were selected to evaluate accurately the propagation of uncertainty in fixed parameters onto model predictions with a reasonably low computational cost.

E

Calibration of a human ventricular action potential model for prediction of changes in action potential duration induced by acute inhibition of two major ionic currents

E.1 Unclamping K^+ and Cl^- concentrations in the new AP model

In the original Grandi *et al.* (2010) model reformulated by Mann *et al.* (2016) (GPB-M), the concentrations of K^+ and Cl^- in the various compartments are considered as fixed. Thus, the intracellular concentrations of these ions are not updated under the effect of the various ionic currents. Therefore, the conservation of charge principle is not upheld in this model (Barral *et al.*, 2022b).

To ensure that the conservation of charge principle is upheld in the model, the concentrations of K^+ and Cl^- were unclamped. The following changes were therefore applied to the GPB-M model:

- K^+ and Cl^- currents were split into currents to the subsarcolemmal and junctional spaces, similarly to other ionic currents. The same repartition of ion channels was assumed for K^+ and Cl^- currents as for Na^+ currents: 90% in the subsarcolemmal space and 10% in the junctional space;
- Reversal potentials used to compute the various K^+ and Cl^- currents were computed for each subcellular compartment;

- Diffusion fluxes between the subcellular compartments were added for K^+ and Cl^-. The diffusion rate constants were assumed to be the same as for Na^+ (O'Hara *et al.*, 2011);
- Initial values for the intracellular concentrations of K^+ and Cl^- were assumed to be the same in all the subcellular compartments;
- Fluxes of K^+ and Cl^- into/out of the corresponding subcellular compartments were summarised with the equation:

$$\frac{\mathrm{d}[\mathrm{A}]}{\mathrm{d}t} = z_{\mathrm{A}} \times I_{\mathrm{A,\,tot}} \times \frac{C_{\mathrm{m}}}{\mathcal{V}F} + J_{\mathrm{A,\,tot}}, \tag{E.1}$$

  with [A] the concentration of the ionic species in the subcellular compartment, z_{A} the valence of A, $I_{\mathrm{A,\,tot}}$ the total ionic current of A in the subcellular compartment, C_{m} the total membrane capacitance per surface area, F the Faraday constant, $\mathcal{V}$ the volume of the subcellular compartment, and $J_{\mathrm{A,\,tot}}$ the total diffusion flux between the subcellular compartment and the other subcellular compartments.

E.2 Duration of pre-pacing to approach steady-state

To determine when the new AP model converged to its limit cycle with sets of parameters tested during optimisation, the new AP model was paced at 1 Hz for 2000 s with scaling factors applied to the conductance parameters that correspond to the 30 random digital twins used in Chapter 6. The normalised AP was read out after different numbers of pre-paces (50, 100, 200, 500, 1000, 1500, 2000 paces) and the distance to the AP obtained after 2000 pre-paces was computed for each digital twin as:

$$\mathrm{distance}(\tau) = \sum_{t=0\ ms}^{t=1000\ ms} |V_{\mathrm{norm},\,\tau(t)} - V_{\mathrm{norm},\,2000}(t)|, \tag{E.2}$$

with τ the number of pre-paces, and V_τ the simulated voltage after τ pre-paces. $\mathrm{distance}_\tau$ was computed for the 30 digital twins, with different values of τ, and with different I_{Kr}/I_{CaL} inhibition (0%/0%, 25%/20%, 50%/40%, 75%/60%, respectively). The results are shown in Figure E.1.

750 pre-paces was selected as a trade-off between reducing computational cost of simulations while preserving the accuracy of simulations. Unless stated otherwise, simulations in Chapter 7 were performed with 1 Hz steady pacing for 750 pre-paces to bring the model to steady-state.

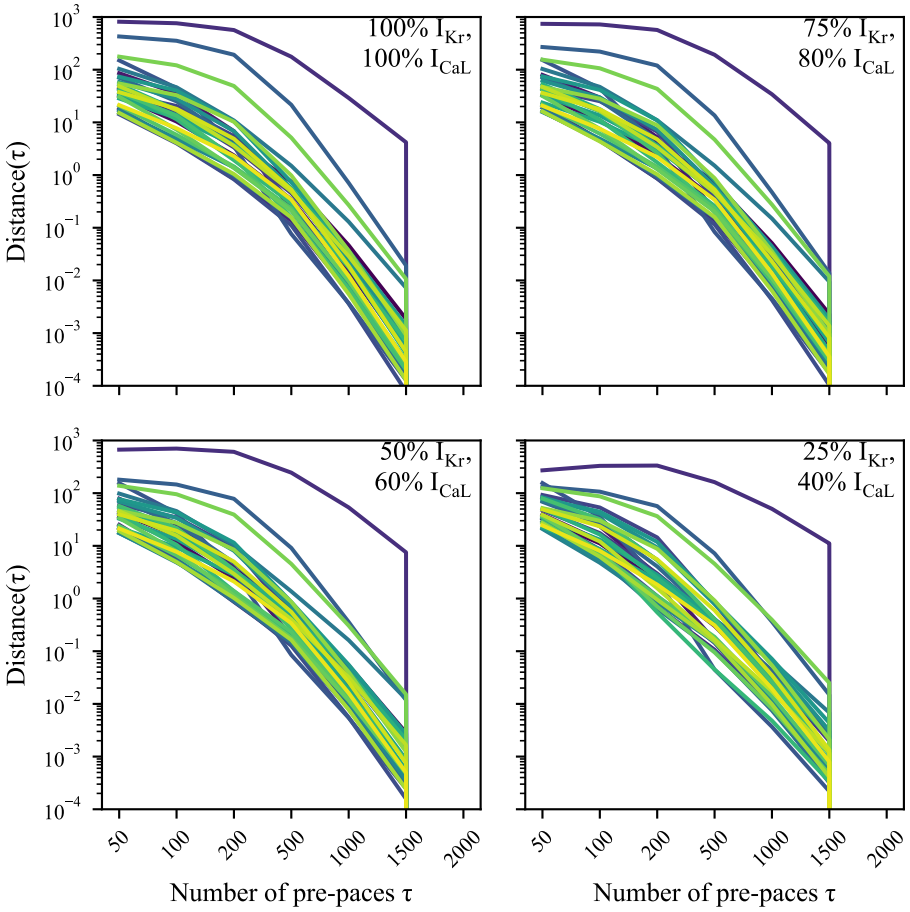

Figure E.1: Distance from the limit cycle AP after different numbers of pre-paces (Eq. D.1), computed for four different fractions of available I_{Kr}/I_{CaL} for 30 different digital twins.

E.3 Identifiability of parameters for training the Gen-NP model

At first, estimates of all conductance parameters and of the net intracellular concentration of un-modelled charges (Γ_0) were obtained from training with the naive-pooled data approach. The parameters are listed in Table E.1.

In Section 6.4.2 in Chapter 6, with model discrepancy, the global optimum of the cost function may be in a narrow "funnel" region of the parameter space. Therefore, the number of repeats (50), $\mathcal{N} = 20$ and $\Sigma_0 = 1.2$ were selected so that the parameter space was carefully explored with the CMA-ES algorithm. The distribution of estimates of $\hat{g}$ for each parameter is plotted in Figure E.2. Given the computational cost of this study (∼4000 CPUs.day), this identifiability test was only performed using Dataset #1

Parameter	Description
Γ_0	Net intracellular concentration of non-specific charges (Barral *et al.*, 2022b)
G_{Kr}	Conductance of the rapid delayed rectifier K^+ current
G_{Ks}	Conductance of the slow delayed rectifier K^+ current
G_{K1}	Conductance of the inward rectifier K^+ current
G_{pK}	Conductance of the pump K^+ current
G_{to}	Conductance of the transient outward K^+ current
G_{CaL}	Permeability of the L-type Ca^{2+} current
G_{CaB}	Conductance of the background Ca^{2+} current
G_{pCa}	Conductance of the pump Ca^{2+} current
G_{NaL}	Conductance of the late Na^+ current
G_{NaB}	Conductance of the background Na^+ current
G_{NaCa}	Permeability of the Na^+-Ca^{2+} exchanger current
G_{NaK}	Permeability of the Na^+-K^+ pump current
G_{ClCa}	Conductance of the Cl^--activated Ca^{2+} current
G_{ClB}	Conductance of the background Cl^- current

Table E.1: Parameters of the new AP model calibrated with the naive-pooled data approach from normalised AP data obtained in all trabeculae exposed to training drugs (Table 7.1). Log-transformed rescaling factors were inferred for maximal conductance parameters (Eq. 7.2).

to compute the I_{Kr} and I_{CaL} inhibition used as inputs for simulations (Table 7.2).

Estimates of G_{CaL}, G_{ClB}, G_{K1}, G_{Kr}, G_{NaCa}, and G_{NaK} were reproducibly found with narrow distributions. For G_{ClCa}, G_{pK}, G_{pCa}, G_{to}, and Γ_0, the parameter estimates were spread over the whole search space, indicating that these parameters were not identifiable. For G_{CaB}, and G_{NaB}, the parameter estimates were found at the limit of the search space ($\hat{g} = -5$). Therefore, the identifiability of G_{CaB} and G_{NaB} could not be verified.

The late sodium current (I_{NaL}) is attributed to the same ion channels as the fast Na^+ current (I_{Na}) (Maltsev *et al.*, 1998). Therefore, the same rescaling factors should be applied to the conductance parameters of these two currents. In the data recorded with sharp electrodes, the upstroke part of the AP was sometimes contaminated by (artefacts of) the biphasic pulse used to pace the tissue (Figure 4.9). Therefore, no information

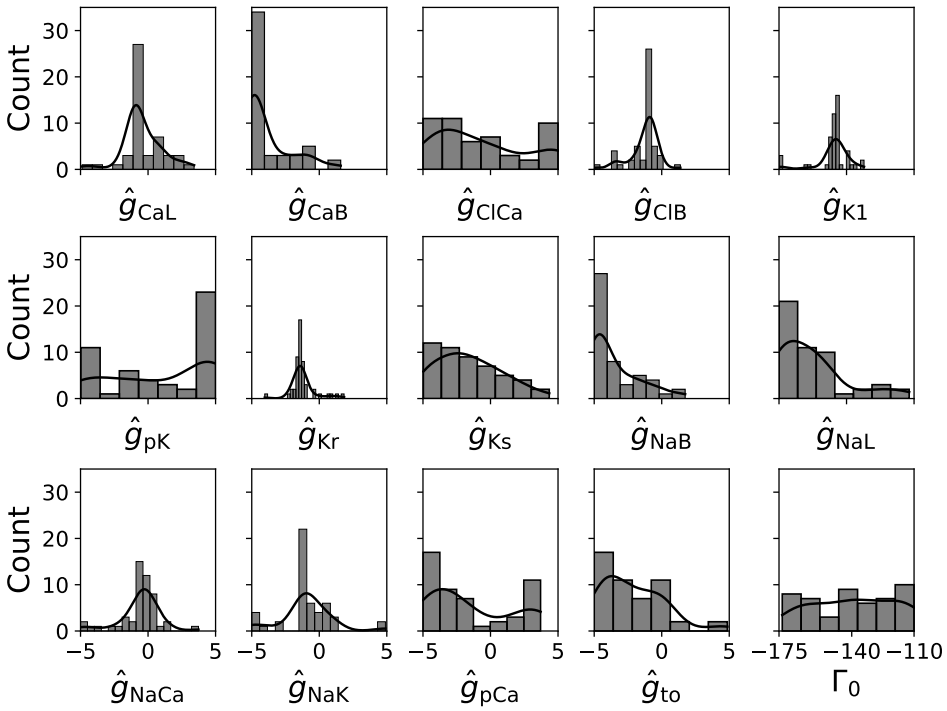

Figure E.2: Estimates of $\hat{g}$ for each parameter obtained by training the new AP model with the naive-pooled data approach, repeated with 50 random starting points.

about I_{Na} was inferred from these data, and the conductance parameters for both currents were left to the values originally published by Mann *et al.* (2016).

The estimate of G_{NaL} varied vastly (Figure E.2), with a weak correlation with the estimate of G_{Ks}. This can be explained with the observation that I_{NaL} and I_{Ks} exhibit opposite and important contributions to the AP in the new AP model. By fixing the value of G_{NaL} during model training, we hypothesised that the identifiability of G_{Ks} was recovered.

Therefore, 7 parameters were calibrated with the naive-pooled data approach: G_{Kr}, G_{CaL}, G_{Ks}, G_{K1}, G_{NaCa}, G_{NaK}, and G_{ClB}. The number of times the global optimum was found with 7 calibrated parameters is reported in Table E.2.

Model	Number of times the global optimum is found
Gen-NP#1	10/50
Gen-NP#2	4/50
Gen-NP#3	15/50
Gen-NP#4	5/50

Table E.2: Reproducibility of the training of the Gen-NP models with 7 calibrated parameters.

The training of the Gen-NP#1 and the Gen-NP#3 models was more reproducible, with up to 15 repeats finding the global optimum. Lower reproducibility was observed for the Gen-NP#2 and the Gen-NP#4 models, but the global optimum was found with at least in 4/50 training repeats. Note that these results depend on the points that are randomly sampled from the search space during the first iteration of the CMA-ES algorithm.

E.4 Identifiability of trabecula-specific parameters and selection of parameters to individualise

The identifiability of trabecula-specific parameters was tested on the normalised AP data recorded in trabecula #2022030802 exposed to Chlorpromazine, using IC_{50} Dataset #1 and the Gen-NP#1 model as a starting point. This trabecula was selected because it exhibited a qualitatively average response to Chlorpromazine.

The cost function $\mathcal{C}_{\#2022030802}$ (Eq. 7.4) was minimised with the CMA-ES algorithm. The optimisation problem was solved by starting from 100 random initial points, using different values for $\mathcal{N}$. The results are reported in Table E.3.

Number of particles $\mathcal{N}$	**6**	**8**	**12**	**24**
Number of repeats finding the global optimum	1/100	1/100	0/100	0/50
Number of repeats finding the second optimum	17/100	19/100	15/100	49/50

Table E.3: Number of times training a trabecula-specific model for #2022030802 yields the global optimum, with different values for the hyperparameter of the CMA-ES algorithm corresponding to the number of particles exploring the parameter space($\mathcal{N}$).

The global optimum was found only in 2/450 repeats, which is even more rare than when training the TP model on synthetic data generated with the ORd-CiPA model (Table 6.6).

Following the same logic as in Section 6.4.2, the surface of $\mathcal{L}$ is investigated. The surface of $\mathcal{L}$ as a function of parameter values is shown in Figure E.3, re-using parameter values sampled during the training of the trabecula-specific model for trabecula #2022030802.

Similarly to results in Section 6.4.2, the global optimum was found in a considerably narrower "funnel region" of the search space than the second optimum, which explains the low number of optimisation repeats that find the global optimum. The flat surface

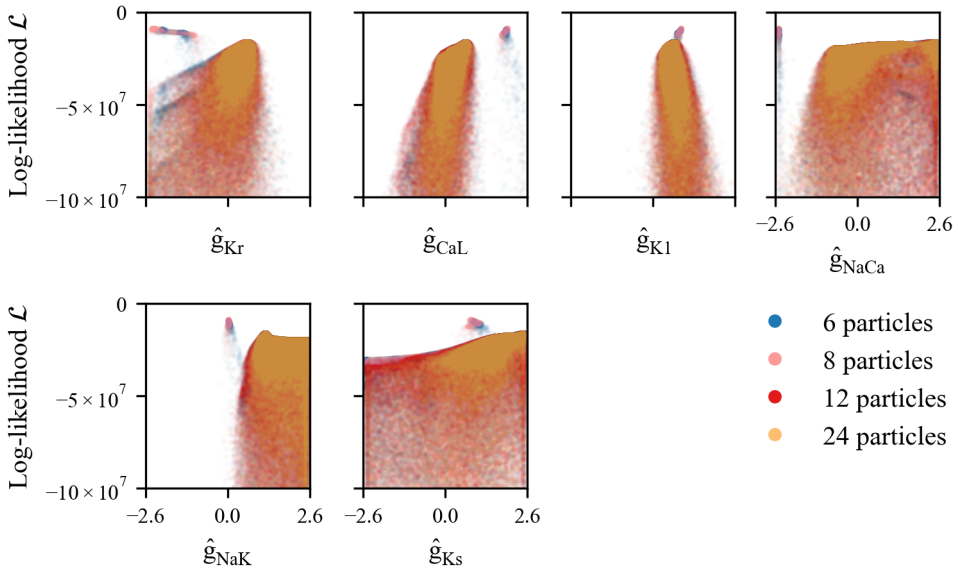

Figure E.3: Log-likelihood $\mathcal{L}_{2022030802}$ (Eq. 7.4) as a function of parameter values sampled during training of a trabecula-specific model for #2022030802. Each point corresponds to one sample in the parameter space explored by the CMA-ES algorithm.

of $\mathcal{L}$ suggested that $\mathcal{L}$ was insensitive to $\hat{g}_{NaCa}$ and $\hat{g}_{Ks}$, and that the corresponding conductance parameters should not be individualised. Furthermore, the optimal values of $\hat{g}_{Ks}$ and $\hat{g}_{NaCa}$ were limited by the boundaries of the search space, further supporting that these scaling factors should not be individualised.

The optimal values of $\hat{g}_{K1}$ corresponding to the global and second optima were similar (0.87 and 0.67, respectively). Given the small width of the funnel region around the global optimum compared with that of the second optimum, the CMA-ES algorithm is expected to rarely find the value of $\hat{g}_{K1}$ corresponding to the global optimum.

Values of $\hat{g}_{Kr}$, $\hat{g}_{CaL}$, and $\hat{g}_{NaK}$ corresponding to the global optimum were more distant to the values corresponding to the second optimum. We hypothesised that G_{Kr}, G_{CaL}, and G_{NaK} can be individualised using a low amount of particles ($\mathcal{N} = 6$) and a narrow initial spread of particles (diagonal elements of Σ_0 set to 0.5). This hypothesis was tested, and the surface of $\mathcal{L}$ as a function of $\hat{g}_{Kr}$, $\hat{g}_{CaL}$, and $\hat{g}_{NaK}$ is plotted in Figure E.4.

Individualising only G_{Kr}, G_{CaL}, and G_{NaK}, the global optimum was found in 96/100 repeats. The three parameters are therefore reproducibly identifiable. With the same logic as in Chapter 6 for the construction of the sets of individualised parameters, two sets of parameters were individualised: (G_{Kr}, G_{CaL}) and (G_{Kr}, G_{CaL}, G_{NaK}).

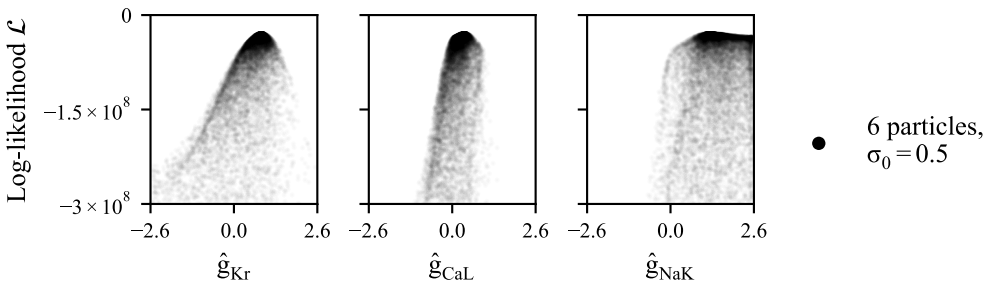

Figure E.4: Log-likelihood $\mathcal{L}_{2022030802}$ (Eq. 7.4) as a function of parameter values sampled during training of a trabecula-specific model for #2022030802, individualising only G_{Kr}, G_{CaL}, and G_{NaK}.

E.5 Detail of the error score for the Gen-NP models

In Figure E.5, $\Delta\mathrm{APD}_{90}$ predicted by the Gen-NP models are compared with the *ex vivo* data. The error in $\Delta\mathrm{APD}_{90}$ is presented as a multiple of the experimental standard error of the mean $\Delta\mathrm{APD}_{90}$, σ_{M}, thus making it a direct visualisation of the contribution to the error measure, E (Eq. 5.2), of each drug treatment.

Light colors in Figure E.5 support that model predictions yield low prediction errors for most drug perturbations, in particular using the Gen-NP#1 and the Gen-NP#4 models.

E was computed with Eq. 5.2 for the four Gen-NP models. The detail of E is shown in Figure E.6, similarly to Figure 5.5.

For the Gen-NP#1 and the Gen-NP#4 models, Clozapine, Fluoxetine, and Nifedipine contributed the most to E. For the Gen-NP#2 and the Gen-NP#3 models, Clozapine, Fluoxetine, Mesoridazine and Nifedipine contributed highly to E, and E was greater or equal to E for the Gen-NP#1 and the Gen-NP#4 models.

E.6 Detailed predictions by Col-NP$_3$ for training drugs

The predictions of Col-NP$_3$ for training drugs are shown in Figure E.7, similarly to Figure 7.8 for Col-NP$_2$.

Similarly to Col-NP$_2$, there was poor agreement between the $\Delta\mathrm{APD}_{90}$ predictions of Col-NP$_3$ and the *ex vivo* data. For low drug concentrations, the variability in predicted $\Delta\mathrm{APD}_{90}$ is underestimated, and it was overestimated for high drug concentrations. The models for trabeculae exposed to Verapamil were not as much outliers as observed in

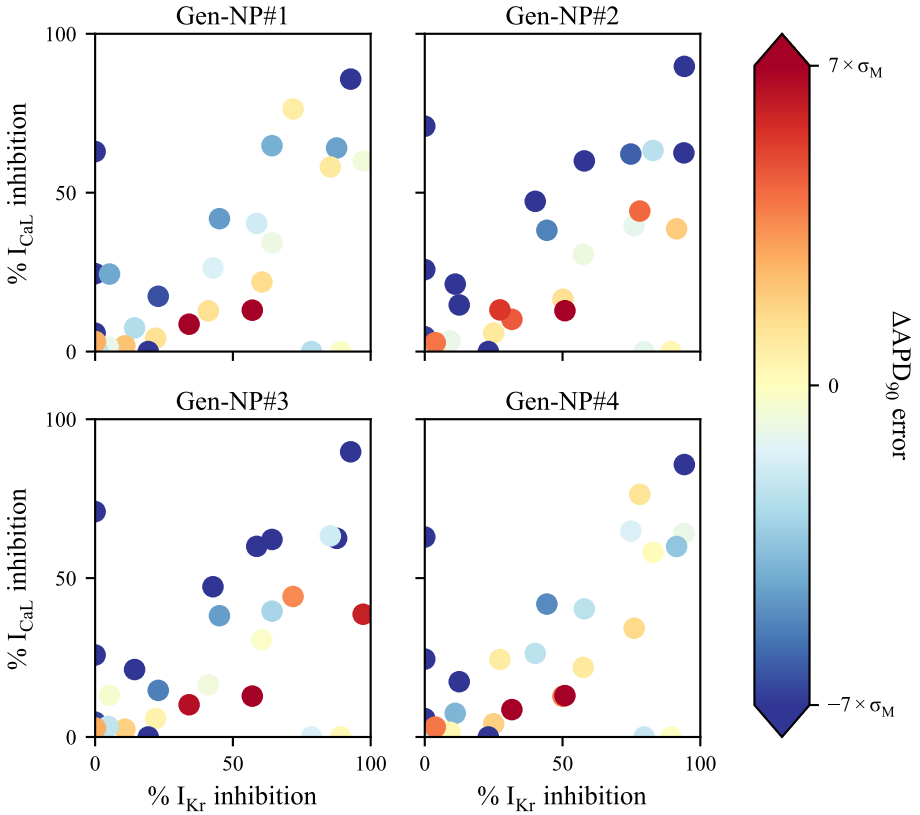

Figure E.5: Comparison of ΔAPD_{90} response to I_{Kr} and/or I_{CaL} inhibition predicted by the Gen-NP models with *ex vivo* data. σ denotes here the experimental variability in ΔAPD_{90} response to each drug perturbation.

Col-NP$_2$, except the model for the trabecula #2015071802. This model predicted APD_{90} under baseline conditions of 554 ms, while the baseline APD_{90} was 327 ms.

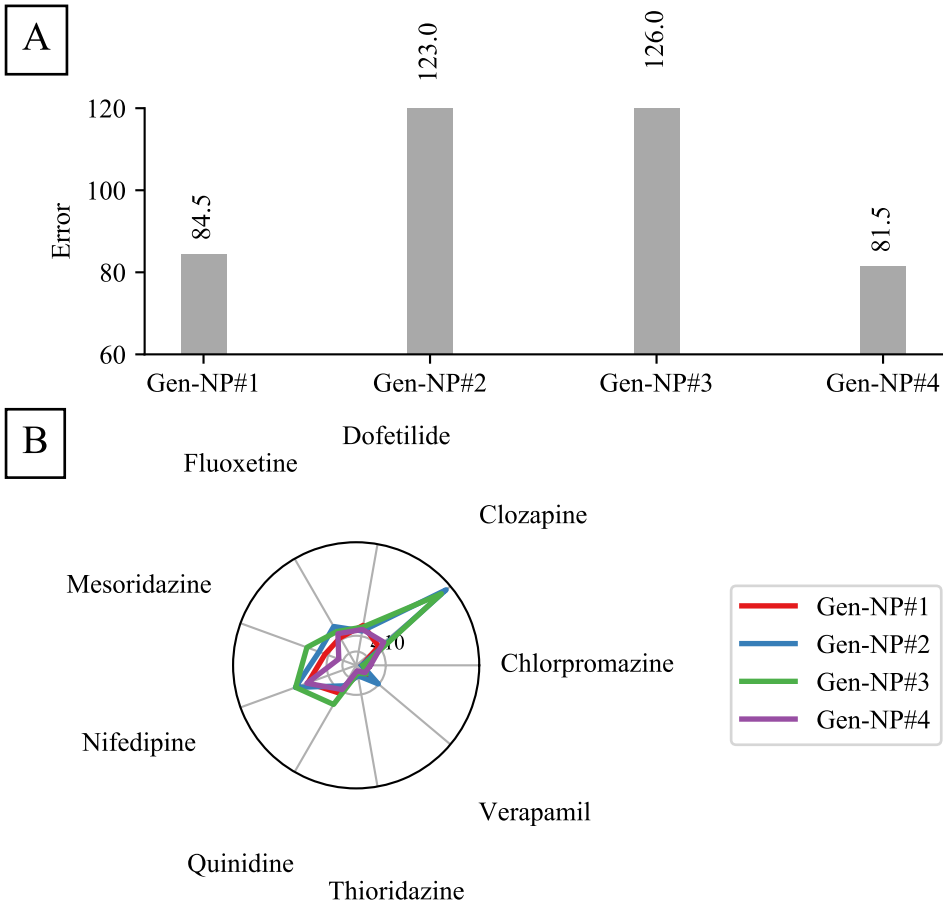

Figure E.6: **A:** The error measure was summed over all the drugs used in Chpater 7. **B:** Detail of the error measures associated with each of the drugs, for each Gen-NP model.

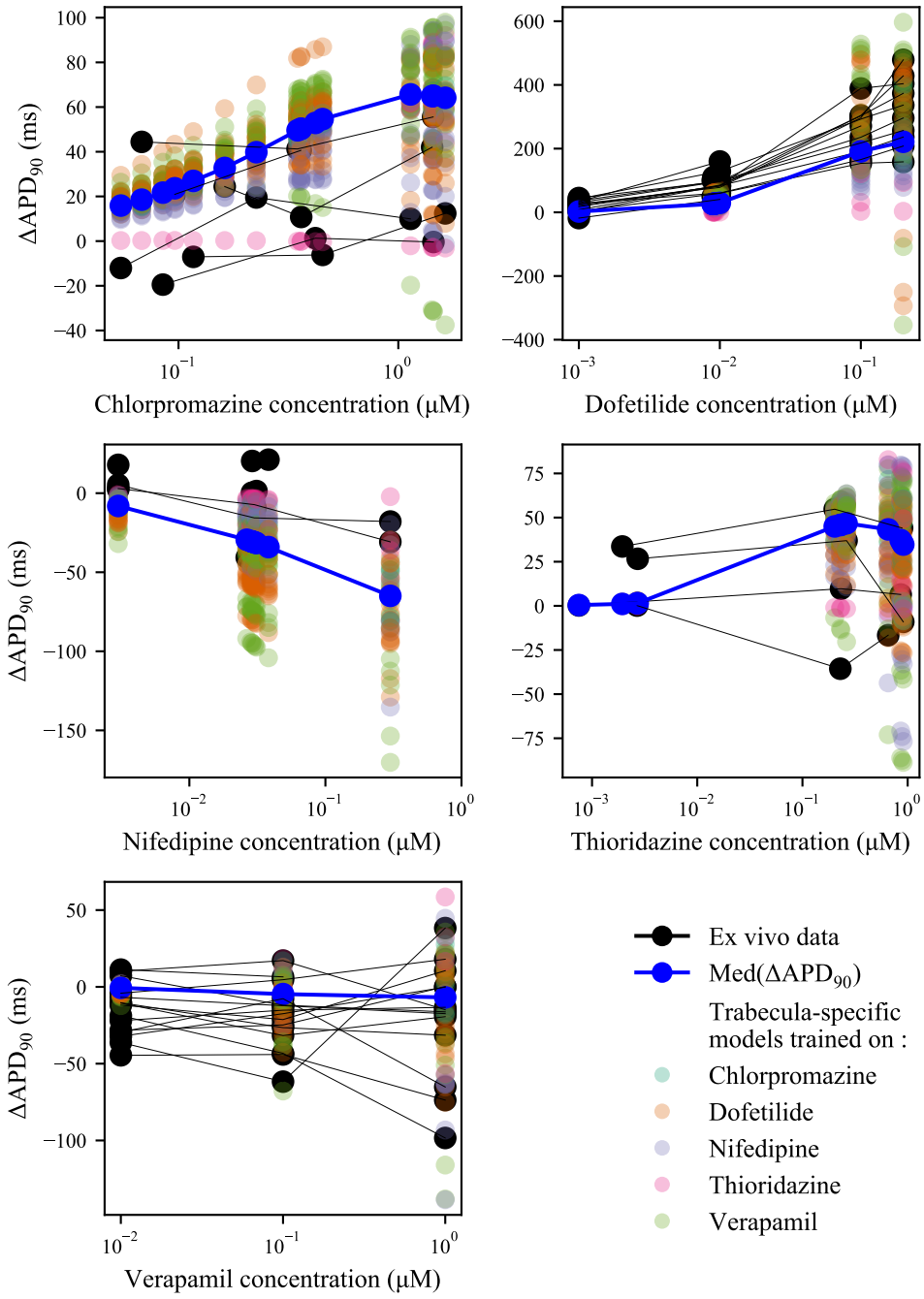

Figure E.7: Predicted ΔAPD_{90} by Col-NP$_3$ for training drugs. ΔAPD_{90} observed in the 57 trabeculae used for model training are plotted in **black**. The median of ΔAPD_{90} predicted by Col-NP$_3$ (Med(ΔAPD_{90})) is plotted in **blue**.

Bibliography

A Agrawal, K Wang, L Polonchuk, J Cooper, M Hendrix, DJ Gavaghan, GR Mirams and M Clerx. 2023. Models of the cardiac L-type calcium current: A quantitative review. *WIREs Mechanisms of Disease*, **15**, e1581. (doi:10.1002/wsbm.1581)

J Aitchison and SD Silvey. 1958. Maximum-likelihood estimation of parameters subject to restraints. *The Annals of Mathematical Statistics*, **29**, 813–828. (doi:10.1214/aoms/1177706538)

C Antzelevitch. 2007. Ionic, molecular, and cellular bases of QT-interval prolongation and torsade de pointes. *Europace*, **9**, iv4–iv15. (doi:10.1093/europace/eum166)

CM Armstrong. 1971. Interaction of tetraethylammonium ion derivatives with the potassium channels of giant axons. *The Journal of General Physiology*, **58**, 413–437. (doi:10.1085/jgp.58.4.413)

K Asakura, CY Cha, H Yamaoka, Y Horikawa, H Memida, T Powell, A Amano and A Noma. 2014. EAD and DAD mechanisms analyzed by developing a new human ventricular cell model. *Progress in Biophysics and Molecular Biology*, **116**, 11–24. (doi:10.1016/j.pbiomolbio.2014.08.008)

K Asakura, S Hayashi, A Ojima, T Taniguchi, N Miyamoto, C Nakamori, C Nagasawa, T Kitamura, T Osada, Y Honda *et al.* 2015. Improvement of acquisition and analysis methods in multi-electrode array experiments with ips cell-derived cardiomyocytes. *Journal of Pharmacological and Toxicological Methods*, **75**, 17–26. (doi:10.1016/j.vascn.2015.04.002)

YSHM Barral, L Polonchuk, GR Mirams, M Clerx, G Page, K Sweat, N Abi-Gerges, K Wang and DJ Gavaghan. Normalisation of action potential data recorded with sharp electrodes maximises its utility for model development. In *2022 Computing in Cardiology Conference (CinC)*, volume 49. IEEE, 2022a.

YSHM Barral, JG Shuttleworth, M Clerx, DG Whittaker, K Wang, L Polonchuk, DJ Gavaghan and GR Mirams. 2022b. A parameter representing missing charge should be considered when calibrating action potential models. *Frontiers in Physiology*, page 616. (doi:10.3389/fphys.2022.879035)

M Barthmes. 2021. Drug effects on human Na+/Ca2+ exchanger and implications for testing new drug candidates. *Japanese Journal of Pharmacology*, **85**, 370–375.

Chiara Bartolucci, Elisa Passini, Jari Hyttinen, Michelangelo Paci and Stefano Severi. 2020. Simulation of the effects of extracellular calcium changes leads to a novel computational model of human ventricular action potential with a revised calcium handling. *Frontiers in Physiology*, **11**, 314. (doi:10.3389/fphys.2020.00314)

AA Baumeister. 2013. The chlorpromazine enigma. *Journal of the History of the Neurosciences*, **22**, 14–29. (doi:10.1080/0964704X.2012.664087)

T Bayes and R Price. 1763. An essay towards solving a problem in the doctrine of chances by the late Rev. Mr. Bayes, communicated by Mr. Price, in a letter to John Canton, MA. and F.R.S. *Philosophical Transactions of the Royal Society of London*, **53**, 370–418. (doi:doi.org/10.1098/rstl.1763.0053)

RC Bean, WC Shepherd, H Chan and Joellen Eichner. 1969. Discrete conductance fluctuations in lipid bilayer protein membranes. *The Journal of General Physiology*, **53**, 741–757. (doi:10.1085/jgp.53.6.741)

GW Beeler and H Reuter. 1977. Reconstruction of the action potential of ventricular myocardial fibres. *The Journal of Physiology*, **268**, 177–210. (doi:10.1113/jphysiol.1977.sp011853)

B Belhassen, A Glick and S Viskin. 2004. Efficacy of quinidine in high-risk patients with Brugada syndrome. *Circulation*, **110**, 1731–1737. (doi:10.1161/01.CIR.0000143159.30585.90)

O Bernus, R Wilders, CW Zemlin, H Verschelde and AV Panfilov. 2002. A computationally efficient electrophysiological model of human ventricular cells. *American Journal of Physiology-Heart and Circulatory Physiology*. (doi:10.1152/ajpheart.00731.2001)

DM Bers, WH Barry and S Despa. 2003. Intracellular Na^+ regulation in cardiac myocytes. *Cardiovascular Research*, **57**, 897–912. (doi:10.1016/S0008-6363(02)00656-9)

M Bilger and WG Manning. 2015. Measuring overfitting in nonlinear models: a new method and an application to health expenditures. *Health Economics*, **24**, 75–85. (doi:https://doi.org/10.1002/hec.3003)

George EP Box. 1976. Science and statistics. *Journal of the American Statistical Association*, **71**, 791–799.

OJ Britton, N Abi-Gerges, G Page, A Ghetti, PE Miller and B Rodriguez. 2017. Quantitative comparison of effects of dofetilide, sotalol, quinidine, and verapamil between human ex vivo trabeculae and in silico ventricular models incorporating inter-individual action potential variability. *Frontiers in Physiology*, **8**, 597. (doi:10.3389/fphys.2017.00597)

OJ Britton, A Bueno-Orovio, K Van Ammel, HR Lu, R Towart, DJ Gallacher and B Rodriguez. 2013. Experimentally calibrated population of models predicts and explains intersubject variability in cardiac cellular electrophysiology. *Proceedings of the National Academy of Sciences*, **110**, E2098–E2105. (doi:10.1073/pnas.1304382110)

J Brynjarsdóttir and A O'Hagan. 2014. Learning about physical parameters: The importance of model discrepancy. *Inverse Problems*, **30**, 114007. (doi:10.1088/0266-5611/30/11/114007)

A Carlsson and M Lindqvist. 1963. Effect of chlorpromazine or haloperidol on formation of 3-methoxytyramine and normetanephrine in mouse brain. *Acta pharmacologica et toxicologica*, **20**, 140–144.

William A Catterall. 2011. Voltage-gated calcium channels. *Cold Spring Harbor Perspectives in Biology*, **3**, a003947. (doi:10.1101/cshperspect.a003947)

GC Cawley and NLC Talbot. 2010. On over-fitting in model selection and subsequent selection bias in performance evaluation. *The Journal of Machine Learning Research*, **11**, 2079–2107. URL http://jmlr.org/papers/v11/cawley10a.html.

M Clerx. Personalisation of cellular electrophysiology models: Utopia? In *2018 Computing in Cardiology Conference (CinC)*, volume 45, pages 1–4, 2018.

M Clerx, P Collins, E de Lange and PGA Volders. 2016. Myokit: a simple interface to cardiac cellular electrophysiology. *Progress in Biophysics and Molecular Biology*, **120**, 100–114. (doi:10.1016/j.pbiomolbio.2015.12.008)

M Clerx, M Robinson, B Lambert, CL Lei, S Ghosh, GR Mirams and DJ Gavaghan. 2019. Probabilistic Inference on Noisy Time Series (PINTS). *Journal of Open Research Software*, **7**, 23. (doi:10.5334/jors.252)

SD Cohen, AC Hindmarsh and PF Dubois. 1996. CVODE, a stiff/nonstiff ODE solver in C. *Computers in Physics*, **10**, 138–143. (doi:10.1063/1.4822377)

T Colatsky, B Fermini, G Gintant, JB Pierson, P Sager, Y Sekino, DG Strauss and N Stockbridge. 2016. The comprehensive in vitro proarrhythmia assay (CiPA) initiative—update on progress. *Journal of pharmacological and toxicological methods*, **81**, 15–20. (doi:10.1016/j.vascn.2016.06.002)

DJ Cole. *Parameter redundancy and identifiability*. Chapman and Hall/CRC, 2020.

L Collado-Torres, A Nellore, K Kammers, SE Ellis, MA Taub, KD Hansen, AE Jaffe, B Langmead and JT Leek. 2017. Reproducible rna-seq analysis using recount2. *Nature Biotechnology*, **35**, 319–321. (doi:10.1038/nbt.3838)

D Colquhoun. 1973. The relation between classical and cooperative models for drug action. *Drug receptors (ed. HP Rang)*, pages 149–182.

J Cooper, M Scharm and GR Mirams. 2016. The cardiac electrophysiology web lab. *Biophysical Journal*, **110**, 292–300. (doi:10.1016/j.bpj.2015.12.012)

J Cooper, RJ Spiteri and GR Mirams. 2015. Cellular cardiac electrophysiology modeling with Chaste and CellML. *Frontiers in Physiology*, **5**, 511. (doi:10.3389/fphys.2014.00511)

C Corrado, A Avezzù, AWC Lee, C Mendoca Costa, CH Roney, M Strocchi, M Bishop and SA Niederer. 2021. Using cardiac ionic cell models to interpret clinical data. *Wiley Interdisciplinary Reviews: Systems Biology and Medicine*, page e1508. (doi:10.1002/wsbm.1508)

A Corrias and ML Buist. 2007. A quantitative model of gastric smooth muscle cellular activation. *Annals of Biomedical Engineering*, **35**, 1595–1607. (doi:10.1007/s10439-007-9324-8)

WJ Crumb Jr, J Vicente, L Johannesen and DG Strauss. 2016. An evaluation of 30 clinical drugs against the comprehensive in vitro proarrhythmia assay (CiPA) proposed ion channel panel. *Journal of pharmacological and toxicological methods*, **81**, 251–262. (doi:10.1016/j.vascn.2016.03.009)

K Csilléry, MGB Blum, OE Gaggiotti and O François. 2010. Approximate Bayesian computation (ABC) in practice. *Trends in Ecology & Evolution*, **25**, 410–418. (doi:10.1016/j.tree.2010.04.001)

AC Daly, M Clerx, KA Beattie, J Cooper, D J Gavaghan and GR Mirams. 2018. Reproducible model development in the Cardiac Electrophysiology Web Lab. *Progress in Biophysics and Molecular Biology*, **139**, 3–14. (doi:10.1016/j.pbiomolbio.2018.05.011)

F De Ponti. Pharmacological and regulatory aspects of QT prolongation. In *Antitargets: Prediction and Prevention of Drug Side Effects*, chapter 3, pages 53–88. Wiley Online Library, 2008.

SS Demir, JW Clark, CR Murphey and WR Giles. 1994. A mathematical model of a rabbit sinoatrial node cell. *American Journal of Physiology: Cell Physiology*, **266**, C832–C852. (doi:10.1152/ajpcell.1994.266.3.c832)

K Dheda, JF Huggett, SA Bustin, MA Johnson, G Rook and A Zumla. 2004. Validation of housekeeping genes for normalizing RNA expression in real-time PCR. *Biotechniques*, **37**, 112–119. (doi:10.2144/04371RR03)

K Dibb, A Trafford, H Zhang and D Eisner. 2015. A model model: a commentary on DiFrancesco and Noble (1985) "a model of cardiac electrical activity incorporating ionic pumps and concentration changes". *Philosophical Transactions of the Royal Society B: Biological Sciences*, **370**, 20140316. (doi:10.1098/rstb.2014.0316)

D DiFrancesco and D Noble. 1985. A model of cardiac electrical activity incorporating ionic pumps and concentration changes. *Philosophical Transactions of the Royal Society of London. B: Biological Sciences*, **307**, 353–398. (doi:10.1098/rstb.1985.0001)

FA Dodge and JW Cooley. 1973. Action potential of the motorneuron. *IBM Journal of Research and Development*, **17**, 219–229. (doi:10.1147/rd.173.0219)

S Dokos, B Celler and N Lovell. 1996. Ion currents underlying sinoatrial node pacemaker activity: a new single cell mathematical model. *Journal of theoretical Biology*, **181**, 245–272. (doi:10.1006/jtbi.1996.0129)

S Dokos and NH Lovell. 2004. Parameter estimation in cardiac ionic models. *Progress in Biophysics and Molecular Biology*, **85**, 407–431. (doi:10.1016/j.pbiomolbio.2004.02.002)

S Dutta, KC Chang, KA Beattie, J Sheng, PN Tran, WW Wu, M Wu, DG Strauss, T Colatsky and Z Li. 2017. Optimization of an in silico cardiac cell model for proarrhythmia risk assessment. *Frontiers in Physiology*, **8**, 616. (doi:10.3389/fphys.2017.00616)

F Dyson. 2004. A meeting with Enrico Fermi. *Nature*, **427**, 297–297. (doi:10.1038/427297a)

S Ebashi and M Endo. 1968. Calcium and muscle contraction. *Progress in Biophysics and Molecular Biology*, **18**, 123–183. (doi:10.1016/0079-6107(68)90023-0)

DL Eckberg. 1983. Human sinus arrhythmia as an index of vagal cardiac outflow. *Journal of Applied Physiology*, **54**, 961–966. (doi:10.1152/jappl.1983.54.4.961)

RC Elkins, MR Davies, SJ Brough, DJ Gavaghan, Y Cui, N Abi-Gerges and GR Mirams. 2013. Variability in high-throughput ion-channel screening data and consequences for cardiac safety assessment. *Journal of Pharmacological and Toxicological Methods*, **68**, 112–122. (doi:10.1016/j.vascn.2013.04.007)

LP Endresen, K Hall, JS Høye and J Myrheim. 2000. A theory for the membrane potential of living cells. *European Biophysics Journal*, **29**, 90–103. (doi:10.1007/s002490050254)

HW Engl, C Flamm, P Kügler, J Lu, S Müller and P Schuster. 2009. Inverse problems in systems biology. *Inverse Problems*, **25**, 123014. (doi:10.1088/0266-5611/25/12/123014)

G Erdemli, AM Kim, H Ju, C Springer, RC Penland and PK Hoffmann. 2012. Cardiac safety implications of hNav1. 5 blockade and a framework for pre-clinical evaluation. *Frontiers in Pharmacology*, **3**, 6. (doi:10.3389/fphar.2012.00006)

AH Erhardt and S Solem. 2022. Bifurcation analysis of a modified cardiac cell model. *SIAM Journal on Applied Dynamical Systems*, **21**, 231–247. (doi:10.1137/21M1425359)

D Esfandyari, BMG Idrissou, K Hennis, Petros A, A Dueck, I El-Battrawy, L Grüter, MA Meier, AC Näger, D Ramanujam *et al.* 2022. MicroRNA-365 regulates human cardiac action potential duration. *Nature Communications*, **13**, 1–15. (doi:10.1038/s41467-021-27856-7)

BS Everitt and A Skrondal. *Cambridge Dictionary of Statistics*. Cambridge University Press, 2010.

SM Feinberg, KA Fariba and A Saadabadi. 2022. Thioridazine. *StatPearls [Internet]*.

M Fink, SA Niederer, EM Cherry, FH Fenton, JT Koivumäki, G Seemann, R Thul, H Zhang, FB Sachse, D Beard *et al.* 2011. Cardiac cell modelling: observations from the heart of the cardiac physiome project. *Progress in Biophysics and Molecular Biology*, **104**, 2–21. (doi:10.1016/j.pbiomolbio.2010.03.002)

M Fink and D Noble. 2009. Markov models for ion channels: versatility versus identifiability and speed. *Philosophical Transactions of the Royal Society A: Mathematical, Physical and Engineering Sciences*, **367**, 2161–2179. (doi:10.1098/rsta.2008.0301)

M Fink, D Noble, L Virag, A Varro and WR Giles. 2008. Contributions of HERG K+ current to repolarization of the human ventricular action potential. *Progress in Biophysics and Molecular Biology*, **96**, 357–376. (doi:10.1016/j.pbiomolbio.2007.07.011)

M Fourment, AF Magee, C Whidden, A Bilge, FA Matsen IV and VN Minin. 2020. 19 dubious ways to compute the marginal likelihood of a phylogenetic tree topology. *Systematic Biology*, **69**, 209–220. (doi:10.1093/sysbio/syz046)

R Frank-Hansen, LA Larsen, P Andersen, C Jespersgaard and M Christiansen. 2005. Mutations in the genes KCND2 and KCND3 encoding the ion channels Kv4. 2 and Kv4. 3, conducting the cardiac fast transient outward current (ITO, f), are not a frequent cause of long QT syndrome. *Clinica Chimica Acta*, **351**, 95–100. (doi:10.1016/j.cccn.2004.08.017)

CH Fry, JPT Ward, VW Twist and T Powell. 1986. Determination of intracellular potassium ion concentration in isolated rat ventricular myocytes. *Biochemical and Biophysical Research Communications*, **137**, 573–578. (doi:10.1016/0006-291X(86)91249-0)

N Gaborit, A Varro, S Le Bouter, V Szuts, D Escande, S Nattel and S Demolombe. 2010. Gender-related differences in ion-channel and transporter subunit expression in non-diseased human hearts. *Journal of Molecular and Cellular Cardiology*, **49**, 639–646. (doi:10.1016/j.yjmcc.2010.06.005)

S Galappaththige, RA Gray, CM Costa, S Niederer and P Pathmanathan. 2022. Credibility assessment of patient-specific computational modeling using patient-specific cardiac modeling as an exemplar. *PLOS Computational Biology*, **18**, e1010541. (doi:10.1371/journal.pcbi.1010541)

LX Gao and XQ Wang. 2020. Intracellular neuronal recording in awake nonhuman primates. *Nature Protocols*, **15**, 3615–3631. (doi:10.1038/s41596-020-0388-3)

N Gaur, F Ortega, AO Verkerk, I Mengarelli, T Krogh-Madsen, DJ Christini, R Coronel and EJ Vigmond. 2020. Validation of quantitative measure of repolarization reserve as a novel marker of drug induced proarrhythmia. *Journal of Molecular and Cellular Cardiology*, **145**, 122–132. (doi:10.1016/j.yjmcc.2020.04.019)

A Gelman, WR Gilks and GO Roberts. 1997. Weak convergence and optimal scaling of random walk metropolis algorithms. *The Annals of Applied Probability*, **7**, 110–120. (doi:10.1214/aoap/1034625254)

J Gomis-Tena, BM Brown, J Cano, B Trenor, P-C Yang, J Saiz, CE Clancy and L Romero. 2020. When does the IC50 accurately assess the blocking potency of a drug? *Journal of Chemical Information and Modeling*, **60**, 1779–1790. (doi:10.1021/acs.jcim.9b01085)

E Gorter and FJEM Grendel. 1925. On bimolecular layers of lipoids on the chromocytes of the blood. *The Journal of Experimental Medicine*, **41**, 439. (doi:10.1084/jem.41.4.439)

AA Grace and AJ Camm. 1998. Quinidine. *New England Journal of Medicine*, **338**, 35–45. (doi:10.1056/NEJM199801013380107)

P Gramatica. 2007. Principles of QSAR models validation: internal and external. *QSAR & Combinatorial Science*, **26**, 694–701. (doi:10.1002/qsar.200610151)

E Grandi, FS Pasqualini and DM Bers. 2010. A novel computational model of the human ventricular action potential and Ca transient. *Journal of Molecular and Cellular Cardiology*, **48**, 112–121. (doi:10.1016/j.yjmcc.2009.09.019)

W Groenendaal, FA Ortega, AR Kherlopian, AC Zygmunt, T Krogh-Madsen and DJ Christini. 2015. Cell-specific cardiac electrophysiology models. *PLoS Computational Biology*, **11**, e1004242. (doi:10.1371/journal.pcbi.1004242)

S Guan, Q Lu and K Huang. 1997. A discussion about the DiFrancesco–Noble model. *Journal of theoretical Biology*, **189**, 27–32. (doi:10.1006/jtbi.1997.0486)

B Gustafsson, M Galvan, P Grafe and H Wigström. 1982. A transient outward current in a mammalian central neurone blocked by 4-aminopyridine. *Nature*, **299**, 252–254. (doi:10.1038/299252a0)

H Guthrie, FS Livingston, U Gubler and R Garippa. 2005. A place for high-throughput electrophysiology in cardiac safety: screening hERG cell lines and novel compounds with the ion works HTTM system. *Journal of Biomolecular Screening*, **10**, 832–840. (doi:10.1177/1087057105280566)

A Habib, X Zhu, UI Can, ML McLanahan, P Zorlutuna and AA Yanik. 2019. Electro-plasmonic nanoantenna: A nonfluorescent optical probe for ultrasensitive label-free detection of electrophysiological signals. *Science Advances*, **5**, eaav9786. (doi:10.1126/sciadv.aav9786)

DG Hackam and DA Redelmeier. 2006. Translation of research evidence from animals to humans. *Journal of American Medical Association*, **296**, 1727–1732. (doi:10.1001/jama.296.14.1731)

N Hansen. 2016. The CMA evolution strategy: A tutorial. *arXiv preprint arXiv:1604.00772*. (doi:10.48550/arXiv.1604.00772)

N Hansen, SD Müller and P Koumoutsakos. 2003. Reducing the time complexity of the derandomized evolution strategy with covariance matrix adaptation (CMA-ES). *Evolutionary Computation*, **11**, 1–18. (doi:https://doi.org/10.1162/106365603321828970)

M Haugh. 2017. MCMC and Bayesian modeling. *IEOR E4703 Monte-Carlo Simulation, Columbia University*.

HB Hayes, AM Nicolini, CA Arrowood, SA Chvatal, DW Wolfson, HC Cho, DD Sullivan, J Chal, B Fermini, M Clements *et al.* 2019. Novel method for action potential measurements from intact cardiac monolayers with multiwell microelectrode array technology. *Scientific reports*, **9**, 1–13. (doi:10.1038/s41598-019-48174-5)

DW Hilgemann and D Noble. 1987. Excitation-contraction coupling and extracellular calcium transients in rabbit atrium: reconstruction of basic cellular mechanisms. *Proceedings of the Royal society of London: Series B. Biological Sciences*, **230**, 163–205. (doi:10.1098/rspb.1987.0015)

AV Hill. 1910. The possible effects of the aggregation of the molecules of haemoglobin on its dissociation curves. *Journal of Physiology*, **40**, 4–8.

Y Himeno, K Asakura, CY Cha, H Memida, T Powell, A Amano and A Noma. 2015. A human ventricular myocyte model with a refined representation of excitation-contraction coupling. *Biophysical Journal*, **109**, 415–427. (doi:10.1016/j.bpj.2015.06.017)

AC Hindmarsh, PN Brown, KE Grant, SL Lee, R Serban, DE Shumaker and CS Woodward. 2005. SUNDIALS: Suite of nonlinear and differential/algebraic equation solvers. *ACM Transactions on Mathematical Software (TOMS)*, **31**, 363–396. (doi:10.1145/1089014.1089020)

AL Hodgkin and AF Huxley. 1952. A quantitative description of membrane current and its application to conduction and excitation in nerve. *The Journal of Physiology*, **117**, 500. (doi:10.1113/jphysiol.1952.sp004764)

AL Hodgkin and B Katz. 1949. The effect of sodium ions on the electrical activity of the giant axon of the squid. *The Journal of Physiology*, **108**, 37. (doi:10.1113/jphysiol.1949.sp004310)

LM Hondeghem, Leif Carlsson and G Duker. 2001. Instability and triangulation of the action potential predict serious proarrhythmia, but action potential duration prolongation is antiarrhythmic. *Circulation*, **103**, 2004–2013. (doi:10.1161/01.CIR.103.15.2004)

R Horn and CA Vandenberg. 1984. Statistical properties of single sodium channels. *The Journal of General Physiology*, **84**, 505–534. (doi:10.1085/jgp.84.4.505)

MP Hortigon-Vinagre, V Zamora, FL Burton, J Green, GA Gintant and GL Smith. 2016. The use of ratiometric fluorescence measurements of the voltage sensitive dye Di-4-ANEPPS to examine action potential characteristics and drug effects on human induced pluripotent stem cell-derived cardiomyocytes. *Toxicological Sciences*, **154**, 320–331. (doi:10.1093/toxsci/kfw171)

N Hu, D Xu, J Fang, H Li, J Mo, M Zhou, B Li, H-J Chen, T Zhang, J Feng *et al.* 2020. Intracellular recording of cardiomyocyte action potentials by nanobranched microelectrode array. *Biosensors and Bioelectronics*, page 112588. (doi:10.1016/j.bios.2020.112588)

TJ Hund, JP Kucera, NF Otani and Y Rudy. 2001. Ionic charge conservation and long-term steady state in the Luo–Rudy dynamic cell model. *Biophysical Journal*, **81**, 3324–3331. (doi:10.1016/S0006-3495(01)75965-6)

TJ Hund and Y Rudy. November 2004. Rate dependence and regulation of action potential and calcium transient in a canine cardiac ventricular cell model. *Circulation Research*, **110**, 3168–3174. ISSN 1524-4539. (doi:10.1161/01.CIR.0000147231.69595.D3)

Guideline ICH. 2005. The non-clinical evaluation of the potential for delayed ventricular repolarization (QT interval prolongation) by human pharmaceuticals. *S7B (http://www. ich. org/products/guidelines/safety/article/safety-guidelines. html)*.

Guideline ICH. 2006. The clinical evaluation of QT/QTc interval prolongation and proarrhythmic potential for non-antiarrhythmic drugs E14. *Recommended for adoption at Step*, **4**.

V Iyer, R Mazhari and RL Winslow. 2004a. A computational model of the human left-ventricular epicardial myocyte. *Biophysical Journal*, **87**, 1507–1525. (doi:10.1529/biophysj.104.043299)

V Iyer, R Mazhari and RL Winslow. September 2004b. A computational model of the human left-ventricular epicardial myocyte. *Biophysical Journal*, **87**, 1507–1525. ISSN 0006-3495. (doi:10.1529/biophysj.104.043299)

V Jacquemet. 2007. Steady-state solutions in mathematical models of atrial cell electrophysiology and their stability. *Mathematical Biosciences*, **208**, 241–269. (doi:10.1016/j.mbs.2006.10.007)

AF James, SCM Choisy and JC Hancox. 2007. Recent advances in understanding sex differences in cardiac repolarization. *Progress in Biophysics and Molecular Biology*, **94**, 265–319. (doi:10.1016/j.pbiomolbio.2005.05.010)

GE Jarvis and AJ Thompson. 2013. A golden approach to ion channel inhibition. *Trends in Pharmacological Sciences*, **34**, 481–488. (doi:10.1016/j.tips.2013.07.004)

DU Jeong, RZ Danadibrata, A Marcellinus and KM Lim. 2022. Validation of in silico biomarkers for drug screening through ordinal logistic regression. *Frontiers in Physiology*, page 2111. (doi:10.3389/fphys.2022.1009647)

Y Jiang, P Park, S-M Hong and K Ban. 2018. Maturation of cardiomyocytes derived from human pluripotent stem cells: current strategies and limitations. *Molecules and Cells*, **41**, 613. (doi:10.14348/molcells.2018.0143)

L Johannesen, J Vicente, JW Mason, C Sanabria, K Waite-Labott, M Hong, P Guo, J Lin, JS Sørensen, L Galeotti *et al.* 2014. Differentiating drug-induced multichannel block on the electrocardiogram: randomized study of dofetilide, quinidine, ranolazine, and verapamil. *Clinical Pharmacology & Therapeutics*, **96**, 549–558. (doi:10.1038/clpt.2014.155)

RH Johnstone. *Uncertainty characterisation in action potential modelling for cardiac drug safety.* PhD thesis, University of Oxford, 2018.

RH Johnstone, ETY Chang, R Bardenet, TP De Boer, DJ Gavaghan, P Pathmanathan, RH Clayton and GR Mirams. 2016. Uncertainty and variability in models of the cardiac action potential: Can we build trustworthy models? *Journal of Molecular and Cellular Cardiology*, **96**, 49–62. (doi:10.1016/j.yjmcc.2015.11.018)

D Jones, C Snider, A Nassehi, J Yon and B Hicks. 2020. Characterising the Digital Twin: A systematic literature review. *CIRP Journal of Manufacturing Science and Technology*, **29**, 36–52. (doi:10.1016/j.cirpj.2020.02.002)

N Jost, A Varro, V Szuts, PP Kovacs, G Seprényi, P Biliczki, C Lengyel, J Prorok, M Bitay, B Ördög *et al.* Molecular basis of repolarization reserve differences between dogs and man, 2008.

MC Kennedy and A O'Hagan. 2001. Bayesian calibration of computer models. *Journal of the Royal Statistical Society: Series B (Statistical Methodology)*, **63**, 425–464. (doi:10.1111/1467-9868.00294)

KM Khan, J Patel and TJ Schaefer. 2019. Nifedipine.

K-S Kim and E-J Kim. 2005. The phenothiazine drugs inhibit hERG potassium channels. *Drug and Chemical Toxicology*, **28**, 303–313. (doi:10.1081/dct-200064482)

J Kramer, HM Himmel, A Lindqvist, S Stoelzle-Feix, KW Chaudhary, D Li, GA Bohme, M Bridgland-Taylor, S Hebeisen, J Fan *et al.* 2020. Cross-site and cross-platform variability of automated patch clamp assessments of drug effects on human cardiac currents in recombinant cells. *Scientific Reports*, **10**, 1–15. (doi:10.1038/s41598-020-62344-w)

J Kramer, CA Obejero-Paz, G Myatt, YA Kuryshev, A Bruening-Wright, JS Verducci and AM Brown. 2013. MICE models: superior to the hERG model in predicting Torsade de Pointes. *Scientific Reports*, **3**, 1–7. (doi:10.1038/srep02100)

T Krogh-Madsen, AF Jacobson, FA Ortega and DJ Christini. 2017. Global optimization of ventricular myocyte model to multi-variable objective improves predictions of drug-induced Torsades de Pointes. *Frontiers in Physiology*, **8**, 1059. (doi:10.3389/fphys.2017.01059)

H Kubinyi. 2002. From narcosis to hyperspace: the history of QSAR. *Quantitative Structure-Activity Relationships*, **21**, 348–356. (doi:10.1002/1521-3838(200210)21:43.0.CO;2-D)

P Kügler, MAK Bulelzai and AH Erhardt. 2017. Period doubling cascades of limit cycles in cardiac action potential models as precursors to chaotic early after-depolarizations. *BMC Systems Biology*, **11**, 1–13. (doi:10.1186/s12918-017-0422-4)

F La Dessertenne. 1966. Tachycardie ventriculaire á deux foyer opposes variables. *Archives des Maladies du Coeur et Vaisseaux*, **59**, 263–72.

B Lambert, CL Lei, M Robinson, M Clerx, R Creswell, S Ghosh, S Tavener and D Gavaghan. 2023. Autocorrelated measurement processes and inference for ordinary differential equation models of biological systems. *Journal of the Royal Society Interface*, page to appear.

TS Lee and D Mumford. 2003. Hierarchical Bayesian inference in the visual cortex. *Journal of the Optical Society of America*, **20**, 1434–1448. (doi:10.1364/josaa.20.001434)

W Lee, MJ Windley, MD Perry, JI Vandenberg and AP Hill. 2019. Protocol-dependent differences in IC50 values measured in human ether-á-go-go–related gene assays occur in a predictable way and can be used to quantify state preference of drug binding. *Molecular Pharmacology*, **95**, 537–550. (doi:10.1124/mol.118.115220)

CL Lei, M Clerx, KA Beattie, D Melgari, JC Hancox, DJ Gavaghan, L Polonchuk, K Wang and GR Mirams. 2019. Rapid characterization of hERG channel kinetics II: temperature dependence. *Biophysical Journal*, **117**, 2455–2470. (doi:10.1016/j.bpj.2019.07.030)

CL Lei, S Ghosh, DG Whittaker, Y Aboelkassem, KA Beattie, CD Cantwell, T Delhaas, C Houston, GM Novaes, AV Panfilov *et al.* 2020. Considering discrepancy when calibrating a mechanistic electrophysiology model. *Philosophical Transactions of the Royal Society A*, **378**, 20190349. (doi:https://doi.org/10.1098/rsta.2019.0349)

RM Lester. 2021. Update on ICH E14/S7B cardiac safety regulations: the expanded role of preclinical assays and the "double-negative" scenario. *Clinical Pharmacology in Drug Development*, **10**, 964–973. (doi:10.1002/cpdd.1003)

G-R Li, J F, L Yue, M Carrier and S Nattel. 1996. Evidence for two components of delayed rectifier K+ current in human ventricular myocytes. *Circulation Research*, **78**, 689–696. (doi:10.1161/01.RES.78.4.689)

G-R Li, B Yang, J Feng, RF Bosch, M Carrier and S Nattel. 1999. Transmembrane ICa contributes to rate-dependent changes of action potentials in human ventricular myocytes. *American Journal of Physiology-Heart and Circulatory Physiology*, **276**, H98–H106. (doi:10.1152/ajpheart.1999.276.1.H98)

M Li and LG Ramos. 2017. Drug-induced QT prolongation and torsades de pointes. *Pharmacy and Therapeutics*, **42**, 473.

W-C Li, SR Soffe and A Roberts. 2004. A direct comparison of whole cell patch and sharp electrodes by simultaneous recording from single spinal neurons in frog tadpoles. *Journal of Neurophysiology*. (doi:10.1152/jn.01238.2003)

Z Li, S Dutta, J Sheng, PN Tran, W Wu, K Chang, T Mdluli, DG Strauss and T Colatsky. 2017. Improving the in silico assessment of proarrhythmia risk by combining hERG (human ether-à-go-go-related gene) channel–drug binding kinetics and multichannel pharmacology. *Circulation: Arrhythmia and Electrophysiology*, **10**, e004628. (doi:10.1161/CIRCEP.116.004628)

Z Li, GR Mirams, T Yoshinaga, BJ Ridder, X Han, JE Chen, NL Stockbridge, TA Wisialowski, B Damiano, S Severi *et al.* 2020. General principles for the validation of proarrhythmia risk prediction models: an extension of the CiPA in silico strategy. *Clinical Pharmacology & Therapeutics*, **107**, 102–111. (doi:10.1002/cpt.1647)

Z Li, BJ Ridder, X Han, WW Wu, J Sheng, PN Tran, M Wu, A Randolph, RH Johnstone, GR Mirams *et al.* 2019. Assessment of an in silico mechanistic model for proarrhythmia risk prediction under the CiPA initiative. *Clinical Pharmacology & Therapeutics*, **105**, 466–475. (doi:10.1002/cpt.1184)

ZC Lin, C Xie, Y Osakada, Y Cui and BX Cui. 2014. Iridium oxide nanotube electrodes for sensitive and prolonged intracellular measurement of action potentials. *Nature Communications*, **5**, 1–10. (doi:10.1038/ncomms4206)

DS Lindblad, CR Murphey, JW Clark and WR Giles. 1996. A model of the action potential and underlying membrane currents in a rabbit atrial cell. *American Journal of Physiology: Heart and Circulatory Physiology*, **271**, H1666–H1696. (doi:10.1152/ajpheart.1996.271.4.H1666)

Y Liu. *Overfitting and forecasting: linear versus non-linear time series models.* PhD thesis, Iowa State University, 2000.

Y Liu, X Xu, Y Zhang, M Li, J Guo, C Yan, F Wang, Y Li, Y Ding, B Li *et al.* 2020. Thioridazine induces cardiotoxicity via reactive oxygen species-mediated hERG channel deficiency and L-type calcium channel activation. *Oxidative Medicine and Cellular Longevity*, **2020**. (doi:https://doi.org/10.1155/2020/3690123)

L Livshitz and Y Rudy. 2009. Uniqueness and stability of action potential models during rest, pacing, and conduction using problem-solving environment. *Biophysical Journal*, **97**, 1265–1276. (doi:10.1016/j.bpj.2009.05.062)

A Llerena, R Berecz, A de la Rubia, M-J Norberto and J Benítez. 2000. Use of the mesoridazine/thioridazine ratio as a marker for CYP2D6 enzyme activity. *Therapeutic Drug Monitoring*, **22**, 397–401.

J Llopis-Lorente, J Gomis-Tena, J Cano, L Romero, J Saiz and B Trenor. 2020. In silico classifiers for the assessment of drug proarrhythmicity. *Journal of Chemical Information and Modeling*, **60**, 5172–5187. (doi:10.1021/acs.jcim.0c00201)

Fernando Llorente, Luca Martino, David Delgado and Javier Lopez-Santiago. 2020. Marginal likelihood computation for model selection and hypothesis testing: an extensive review. *arXiv preprint arXiv:2005.08334*.

W-L Loh. 1996. On latin hypercube sampling. *The Annals of Statistics*, **24**, 2058–2080. (doi:10.1214/aos/1069362310)

NH Lovell, SL Cloherty, BG Celler and S Dokos. 2004. A gradient model of cardiac pacemaker myocytes. *Progress in Biophysics and Molecular Biology*, **85**, 301–323. (doi:10.1016/j.pbiomolbio.2003.12.001)

CH Luo and Y Rudy. 1991. A model of the ventricular cardiac action potential. Depolarization, repolarization, and their interaction. *Circulation Research*, **68**, 1501–1526. (doi:10.1161/01.res.68.6.1501)

CH Luo and Y Rudy. 1994. A dynamic model of the cardiac ventricular action potential. I. Simulations of ionic currents and concentration changes. *Circulation Research*, **74**, 1071–1096. (doi:10.1161/01.RES.74.6.1071)

Madhero88. Electrical conduction system of the heart. https://commons.wikimedia.org/wiki/File:Conductionsystemoftheheart.png, 2010. Published under the Creative Commons Attribution 3.0 Unported license. No changes were applied.

J Magyar, N Szentandrássy, T Bányász, L Fülöp, A Varró and PP Nánási. 2002. Effects of thymol on calcium and potassium currents in canine and human ventricular cardiomyocytes. *British Journal of Pharmacology*, **136**, 330–338. (doi:10.1038/sj.bjp.0704718)

VA Maltsev, HN Sabbah, RSD Higgins, N Silverman, M Lesch and AI Undrovinas. 1998. Novel, ultraslow inactivating sodium current in human ventricular cardiomyocytes. *Circulation*, **98**, 2545–2552. (doi:10.1161/01.cir.98.23.2545)

SA Mann, M Imtiaz, A Winbo, A Rydberg, MD Perry, J-P Couderc, B Polonsky, S McNitt, W Zareba, AP Hill *et al.* 2016. Convergence of models of human ventricular myocyte electrophysiology after global optimization to recapitulate clinical long QT phenotypes. *Journal of Molecular and Cellular Cardiology*, **100**, 25–34. (doi:10.1016/j.yjmcc.2016.09.011)

S Matsuoka, N Sarai, S Kuratomi, K Ono and A Noma. 2003. Role of individual ionic current systems in ventricular cells hypothesized by a model study. *The Japanese Journal of Physiology*, **53**, 105–123. (doi:10.2170/jjphysiol.53.105)

RE McAllister, D Noble and RW Tsien. 1975. Reconstruction of the electrical activity of cardiac purkinje fibres. *The Journal of Physiology*, **251**, 1–59. (doi:10.1113/jphysiol.1975.sp011080)

JT Milnes, HJ Witchel, JL Leaney, DJ Leishman and JC Hancox. 2010. Investigating dynamic protocol-dependence of hERG potassium channel inhibition at 37°C: Cisapride versus Dofetilide. *Journal of Pharmacological and Toxicological Methods*, **61**, 178–191. (doi:10.1016/j.vascn.2010.02.007)

GR Mirams, Y Cui, A Sher, M Fink, J Cooper, BM Heath, NC McMahon, DJ Gavaghan and D Noble. 2011. Simulation of multiple ion channel block provides improved early prediction of compounds' clinical torsadogenic risk. *Cardiovascular Research*, **91**, 53–61. (doi:10.1093/cvr/cvr044)

GR Mirams, MR Davies, SJ Brough, MH Bridgland-Taylor, Y Cui, DJ Gavaghan and N Abi-Gerges. 2014. Prediction of thorough QT study results using action potential

simulations based on ion channel screens. *Journal of Pharmacological and Toxicological Methods*, **70**, 246–254. (doi:10.1016/j.vascn.2014.07.002)

CE Molina, E Jacquet, P Ponien, C Muñoz-Guijosa, I Baczkó, LS Maier, P Donzeau-Gouge, D Dobrev, R Fischmeister and A Garnier. 2018. Identification of optimal reference genes for transcriptomic analyses in normal and diseased human heart. *Cardiovascular Research*, **114**, 247–258. (doi:10.1093/cvr/cvx182)

KL Moore and AM Agur. *Essential Clinical Anatomy: Third Edition*. Lippincott Williams & Wilkins, 2007. ISBN 978-0-7817-6274-8.

B Mostofian and DM Zuckerman. 2019. Statistical uncertainty analysis for small-sample, high log-variance data: Cautions for bootstrapping and Bayesian bootstrapping. *Journal of Chemical Theory and Computation*, **15**, 3499–3509. (doi:10.1021/acs.jctc.9b00015)

FT Musuamba, I Skottheim Rusten, R Lesage, G Russo, R Bursi, L Emili, G Wangorsch, E Manolis, KE Karlsson, A Kulesza *et al.* 2021. Scientific and regulatory evaluation of mechanistic in silico drug and disease models in drug development: building model credibility. *CPT: Pharmacometrics & Systems Pharmacology*. (doi:10.1002/psp4.12669)

A Muszkiewicz, OJ Britton, P Gemmell, E Passini, C Sánchez, X Zhou, A Carusi, TA Quinn, K Burrage, A Bueno-Orovio *et al.* 2016. Variability in cardiac electrophysiology: using experimentally-calibrated populations of models to move beyond the single virtual physiological human paradigm. *Progress in Biophysics and Molecular Biology*, **120**, 115–127. (doi:10.1016/j.pbiomolbio.2015.12.002)

AA Neath and JE Cavanaugh. 2012. The Bayesian information criterion: background, derivation, and applications. *Wiley Interdisciplinary Reviews: Computational Statistics*, **4**, 199–203. (doi:10.1002/wics.199)

Walther Nernst. 1889. Die elektromotorische wirksamkeit der jonen. *Zeitschrift für physikalische Chemie*, **4**, 129–181.

SA Niederer, M Fink, D Noble and NP Smith. 2009. A meta-analysis of cardiac electrophysiology computational models. *Experimental Physiology*, **94**, 486–495. (doi:10.1113/expphysiol.2008.044610)

J Nielsen, P Damkier, H Lublin and D Taylor. 2011. Optimizing clozapine treatment. *Acta Psychiatrica Scandinavica*, **123**, 411–422. (doi:10.1111/j.1600-0447.2011.01710.x)

A Nieto Ramos, FH Fenton and EM Cherry. 2022. Bayesian inference for fitting cardiac models to experiments: estimating parameter distributions using Hamiltonian Monte Carlo and approximate Bayesian computation. *Medical & Biological Engineering & Computing*, pages 1–21. (doi:10.1007/s11517-022-02685-y)

D Noble. 1962. A modification of the Hodgkin–Huxley equations applicable to Purkinje fibre action and pacemaker potentials. *The Journal of Physiology*, **160**, 317. (doi:10.1113/jphysiol.1962.sp006849)

D Noble, SJ Noble, GCL Bett, YE Earm, WK Ho and IK So. 1991. The role of sodium-calcium exchange during the cardiac action potential. *Annals of the New York Academy of Sciences*, **639**, 334–353. (doi:10.1111/j.1749-6632.1991.tb17323.x)

FC Nucifora, M Mihaljevic, BJ Lee and A Sawa. 2017. Clozapine as a model for antipsychotic development. *Neurotherapeutics*, **14**, 750–761. (doi:10.1007/s13311-017-0552-9)

A Nygren, C Fiset, L Firek, JW Clark, DS Lindblad, RB Clark and WR Giles. 1998. Mathematical model of an adult human atrial cell: the role of K^+ currents in repolarization. *Circulation Research*, **82**, 63–81. (doi:10.1161/01.RES.82.1.63)

T O'Hara, L Virág, A Varró and Y Rudy. 2011. Simulation of the undiseased human cardiac ventricular action potential: model formulation and experimental validation. *PLoS Computational Biology*, **7**, e1002061. (doi:10.1371/journal.pcbi.1002061)

OpenStax College. Chordae tendinae papillary muscles. https://commons.wikimedia.org/wiki/File:2010_Chordae_Tendinae_Papillary_Muscles.jpg, 2010.

Published under the Creative Commons Attribution 3.0 Unported license. No changes were applied.

G Page, P Ratchada, Y Miron, G Steiner, A Ghetti, PE Miller, JA Reynolds, K Wang, A Greiter-Wilke, L Polonchuk *et al.* 2016. Human ex-vivo action potential model for pro-arrhythmia risk assessment. *Journal of Pharmacological and Toxicological Methods*, **81**, 183–195. (doi:10.1016/j.vascn.2016.05.016)

M Pan, PJ Gawthrop, K Tran, J Cursons and EJ Crampin. 2018. Bond graph modelling of the cardiac action potential: implications for drift and non-unique steady states. *Proceedings of the Royal Society: Series A. Mathematical, Physical and Engineering Sciences*, **474**, 20180106. (doi:https://doi.org/10.1098/rspa.2018.0106)

J Parikh, V Gurev and JJ Rice. 2017. Novel two-step classifier for torsades de pointes risk stratification from direct features. *Frontiers in Pharmacology*, **8**, 816. (doi:10.3389/fphar.2017.00816)

E Passini, OJ Britton, HR Lu, J Rohrbacher, AN Hermans, DJ Gallacher, RJH Greig, A Bueno-Orovio and B Rodriguez. 2017. Human in silico drug trials demonstrate higher accuracy than animal models in predicting clinical pro-arrhythmic cardiotoxicity. *Frontiers in Physiology*, **8**, 668. (doi:10.3389/fphys.2017.00668)

M Peirlinck, F Sahli Costabal and E Kuhl. 2021. Sex differences in drug-induced arrhythmogenesis. *Frontiers in Physiology*, page 1245. (doi:10.3389/fphys.2021.708435)

B Pelzmann, P Schaffer, E Bernhart, P Lang, H Mächler, B Rigler and B Koidl. 1998. L-type calcium current in human ventricular myocytes at a physiological temperature from children with tetralogy of Fallot. *Cardiovascular Research*, **38**, 424–432. (doi:10.1016/S0008-6363(98)00002-9)

M Planck. *Acht vorlesungen über theoretische physik: gehalten an der Columbia university in the city of New York im frühjahr 1909*. S. Hirzel, 1910.

A Pohl, A Wachter, N Hatam and S Leonhardt. 2016. A computational model of a human single sinoatrial node cell. *Biomedical Physics & Engineering Express*, **2**, 035006. (doi:10.1088/2057-1976/2/3/035006)

L Priebe and DJ Beuckelmann. 1998. Simulation study of cellular electric properties in heart failure. *Circulation Research*, **82**, 1206–1223. (doi:10.1161/01.RES.82.11.1206C)

M Purhonen, H Koponen, J Tiihonen and A Tanskanen. 2012. Outcome of patients after market withdrawal of thioridazine: a retrospective analysis in a nationwide cohort. *Pharmacoepidemiology and Drug Safety*, **21**, 1227–1231. (doi:10.1002/pds.3346)

D Purves, G Augustine, D Fitzpatrick, L Katz, A LaMantia, J McNamara and S Williams. Neuroscience, 2nd edition, 2001.

Z Qu. 2011. Chaos in the genesis and maintenance of cardiac arrhythmias. *Progress in Biophysics and Molecular Biology*, **105**, 247–257. (doi:10.1016/j.pbiomolbio.2010.11.001)

D Ramaekers, H Ector, AE Aubert, A Rubens and F Van de Werf. 1998. Heart rate variability and heart rate in healthy volunteers. is the female autonomic nervous system cardioprotective? *European Heart Journal*, **19**, 1334–1341. (doi:10.1053/euhj.1998.1084)

A Raue, C Kreutz, T Maiwald, J Bachmann, M Schilling, U Klingmüller and J Timmer. 2009. Structural and practical identifiability analysis of partially observed dynamical models by exploiting the profile likelihood. *Bioinformatics*, **25**, 1923–1929. (doi:10.1093/bioinformatics/btp358)

M Reardon and M Malik. 1996. QT interval change with age in an overtly healthy older population. *Clinical Cardiology*, **19**, 949–952. (doi:10.1002/clc.4960191209)

WS Redfern, L Carlsson, AS Davis, WG Lynch, Il MacKenzie, S Palethorpe, PKS Siegl, I Strang, AT Sullivan, R Wallis *et al.* 2003. Relationships between preclinical cardiac electrophysiology, clinical QT interval prolongation and torsade de pointes for a broad range of drugs: evidence for a provisional safety margin in drug development. *Cardiovascular Research*, **58**, 32–45. (doi:10.1016/s0008-6363(02)00846-5)

CR Reeves. 1996. Heuristic search methods: A review. *Operational Research-Keynote Papers*, pages 122–149.

BJ Ridder, DJ Leishman, M Bridgland-Taylor, M Samieegohar, X Han, WW Wu, A Randolph, P Tran, J Sheng, T Danker *et al.* 2020. A systematic strategy for estimating herg block potency and its implications in a new cardiac safety paradigm. *Toxicology and Applied Pharmacology*, **394**, 114961. (doi:10.1016/j.taap.2020.114961)

C Robert. *The Bayesian choice: from decision-theoretic foundations to computational implementation*. Springer Science & Business Media, 2007.

DM Roden. Taking the "idio" out of "idiosyncratic": predicting torsades de pointes, 1998. (doi:10.1111/j.1540-8159.1998.tb00148.x).

L Romero, J Cano, J Gomis-Tena, B Trenor, F Sanz, M Pastor and J Saiz. 2018. In silico QT and APD prolongation assay for early screening of drug-induced proarrhythmic risk. *Journal of Chemical Information and Modeling*, **58**, 867–878. (doi:10.1021/acs.jcim.7b00440)

H Roukoz and W Saliba. 2007. Dofetilide: a new class III antiarrhythmic agent. *Expert Review of Cardiovascular Therapy*, **5**, 9–19. (doi:10.1586/14779072.5.1.9)

Y Rudy and JR Silva. 2006. Computational biology in the study of cardiac ion channels and cell electrophysiology. *Quarterly Reviews of Biophysics*, **39**, 57. (doi:10.1017/S0033583506004227)

PT Sager, G Gintant, JR Turner, S Pettit and N Stockbridge. 2014. Rechanneling the cardiac proarrhythmia safety paradigm: a meeting report from the cardiac safety research consortium. *American Heart Journal*, **167**, 292–300. (doi:10.1016/j.ahj.2013.11.004)

F Sahli-Costabal, K Seo, E Ashley and E Kuhl. 2020. Classifying drugs by their arrhythmogenic risk using machine learning. *Biophysical Journal*, **118**, 1165–1176. (doi:10.1016/j.bpj.2020.01.012)

B Sakmann and E Neher. 1984. Patch clamp techniques for studying ionic channels in excitable membranes. *Annual Review of Physiology*, **46**, 455–472. (doi:10.1146/annurev.ph.46.030184.002323)

DA Sampedro-Puente, J Fernandez-Bes, B Porter, S Van Duijvenboden, P Taggart and E Pueyo. 2019. Mechanisms underlying interactions between low-frequency oscillations and beat-to-beat variability of celullar ventricular repolarization in response to sympathetic stimulation: implications for arrhythmogenesis. *Frontiers in Physiology*, page 916. (doi:10.3389/fphys.2019.00916)

MC Sanguinetti, C Jiang, ME Curran and MT Keating. 1995. A mechanistic link between an inherited and an acquird cardiac arrthytmia: HERG encodes the IKr potassium channel. *Cell*, **81**, 299–307. (doi:10.1016/0092-8674(95)90340-2)

MC Sanguinetti and NK Jurkiewicz. 1990. Two components of cardiac delayed rectifier K+ current. differential sensitivity to block by class III antiarrhythmic agents. *Journal of General Physiology*, **96**, 195–215. (doi:10.1085/jgp.96.1.195)

Sasha River Santilla. Blood oxygenation to the pulmonary and systemic circulation. https://commons.wikimedia.org/wiki/File:Blood_oxygenation_to_the_pulmonary_and_systemic_circulation.svg, 2022. Published under the Creative Commons Attribution-Share Alike 4.0 International license. No changes were applied.

D Sato, LH Xie, AA Sovari, DX Tran, N Morita, F Xie, H Karagueuzian, A Garfinkel, JN Weiss and Z Qu. 2009. Synchronization of chaotic early afterdepolarizations in the genesis of cardiac arrhythmias. *Proceedings of the National Academy of Sciences*, **106**, 2983–2988. (doi:10.1073/pnas.0809148106)

DJ Schulz, J-M Goaillard and E Marder. 2006. Variable channel expression in identified single and electrically coupled neurons in different animals. *Nature Neuroscience*, **9**, 356–362. (doi:10.1038/nn1639)

G Schwarz. 1978. Estimating the dimension of a model. *The Annals of Statistics*, pages 461–464.

Sentewolf. Concept of directional optimization in CMA-ES algorithm. https://commons.wikimedia.org/wiki/File:Concept_of_directional_optimization_in_CMA-ES_algorithm.png, 2008.

CE Shannon. 1949. Communication in the presence of noise. *Proceedings of the IRE*, **37**, 10–21.

TR Shannon, F Wang, J Puglisi, C Weber and DM Bers. 2004. A mathematical treatment of integrated Ca dynamics within the ventricular myocyte. *Biophysical Journal*, **87**, 3351–3371. (doi:10.1529/biophysj.104.047449)

LB Sheiner and SL Beal. 1980. Evaluation of methods for estimating population pharmacokinetic parameters. I. Michaelis-Menten model: routine clinical pharmacokinetic data. *Journal of Pharmacokinetics and Biopharmaceutics*, **8**, 553–571. (doi:10.1007/BF01060053)

BN Singh, G Ellrodt and CT Peter. 1978. Verapamil: a review of its pharmacological properties and therapeutic use. *Drugs*, **15**, 169–197. (doi:10.2165/00003495-197815030-00001)

D Smirnov, A Pikunov, R Syunyaev, R Deviatiiarov, O Gusev, K Aras, A Gams, A Koppel and IR Efimov. 2020. Genetic algorithm-based personalized models of human cardiac action potential. *PLoS One*, **15**, e0231695. (doi:10.1371/journal.pone.0231695)

P Stewart, OV Aslanidi, D Noble, PJ Noble, MR Boyett and H Zhang. 2009. Mathematical models of the electrical action potential of Purkinje fibre cells. *Philosophical Transactions of the Royal Society A: Mathematical, Physical and Engineering Sciences*, **367**, 2225–2255. (doi:10.1098/rsta.2008.0283)

EW Steyerberg, SE Bleeker, HA Moll, DE Grobbee and KGM Moons. 2003. Internal and external validation of predictive models: a simulation study of bias and precision in small samples. *Journal of Clinical Epidemiology*, **56**, 441–447. (doi:10.1016/s0895-4356(03)00047-7)

EW Steyerberg and FE Harrell Jr. 2016. Prediction models need appropriate internal, internal-external, and external validation. *Journal of Clinical Epidemiology*, **69**, 245. (doi:10.1016/j.jclinepi.2015.04.005)

E Surovyatkina, D Noble, D Gavaghan and A Sher. 2010. Multistability property in cardiac ionic models of mammalian and human ventricular cells. *Progress in Biophysics and Molecular Biology*, **103**, 131–141. (doi:10.1016/j.pbiomolbio.2010.01.004)

Z Syed, E Vigmond, Stanley Nattel and LJ Leon. 2005. Atrial cell action potential parameter fitting using genetic algorithms. *Medical and Biological Engineering and Computing*, **43**, 561–571. (doi:10.1007/BF02351029)

KHWJ Ten Tusscher, D Noble, P-J Noble and AV Panfilov. 2004. A model for human ventricular tissue. *American Journal of Physiology-Heart and Circulatory Physiology*, **286**, H1573–H1589. (doi:10.1152/ajpheart.00794.2003)

KHWJ Ten Tusscher and AV Panfilov. 2006. Alternans and spiral breakup in a human ventricular tissue model. *American Journal of Physiology-Heart and Circulatory Physiology*, **291**, H1088–H1100. (doi:10.1152/ajpheart.00109.2006)

JCA Thomas Jr, PA Springer, GE Loeb, Y Berwald-Netter and LM Okun. 1972. A miniature microelectrode array to monitor the bioelectric activity of cultured cells. *Experimental cell Research*, **74**, 61–66. (doi:10.1016/0014-4827(72)90481-8)

MB Thomsen, SC Verduyn, M Stengl, JDM Beekman, G de Pater, J van Opstal, PGA Volders and MA Vos. 2004. Increased short-term variability of repolarization predicts d-sotalol–induced torsades de pointes in dogs. *Circulation*, **110**, 2453–2459. (doi:10.1161/01.CIR.0000145162.64183.C8)

M Tomaiuolo, R Bertram, G Leng and J Tabak. 2012. Models of electrical activity: calibration and prediction testing on the same cell. *Biophysical Journal*, **103**, 2021–2032. (doi:10.1016/j.bpj.2012.09.034)

J Tomek, A Bueno-Orovio, E Passini, X Zhou, A Minchole, O Britton, C Bartolucci, S Severi, A Shrier, L Virag *et al.* 2019. Development, calibration, and validation of a novel human ventricular myocyte model in health, disease, and drug block. *eLife*, **8**, e48890. (doi:10.7554/eLife.48890)

J Tomek, A Bueno-Orovio and B Rodriguez. 2020. ToR-ORd-dynCl: an update of the ToR-ORd model of human ventricular cardiomyocyte with dynamic intracellular chloride. *BioRxiv*. (doi:10.1101/2020.06.01.127043)

G Tononi, O Sporns and GM Edelman. 1999. Measures of degeneracy and redundancy in biological networks. *Proceedings of the National Academy of Sciences*, **96**, 3257–3262. (doi:10.1073/pnas.96.6.3257)

C Tricarico, P Pinzani, S Bianchi, M Paglierani, V Distante, M Pazzagli, SA Bustin and C Orlando. 2002. Quantitative real-time reverse transcription polymerase chain reaction: normalization to rrna or single housekeeping genes is inappropriate for human tissue biopsies. *Analytical Biochemistry*, **309**, 293–300. (doi:10.1016/s0003-2697(02)00311-1)

C Trovato, M Mohr, F Schmidt, E Passini and B Rodriguez. 2022. Cross clinical-experimental-computational qualification of in silico drug trials on human cardiac Purkinje cells for proarrhythmia risk prediction. *Frontiers in Toxicology*, page 124. (doi:10.3389/ftox.2022.992650)

C Trovato, E Passini, N Nagy, A Varró, N Abi-Gerges, S Severi and B Rodriguez. 2020. Human Purkinje in silico model enables mechanistic investigations into automaticity and pro-arrhythmic abnormalities. *Journal of Molecular and Cellular Cardiology*. (doi:10.1016/j.yjmcc.2020.04.001)

LS Tsimring. 2014. Noise in biology. *Reports on Progress in Physics*, **77**, 026601. (doi:10.1088/0034-4885/77/2/026601)

R Tuo and CFJ Wu. 2015. Efficient calibration for imperfect computer models. *The Annals of Statistics*, **43**, 2331–2352. (doi:10.1214/15-AOS1314)

GI Valderrama-Bahamóndez and H Fröhlich. 2019. MCMC techniques for parameter estimation of ODE based models in systems biology. *Frontiers in Applied Mathematics and Statistics*, **5**, 55. (doi:10.3389/fams.2019.00055)

RW Van Dyke and BF Scharschmidt. 1987. Effects of chlorpromazine on Na+–K+-ATPase pumping and solute transport in rat hepatocytes. *American Journal of Physiology-Gastrointestinal and Liver Physiology*, **253**, G613–G621. (doi:10.1152/ajpgi.1987.253.5.G613)

HP Van Geijn, JE Lenglet and AC Bolte. 2005. Nifedipine trials: effectiveness and safety aspects. *BJOG: An International Journal of Obstetrics & Gynaecology*, **112**, 79–83. (doi:10.1111/j.1471-0528.2005.00591.x)

D Van Ravenzwaaij, P Cassey and SD Brown. 2018. A simple introduction to Markov Chain Monte–Carlo sampling. *Psychonomic Bulletin & Review*, **25**, 143–154. (doi:10.3758/s13423-016-1015-8)

HM Vargas, MG Rolf, TA Wisialowski, W Achanzar, A Bahinski, A Bass, CT Benson, KW Chaudhary, N Couvreur, C Dota *et al.* 2021. Time for a fully integrated nonclinical–clinical risk assessment to streamline qt prolongation liability determinations: A pharma industry perspective. *Clinical Pharmacology & Therapeutics*, **109**, 310–318. (doi:10.1002/cpt.2029)

A Varghese and GR Sell. 1997. A conservation principle and its effect on the formulation of Na–Ca exchanger current in cardiac cells. *Journal of theoretical Biology*, **189**, 33–40. (doi:10.1006/jtbi.1997.0487)

M Varshneya, X Mei and EA Sobie. 2021. Prediction of arrhythmia susceptibility through mathematical modeling and machine learning. *Proceedings of the National Academy of Sciences*, **118**. (doi:10.1073/pnas.2104019118)

K Veys, AJ Labro, E De Schutter and DJ Snyders. 2012. Quantitative single-cell ion-channel gene expression profiling through an improved qRT-PCR technique combined with whole cell patch clamp. *Journal of Neuroscience Methods*, **209**, 227–234. (doi:10.1016/j.jneumeth.2012.06.008)

J Vicente, R Zusterzeel, L Johannesen, J Mason, P Sager, V Patel, MK Matta, Z Li, J Liu, C Garnett *et al.* 2018. Mechanistic model-informed proarrhythmic risk assessment of drugs: review of the "CiPA" initiative and design of a prospective clinical validation study. *Clinical Pharmacology & Therapeutics*, **103**, 54–66. (doi:10.1002/cpt.896)

AF Villaverde, S Bongard, K Mauch, D Müller, E Balsa-Canto, J Schmid and JR Banga. 2015. A consensus approach for estimating the predictive accuracy of dynamic models in biology. *Computer Methods and Programs in Biomedicine*, **119**, 17–28. (doi:10.1016/j.cmpb.2015.02.001)

AF Villaverde, E Raimúndez, J Hasenauer and JR Banga. 2019. A comparison of methods for quantifying prediction uncertainty in systems biology. *IFAC-PapersOnLine*, **52**, 45–51. (doi:10.1016/j.ifacol.2019.12.234)

AF Villaverde, E Raimúndez, J Hasenauer and JR Banga. 2022. Assessment of prediction uncertainty quantification methods in systems biology. *IEEE/ACM Transactions on Computational Biology and Bioinformatics*. (doi:10.1109/TCBB.2022.3213914)

A Wald and J Wolfowitz. 1940. On a test whether two samples are from the same population. *The Annals of Mathematical Statistics*, **11**, 147–162. (doi:10.1214/aoms/1177731909)

J Walmsley, GR Mirams, J Pitt-Francis, B Rodriguez and K Burrage. 2015. Application of stochastic phenomenological modelling to cell-to-cell and beat-to-beat electrophysiological variability in cardiac tissue. *Journal of Theoretical Biology*, **365**, 325–336. (doi:10.1016/j.jtbi.2014.10.029)

KB Walsh, J Zhang, JW Fuseler, N Hilliard and GH Hockerman. 2007. Adenoviral-mediated expression of dihydropyridine-insensitive L-type calcium channels in cardiac ventricular myocytes and fibroblasts. *European Journal of Pharmacology*, **565**, 7–16. (doi:10.1016/j.ejphar.2007.02.049)

K Wang, P Lee, GR Mirams, P Sarathchandra, TK Borg, DJ Gavaghan, P Kohl and C Bollensdorff. 2015. Cardiac tissue slices: preparation, handling, and successful optical

mapping. *American Journal of Physiology - Heart and Circulatory Physiology*, **308**, H1112–H1125. (doi:10.1152/ajpheart.00556.2014)

DG Whittaker, M Clerx, CL Lei, DJ Christini and GR Mirams. 2020. Calibration of ionic and cellular cardiac electrophysiology models. *Wiley Interdisciplinary Reviews: Systems Biology and Medicine*, **12**, e1482. (doi:10.1002/wsbm.1482)

F-G Wieland, AL Hauber, M Rosenblatt, C Tönsing and J Timmer. 2021. On structural and practical identifiability. *Current Opinion in Systems Biology*.

R Wilders, HJ Jongsma and AC Van Ginneken. 1991. Pacemaker activity of the rabbit sinoatrial node. A comparison of mathematical models. *Biophysical Journal*, **60**, 1202–1216. (doi:10.1016/S0006-3495(91)82155-5)

RL Woosley and KA Romer. Qtdrugs list. "Www.Crediblemeds.Org", 1999. Accessed 2021-09-01.

Y Yoo, DU Jeong, A Marcellinus and KM Lim. 2021. An artificial neural network-based drug proarrhythmia assessment using electrophysiological characteristics of cardiomyocytes. *Journal of Biomedical Engineering Research*, **42**, 287–294. (doi:10.9718/JBER.2021.42.6.287)

T Yu, CM Lloyd, DP Nickerson, MT Cooling, AK Miller, A Garny, JR Terkildsen, J Lawson, RD Britten, PJ Hunter *et al.* 2011. The Physiome Model Repository 2. *Bioinformatics*, **27**, 743–744. (doi:10.1093/bioinformatics/btq723)

A Zaza and M Rosen. *An introduction to cardiac electrophysiology*. CRC Press, 2000.

YH Zhang and JC Hancox. 2002. Mode-dependent inhibition by quinidine of Na+–Ca2+ exchanger current from guinea-pig isolated ventricular myocytes. *Clinical and Experimental Pharmacology and Physiology*, **29**, 777–781. (doi:10.1046/j.1440-1681.2002.03731.x)

X Zhou, Y Qu, E Passini, A Bueno-Orovio, Y Liu, HM Vargas and B Rodriguez. 2020. Blinded in silico drug trial reveals the minimum set of ion channels for torsades de pointes risk assessment. *Frontiers in Pharmacology*, **10**, 1643. (doi:10.3389/fphar.2019.01643)